CHARACTERIZATION OF LEAD-FREE SOLDERS FOR ELECTRONIC PACKAGING

Except where reference is made to the work of others, the work described in this dissertation is my own or was done in collaboration with my advisory committee. This dissertation does not include proprietary or classified information.

Hongtao Ma

Certificate of Approval:

R. Wayne Johnson, Co-Chair
Ginn Distinguished Professor
Electrical and Computer Engineering

Jeffrey C. Suhling, Co-Chair
Quina Distinguished Professor
Mechanical Engineering

Thaddeus Roppel
Associate Professor
Electrical and Computer Engineering

Stuart Wentworth
Associate Professor
Electrical and Computer Engineering

Joe F. Pittman
Interim Dean
Graduate School

CHARACTERIZATION OF LEAD-FREE SOLDERS
FOR ELECTRONIC PACKAGING

Hongtao Ma

A Dissertation

Submitted to

the Graduate Faculty of

Auburn University

in Partial Fulfillment of the

Requirements for the

Degree of

Doctor of Philosophy

Auburn, Alabama
May 10, 2007

CHARACTERIZATION OF LEAD-FREE SOLDERS

FOR ELECTRONIC PACKAGING

Hongtao Ma

Signature of Author

Date of Graduation

VITA

Hongtao Ma, son of Peiwu Ma and Xinfang Feng, was born September 9, 1975, in Lantian, Shaanxi Province, People's Republic of China. He graduated from BeiGuan High School in Lantian in July 1990. He attended Xi'an Jiaotong University for four years and graduated with a Bachelor of Engineering degree in Materials Science and Engineering in July 1997. After gradation, he entered the Northwest Institute for Nonferrous Metal Research in Xi'an as a materials engineer. His work was in the areas of research and development of Titanium and Titanium alloys for new applications. He enrolled at Auburn University in March 2000 and earned his Masters of Science degree in Materials Engineering in May 2002. Immediately after earning his M.S. degree, he began pursuing his PhD degree in Electrical and Computer Engineering in the area of electronic packaging. He is very happy to have married Ms. Hui Pan in July 2003.

DISSERTATION ABSTRACT

CHARACTERIZATION OF LEAD-FREE SOLDERS FOR ELECTRONIC PACKAGING

Hongtao Ma

Doctor of Philosophy, May 10, 2007
(M.S., Auburn University, 2002)
(B.E., Xi'an Jiaotong University, 1997)

214 Typed Pages

Directed by Jeffrey C. Suhling and R. Wayne Johnson

The characterization of lead-free solders, especially after isothermal aging, is very important in order to accurately predict the reliability of solder joints. However, due to lack of experimental testing standards and the high homologous temperature of solder alloys ($T_h > 0.5T_m$ even at room temperature), there are very large discrepancies in both the tensile and creep properties provided in current databases for both lead-free and Sn-Pb solder alloys. In this research, mechanical measurements of isothermal aging effects and the resulting changes in the materials behavior of lead-free solders were performed. A novel specimen preparation procedure was developed where the solder uniaxial test specimens are formed in high precision rectangular cross-section glass tubes using a vacuum suction process. Using specimens fabricated with the developed procedure, isothermal aging effects and viscoplastic material behavior evolution have been characterized for 95.5Sn-4.0Ag-0.5Cu (SAC405) and 96.5Sn-3.0Ag-0.5Cu (SAC305) lead-free solders, which are commonly used as the solder ball alloy in lead-free BGAs and other components. Analogous tests were performed with 63Sn-37Pb eutectic solder samples for comparison purposes. Up to 40% reduction in tensile strength was observed for water quenched specimens after two months of aging at room temperature. Creep deformation also increased dramatically with increasing aging durations. Microstructural changes during room temperature aging were also observed and recorded for the solder alloys and correlated with the observed mechanical behavior changes.

Aging effects at elevated temperatures for up to 6 months were also investigated. Thermal aging caused significant tensile strength loss and deterioration of creep deformation. The thermal aging results also showed that after an initial tensile strength drop, the Sn-Pb eutectic solder reached a relatively stable stage after 200 hours of aging. However, for SAC alloy, both the tensile and creep properties continuously changed with increasing aging time. The creep resistance of SAC alloy was lower than that of Sn-Pb at longer aging durations at elevated temperature. Solder alloys are extremely sensitive to changes in both temperature and strain rate. A linear relationship was found between the temperature and the tensile properties, while a power law relationship was found between strain rate and tensile properties. Constitutive models have also been developed with multiple variables of strain rate and temperature. Creep testing was conducted at different stress levels and temperatures to explore the constitutive modeling. SAC alloy was found to have higher creep resistance and activation energy than the Sn-Pb solder without thermal aging.

ACKNOWLEDGEMENTS

The author would like to thank his advisors Dr. Jeffrey Suhling and Dr. Wayne Johnson for their support, guidance and mentorship throughout this research. Sincere gratitude and appreciation are also extended to my committee members, Dr. Thaddeus Roppel and Dr. Stuart Wentworth for their valuable insights and precious time in the course of this research. The author particularly thanks Dr. Michael Bozack for his corporation and many discussions regarding the progress of the lead-free soldering project. Thanks are also extended to all my lab-mates, coworkers and friends, Dr. Kaysar Rahim, Chang Lin, Yifei Zhang, Jordan Roberts, and John Marcell, for their encouragement and friendship. The author is in debt to his parents, who support him endlessly although they are so far away. Finally, the author wants to thank his beautiful wife, Hui Pan. Without her understanding and love, all of this would not be possible.

Style manual or journal used: Guide to Preparation and Submission of Theses and Dissertations

Computer software used: Microsoft Office 2003, Mathcad, Excel, Curvefit Expert 3.1, Datafit 8.1 and Sigmaplot 8.0

TABLE OF CONTENTS

LIST OF FIGURES

LIST OF TABLES

CHAPTER 1

INTRODUCTION

1.1 Lead-free Solders in Electronics

The use of solder alloys as metal joint materials can be dated back thousands of years. With the emergence of the modern electronic packaging technology over the last few decades, solder alloys have been used as the interconnecting material in electronic packaging. Solder joints provide both the electrical connection and mechanical support in electronic packaging modules.

Eutectic or near eutectic tin/lead (Sn-Pb) solder (melting temperature T_M = 183 °C) has long been the predominant choice of the electronics industry due to its outstanding solderability and reliability. However, legislation that mandates the removal of lead from electronics has been actively pursued in the European Union and worldwide during the last 15 years due to environmental and health concerns regarding the high lead content in eutectic Sn-Pb solder. Lead is a proven toxic substance which can cause a range of negative impacts to both the environment and the human body [1]. Due to the current rapid improvements in electronic technology and the high cost of recycling processes, the recycling rate of electronic devices is very low, especially for high technology products, such as computers. It has been reported that less than 2% of the computers produced were recycled in 1998 [2]. The majority of the used electronics will end up in landfills where the lead content will eventually leach out into the soil and hence the local ecosystem.

The European Union is particularly aggressive in pursuing the banning of lead from electronics. In June 2000, the EU adopted two directives, the Waste of Electrical and Electronic Equipment (WEEE) and the Directive of the Restriction of the Use of Certain Hazardous Substances (RoHS) [3]. The WEEE directive requires that lead has to be removed from any end-of-life electrical or electronic components. The RoHS specifically bans lead from electrical and electronic components manufactured after July 1, 2006. As a result of the enforcement of the directives, all electrical or electronic equipment and devices produced in or imported to E.U. member states must comply with these lead-free standards except those items that are exempted from the bans.

In Japan, although there is no specific government ban of lead in electronic components, in 1998, the advisory committee of JEIDA (Japan Institute of Electronics Industry Development Association) put forward a roadmap for the commercialization of lead-free solders [4], and recommended lead-free alternatives for industry. The electronic industry in Japan is very active in pursuing lead-free products and many companies have brought their lead-free products onto the market much earlier than the E.U. directives' effective dates [1, 5], including Panasonic in 2001, Sony in 2001: Toshiba in 2000, NEC in 2002, and Hitachi in 2001.

In the United States, there is again no specific government ban of lead from electrical and electronic devices. However, the U.S. Environmental Protection Agency (EPA) has listed lead among the top 17 chemicals that pose the greatest threat to human health [1]. The IPC (formerly known as the Institute of Interconnecting and Packaging

Electrical Circuits) has also developed a roadmap for the lead-free movement in the U.S. [6]. The roadmap is designed to encourage both industry and academic institutes to actively research and development of lead-free assembly processes and to be prepared to respond to the worldwide lead-free movement. In recent years, many U.S. companies, including Motorola, Cisco, and Intel, have also been actively pursuing lead-free products in order to protect their world wide market shares. Many universities have also been actively funding lead-free related research.

Other countries, such as China, and South Korea, which are emerging electronic manufacturing bases, have also adopted directives similar to those of the European Union. Although the implementation deadlines and products covered by such legislation continue to evolve worldwide, it is clear that laws requiring the conversion to lead-free electronics are becoming a reality worldwide. Other factors that are affecting the push towards the elimination of lead in electronics are the market differentiation and advantage being realized by companies producing so-called “green” products that are lead-free. The companies who first successfully move into lead-free products will have a definite “first move” advantage over their competitors, which in today’s competitive markets translates to profits and survival.

1.2 Lead-free Solders

1.2.1 Overview

To be considered an alternative to Sn-Pb solder, lead-free candidates should have similar or better properties and reliability to those possessed by eutectic or near eutectic Sn-Pb solders. According to recent reports [7, 8], Pb in solders contributes outstanding properties to the overall reliability of the Sn-Pb solder, such as the following:

- Pb reduces the surface tension of pure tin to improve the wetting ability.
- Pb enables tin and copper to rapidly form intermetallic compounds by diffusion.
- Pb provides ductility to Sn-Pb solders.
- the addition of Pb prevents the transformation of β-tin to α-tin. If the transformation occurs, it will cause dramatic volume increase and loss of structural integrity and hence a loss of reliability. The β-tin to α-tin transformation in lead-free solders is also called “tin pest” or “tin disease”. Karlya et al. observed significant “tin pest” phenomena in their lead-free solder specimens [9].
- Sn-Pb solders have a low melting temperature of 183 °C for eutectic solder, which allows the use of a low reflow temperature in the electronic packaging process and ensures the reliability of the packages.

Besides all of the above benefits of Pb, the cost of Pb is also low and it is very abundant. However, Pb is toxic, which causes the pressure from legislations worldwide.

Lee proposed some basic criteria for “perfect” lead-free alternatives [10]. The lead-free solder needs to have a similar melting temperature to existing Sn-Pb solders, particularly eutectic and near eutectic solders, in order have a similar reflow profile during the manufacturing process; good wetting ability to ensure good metallization in the manufacturing process; the same or better electrical properties to efficiently transmit the electrical signals; and adequate mechanical properties, such as creep, and fatigue, etc. to preserve the reliability of the electronic packaging products. The new lead-free solders also need to be non-toxic and relatively inexpensive.

A great deal of research is currently underway in the lead-free solder area, including projects organized by consortia including the HDPUG (High Density Packaging Users Group), the National Center for Manufacturing Sciences (NCMS), the National Institute for Standard and Technology (NIST), the National Electronics Initiative (NEMI), and the Japan Electronic Industry Development Association (JEDIA). Although no "drop in" replacement has been identified that is suitable for all applications, Sn-Ag, Sn-Ag-Cu (SAC), and other alloys involving elements such as Sn, Ag, Cu, Bi, In, and Zn have been identified as promising replacements for standard 63Sn-37Pb eutectic solder. Several SAC alloys have been proposed by industrial consortiums. These include 96.5Sn-3.0Ag-0.5Cu (SAC 305) in Japan, 95.5Sn-3.8Ag-0.7Cu (SAC 387) in the EU, and 95.5Sn-3.9Ag-0.6Cu (SAC 396) in the USA. In addition, 95.5Sn-4.0Ag-0.5Cu (SAC405) has been widely adopted as an alloy for use in BGA solder joints. The main benefits of the various SAC alloy systems are their relatively low melting temperatures compared with the 96.5Sn–3.5Ag binary eutectic alloy, as well as their superior mechanical and solderability properties when compared to other lead-free solders. A survey conducted by Soldertec shows approximately 70% of the market for reflowing lead-free solders are in the SAC series (Figure 1.1) [11]. There are some major challenges for the current series of lead-free solders. SAC series alloys have a higher melting temperature, around 217 °C, compared to 183 °C for the eutectic Sn-Pb solders. They thus require higher reflow temperature during the manufacturing process, which lead to reliability problems. The excessive build up of intermetallics formed at the interface between the solder joints and the copper pad can cause reliability problems. High costs are another issue for lead-free solders. As shown in Table1.1 [7], the price of

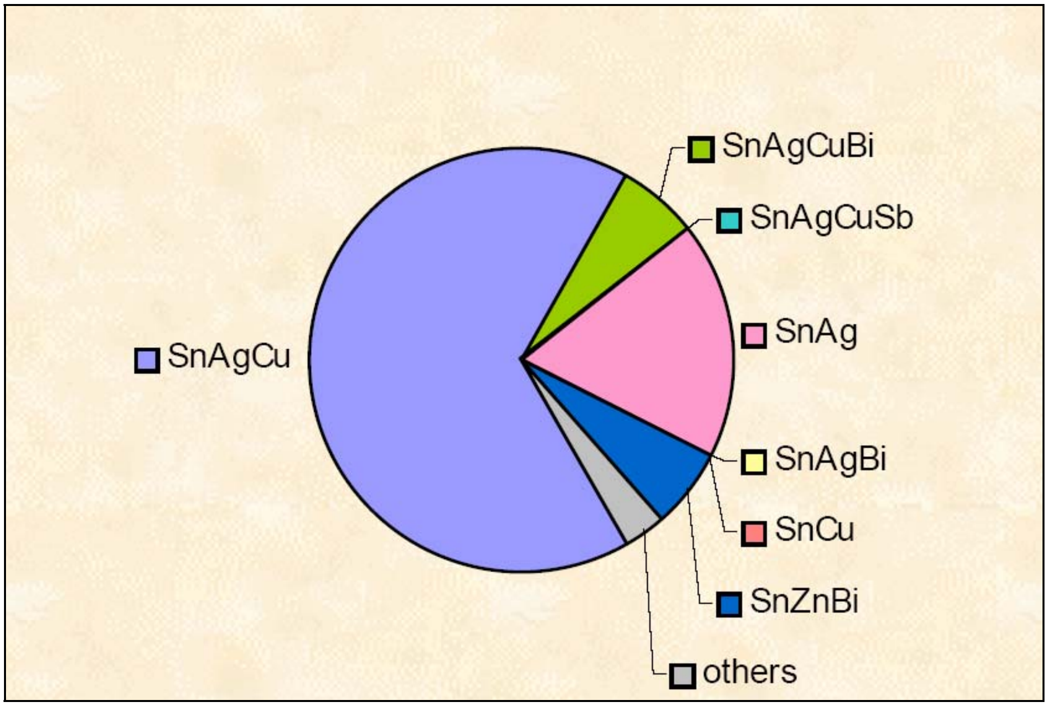

Figure 1.1 The Market Share of Different Lead-free Solders [11].

Table 1.1 Cost of Basic Solder Elements [7].

Metal Element	Cost (US$/kg)
Lead	1.10
Zinc	1.08
Copper	2.24
Antimony	2.64
Bismuth	7.15
Tin	8.67
Silver	153.19
Indium	194.59

Ag is 150 times higher than that of Pb, and Cu is twice the price of Pb. Even though the Ag and Cu content is very low, the overall price of lead-free solders will inevitably be much higher than that of Sn-Pb. A typical SAC solder is reported to be over twice the price of the Sn-Pb eutectic solders [7]. The only good news about cost is that using SAC alloys will reduce the recycling cost by $0.13/Kg, which will also increase the overall electronics recycling rate in the future [12]. Regardless all of these problems, the SAC series lead-free solders have been widely accepted by both industry and academic institutions. However, unless a "perfect" lead-free solder is found to replace the Sn-Pb series solders, research into new lead-free solders will continue for years to come.

1.2.2 Sn-Ag-Cu Lead-free Solders Series

Of the many lead-free solder series proposed in the last decade or so, Sn-Ag-Cu (SAC) series alloys have emerged as the most widely accepted (Figure 1.1). Soldertec's survey shows that the most popular SAC are the near eutectic SAC alloys [11], which consist of 3.0-4.0% of Ag and 0.5-1.0% of Copper (Figure 1.2). The melting point of these near eutectic SAC alloys is 217°C, which is lower than the 96.5Sn–3.5Ag binary eutectic alloy at 221 °C. In the SAC system, the addition of Cu both lowers the melting temperature and improves the wettability [13].

Figure 1.3 shows a typical 3-D ternary phase diagram. The contours on the top surfaces of the figure represent the isothermal lines. Each of the 3 sectors represents the binary phase diagram of two of the three elements. The center of the diagram, where the isothermal lines reach the common, lowest point, is the eutectic point of the ternary system [14]. Figure 1.4 is the top view (2-D) of the ternary phase diagram of Sn-Ag-Cu.

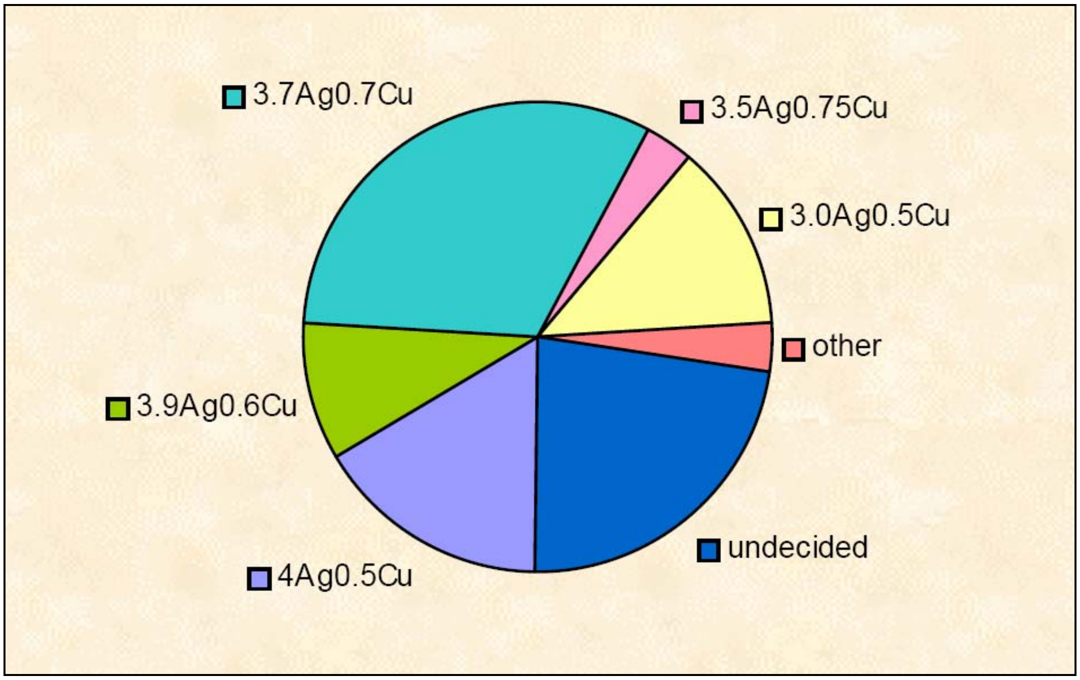

Figure 1.2 Survey of the Market Share of Different Types of SAC Alloys [11].

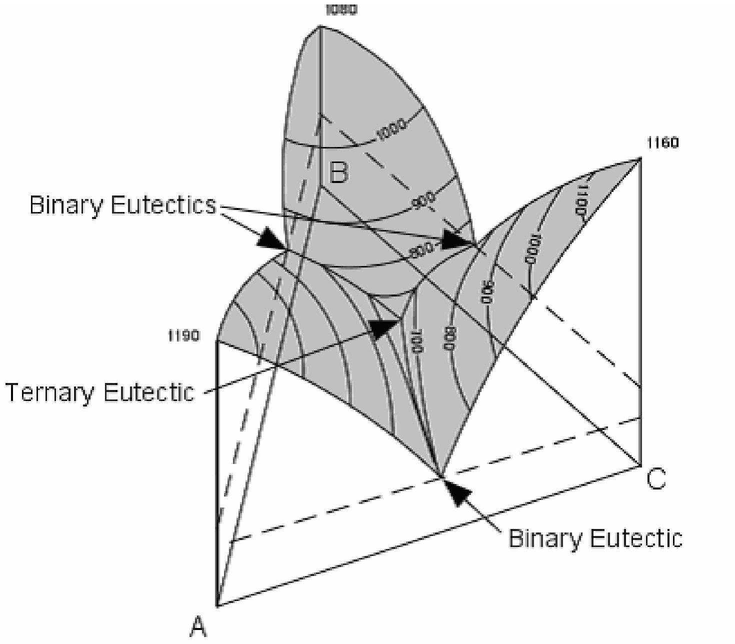

Figure 1.3 Typical 3-D Ternary Phase Diagram [14].

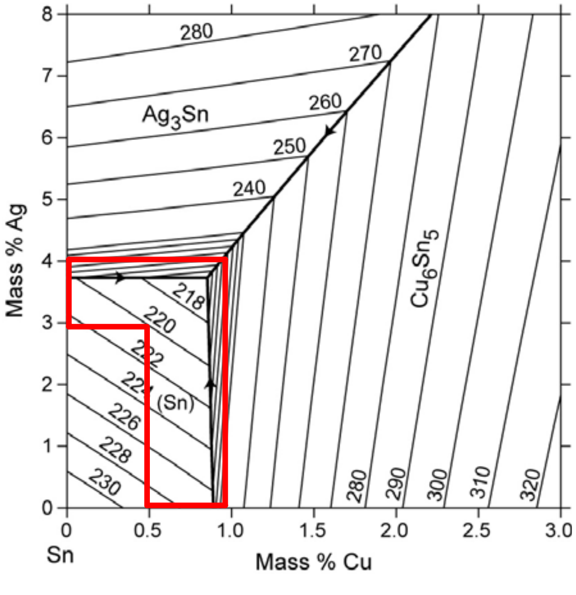

Figure 1.4 Sn-Ag-Cu Ternary Phase Diagram [15].

The area indicated in the red box is the near eutectic region. Most of the SAC alloy compositions currently on the market are within this region. The eutectic and near eutectic melting temperature has been determined to be 217 °C, although the precise eutectic point is not known [13].

In SAC alloys, the formation of intermetallic compounds between the primary elements Sn and Ag, and Cu affect all the properties of the alloys. According to the binary phase diagram shown in Figures 1.5-1.7, there are three possible intermetallic compounds that may be formed: Ag_3Sn forms due to the reaction between Sn and Ag (Figure 1.5) and Cu_6Sn_5 forms due to the Sn and Cu reaction (Figure 1.6), but Cu_3Sn will not form at the eutectic point unless the Cu content is high enough for the formation of Cu_3Sn at higher temperatures, so in bulk specimens Cu_3Sn is not presented. Ag can also react with Cu to form Ag rich α phase and Cu rich β phase (Figure 1.7). However, there is no reaction between Ag and Cu to form any kind of intermetallic compounds. Figure 1.8 shows a typical SAC structure with eutectic Sn matrix (2 in the picture) with Ag_3Sn (1 in the picture) intermetallic compounds [16]. The particles of intermetallic compounds possess much higher strength than the bulk material [17, 18]. Fine intermetallic particles in the Sn matrix can therefore strengthen the alloys. The intermetallic compounds can also improve the fatigue life of the solders, as SAC alloys are reported to be 3-4 times better fatigue properties than the Sn-Pb eutectic solders [19]. The higher fatigue resistance is believed to be contributed by the interspersed Ag_3Sn and Cu_6Sn_5 particles, which pin and block the movement of dislocations [19]. The many patents that have been granted for SAC systems have limited their use and hindered research on several of the SAC alloys, but fortunately the alloy Sn-4.0Ag-0.5Cu has not been patented [20].

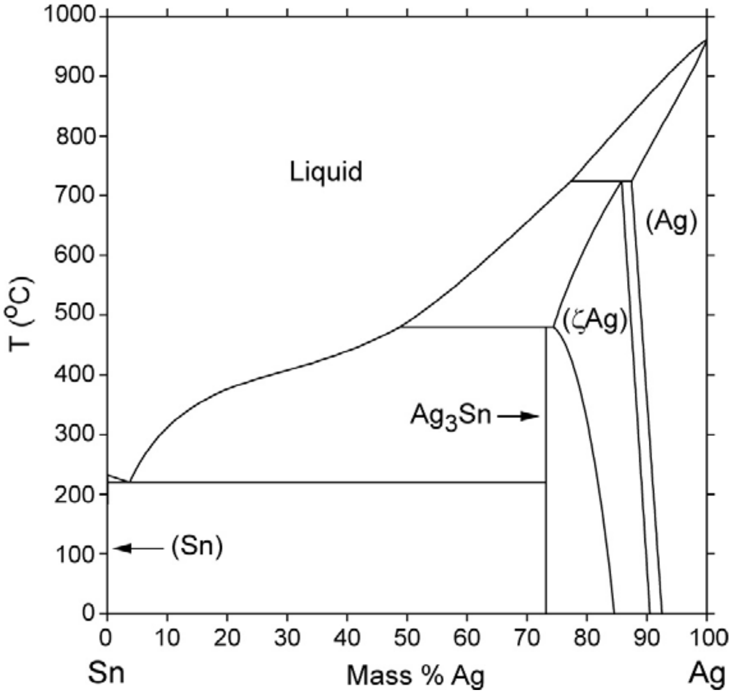

Figure 1.5 Sn-Ag Binary Phase Diagram [15].

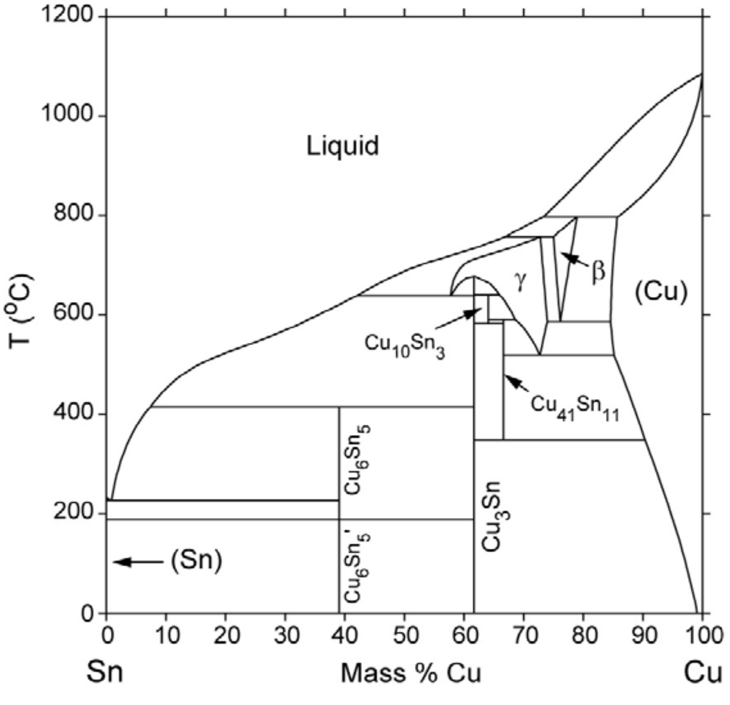

Figure 1.6 Sn-Cu Binary Phase Diagram [15].

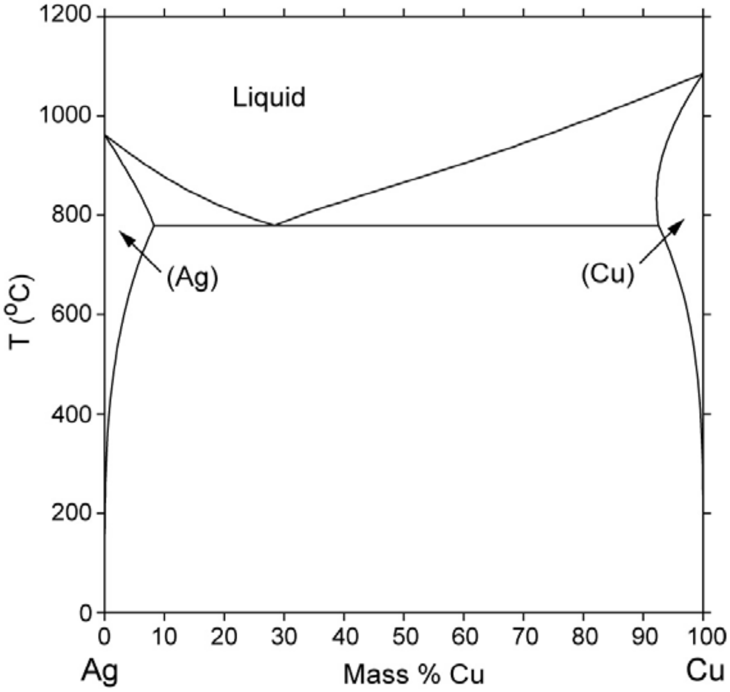

Figure 1.7 Ag-Cu Binary Phase Diagram [15].

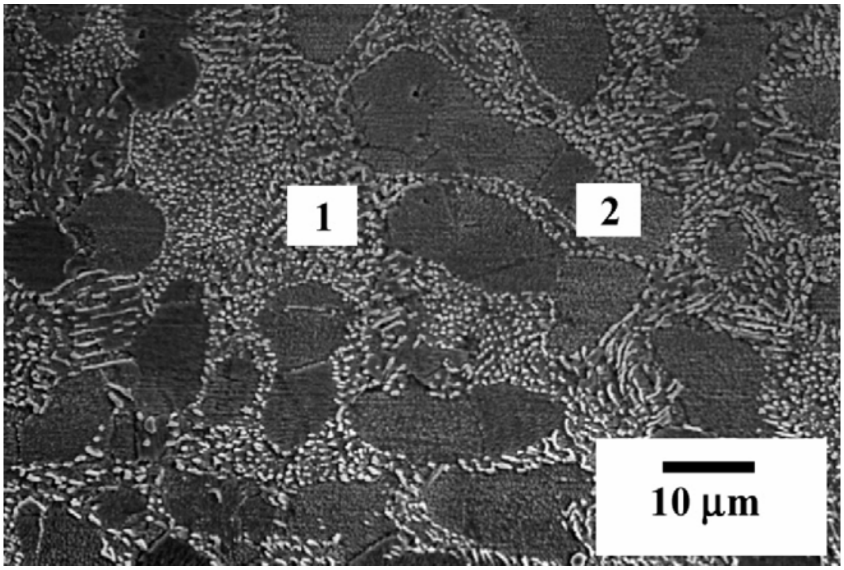

Figure 1.8 Typical Microstructure of SAC Alloys [16].

1.3 Mechanical Properties

In addition to conducting electricity, solder joints provide mechanical support for electronic devices. The mechanical properties of solder alloys are therefore critically important in producing reliable products. In determining the mechanical properties of solders, tensile properties and creep are of particular concern and have thus been most intensively investigated.

1.3.1 Tensile Properties

Tensile properties are generally described by stress-strain curves. In engineering practice *engineering stress* and *engineering strain* are defined as follows [21]:

$$\sigma = \frac{P}{A_0} \tag{1.1}$$

$$\varepsilon = \frac{l_f - l_0}{l_0} \tag{1.2}$$

where P is the load, A_0 is the initial cross-sectional area, l_f is the final gage length and l_0 is the initial gage length.

As shown in Figure 1.9, a typical engineering stress-strain curve for solder alloys consists of an elastic region and a plastic region. In the elastic region, the engineering stress is linear, with the engineering strain conforming to Hooke's law as follows [22]:

$$\sigma = E\varepsilon \tag{1.3}$$

E is the elastic modulus (Young's modulus), which can be determined from the slope of the elastic portion of the stress-strain curve. σ is the engineering stress and ε is the engineering strain. In the elastic region, if the load is removed the specimen can return to its original dimensions.

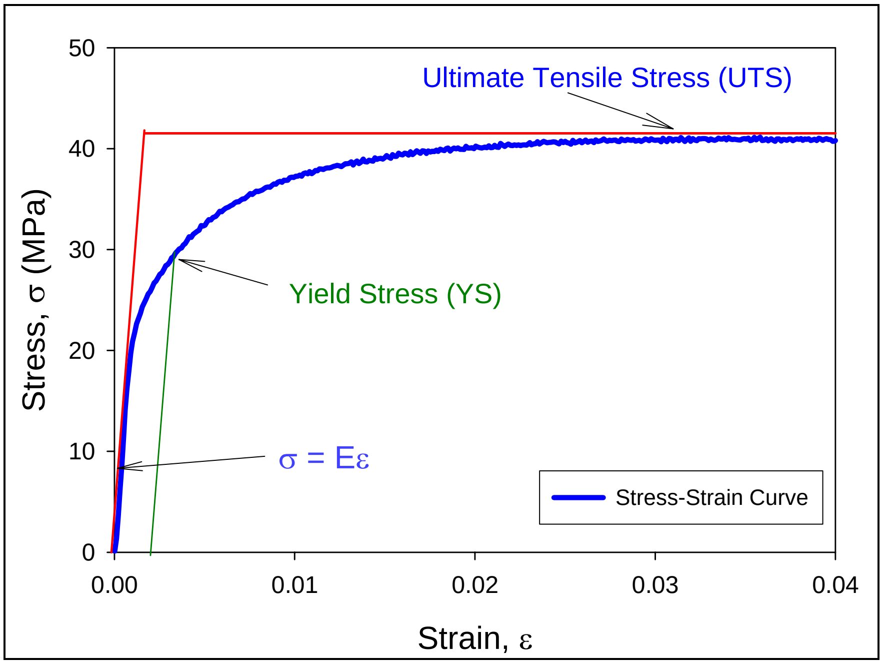

Figure 1.9 Typical Stress-Strain Curve.

There is a wide range of values for the elastic modulus for different materials. Hertzberg described that the modulus of elasticity corresponds to the interatomic forces between adjacent atoms [21]. Gilman showed that the elastic modulus is negatively proportional to a power of the equilibrium adjacent atom distance X_0 as follows [23]:

$$E \propto \frac{1}{(X_0)^n} \tag{1.4}$$

Thus, when the distance between the atoms is larger the elastic modulus will be smaller. Ralls *et al.* showed that the elastic modulus of metal will decrease with increasing temperature [24]. The underlying reason for this is because the distance between adjacent atoms increases at higher temperatures. In engineering practice, the value of the elastic modulus obtained from the slope of the stress-strain curve is the static modulus, which is generally referred as the apparent or effective elastic modulus and also includes small inelastic deformations or time-dependent deformations such as creep. The apparent elastic modulus is usually smaller than the dynamic modulus measured by the acoustic or ultrasonic wave method, which largely eliminates the inelastic deformation due to rapid wave propagation [62, 67, 82].

When the load is high enough to exceed the elastic limits the material will experience plastic deformation, which is permanent. Specimens subject to plastic deformation will simultaneously elongate and decrease in diameter. The Yield Stress (YS) is defined as just enough stress to cause the onset of plastic deformation. However, YS is difficult to determine. In engineering practice, a specified small amount of plastic deformation is used, with 0.2% being the widely accepted value [21]. This is determined by a parallel line drawn at 0.2% of the strain to the elastic slope (Figure 1.9). When the load is removed at a point above the yield stress, the stress-strain curve will be approximately parallel to the initial modulus. The Ultimate Tensile Stress (UTS) is the maximum stress level that the material can withstand before failure under uniaxial loading.

1.3.2 Creep of Solders

Electronic packaging components constantly experience stresses due to CTE (Coefficient of Thermal Expansion) mismatches in the packaging modules. Creep deformation is one of the major failure modes of solder joints for various electronic packaging modules due to its high homologous temperature [25]. The homologous temperature is the ratio of the temperature of the material and its melting temperature in degrees Kelvin [26].

$$T_h = \frac{T}{T_m} \tag{1.5}$$

The homologous temperature is an empirical value. When T_h is greater than $0.5T_m$, the creep deformation will be the dominate deformation mode in metallic materials [26]. Solders have extremely high homologous temperatures even at room temperature due to their low melting temperature. T_h of Sn-Pb eutectic is $0.65T_m$ at room temperature (T_m = 183 °C), while the T_h of SAC alloys is $0.61T_m$ at room temperature (T_m = 217 °C). Both of these homologous temperatures are greater than $0.5T_m$, and so are considered “hot” at room temperature. Consequently, solder alloys will undergo creep even at room temperature. In actual electronic applications, where circuits typically operate over a -40 °C to +125 °C range, eutectic solder is working at $0.51\text{-}0.87T_m$, while an SAC solder is working at $0.48 - 0.81T_m$. Both of these ranges are within the rapid creep deformation range when devices are under stress.

1.3.3 Creep and Creep Curves

Creep generally refers to the time-dependent strain plastic deformations at constant uniaxial stress [27]. Creep deformation tends to be rapid when the homologous temperature is above $0.5T_m$. Creep testing can be carried out with a constant load at elevated temperature by either tension or compression [28].

Figure 1.10 shows a typical creep curve, which generally consists of three stages after the initial instantaneous strain when a constant load is applied [27]. The initial strain may consist of elastic or time-independent plastic deformation as soon as the load is applied. In this first stage, which is referred to as *Primary Creep*, the strain rate decreases rapidly over time. This is caused by working hardening, which restricts the deformation. Stage two is the *Secondary Creep*, or *Steady-State Creep*, which is very important since most of the plastic deformation and lifetime of products takes place in this period, and it is the dominant deformation for metals when the homologous temperature is above $0.5T_m$. In this stage, the strain rate is retarded by strain-hardening, which decreases the deformation speed, while the associated recovery and recrystallization (softening) tend to accelerate the creep rate [21]. The two processes of hardening and softening achieve a dynamic balance in the secondary creep stage and the strain-rate is relatively stable. The third stage is *Tertiary Creep*, where the nucleation and growth of cavities has been induced [27]. Necking and micro-cracking will subsequently occur, which will eventually lead to creep rupture of the specimen.

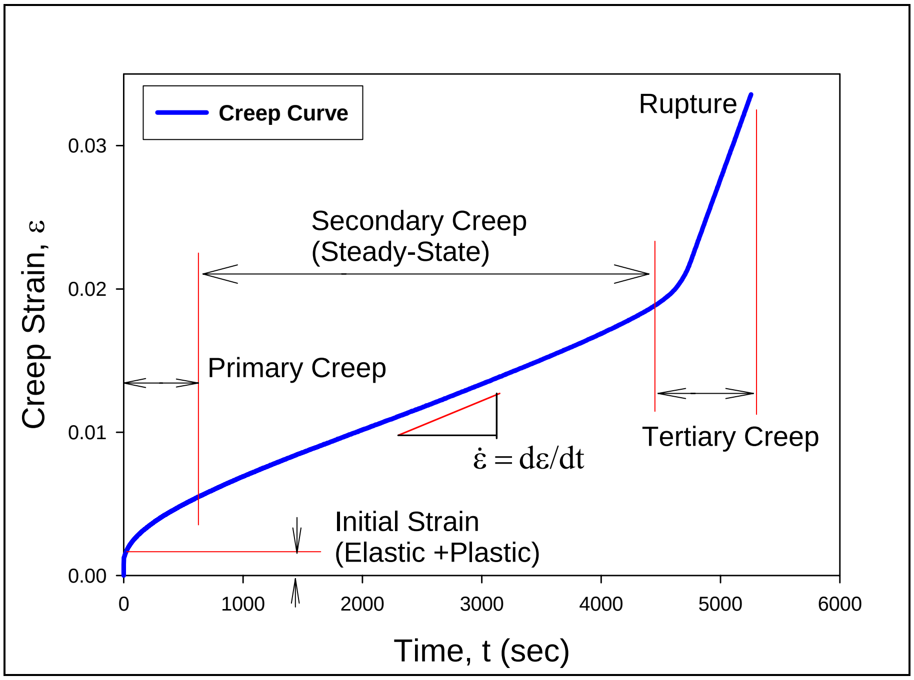

Figure 1.10 Typical Creep Curve.

1.3.4 Mechanisms of Creep Deformation

Many creep mechanisms have been proposed. The major creep mechanisms, such as dislocation glide, dislocation creep, grain boundary diffusion, and lattice diffusion, can be summarized in a creep deformation map, as shown in Figure 1.11 [27, 28]. The deformation diagram was first introduced by Ashby in 1972 [29], and has been widely accepted and studied by other researchers in the area. The deformation map is normally constructed with axes of normalized tensile or shear stress and homologous temperature. The top of the map is bounded to the theoretical or ideal stress, below which is the onset of dislocation glide. *Dislocation glide* occurs at high stress levels over the entire homologous temperature range. The deformation mechanism involves the dislocation moving along the slip planes [28]. *Dislocation creep* usually occurs at high temperatures, with T_h greater than $0.5T_m$, and intermediate high stress. This creep mechanism was first introduced by Weertman [30]. The deformation is believed to be controlled by diffusion controlled dislocation movement, with dislocations climbing away from dislocation barriers. This model is important because it can actually predict the strain rate through quantitative estimation. Coble proposed a *grain boundary based diffusion* mechanism, which involves the atomic or ionic diffusion along the grain boundaries [31]. The deformation occurs at intermediate low stress levels over an intermediate to low temperature range.

At low stress level and high temperature, *lattice or bulk diffusion* is believed to be the primary deformation mechanism [21]. This is also known as Nabarro-Herring Creep, since it was first reported by Nabarro and Herring independently [21, 32, 33]. The deformation is believed to involve the migration of interstitial atoms and lattice vacancies

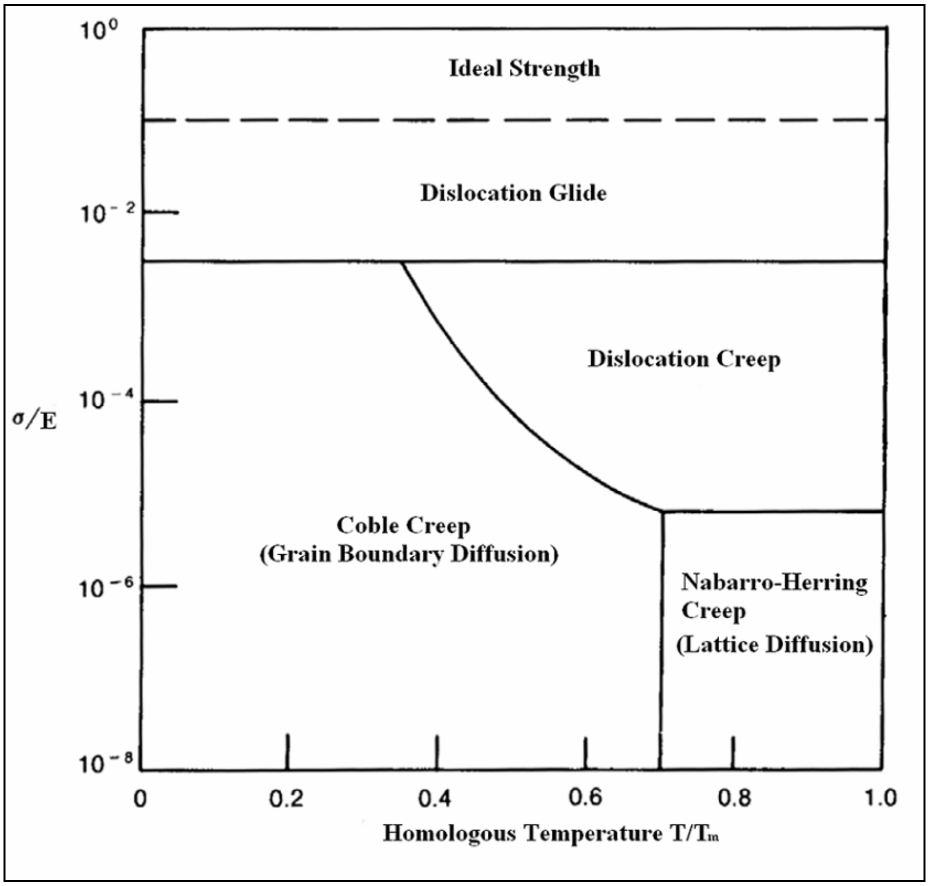

Figure 1.11 A Typical Creep Deformation Map [27, 28].

along the gradient of a grain boundary in the presence of tension or compression pressure in reversed directions. When there is no pressure the interstitial atoms and lattice vacancies will migrate proportional to the gradient of their concentrations. However, under pressure these lattice defects tend to move in whichever direction will relieve the imbalance of pressure, which will eventually cause creep deformation [33].

At high temperatures, grain-boundary sliding may also be involved in the creep deformation [21]. The displacement of grains can be induced by stress at high temperatures. Grain boundary sliding is not an independent deformation mechanism, but may accompany one or more of the above deformation mechanisms.

Solder alloys possess high homologous temperatures greater than $0.5T_m$ in their typical operating range. The creep deformation mechanism depends mainly on the stress level. At lower stress levels, the deformation will be due to lattice diffusion and grain-boundary diffusion, at intermediate stress levels dislocation creep is involved, and at high stress creep involves dislocation gliding.

Shi *et al.* recently proposed a new set of deformation maps for Sn-Pb eutectic solder [34]. It is believed that dislocation-controlled and lattice diffusion-controlled creep is the major deformation mode for eutectic solder.

1.3.5 Constitutive Equations of Secondary Creep

Secondary, or steady-state creep is the dominate deformation experienced by solder alloys. The steady-state creep rate can be quantitatively estimated, and a series of constitutive models have been proposed. The following two models are the most widely accepted for the characterization of solder alloys by considering the diffusion controlled creep deformation mechanism.

Dorn Power Law [35]:

$$\dot{\varepsilon} = A\sigma^{n} \exp\left(-\frac{Q}{RT}\right) \tag{1.6}$$

Garofalo Hyperbolic Sine Law [27]:

$$\dot{\varepsilon} = C[\sinh(\alpha\sigma)]^{n} e^{\left(\frac{-Q}{RT}\right)} \tag{1.7}$$

where R is the universal gas constant, T is the temperature in Kevin, σ is the applied stress, A and C are material dependent constants, n is the stress exponent, and Q is the activity energy. The models show that the steady state creep strain rates are strongly stress and temperature dependent.

1.4 Objectives of This Research

Due to the uniqueness of solder alloys and the lack of standards for characterizing of solder alloys, current databases of the properties of lead-free solders are inadequate. The objective of this research is to consistently study the microstructure and mechanical behavior of lead-free solders, and to achieve the following objects:

- Develop of test specimen preparation procedures that produce uniaxial test samples with comparable microstructures to the lead-free solder materials used in actual electronic packaging solder joints.
- Measure consistent mechanical properties for lead-free solder materials for use in lead-free electronics through controlling the thermal profile and microstructure in the uniaxial test specimen preparation procedure.
- Determine the effects of isothermal aging of the test specimens at room

temperature and elevated temperatures on the uniaxial stress-strain curves and mechanical properties of the lead-free solders.

- Measure stress-strain curves for lead-free solders over a wide range of temperatures, strain rates, and aging conditions (Preconditioning), and determine the constitutive models of the key mechanical properties related to temperature and strain rate.
- Measure creep curves for lead-free solders over a wide range of temperatures, applied stresses, and aging conditions (Preconditioning).
- Elucidate the basic constitutive laws and mechanical properties of different lead-free solder materials for use in finite element reliability simulations.
- Obtain the material property data needed to compare different lead-free solder materials and to select the best alternative to tin-lead solder for a given application.

1.5 Organization of the Dissertation

In Chapter 2, a wide-ranging survey of the literature on specimen preparation, room temperature aging effects, thermal aging effects, temperature and strain rate effects, and constitutive modeling of creep is discussed. The literature reviews focus primarily on the SAC alloy series. In Chapter 3 the experimental procedure used for the bulk specimen preparation procedure is described, and the Micro-Tensile testing machine is introduced. A model of the stress-strain curve developed to accurately average experimental measurements is also presented in this chapter. Room temperature aging effects on tensile and creep properties are summarized and discussed in Chapter 4. In

Chapter 5, thermal aging effects on the tensile and creep properties will be discussed. Chapter 6 reports on an investigation of the effects of strain rate and temperature effects on the tensile behavior of lead-free solders compared with Sn-Pb eutectic solder, including a discussion of the constitutive models developed with the variables of strain rates and temperature. Chapter 7 summarizes the investigations on constitutive models for SAC alloys and their comparison with Sn-Pb solder. Chapter 8 summarizes the entire study and concludes the dissertation.

CHAPTER 2

LITERATURE REVIEW

2.1 Introduction

Due to the continuous pressure of the EU's WEEE and RoHS directives to ban of lead-free solders from electronic components, research and development into lead-free solders have attracted more and more attention from both industry and academic institutions. Inputting the key words "lead-free solder" to the "Google" searching engine resulted in 162,000 links in March 2005, increasing to 1.44 million by September 2006. There are numerous technical research reports and articles in the area of mechanical characterization of lead-free solders. However, due to a lack of uniform standards and the uniqueness of the properties of the solder alloys, there are large discrepancies in the current database of the mechanical properties of lead-free solders.

2.2 Data Discrepancies in the Literature

Solder joint fatigue is one of the predominant failure mechanisms in electronic assemblies exposed to thermal cycling. Reliable, consistent, and comprehensive solder constitutive equations and material properties are needed for mechanical design, reliability assessment, and process optimization. Accurate mechanical characterization of solder materials has always been hampered by the difficulty of preparing test specimens that accurately reflect the material used in the actual solder joints (i.e. that match the solder microstructure). Solder uniaxial samples have generally been fabricated by either machining the bulk solder material [36-41] or by melting the solder paste in a mold [42-50]. Using bulk solder bars is undesirable because they will have significantly different microstructures than those present in the small solder joints used in microelectronics assembly. Machining can develop internal/residual stresses in the specimen, and the heat generated during turning operations can cause significant microstructural changes due to the low melting temperatures of solder alloys, which will cause a further deviation of mechanical properties. Reflow of solder paste in a mold leads to challenges with flux removal, minimization of voids, microstructure control, and extraction of the sample from the mold. Many of the approaches also lead to specimens with shapes that significantly deviate from the ideal long slender rods. Thus, undesired non-uniaxial stress states will inevitably be produced during loading.

Other investigators have attempted to extract the constitutive properties of solders by directly loading [40, 51-58] or indenting [54, 59] actual solder joints such as flip chip solder bumps or BGA solder balls. While such approaches are attractive because the true solder microstructure is involved, the unavoidable non-uniform stress and strain states in the joint make the extraction of the correct mechanical properties or stress-strain curves from the recorded load-displacement data very challenging.

The mechanical properties of most metals are both strain rate and temperature dependent [21]. The mechanical properties of solder alloys are heavily dependent to temperature and strain rate due to their high homologous temperature. Unless the testing conditions for both temperature and strain rate are the same, the data will therefore not be comparable. The lack of testing standards thus makes it very hard to compare the data in the current data pool since different research groups use different specimen preparation methods and different testing conditions, such as strain rates and temperatures.

Table 2.1 provides a summary of the mechanical properties in the current research database of the major lead-free solders. All the data in the table were recorded at room temperature. There are large discrepancies in the tensile property values as well as the specimen preparation and testing approaches. The elastic modulus for SAC ranges from 30-54 GPa, although the majority of the values lie in the range of 40-50 GPa (Figure 2.1). The UTS values vary from 30 to 60 MPa, with the majority in the range of 35-45 MPa (Figure 2.2). The yield stresses range from 20 to 47 MPa, with the majority in the range of 25-35 MPa (Figure 2.3).

All the differences in testing conditions, such as specimen geometry, testing methods, and testing strain rates, are likely to contribute to the variations. Vianco's SAC mechanical properties have been widely referenced [60-63]. Figure 2.4 shows the bulk specimen used for compression testing in their experiment. As mentioned earlier, due to the low melting temperature of solder alloys, machining operations will cause significant changes in the microstructure and properties of solders. Residue stresses due to machining will also be significant. Their research used compression testing, which may pose problems due to confinement issues affecting the uniaxial testing results. Their results, shown in Figure 2.5, seem to be abnormal with the changes of testing temperature [61], and their testing results show large deviations across all the temperatures tested in their testing data.

Table 2.1 Tensile Properties of SAC Alloys.

Solder Alloy	**Elastic Modulus, E(GPa)**	**UTS (MPa)**	**YS (MPa)**	**Strain Rate (sec^{-1})**	**Specimen Preparation**	**Testing Method**	**Reference Sources**
Sn-3.9Ag-0.5Cu	50.3	36.2	31.9	$4.2x10^{-5}$	Machined, Cylindrical	Compression	Vianco [60-63]
	54				Machined, Cylindrical	Dynamic/Acoustic	Vianco [60-63]
		60		$1.78x10^{-3}$	Cast, Dog-bone, Water Quenched	Tension	Xiao [48,49]
		41		$1.78x10^{-3}$	Aged 35 Days at 25°	Tension	
Sn-3.8Ag-0.7Cu	43.1				Solder Joints	Nano-indentation	Xu [64]
	45	40	35	6.68×10^{-4}	Cast, Cylindrical	Tension	Hwang [36]
	50	45		1.67×10^{-3}	Cast, Cylindrical	Tension	Fouassier [65]
	44.4	39.6	35.1	5.6×10^{-4}	Cast, Dog-bone	Tension	Pang [66]
	46			10^{-4}	Cast, Dog-bone	Tension	Schubert [67, 68]
	44.9				Solder Joints	Nano-indentation	Li [69]
	41	39	32	10^{-3}	Cast, Dog-bone	Tension	Lin [45]
	46		47.1		Solder Joints	Dynamic Analyzer	Harrsion [70]
Sn-4.1Ag-0.5Cu	43	36	33	6.86×10^{-4}	Cast, Cylindrical	Tension	Hwang [36]
Sn-4.0Ag-0.5Cu	40				Cast, Dog-bone	Tension	Schubert [67]
	48.3				Solder Joint	Nano-indentation	Rhee [71]
	45				Bulk Solder	Nano-indentation	Allen [72, 73]
		51		10^{-3}	Cast, Dog-bone	Tension	Xiao [74]
Sn-3.0Ag-0.5Cu	54	41.8	25.3	4×10^{-3}	Machined, Cylindrical	Tension	Kanchanomai [75]
	37.4	43	37	5×10^{-4}	Cast, Dog-bone	Tension	Zhu [76]

Table 2.1 Tensile Properties of SAC Alloys (continued).

Solder Alloy	**Elastic Modulus, E(GPa)**	**UTS (MPa)**	**YS (MPa)**	**Strain Rate (sec^{-1})**	**Specimen Preparation**	**Testing Method**	**Reference Sources**
Sn-3.1Ag-0.5Cu	45	49	40	6.86×10^{-4}	Cast, Cylindrical	Tension	Hwang [36]
Sn-3.2Ag-0.8Cu		32 30	28 20		Cast, Cylindrical Quenched Air-cooled	Tension	Medini [77]
Sn-3.5Ag-0.7Cu		46.6			Cast, Dog-Bone	Tension	Schubert [67] Biglari [78]
SAC1 *	30	38.1	28		Cast, Cylindrical	Tension	AIM Solder Guide [79, 80]
SAC2 *	51	39.5	33.5		Cast, Cylindrical	Tension	AIM Solder Guide [79, 80]

* The Solder Composition was not Specified.

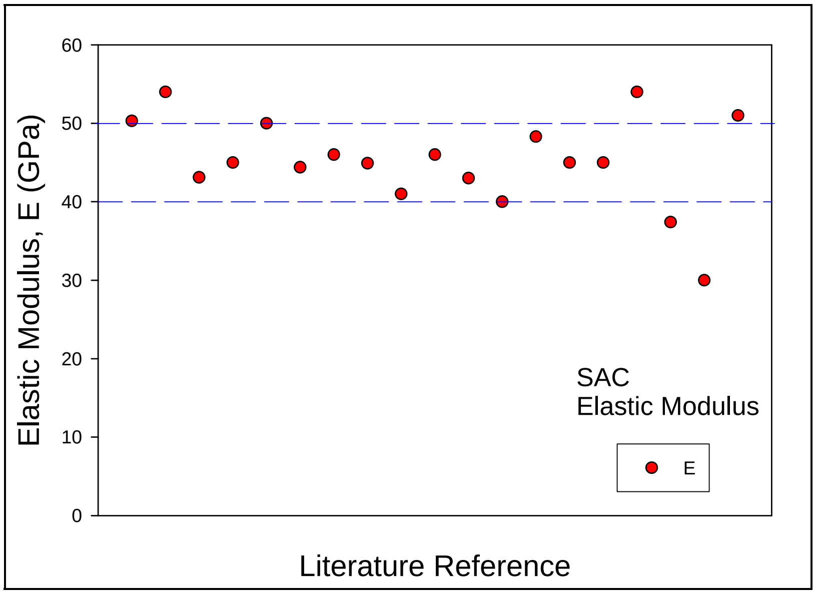

Figure 2.1 Variation in the Elastic Modulus of SAC Solders.

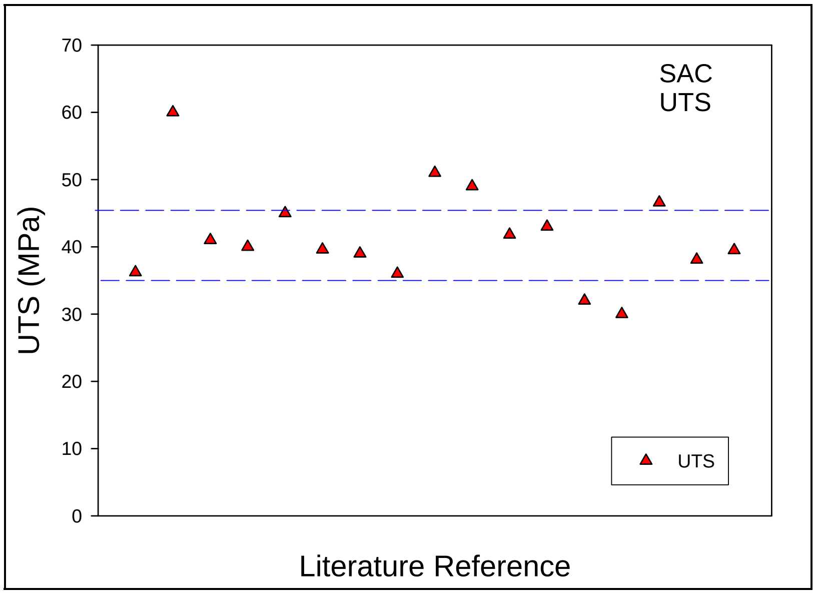

Figure 2.2 Variation in the UTS for SAC Solders.

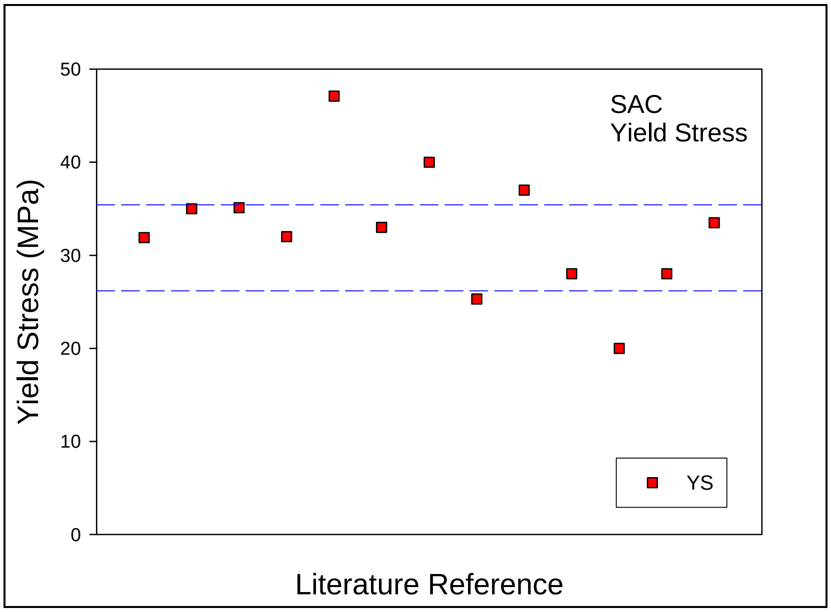

Figure 2.3 Variation in the of Yield Stress for SAC Solders.

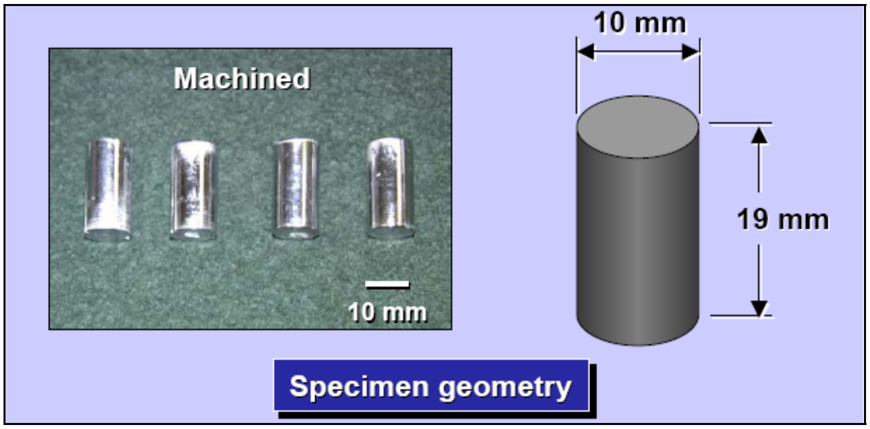

Figure 2.4 Machined Cylindrical Solder Specimen for Compression Testing [61].

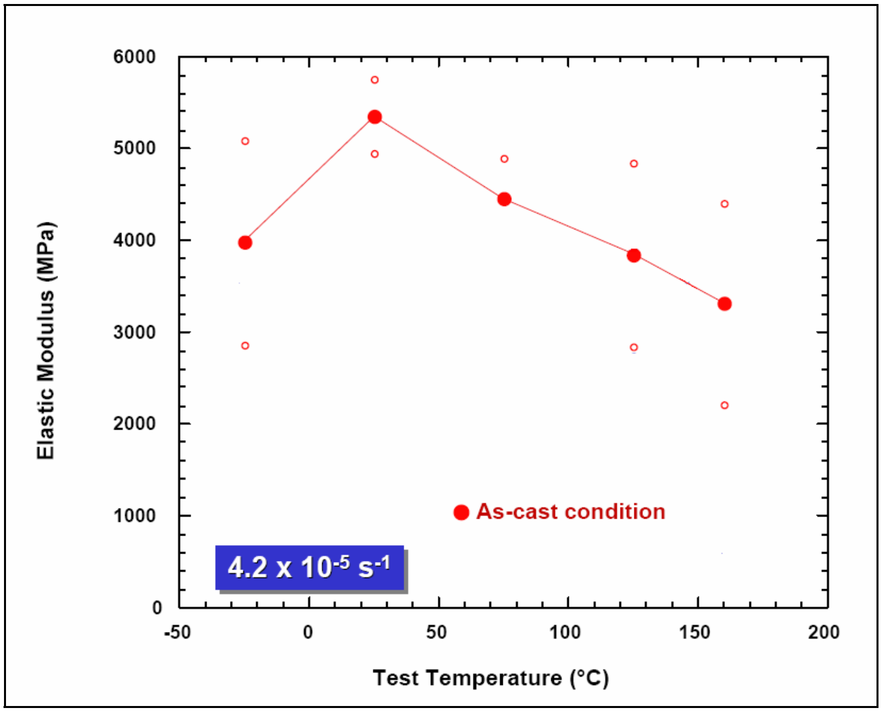

Figure 2.5 The Elastic Modulus of SAC Solders by Compression Testing [61].

As shown in Figure 2.6, Schubert *et al.* concluded that there are large discrepancies for the elastic modulus of both lead-free solders and Sn-Pb eutectic from different research reports due to variations in the testing conditions [67-68, 78, 83, 90-91]. Pang *et al.* found that there are about 50% of variations in the values UTS for SAC alloys (Figure 2.7) [66, 75, 92-95].

Table 2.2 gives a brief summary of the mechanical properties of Sn-Pb eutectic solders. The collected data shows there are also large variations in the mechanical properties published for eutectic Sn-Pb solder, with the elastic modulus ranging from 16 to 36 GPa, the UTS values ranging from 26 to 47 MPa and the Yield stress ranging from 27 to 41 MPa. MacCabe and Fine reviewed the elastic modulus of Sn-eutectic solders and found a wide range, varying from 15 to 40 GPa [82]. They concluded that the large differences were caused by the contribution of the inelastic deformation (plastic) from the slope of the stress-strain curve due to the high homologous temperature of solders. The slope of the stress-strain curve therefore does not represent the true elastic modulus.

As the above data shows, there are large discrepancies in the current database of mechanical properties for both lead-free and Sn-Pb solders. These discrepancies may have been caused by the lack of accepted standards for testing methods, specimen preparation and testing conditions. However, none of the resources recognized the effect of room temperature aging, which may also lead to data variations even for the same testing conditions due to the high homologous temperature of solder alloys. The room temperature aging effects may have played a significant role in the discrepancies in the published data.

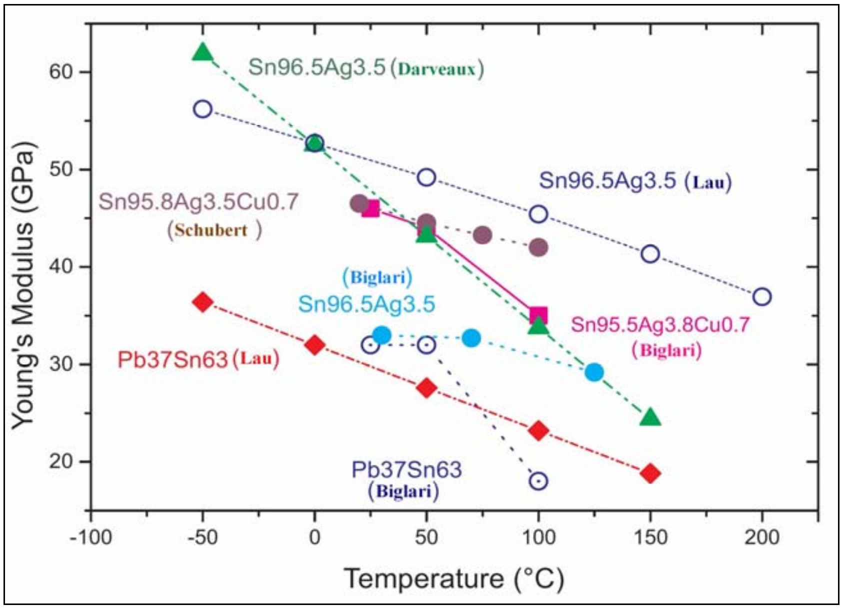

Figure 2.6 Schubert's Comparison of the elastic modulus of Lead-free Solders [67].

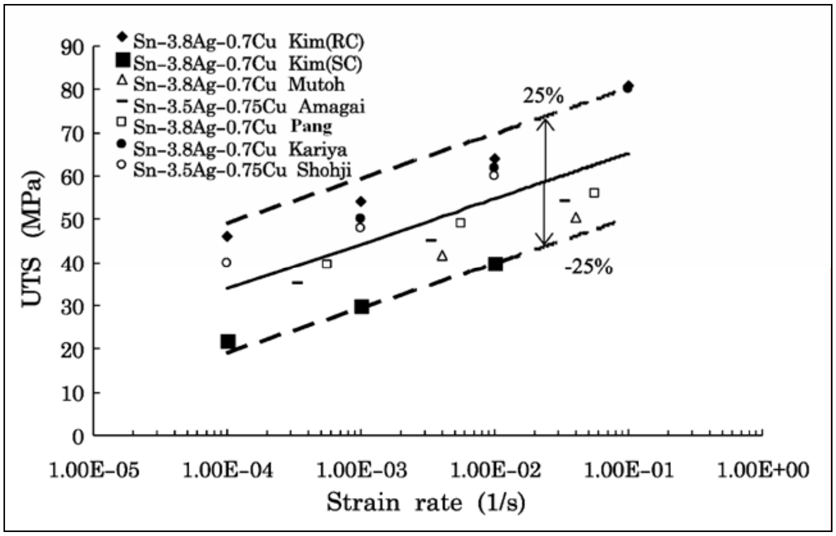

Figure 2.7 Pang's Comparison of the UTS of Lead-free Solders [66].

Table 2.2 The Tensile Properties of Sn-37Pb Eutectic Solder.

Solder Alloy	**Elastic Modulus, E (GPa)**	**UTS (MPa)**	**YS (MPa)**	**Strain Rate (sec^{-1})**	**Specimen Preparation**	**Testing Method**	**References Sources**
Sn-Pb Eutectic	33.5	33.9	30.2		Cast, Cylindrical	Tension	Seelig [79]
	27	47	41	6.86×10^{-4}	Cast, Cylindrical	Tension	Hwang [36]
	32	39		1.67×10^{-3}	Cast, Cylindrical	Tension	Fouassier [65]
	32		32.5		Solder Joints	Dynamic Analyzer	Harrison [70]
	36	54		2×10^{-2}	Lap-Joints	Tension/ Shearing	Enke [81]
	35	26		10^{-3}	Machined, Cylindrical	Tension	MacCabe [82]
	29		29				Lau [83]
	15.7	30.6	27.2				NCMS [84]
	32.1						Lau [85]
	30.2						Wong [86]
		31-46					Sigolko [87]
		46.2					Welco Casting [88]
		40.3					Hernadez [89]

2.3 Isothermal Aging Effects

The effects of aging on the mechanical properties and microstructure have been widely studied. However, most of the research has focused on elevated thermal aging effects, which dramatically change the mechanical properties and microstructure of solders. Room temperature aging effects have been largely ignored.

2.3.1 Effects of Aging on Tensile Properties

The microstructure, mechanical response, and failure behavior of lead-free solder joints in electronic assemblies are constantly changing when exposed to isothermal aging and/or thermal cycling environments [46, 48-49, 55-56, 96-110]. The observed material behavior variation during thermal aging/cycling is universally detrimental to reliability and includes reductions in stiffness, yield stress, ultimate strength, and strain to failure, as well as highly accelerated creep. Such aging effects are greatly exacerbated at the higher temperatures that are typically used in thermal cycling qualification tests. However, significant changes occur with aging even at room temperature [46, 48-49, 55-56, 96-104].

As early as 1956, Medvedev [96] observed a 30% loss of tensile strength for bulk solder Sn/Pb solder stored for 450 days at room temperature. In addition, he reported 4-23% loss of tensile strength for solder joints subjected to room temperature storage for 280-435 days. In 1976, Lampe [97] found losses in shear strength and hardness of up to 20% in Sn-Pb and Sn-Pb-Sb solder alloys stored for 30 days at room temperature (Figure 2.8). Lampe explained that the softening at room temperature due to aging was caused by the equilibrium process of the solder as tin precipitated out of the supersaturated lead-rich phase, thus causing the reduction in strength [97].

Miyazawa and Ariga [98-99] measured significant hardness losses and microstructural coarsening for Sn-Pb, Sn-Ag, and Sn-Zn eutectic solders stored at 25 °C for 1000 hours, while Chilton and co-workers [100] observed a 10-15% decrease in the fatigue life of single SMD joints after room temperature aging. Coyle *et al*. reported a shearing stress reduction of up to 20% after 240 hours at room temperature for BGA packaging (Figure 2.9) [102]. Lee *et al*. also found that the shearing stress dropped by up to 10% after 3 days room temperature aging after reflow (Figure 2.10) [104].

Several other studies [101, 103] have also documented the degradation of Sn-Pb and SAC solder ball shear strength (10-35%) in area array packages subjected to room temperature aging. Both Lampe and Coyle *et al*. observed dramatic coarsening of the phase microstructure [97, 102]. The effects of room temperature isothermal aging on constitutive behavior have also been reported [46, 48-49]. Chuang, *et al*. [46] characterized the reductions in yield stress and increases in elongations obtained in Sn-Zn eutectic solder during aging at room temperature. In addition, Xiao and Armstrong [48-49] recorded stress-strain curves for SAC 396 specimens subjected to various durations of room temperature aging, and finding losses of ultimate tensile strength of up to 25% over 60 days of room temperature aging.

Thermal aging effects are the most widely studied due to the dramatic changes in the microstructure and mechanical properties that result. Aging softening has also been observed for solder subjected to elevated temperature aging (e.g. 125 ^{o}C) [45-46, 48-49, 105-110]. Pang *et al*. [55] measured microstructure changes, intermetallic layer growth, and shear strength degradation in SAC single ball joints aging at elevated temperature.

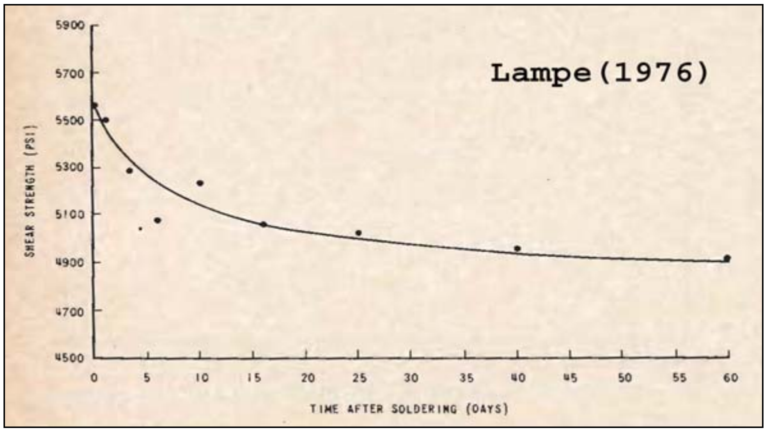

Figure 2.8 Room Temperature Aging Effects on Sn-Pb Solder [97].

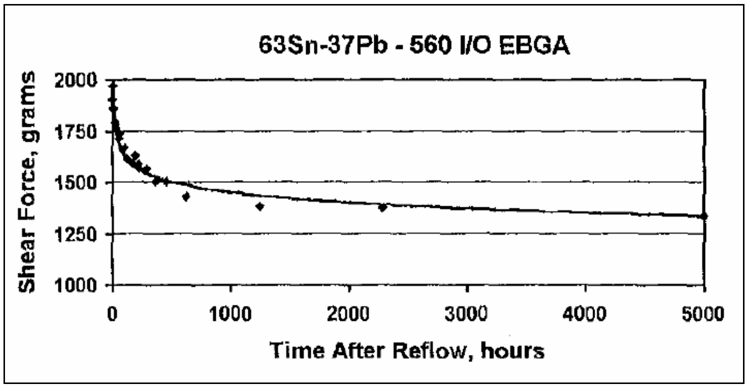

Figure 2.9 Shear Strength of BGA Solder Balls after 240 hours at RT [102].

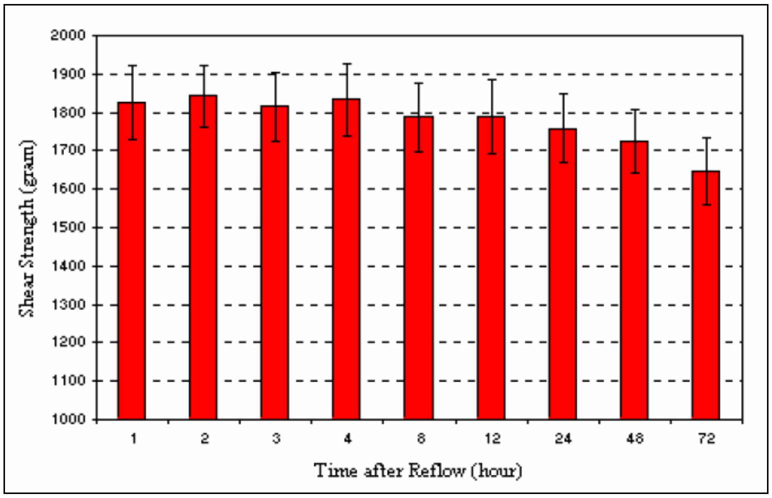

Figure 2.10 Reduction in Ball Shearing Strength after 3 days at RT [104].

Darveaux [56] performed an extensive experimental study on the stress-strain and creep behavior of area array solder balls subjected to shear. He found that aging for 1 day at 125 °C caused significant changes in the observed stress-strain and creep behavior. In addition to the room temperature aging experiments described above, Xiao and Armstrong also measured stress-strain curves for SAC 396 specimens subjected to elevated temperature aging at 180 °C [48-49]. At this highly elevated temperature, they observed a quick softening of the material during the first 24 hours, followed by a gradual hardening with time. Several studies have been performed on the degradation of BGA ball shear strength with elevated temperature aging at 125 °C or 150 °C [105-109]. All of these investigations documented both microstructure coarsening and intermetallic layer growth. In addition, Hasegawa, *et al.* [105] measured elastic modulus reductions with aging by testing thin solder wires. Wang *et al.* [109] found significant drop in tensile properties after aging at 125 °C for various periods of time. Vianco also found large reductions in the elastic modulus and yield stress after thermal aging at 125 °C for 24 hours for SAC alloys [60-63]. Finally, Ding, *et al.* [110] explored the evolution of fracture behavior of Sn-Pb tensile samples with elevated temperature aging.

The underlying mechanism for this reduction in strength in solder alloys after aging must be related to the microstructure coarsening process. When the grain structure is coarser, there are fewer grain boundaries to block the dislocation movement, causing a loss of strength of the material. Based on experimental data, Hall and Petch independently found that the yield strength of a polycrystalline material is inversely proportional to its grain size [21,130,131], as shown in Equation 2.1:

$$\sigma_y = \sigma_i + kd^{-0.5} \tag{2.1}$$

where σ_y is yield strength of the polycrystalline material, σ_i is the constant for the material, which represents the overall resistance of the lattice to dislocation movement; k is a constant which measures the contribution of hardening due to grain boundaries; and d represents the grain size. The Hall-Petch theory states that increasing grain size degrades the strength of materials. The increasing grain size will cause the amount of grain boundaries to decrease, and with fewer grain boundaries to resist the movement of dislocations the hardening contribution due to grain boundaries will be diminished, and the material loses strength.

The grain and phase structure coarsening is promoted by the self diffusion of atoms, interstitials, and vacancies. According to the diffusion fundamental equation (Eq. 2.2) [22],

$$D = D_0 \exp\left(-\frac{Q}{RT}\right) \tag{2.2}$$

where D is diffusivity, D_0 is a constant that is independent of temperature, R is the Boltzmann constant, Q is the activation energy, and T is the absolute temperature. Higher temperatures will increase the diffusivity of the atoms, interstitials and vacancies, leading to grain growth.

As previously stated in Chapter 1, the elastic modulus is only related to the interatomic forces between adjacent atoms [21]. Under normal conditions, the atoms reach an equilibrium position to balance the attraction and repulsion forces. When an external force is applied within the elastic region no interatomic bonds are broken, and only the balance of the attraction and repulsion forces changes. When the external force is relieved, the atoms will return to their original equilibrium positions. Consequently, microstructural changes have little effect on the value of the true modulus. However, in engineering practice, the apparent elastic modulus is obtained from the slope of the stress-strain curves and includes time-dependent inelastic deformations such as creep. Creep is strongly dependent on the dislocation movement and grain size. Coarser grains will cause more grain gliding and dislocation movement, and thus lead to more severe creep deformation. The contribution of plastic deformation to the apparent elastic modulus will therefore increase with increasing grain size. This explains why isothermal aging can cause a reduction in the apparent elastic modulus. Due to the high homologous temperature of solder alloys even at room temperature, creep deformation is more significant compared to other metals with higher melting temperature. The aging effects also contribute more to the apparent elastic modulus for solder alloys.

2.3.2 Effects of Aging on Creep

No reports on the effects of room temperature aging on creep deformation were found. All the current research reports have focused solely on the effect of elevated temperatures on creep deformation. It is believed that thermal aging accelerates the creep deformation due to the growth of the grain structure and coarsening of the second phase in lead-free solders. Darveaux found that aged specimens creep much faster than un-aged ones by a factor of up to 20 times after aging at 125 °C for 24 hours for both SAC405 and SAC305 solder alloys (Figure 2.11) [111]. Note, however, that the lap shear joint specimens used in Darveaux's tests may create non-uniform stress and strain states in the specimens. Several other studies have observed similar behavior regarding the aging deterioration of creep deformation [48, 62, 112-114].

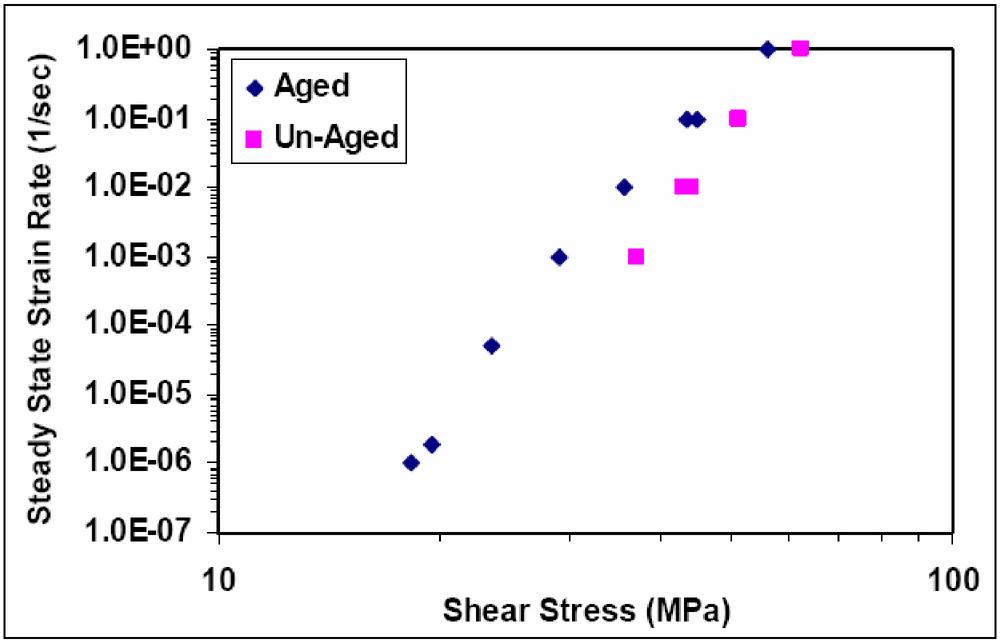

(a) SAC405

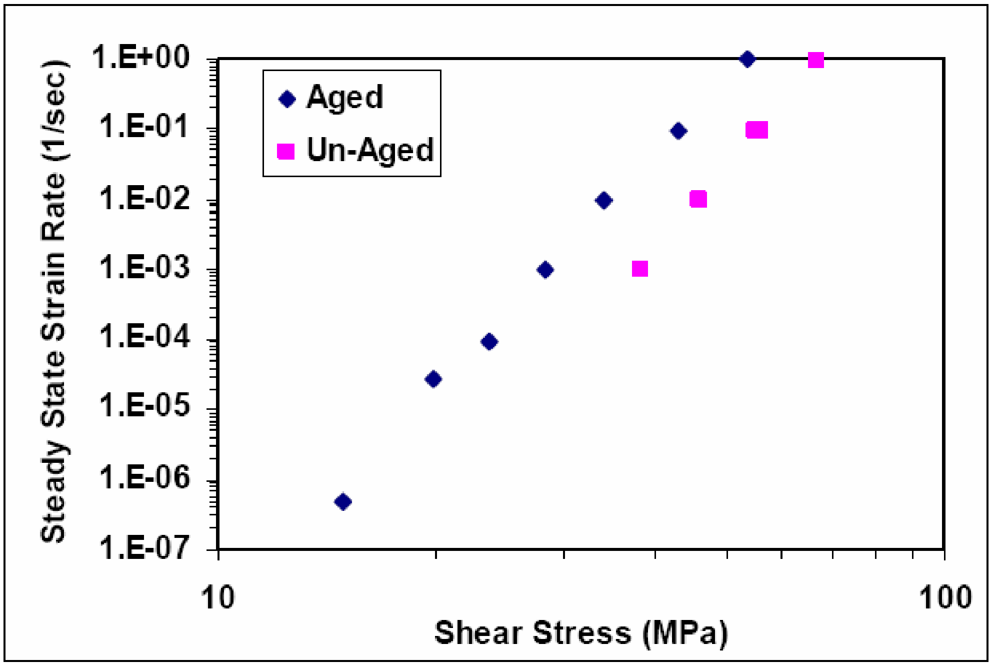

(b) SAC305

Figure 2.11 Effects of Aging on Creep Deformation of SAC Solders [111].

Sasaki *et al*. found that bulk specimens after thermal cycling experience a much higher creep deformation rate [115].

2.4 Effects of Strain Rate and Temperature on Tensile Properties

Mechanical properties are temperature and strain rate dependent for most metal alloys, especially for metals with low melting and high homologous temperatures. High temperatures induce transitions in macroscopic fracture, and these transitions parallel the changes in the strength and ductility of materials [21]. Materials lose strength at higher temperatures. Hertzberg stated that the material strength increases with the testing strain rate, following a form similar to Holloman's Equation [21]:

$$\sigma = C\dot{\varepsilon}^{m} \tag{2.3}$$

where m is the strain-rate sensitivity factor, or strain hardening exponent; $\dot{\varepsilon}$ is the strain rate; C is the material constant; and σ is the stress.

Solder alloys possess very high homologous temperatures. The properties of solder alloys are strongly dependent on both the temperature and strain rate. Jones *et al.* have observed an approximately linear relationship between the strength and temperature [116-117]:

$$\sigma = -\alpha T + \beta \tag{2.4}$$

where α is temperature strengthening coefficient; β is the strength at 0 °C in MPa, and T is the testing temperature in °C. Pang, Shi and co-workers have observed similar experimental results, with a near linear relationship with temperature and a power law relation (Eq. 2.3) with the strain rate [39, 118]. Several other studies have also observed similar materials behavior for both Sn-Pb eutectic and lead-free solder alloys [119-122].

2.5 Constitutive Modeling of Creep Deformation

Constitutive modeling of creep deformation has been a heavily studied and researched area due to the importance of being able to predict the end of life of electronic packaging using finite element analysis tools. Many models have been proposed and modified by researchers. As mentioned in Chapter 1, the Dorn power-law and Garofalo Hyperbolic models are the most widely accepted models for solder alloys. The constitutive model can be determined by creep testing at different temperature and stress levels. Table 2.3 and Table 2.4 summarize some of the current data for both lead-free solder alloys and Sn-Pb; all the models are based on steady-state creep. Materials constants, specimens, and testing methods are compared in the tables. The majority of the data can be fitted into the Hyperbolic Sine model. As with the testing of tensile properties, there are large discrepancies in the creep data and materials constants vary over a very large range. The materials constants are important in determining the accuracy of end-of–life prediction for solder joints using finite element analysis. Large discrepancies would degrade the accuracy of these predictions.

Figure 2.12 summarize several of the hyperbolic sine models for SAC alloys at 125 °C, showing how the steady-state creep rate varies over a very large range. Clech reviewed creep modeling for both Sn-Pb and lead-free solder alloys based on the currently available data under a NIST project [129], and commented that the current database are widely scattered. Discrepancies may be caused by differences in the specimen, testing method, and testing conditions. However, none of the previously documented data has recognized the possible effects of room temperature aging on creep deformation, which may be one of the major reasons causing these the data discrepancies.

Table 2.3 Garofalo Hyperbolic Creep Models of Solder Alloys.

Constitutive Models Garofalo Hyperbolic Sine Law	Solder Alloy	Constants				Specimen Testing Method	Reference Sources
		C	α (MPa^{-1})	n	Q (kJ /mol)		
$\dot{\varepsilon} = C[\sinh(\alpha\sigma)]^n e^{\left(\frac{-Q}{RT}\right)}$	Sn-40Pb	0.1114	751	3.3	53.0	Lap-joints, Shear/Tensile	Darveaux [123]
	Sn-37Pb	0.158	0.406	1.38	50.0	Cast Bulk, Tensile	Xiao [124]
		10.0	0.1	2	44.9	Flip Chip Joints, Tensile	Wiese [67]
		2.87×10^{-5}	1300	3.3	52.8		Shi [34]
		1999.4	0.2	2.1	54.1	Lap-Joint, Tensile	Zhang [127]
	Sn-3.5Ag	178.5	0.115	4.75	57.1	Bulk, tensile	Wiese [67]
		23.17	0.0509	5.04	41.6	Bulk, tensile	Clech [129]
		8.18×10^{11}	0.0266	8.67	77.4	Lap Joint, Shear	Clech [129]
		2.46×10^{5}	0.0913	5.5	72.5	Lap Joint, Shear	Clech/ Darveaux [90,129]
	Sn-3.0Ag-0.5Cu	2631	0.0453	5.0	52.4		Vianco [62]
	Sn-3.9Ag-0.6Cu	0.184	0.221	2.89	62.0	Cast Bulk, Tensile	Xiao [124]
		4.41×10^{5}	0.005	4.2	45	Bulk, Compression	Lau & Vianco [125]
		3.49×10^{4}	0.005	4.3	43.13	Bulk, Compression	Vianco [61]
		248.4	0.188	3.79	62.3	Lap-Joint, Tensile	Zhang [127]
	Sn-3.8Ag-0.7Cu	3.2×10^{4}	0.037	5.1	65.3	Bulk, Tensile	Pang [126]
		2.78×10^{5}	0.0245	6.41	54.2		Schubert [128]
	SAC Series	7.93×10^{5}	0.0356	5	67.9	Fitting Data	Clech [129]

Table 2.4 Dorn Power Law Creep Models of Solder Alloys.

Constitutive Models	Solder Alloy	Constants			Specimen Testing Method	Reference Sources
Dorn Power Law		**A (s^{-1})**	**n**	**Q**		
$\dot{\varepsilon} = A\sigma^{n} \exp\left(-\frac{Q}{RT}\right)$	Sn-3.5Ag	5×10^{-6}	11	79.8	Flip chip, tensile	Wiese [67]
		9.44×10^{-5}	6.05	61.1	Bulk, tensile	Clech [129]
	Sn-4.0Ag-0.5Cu	2×10^{-21}	18	83.1	Flip chip, tensile	Wiese [67]

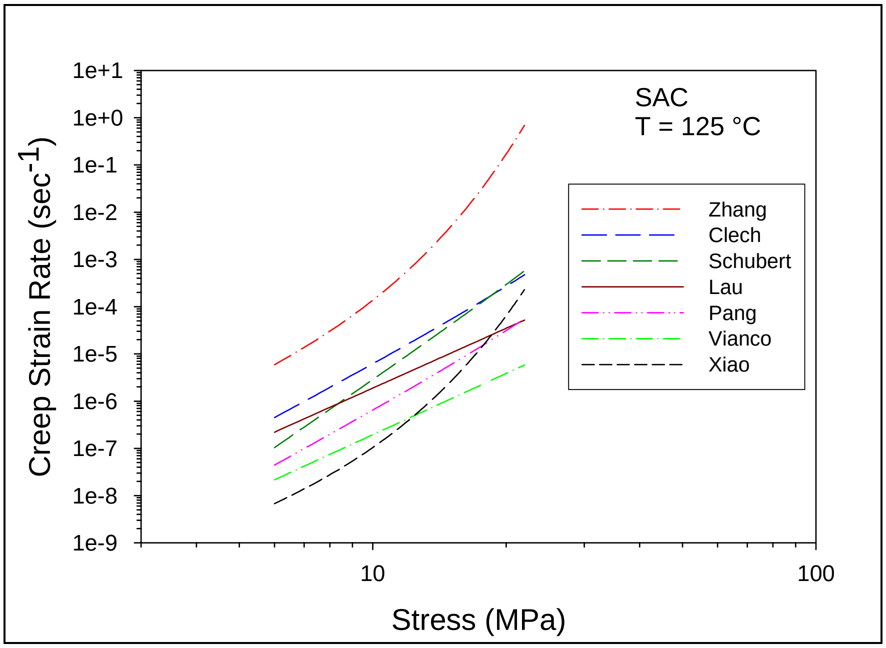

Figure 2.12 Discrepancies in the Creep Models.

Both the Garofola Hyperbolic Sine model and Dorn Power-Law model focus on steady-state creep data, which only involve the time dependent creep deformation. Recently, more research has been carried out to investigate the Anand model, which is also offered in the ANSYS code. The Anand model was initially proposed by Anand [137], and is considered to be a unified model that does not require explicit yield conditions or loading/unloading criteria. The instantaneous response of the material is dependent on its current state. The Anand model also employs a single scalar internal variable "s" to represent the isotropic resistance to inelastic flow of the material. There are series of equations for the Anand model. The flow equation is expressed as follows:

$$\dot{\varepsilon}_P = A\left[\sinh\left(\frac{\xi\sigma}{s}\right)\right]^{\frac{1}{m}} \exp\left(-\frac{Q}{RT}\right) \tag{2.5}$$

where $\dot{\varepsilon}_p$ is the inelastic strain rate, A is a constant, ξ is the stress multiplier, σ is the stress, R is the gas constant, m is the strain rate sensitivity, Q is the activation energy and T is absolute temperature. The flow equation can be easily modified to represent the hyperbolic sine model for secondary creep rate (Eq.1.7).

The scalar variable is believed to be related to the dynamic process of strain hardening and dynamic recovery, expressed as follows:

$$\dot{s} = \left\{\left[h_0\left|1-\frac{s}{s*}\right|\right]\frac{\left(1-\frac{s}{s^*}\right)}{\left|1-\frac{s}{s*}\right|}\right\}\dot{\varepsilon}_p \tag{2.6}$$

and

$$s^* = \hat{s}\left[\frac{\dot{\varepsilon}_p}{A}\exp\left(\frac{Q}{RT}\right)\right]^n \tag{2.7}$$

where s* represents a saturation value at a given temperature and strain rate, $\hat{s}$ is a coefficient and n is the strain rate sensitivity at the saturation condition.

There are a total of nine constants from the above equations, A, Q, m, n, a, h_0, ξ, $\hat{s}$, and s_0, the initial value of the deformation resistance, that need to be determined for the viscoplastic Anand model. Currently, most researchers use multiple variable fitting methods to determine the constants based on experimental data. However, as with the previously documented data, there are large variations in the current database for these constants, even for the same solder material under the same conditions [138-140].

2.6 Summary

This review of the research literature has documented the dramatic changes that occur in the constitutive and failure behavior of solder materials and solder joint interfaces during isothermal aging. However, these effects have been largely ignored in most previous studies involving solder material characterization or finite element predictions of solder joint reliability during thermal cycling. It is widely acknowledged that the large discrepancies in measured solder mechanical properties from one study to another arise due to differences in the microstructures of the tested samples. This problem is exacerbated by the aging issue, as it is clear that the microstructure and material behavior of the samples used in even a single investigation are moving targets that change rapidly even at room temperature. Furthermore, the effects of aging on solder behavior must be better understood so that more accurate viscoplastic constitutive equations can be developed for SnPb and SAC solders. Without such well-defined relationship, it is doubtful that finite element reliability predictions can ever reach their full potential.

For the current study, mechanical measurements of room temperature and thermal aging effects and material behavior evolution of lead-free solders were performed. A broad range of room temperature research was conducted for Sn-Pb and SAC solders for both water-quenched and reflowed samples. This study has avoided the specimen preparation pitfalls experienced in previous studies by a using a novel procedure where solder uniaxial test specimens were formed in high precision rectangular cross-section glass tubes using a vacuum suction process. The tubes were then cooled by water quenching or sent through an SMT reflow to re-melt the solder in the tubes and subject them to any desired temperature profile to match those experienced by actual solder joints.

Using specimens fabricated with the newly developed procedure, changes in the isothermal aging effects and viscoplastic material behavior evolution were characterized for 95.5Sn-4.0Ag-0.5Cu (SAC405) and 96.5Sn-3.0Ag-0.5Cu (SAC305) lead-free solders, which are commonly used as the solder ball alloy in lead-free BGAs and other components. Analogous tests were performed with 63Sn-37Pb (Sn-Pb) eutectic solder samples for comparison purposes. The samples were solidified with both reflowed and water quenched temperature profiles, and isothermal aging was performed at room temperature (25 ^{o}C) and elevated temperatures (125 ^{o}C and 150 ^{o}C). In this study, the of the room temperature (RT) aging experiment were extensively investigated to provide a baseline database for thermal aging, strain rate and temperature effects, as well as for use in the constitutive modeling of creep.

CHAPTER 3

SPECIMEN PREPARATION AND UNIAXIAL TENSILE TESTING

3.1 Introduction

As the literature review in Chapter 2 shows, there are various approached to produce bulk specimens, but due to the lack of standards for the specimen making process, the mechanical data are widely scattered. A unique and microstructurally controllable process has been developed in this study.

3.2 Uniaxial Test Specimen Preparation Procedure

The solder specimens for this study were formed in rectangular cross-section glass tubes using a vacuum suction process. The solder is first melted in a quartz crucible using a pair of circular heating elements (see Figure 3.1). A thermocouple attached to the crucible and a temperature control module are used to direct the melting process. One end of the glass tube is inserted into the molten solder, and suction is applied to the other end via a rubber tube connected to the house vacuum system. The suction forces are controlled through a regulator on the vacuum line so that only a desired amount of solder is drawn into the tube. The specimens are then cooled to room temperature using a user-selected cooling profile.

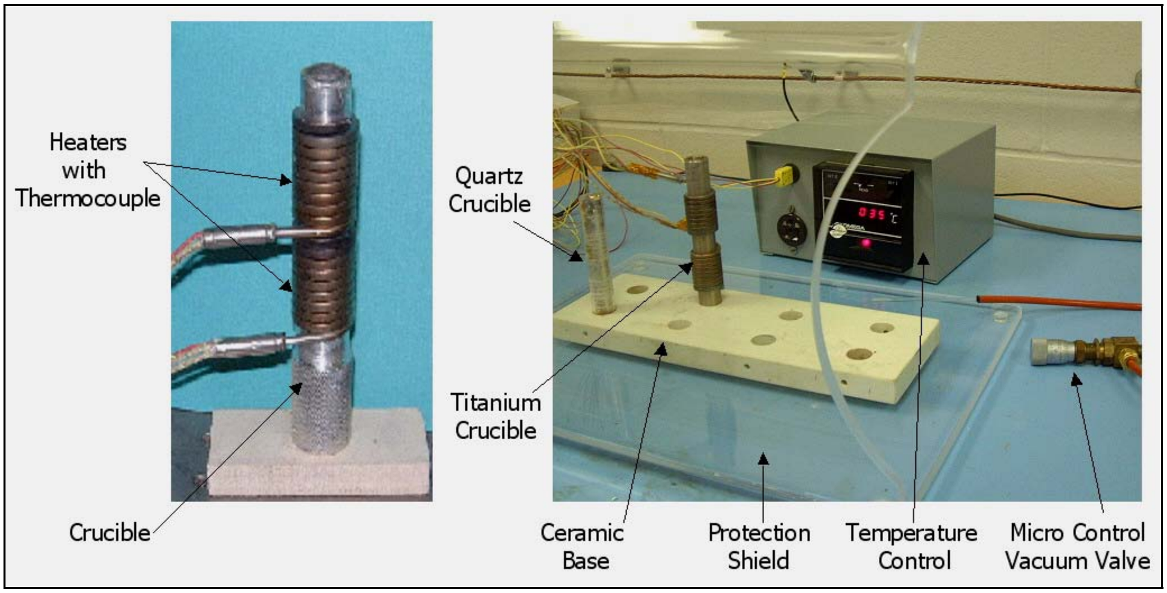

Figure 3.1 Specimen Preparation Hardware.

In order to observe the extreme variations possible in the mechanical behavior and microstructure, a large spectrum of cooling rates were explored including water quenching of tubes (fast cooling rate), air cooling with natural and forced convection (slow cooling rates), and controlled cooling using a surface mount technology solder reflow oven. Typical temperature versus time plots for water quenching and air cooling of the test samples are shown in Figure 3.2. For the reflow oven controlled cooling, the solder in the tubes is first cooled by water quenching, and then sent through a reflow oven (9 zone Heller 1800EXL) to re-melt the solder in the tubes and subject them to the desired temperature profile. Thermocouples are attached to the glass tubes and monitored continuously using a radio-frequency KIC temperature profiling system to ensure that the samples are formed using the desired temperature profile, to match that of the actual solder joints. Figure 3.3 illustrates the reflow temperature profiles used in this work for the SAC and Sn-Pb solder specimens.

Typical glass tube assemblies filled with solder and a final extracted specimen are shown in Figure 3.4. For some cooling rates and solder alloys, the final solidified solder samples can be easily pulled from the tubes due to the differential expansions that occur when cooling the low CTE glass tube and higher CTE solder alloy. Other options for more destructive sample removal involve breaking the glass or chemical etching of the glass. The final test specimen dimensions are governed by the useable length of the tube that can be filled with solder, and the cross-sectional dimensions of the hole running the length of the tube. For the current work, uniaxial samples with nominal dimensions of 80 x 3 x 0.5 mm were utilized. A thickness of 0.5 mm was chosen because this matches the

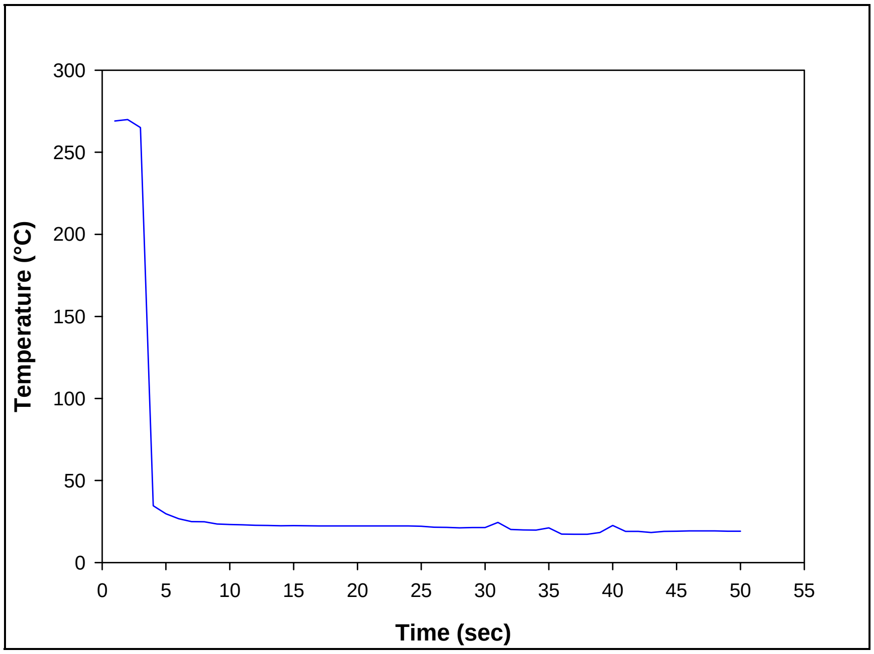

(a) Water Quenched

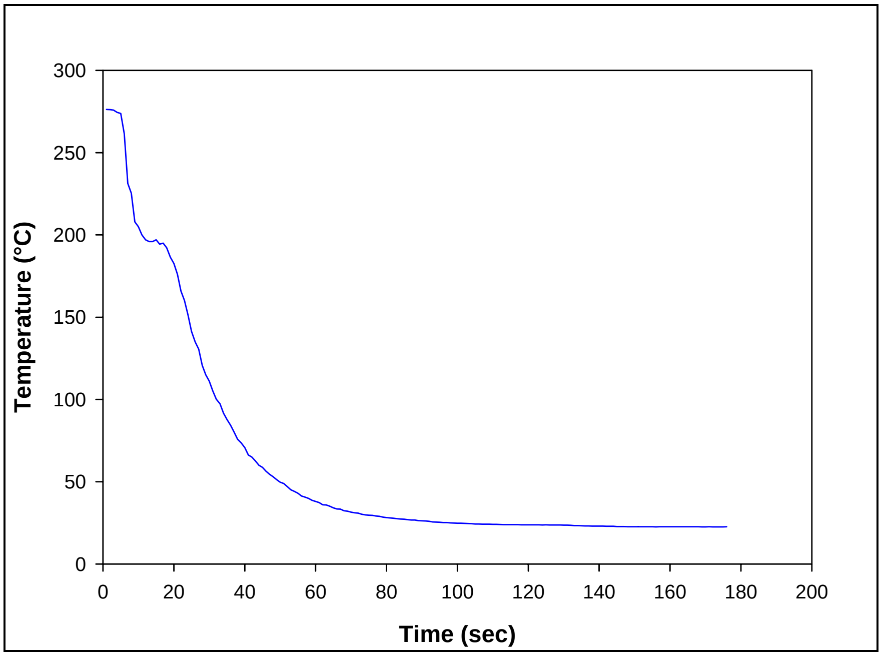

(b) Air Cooled

Figure 3.2 Sample Cooling Profiles.

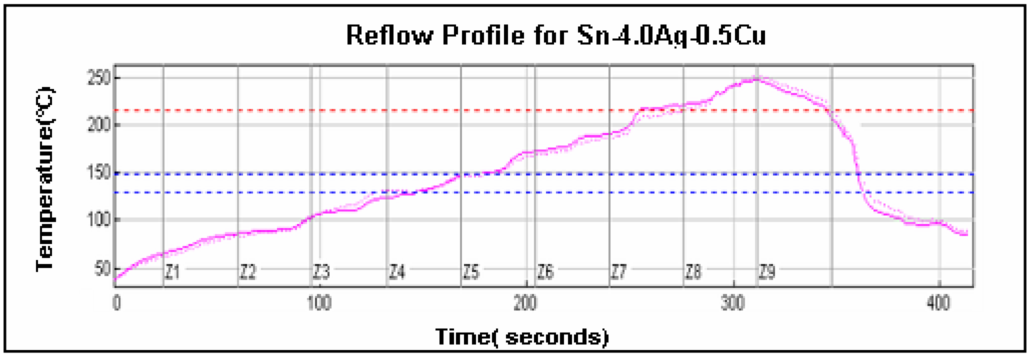

(a) SAC Alloys

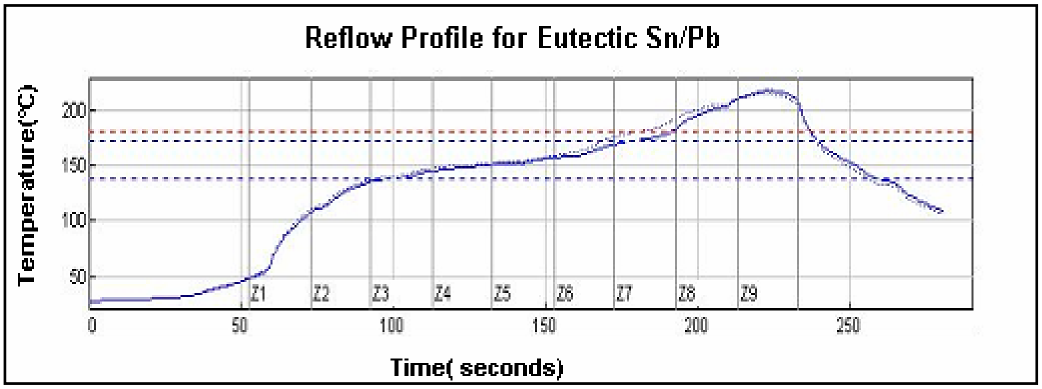

(b) Sn-Pb

Figure 3.3 Solder Reflow Temperature Profiles.

(a) Within Glass Tubes.

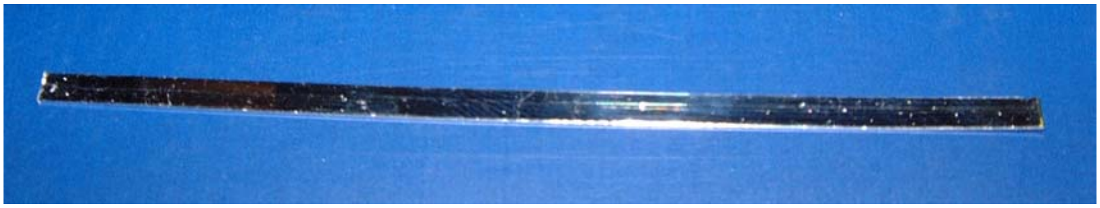

(b) After Extraction.

Figure 3.4 Solder Uniaxial Test Specimens.

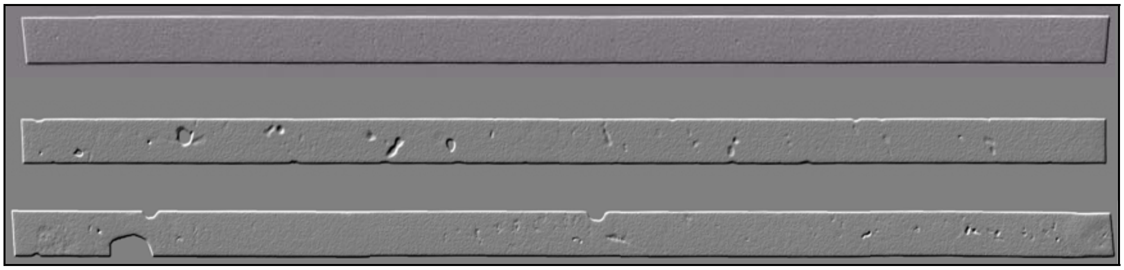

Figure 3.5 X-Ray Inspection of Solder Test Specimens (Good and Bad Samples).

height of typical BGA solder balls. The sample preparation procedure described above yielded repeatable samples with controlled cooling profiles (i.e. microstructures), oxide free surfaces, and uniform dimensions. Samples were inspected using a micro-focus x-ray system to detect flaws such as notches and external indentations, and/or internal voids that are non-visible. Figure 3.5 illustrates the results for good (top) and poor specimens (middle and bottom). With careful experimental techniques, samples with no flaws and voids could be reliably produced.

3.3 Mechanical Testing System

An MT-200 tension/torsion thermo-mechanical test system from Wisdom Technology, Inc., shown in Figure 3.6, was used to test the samples in this study. The system provides an axial displacement resolution of 0.1 microns and a rotation resolution of 0.001°. Testing can be performed in tension, shear, torsion, bending, and combinations of these loadings on small specimens such as thin films, solder joints, gold wire, fibers, etc. Cyclic (fatigue) testing can also be performed at frequencies of up to 5 Hz. In addition, a universal 6-axis load cell was utilized to simultaneously monitor three forces and three moments/torques during sample mounting and testing. The base environmental chamber provided with the system is capable of a temperature range of approximately -175 ^{o}C to 300 ^{o}C.

During uniaxial testing, forces and displacements were measured. The axial stress and axial strain were calculated from the applied force and measured cross-head displacement using

$$\sigma = \frac{F}{A} \qquad \varepsilon = \frac{\Delta L}{L} = \frac{\delta}{L} \tag{3.1}$$

(a) With Thermal Chamber.

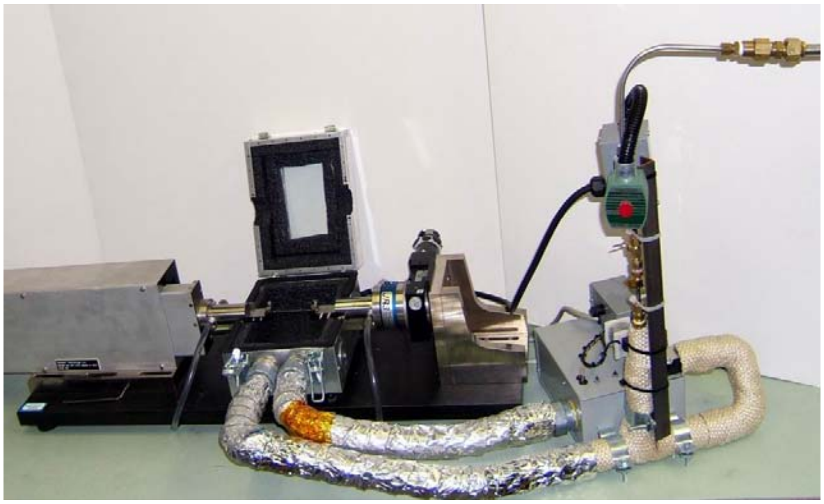

(b) With Cooling Chamber.

Figure 3.6 MT-200 Testing System with Environmental Chamber.

where σ is the uniaxial stress, ε is the uniaxial strain, F is the measured uniaxial force, A is the original cross-sectional area, δ is the measured crosshead displacement, and L is the specimen gage length (initial length between the grips). The gage length of the specimens in this study was 60 mm. Most uniaxial stress-strain testing in this work was conducted at room temperature (25 ^{o}C) with a strain rate of $\dot{\varepsilon} = 0.001$ sec^{-1}.

A typical recorded tensile stress-strain curve with labeled standard material properties is shown in Figure 3.7. Hence, the notation "E" is taken to be the effective elastic modulus, which is the initial slope of the stress-strain curve. Since solder is viscoplastic, this effective modulus will be rate dependent and will approach the true elastic modulus as the testing strain rate approaches infinity. The yield stress (YS) is taken to be the standard .2% yield stress (upon unloading, the permanent strain is equal to $\varepsilon = 0.002$). Finally, the ultimate tensile strength σ_u (UTS) is taken to be the maximum stress realized in the stress-strain data. As shown in Figure 3.7, the solders tested in this work illustrated nearly perfect elastic-plastic behavior, with the exception of a small transition region connecting the elastic and plastic regions. As the strain level becomes extremely high and failure is imminent, extensive localized necking takes place. These visible reductions in cross-sectional area lead to non-uniform stress-states in the specimen and drops in the applied loading near the end of the stress-strain curve.

Creep testing was also carried out using the micro testing system. The solder specimens were tested under constant loads at various temperatures and stress levels. The various testing temperatures were achieved by using environmental chambers (Figure 3.6), capable of temperatures from -175 °C to 300 °C.

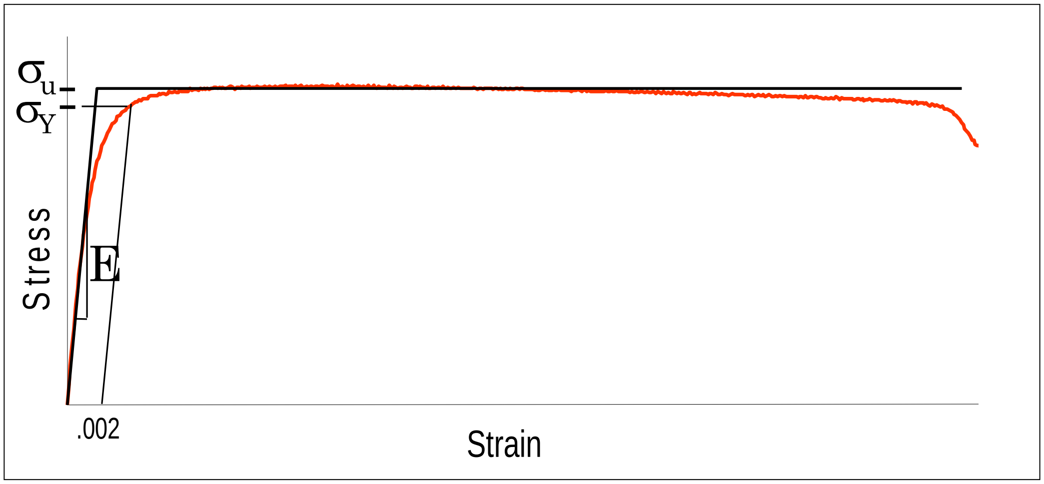

Figure 3.7 Typical Solder Stress-Strain Curve and Material Properties.

3.4 Microstructure Observations

The microstructure of the samples was explored using a JEOL JSM-840 Scanning Electronic Microscope (SEM). The microstructure of the solder alloys was found to be evolving rapidly even at room temperature, especially immediately after solidification. Thus, it is very difficult to prepare potted SEM samples without significantly affecting the results due to time delays and the higher temperatures present during curing of the molding compound.

In this study, an SEM sample preparation procedure was developed that avoids potting and is relatively fast. In the utilized method, a small length of the tensile specimen is attached to a pre-prepared resin stub using a fairly rigid double sided tape immediately after the specimen was cooled. The exposed cross-sectional area of the uniaxial specimen was then carefully polished with the resin stub serving as a convenient grip. For the SAC specimens, etching with a mixture of 5% hydrochloride and 95% methanol was also performed for 5-10 seconds. After the specimens were polished and etched, they were removed from the resin stubs and stuck to analogous aluminum stubs using carbon or copper double-side tape in order to get good conduction within the SEM.

This procedure avoids the time required by resin solidification and gold coating. Generally, it takes 24 hours for typical epoxy resins to solidify at room temperature, or 1 hour at 80 °C. The microstructure would be changed undesirably by either approach. Using the developed procedure, SEM samples were prepared for observation in less than one hour after casting of the tensile specimens. This ensures that the first observations can be made during the early stages of the microstructure evolution. Energy Dispersive

X-ray Spectrometry (EDS/EDX) analysis was also used to identify the second phase in the SAC alloys.

The tensile specimens were found to have a relatively uniform microstructure across their cross-sectional area, with the exception of a fine layer on their outside surface. Typical observed microstructures near the centers of SAC405 and 63Sn-37Pb solder specimens are shown in Figure 3.8. The phase size/structure of the final samples can be controlled by careful choice of the cooling rate (e.g. faster cooling rate will result in finer the phase structure).

3.5 Mechanical Testing Results

3.5.1 General Test Descriptions

Using specimens fabricated with the casting procedure described above, RT aging effects and viscoplastic material behavior evolution were characterized for SAC405 and SAC305 lead-free solders. Uniaxial stress-strain curves were recorded at room temperature and $\dot{\varepsilon}$ = 0.001 sec^{-1} after various durations of room temperature (25 ^{o}C) aging. For each set of test conditions, a total of 10 specimens were tested and a set of averaged material properties were extracted. Variations of the average temperature dependent mechanical properties (elastic modulus, yield stress, ultimate strength, creep compliance, etc.) were observed and modeled as a function of aging time.

In the SAC creep experiments, constant stress levels on the order of 40-50% of the observed UTS were applied. Due to the long test times involved, only 1-3 specimens were tested for any given set of test conditions. The strain versus time responses was recorded, as were the "steady state" creep strain rates (creep compliance) in the

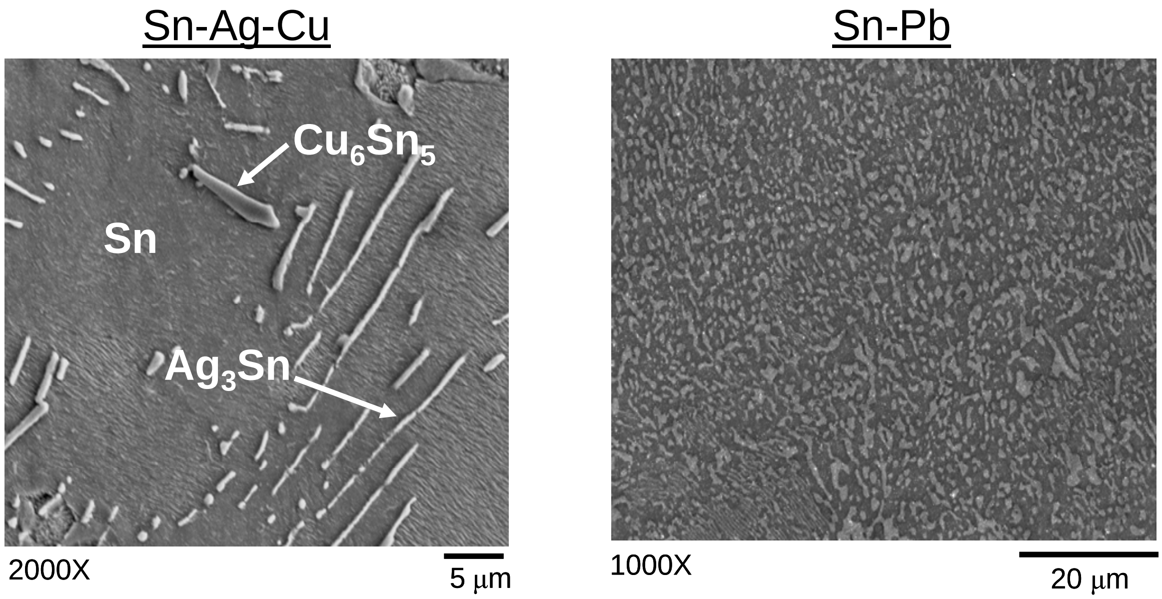

Figure 3.8 Typical Solder Microstructures.

secondary creep region. In this work, the "steady state" secondary creep rate was defined to be the minimum value of the observed $\dot{\varepsilon}$ versus t response.

The lead-free solder test samples in this investigation were solidified and tested with both water quenching (Figure 3.2a) and reflowed (Figure 3.3) cooling profiles. The water quenching profile provided an ultra-fast cooling rate that resulted in test specimens with extremely fine initial microstructure, high values of the material properties (E, YS, UTS), and relatively low creep strain rates. The reflow cooling profile, however, provides a cooling rate that more closely approximates that seen by actual solder joints during PCB assembly. Finally, in all of the lead-free (SAC) testing performed, analogous experiments were also performed with Sn-Pb eutectic solder samples for comparison.

3.5.2 Typical Stress-Strain Data and Empirical Model

Figure 3.9 illustrates a set of typical solder stress-strain curves for solder at T = 25 ^{o}C. In this case, 10 curves were recorded for SAC405 samples prepared with the same cooling profile (water quenching) and subjected to the same room temperature aging environment (63 days aging at RT). The observed variation in the data between different tests is typical for solder samples subjected to very similar aging exposures, although considerably much more variation will be present if the aging is not well controlled. The observed high strain behavior is close to ideally plastic, as the stress remains constant. In addition, the curves are well matched except in their failure behavior at high strains, where extensive localized reductions in the cross-sectional area (necking down) are observed. These large deformations lead to non-uniform stress-states in the specimen, as well as drops in the applied loading near the end of the stress-strain curve. In this

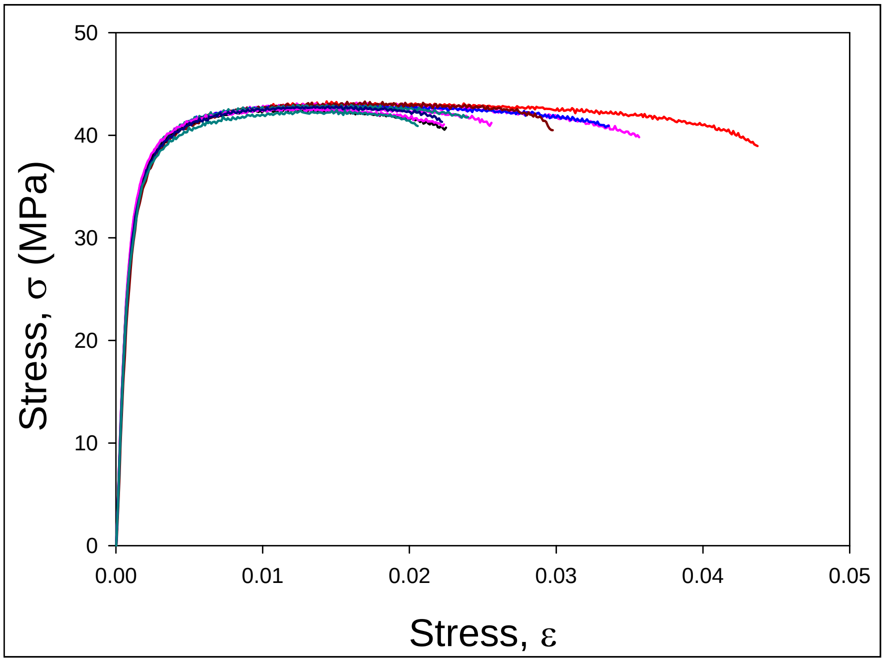

Figure 3.9 Typical Set of Stress-Strain Curves for a Given Set of Constant Conditions.

study, the analysis of tensile properties focus on the portions of the stress-strain curve before extensive visible necking occurs (typically ε < 2-3%). For example, the truncated curves in Figure 3.10 represent the data from Figure 3.9 with ε < 0.02 = 2%. The curves in Figure 3.10 are closely distributed, and well suited for mathematical representation.

In this study, the object was to replace the set of 10 recorded stress-strain curves for a certain testing configuration with a single "average" curve that accurately represents the observed response for all strain levels. Several different mathematical models could be used to represent the observed data. In this work, a linear model was used for extremely small strains ($\varepsilon << 0.0001$), and a four parameter empirical representation called the Weibull model for larger strains:

$$\begin{aligned} \sigma(\varepsilon) &= E\varepsilon & \varepsilon \le \varepsilon^* \\ \sigma(\varepsilon) &= C_0 - C_1 e^{-C_2 \varepsilon^{C_3}} & \varepsilon \ge \varepsilon^* \end{aligned} \tag{3.2}$$

where E is the initial elastic modulus; C_0, C_1, C_2, C_3 are material constants to be determined; and ε* is the strain level where the two functions intersect (become equal). The two function approach is typical for elastic-plastic materials, where it is desirable to model the initial portion of the stress-strain curve as perfectly linear (elastic), and the remaining portion of the curve as nonlinear. It is noted that the Weibull model is unable to match the extremely small strain behavior of solder accurately. In particular, the slope of the Weibull model mathematically becomes infinite at small strains (when $C_3 < 1$). Constant C_0 in the Weibull model gives the limiting value of the stress for high strains, which is the ultimate tensile strength (UTS):

$$C_0 = \sigma_u = \mathrm{UTS} \tag{3.3}$$

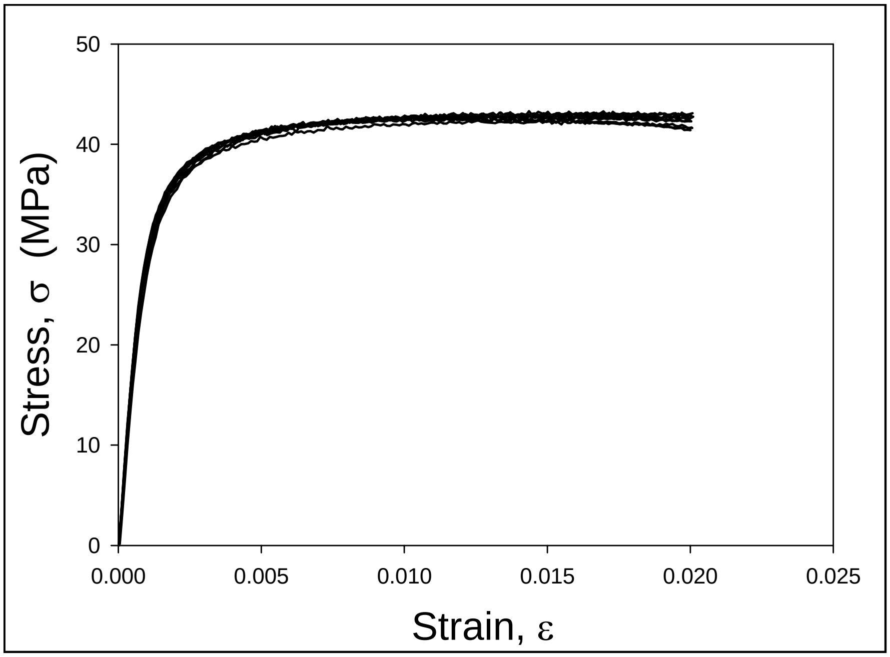

Figure 3.10 Typical Set of Truncated Stress-Strain Curves for a Given Set of Constant Conditions.

To utilize the model in Eq. 3.2 to fit a set of stress-strain data (e.g. the curves in Figure 3.10), the six constants E, C_0, C_1, C_2, C_3, and ε^* must be determined. In this work, the initial elastic modulus was found for each recorded curve by fitting the stress-strain data at very small strains using a linear regression analysis. The calculated modulus values for the set of 10 curves recorded under the same conditions were then averaged to generate the single elastic modulus E for the set. Secondly, a nonlinear regression analysis was performed to simultaneously fit the Weibull model to the combined data for all 10 stress-strain curves recorded under the same conditions. This yielded constants C_0, C_1, C_2, C_3. Finally, constant ε^* was then found by solving the nonlinear equation that expresses the condition for the two functions in Eq. 3.2 to intersect:

$$\sigma(\varepsilon^*) = \mathrm{E}\varepsilon^* = \mathrm{C}_0 - \mathrm{C}_1 e^{-\mathrm{C}_2 (\varepsilon^*)^{\mathrm{C}_3}} \tag{3.4}$$

With this procedure, the six material constants in Eq. 3.2 can be evaluated for any set of recorded stress-strain curves. For example, the fit of the empirical model in Eq. 3.2 to the curves in Figure 3.10 is shown in Figure 3.11. In this case, the material constants in the empirical model are E = 39.9 GPa, C_0 = 42.4 MPa, C_1 = 48.6 MPa, C_2 = 229.9, C_3 = 0.763, ε^* = .0002.

The excellent representation provided by the elastic-plastic empirical model suggests that it does indeed provide an accurate mathematical description of a suitable “average” stress-strain curve for a set of experimental curves measured under fixed test conditions.

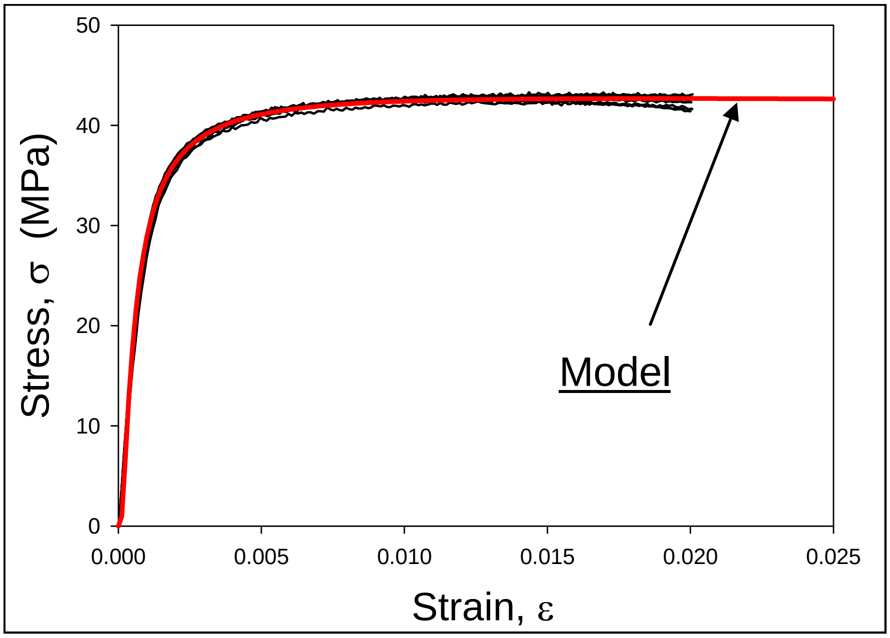

Figure 3.11 Model Fit to a Typical Set of Stress-Strain Curves.

CHAPTER 4

EFFECTS OF ROOM TEMPERATURE AGING ON THE PROPERTIES OF SOLDERS

4.1 Introduction

Solder alloys have high homologous temperatures for most normal operating conditions of electronic components, being greater than $0.5T_m$ (T_m is melting temperature) even at room temperature. At 25 °C, the homologous temperature is $0.65T_m$ for Sn-Pb eutectic solder and $0.61T_m$ for SAC405 and SAC305. The unique properties of solder lead to significant aging effects on tensile and creep properties for solders even at room temperature. However, the effects of room temperature have been overlooked by most researchers in both industry and academic institutions. This chapter reports on research into the effects of room temperature aging on both tensile strength and creep properties.

4.2 Effects of Room Temperature Aging on Tensile Properties

Several sets of 10 solder test specimens were prepared with water quenched and reflowed cooling profiles, as described in the previous chapter. The solder alloys are SAC405, SAC305 and Sn-37Pb. The sample sets were aged at room temperature (T = 25 °C) for carefully controlled time periods, and then mechanically tested. A single "average" stress-strain curve was found for each sample set with a defined cooling profile and aging duration, using the empirical model in Eq. 3.2, and the procedure described in Chapter 3. For each solder alloy and cooling profile considered, nine sample sets (90 specimens) were fabricated. Each set was then tested after a different duration of RT aging. The periods considered were: no aging, 5 hours, 1 day, 3 days, 6 days, 9 days, 21 days, 42 days, and 63 days. The average material properties (E, UTS, YS) were extracted from the recorded stress-strain data for each set of samples.

The effects of RT aging on the stress-strain behavior of water quenched SAC405 samples are illustrated in Figure 4.1. It can be seen that the initial linear behavior of the average stress-strain curves is only slightly affected, while the post yield behavior changes dramatically with aging. These conclusions are easily justified by extracting the material properties from the average curves in Figure 4.1. Plots of the variation of the effective elastic modulus E and failure stresses (YS and UTS) with aging are shown in Figures 4.2 and 4.3, respectively. During the 63 days of RT aging, the effective modulus dropped only 7.6%, from 43.0 MPa to 39.7 MPa. However, the ultimate tensile strength UTS reduced by 38.6% (67.3 to 41.3 MPa), while the yield stress YS fell by 32.3% (57.6 to 39.0 MPa).

Similar data were collected for reflowed SAC405 samples. The stress-strain curve variation with RT aging is shown in Figure 4.4, while the extracted material property dependence on aging is shown in Figures 4.5-4.6. For this solidification profile, the elastic modulus dropped 6.1% with aging, while the UTS and YS degraded by 24.6% and 22.9%, respectively. Note that there were only slight differences between the magnitudes and aging behavior of the elastic modulus for the water quenched and reflowed samples. However, the results in Figures 4.4 and 4.6 clearly demonstrate that

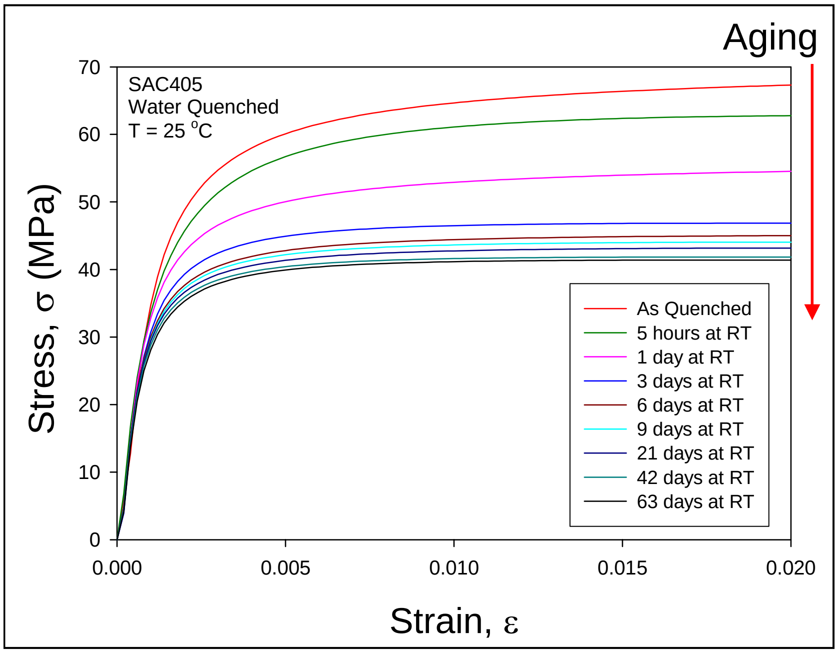

Figure 4.1 SAC405 Stress Strain Curves for Various Room Temperature Aging Times (Water Quenched).

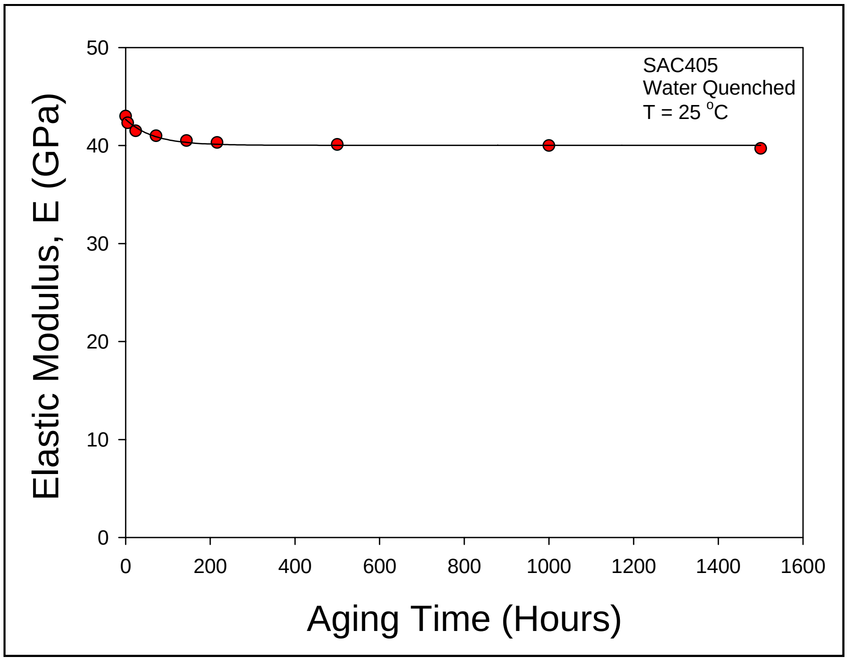

Figure 4.2 Elastic Modulus vs. RT Aging Time (SAC405, Water Quenched).

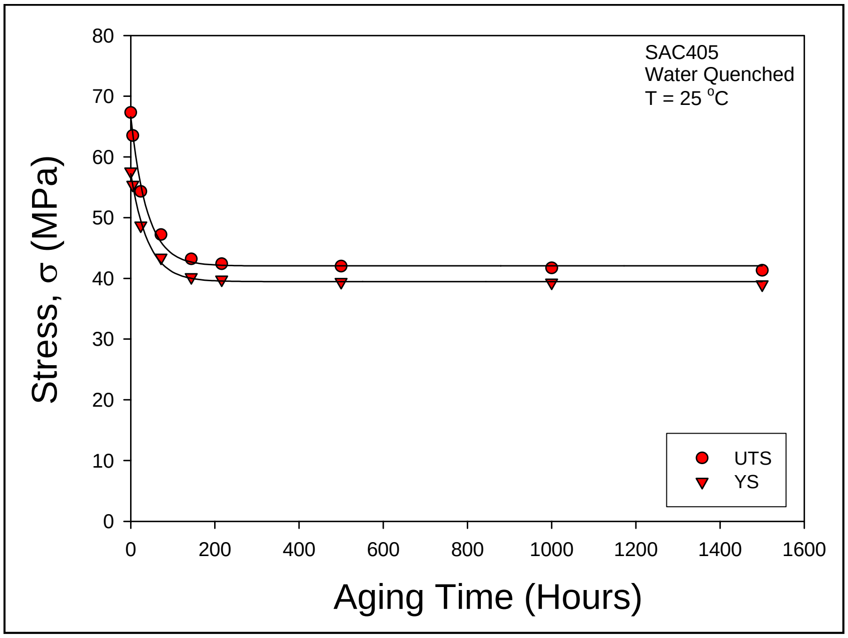

Figure 4.3 Failure Stresses vs. RT Aging Time (SAC405, Water Quenched).

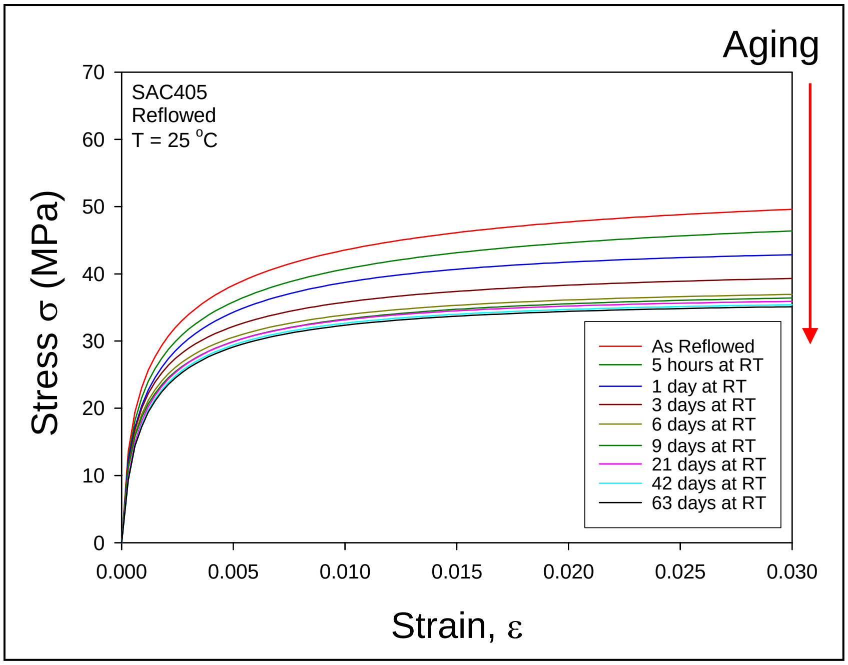

Figure 4.4 SAC405 Stress Strain Curves for Various Room Temperature Aging Times (Reflowed).

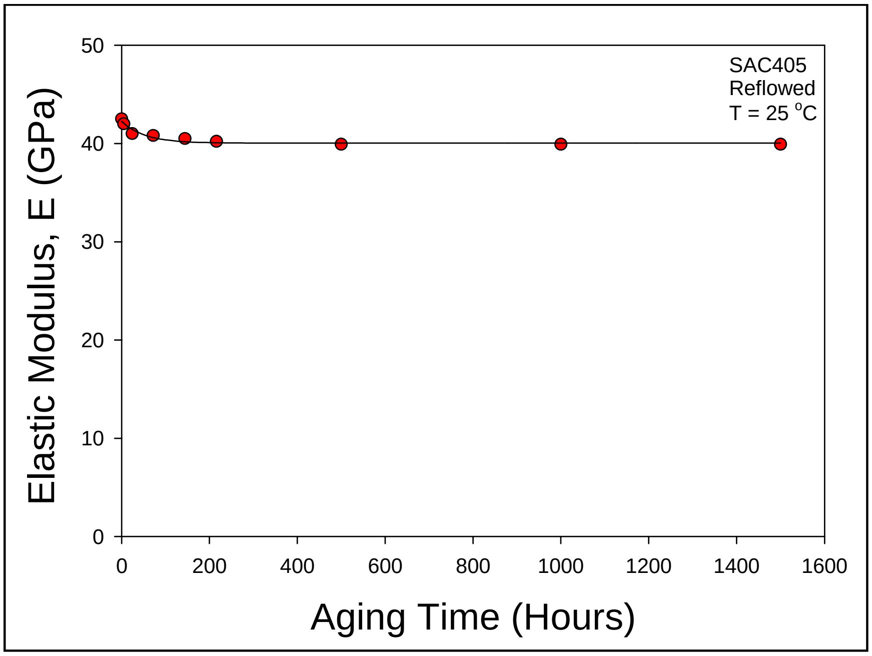

Figure 4.5 Elastic Modulus vs. RT Aging Time (SAC405, Reflowed).

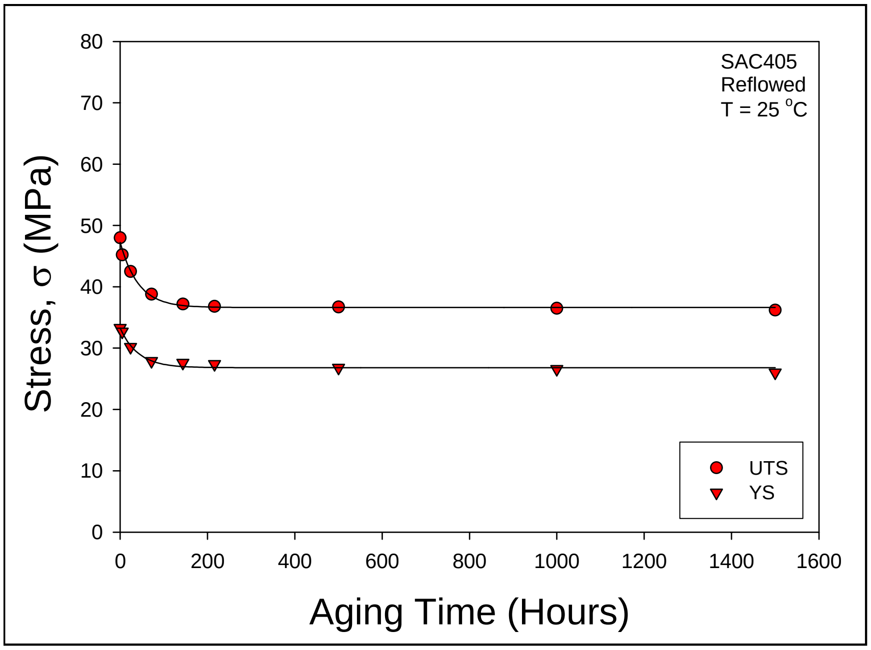

Figure 4.6 Failure Stresses vs. RT Aging Time (SAC405, Reflowed).

the failure stresses (YS and UTS) of the reflowed samples are much smaller than those of the water quenched samples at all aging times. This reaffirms the strong dependence on the failure properties of solder joints on the cooling profile used in their formation. For SAC405, it is clear that slightly stiffer and considerably stronger joints can be obtained with faster cooling during solidification.

These results indicate that the material properties of the SAC405 solder continue to decline with further room temperature aging past 63 days. However, the rates of these further reductions are extremely small. The majority of the degradations in the effective elastic modulus and failure properties occur during the first 10 days (240 hours) of RT aging for both the water quenched and reflowed samples. The data points in Figures 4.4 and 4.6 were fitted using an empirical model that reflects this stabilization and asymptotic behavior:

$$\text{Material Property} = C_0 + \frac{C_1}{1+e^{-\left(\frac{t-C_2}{C_3}\right)}} \qquad t \leq 240 \text{ Hours} \qquad (4.1)$$

$$\text{Material Property} = -\alpha t + \beta \qquad t \geq 240 \text{ Hours} \qquad (4.2)$$

When the aging time is less than 240 hours (10 days), the relationship follows Eq. 4.1. For longer aging times, the tensile properties are a relatively stable, and follow a near linear relationship, with a small slope (Eq. 4.2). The experimental data indicates that the tensile properties of lead-free solders continue to change at room temperature aging, although at a very low rate after the initial aging durations. The linear relationship can be obtained based on the experimental data.

The same sets of stress-strain versus RT aging experiments have been performed for both SAC305 and Sn-Pb eutectic solder samples. For each alloy, both water quenching and reflow cooling profiles have been utilized. Figures 4.7-4.9 contain the observed stress-strain curves and extracted material properties for the water quenched SAC305 samples, while Figures 4.10-4.12 show the analogous results for the reflowed SAC305 specimens.

Comparison of the results for SAC405 and SAC305 reveals that there are only small differences in the uniaxial stress-strain responses of these alloys. Both solders demonstrated significantly increased mechanical properties for the quick water quenching cooling profile relative to a standard reflow cooling profile. Also, the variations of the mechanical properties with duration of RT aging showed similar trends. Relative to the SAC405 response, the SAC305 stress-strain curves did illustrate slightly sharper transitions between the initial linear “elastic” regions and the near horizontal plastic regions. In addition, the effective elastic modulus of SAC405 was observed to be 3-5% higher than that of SAC305 after solidification, and this separation remained even as RT aging progressed. The SAC405 alloy also demonstrated a similar 3-5% advantage in the UTS after solidification. However, after 63 days of RT aging, the UTS values for the SAC405 and SAC305 alloys were essentially identical. Based on the experimental data for E, UTS, YS, Table 4.1 summarizes the near linear relationship (Eq. 4.2) of room temperature aging effects with the tensile properties of both lead-free solders at long aging times. With increasing aging time at room temperature, the tensile properties steadily decrease. The underlying reason for the continuous aging effects is due to the high homologous temperature of solders. From these results for lead-free solders, aging over 20 years at room temperature would raise concerns for reliability.

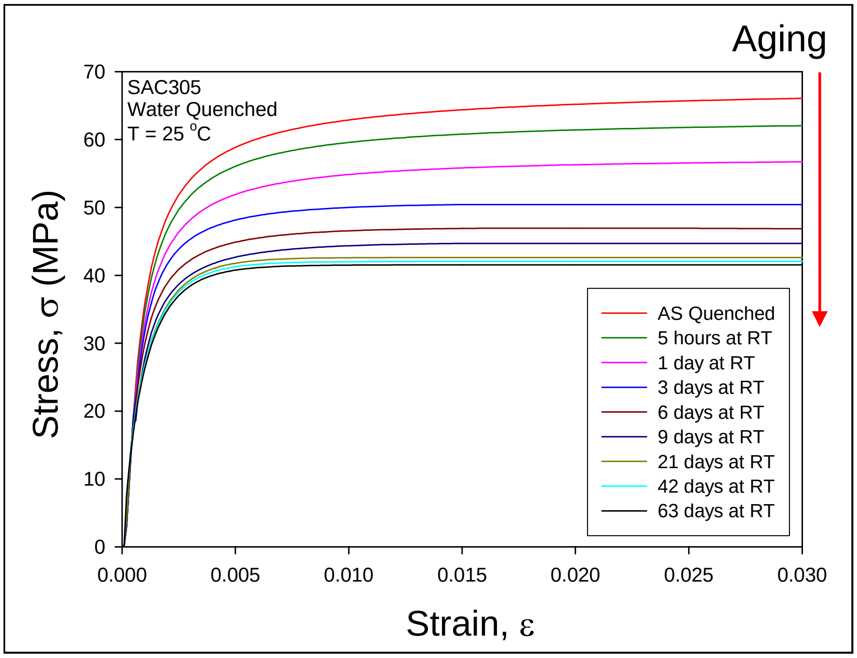

Figure 4.7 SAC305 Stress Strain Curves for Various Room Temperature Aging Times (Water Quenched).

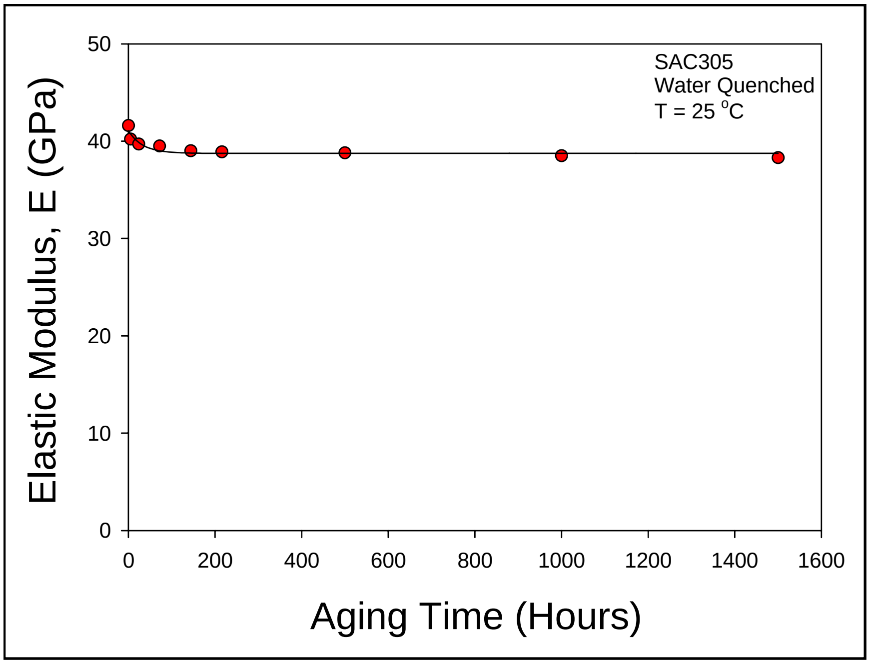

Figure 4.8 Elastic Modulus vs. RT Aging Time (SAC305, Water Quenched).

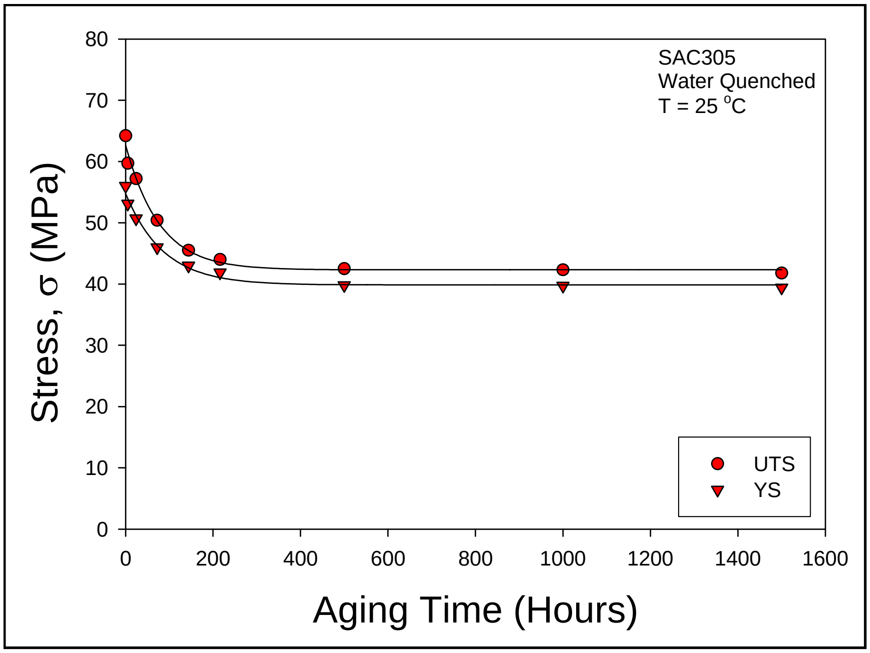

Figure 4.9 Failure Stresses vs. RT Aging Time (SAC305, Water Quenched).

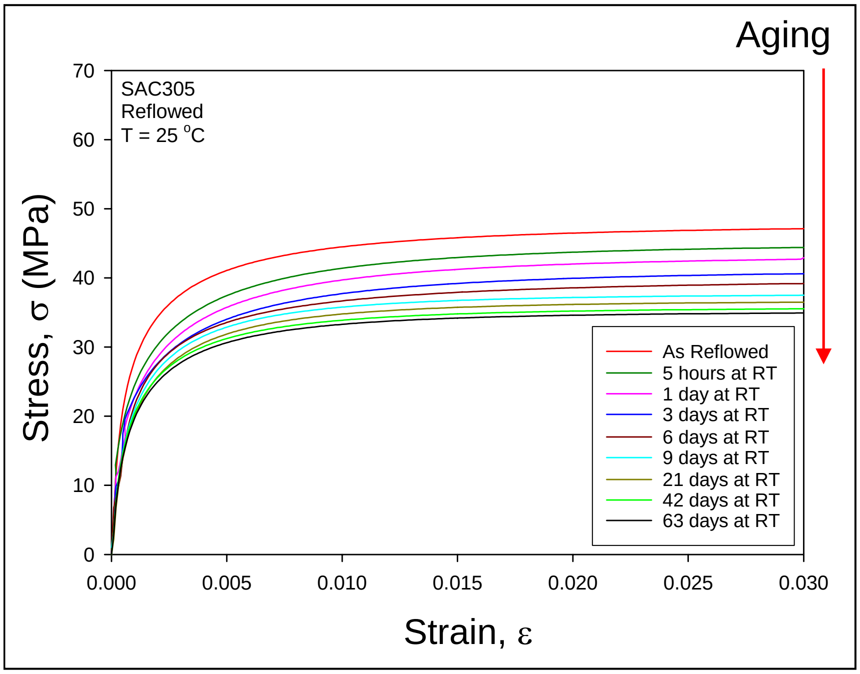

Figure 4.10 SAC305 Stress Strain Curves for Various Room Temperature Aging Times (Reflowed)

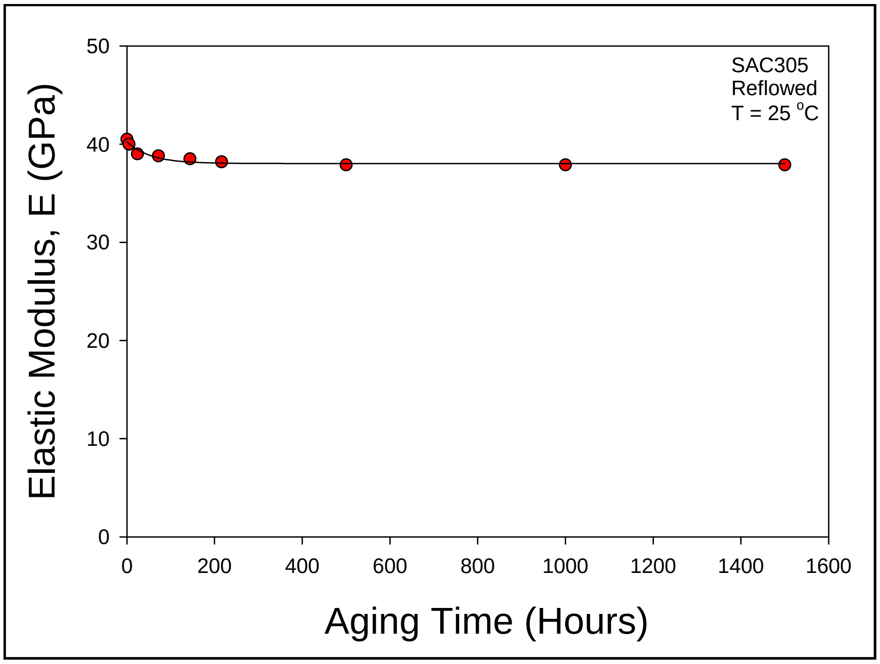

Figure 4.11 Elastic Modulus vs. RT Aging Time (SAC305, Reflowed).

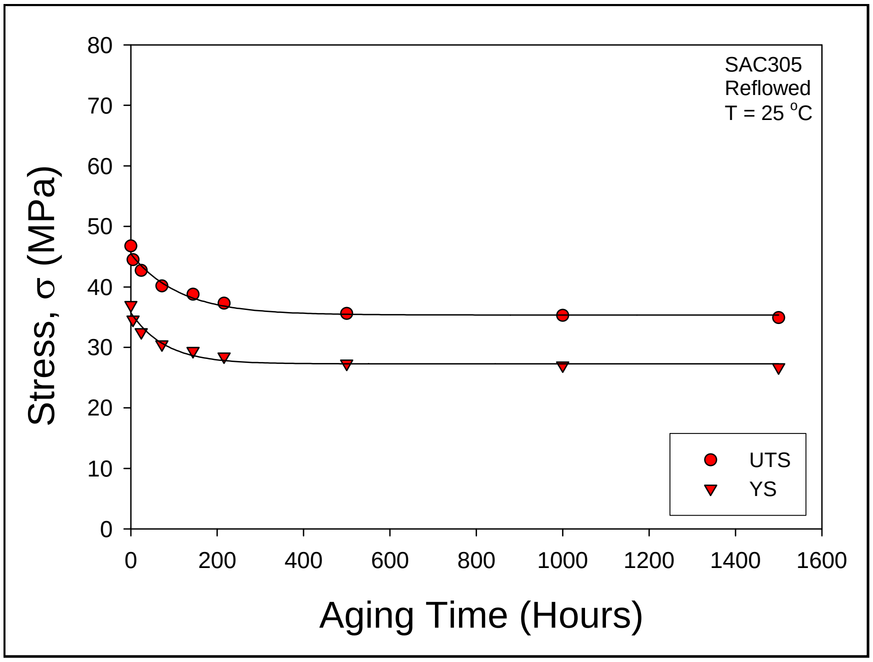

Figure 4.12 Failure Stresses vs. RT Aging Time (SAC305, Reflowed).

Table 4.1 Effects of Room Temperature Aging on Tensile Properties (t > 240 hours)

Solders		Tensile Properties	Aging Time Dependence	R^2
SAC405	Water Quenched	E (GPa)	-0.0004t + 40.33	0.9231
		UTS (MPa)	-0.0008t + 42.50	0.9770
		YS (MPa)	-0.0005t + 39.53	0.9849
	Reflowed	E (GPa)	-0.0002t + 40.12	0.9747
		UTS (MPa)	-0.0005t + 36.92	0.9857
		YS (MPa)	-0.0008t + 27.27	0.9231
SAC305	Water Quenched	E (GPa)	-0.0005t + 39.02	0.9916
		UTS (MPa)	-0.0007t + 42.90	0.9423
		YS (MPa)	-0.0004t + 40.03	0.9231
	Reflowed	E (GPa)	-0.0002t + 38.12	0.9727
		UTS (MPa)	-0.0007t + 35.96	0.9957
		YS (MPa)	-0.0006t + 27.60	0.9987

The experimental results for the Sn-Pb alloy are contained in Figures 4.13-4.15 and Figures 4.16-4.18 for the water quenching and reflow cooling profiles, respectively. The Sn-Pb stress-strain data revealed several different trends than the previously discussed data for SAC405 and SAC305. In particular, the reflowed Sn-Pb samples uniformly showed better (higher) mechanical properties than the water quenched samples, and larger changes were observed during aging for the reflowed samples relative to the quenched samples. This was in direct contradiction to the results found for the high tin content lead-free SAC alloys, where the water quenched samples illustrated superior mechanical properties, and the quenched samples experienced the larger changes in mechanical behavior with aging. It does, however, correspond to the microstructure observed for the solder alloys, which will be explored in the next section. Other possible reasons maybe lie in the specimen preparation procedure. Sn-Pb has far superior wetting ability compared to the SAC alloys. From observations of the new specimen preparation procedure used for this study, Sn-Pb fills the glass mold much faster than the SAC alloys, which may trap vaporized gas in the solder materials, without the time the SAC specimens have allow for the gas to be expelled. During the reflow process, all the trapped gas may have been released, and thus causing the difference in properties.

The Sn-Pb samples also exhibited significant (25%) differences in the effective elastic moduli found for the water quenched and reflowed samples. For the lead-free alloys discussed above, these differences were less than 2.5% for both SAC305 and SAC405. The tensile properties for longer aging time were more stable than those of the SAC alloys. Table 4.2 contains a summary of the extreme values of the elastic modulus and ultimate tensile strength (before and after RT aging) for the 3 tested solder alloys.

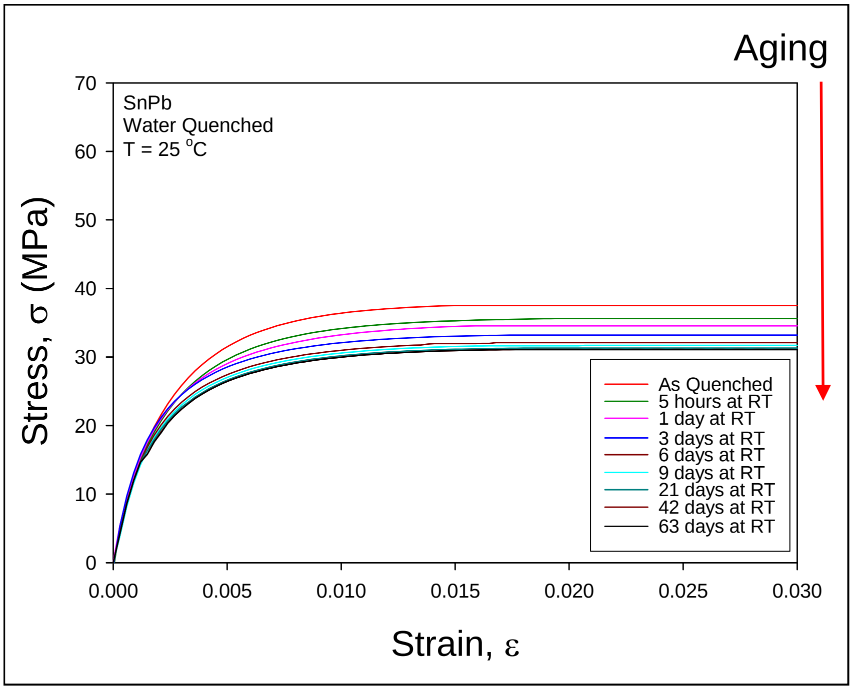

Figure 4.13 Sn-Pb Stress Strain Curves for Various Room Temperature Aging Times (Water Quenched).

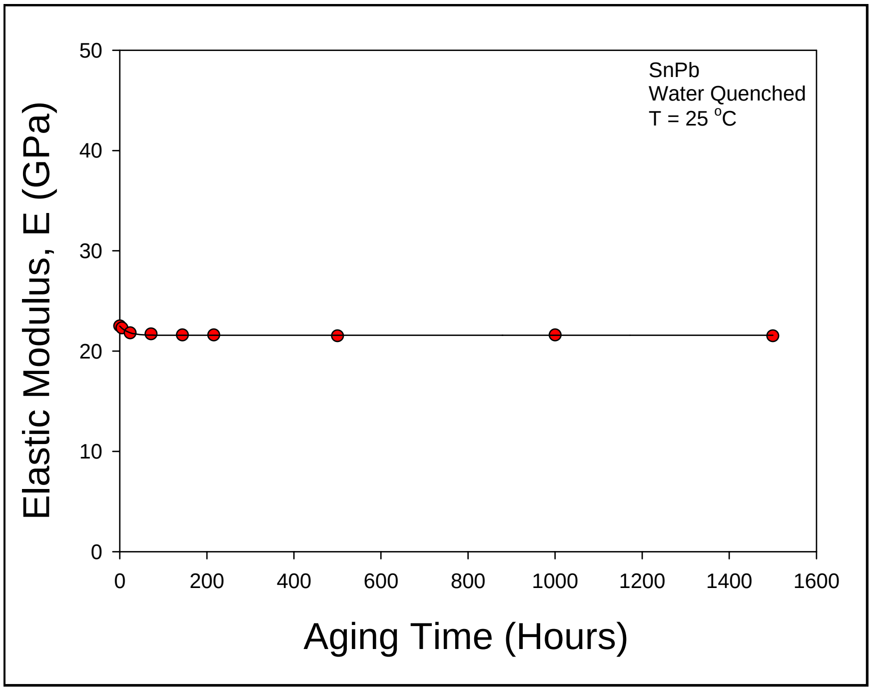

Figure 4.14 Elastic Modulus vs. RT Aging Time (Sn-Pb, Water Quenched).

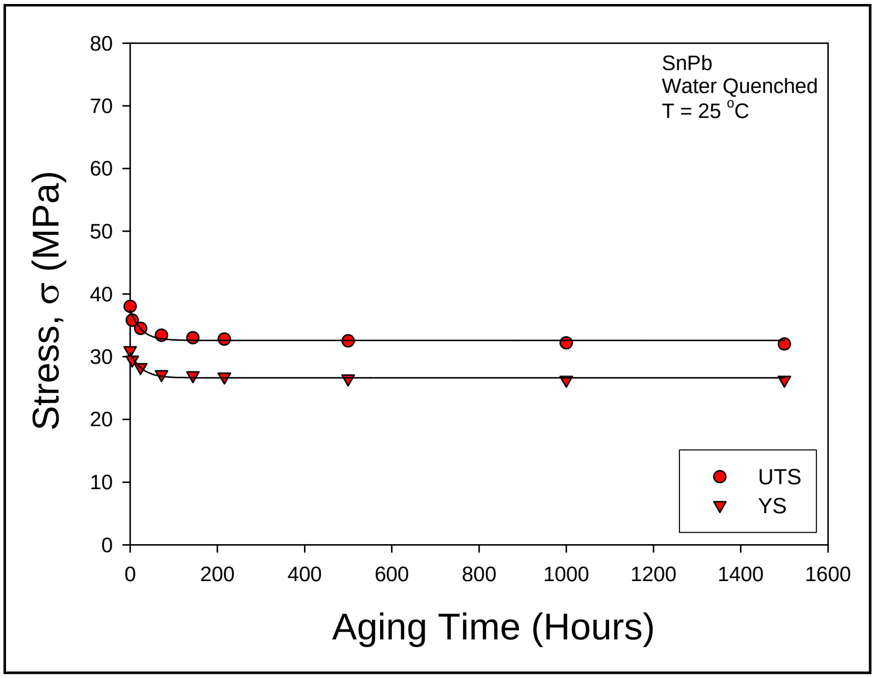

Figure 4.15 Failure Stresses vs. RT Aging Time (Sn-Pb, Water Quenched).

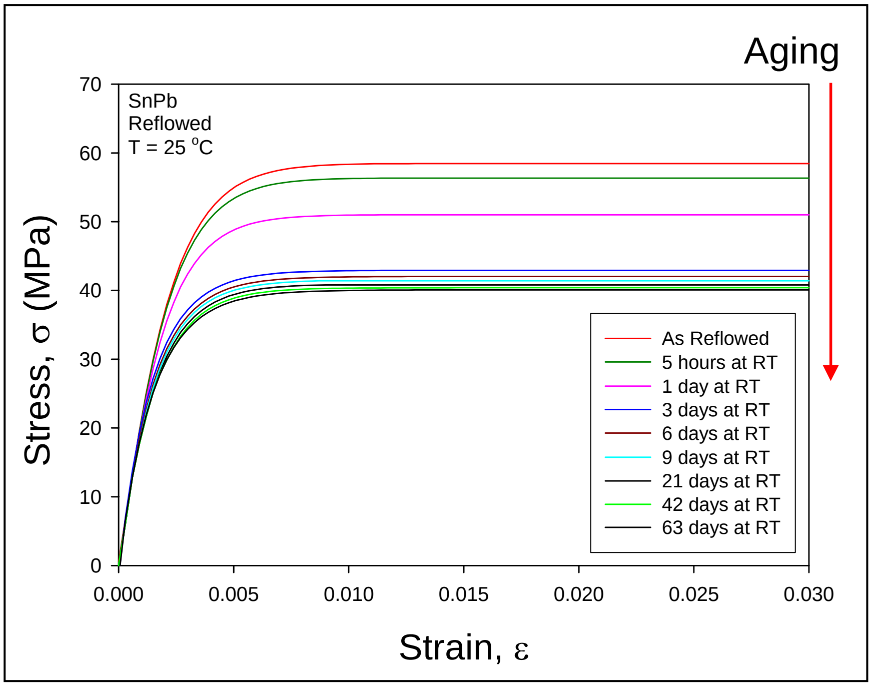

Figure 4.16 Sn-Pb Stress Strain Curves for Various Room Temperature Aging Times (Reflowed).

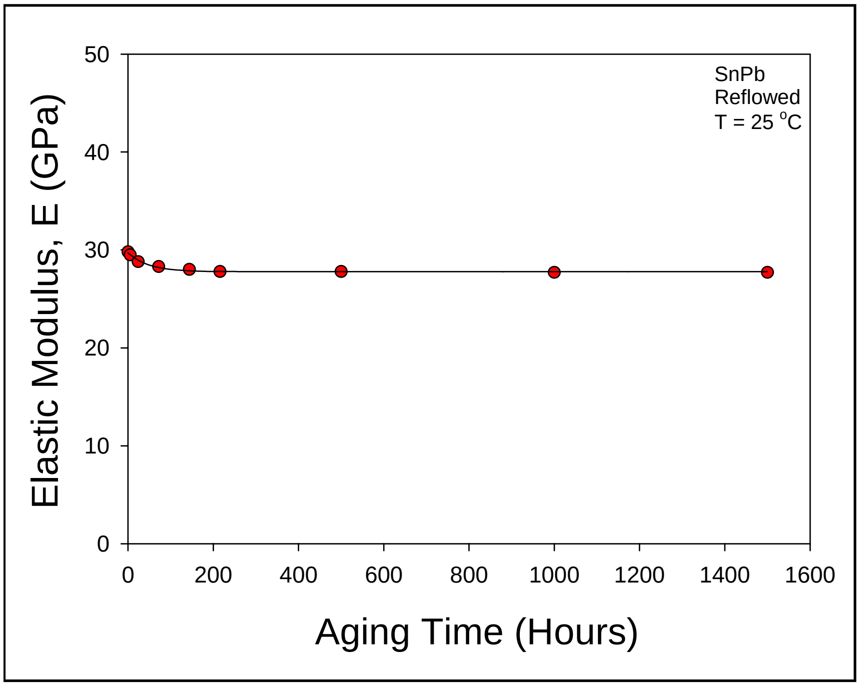

Figure 4.17 Elastic Modulus vs. RT Aging Time (Sn-Pb, Reflowed).

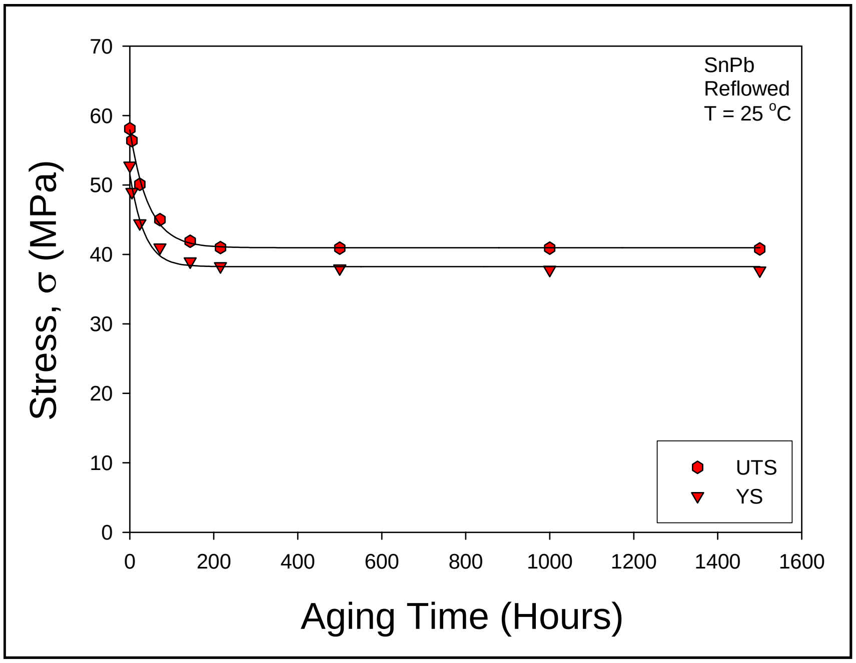

Figure 4.18 Failure Stresses vs. RT Aging Time (Sn-Pb, Reflowed).

Table 4.2 Maximum and Minimum Material Property Values During Aging at Room Temperature.

Solder Alloy & Cooling Profile	E_{max} (GPa)	E_{min} (GPa)	UTS_{max} (MPa)	UTS_{min} (MPa)
SAC405, Quenched	43.0	39.7	67.3	41.3
SAC405, Reflowed	42.5	39.9	48.0	36.2
SAC305, Quenched	41.6	38.3	64.2	41.8
SAC305, Reflowed	40.5	37.9	46.8	34.9
SnPb, Quenched	22.5	21.5	38.0	32.0
SnPb, Reflowed	29.8	27.7	58.1	40.8

4.3 Effects of Room Temperature Aging on Microstructure

The microstructure changes that occur during room temperature aging of the SAC405 solder specimens are shown in Figure 4.19. The mounting procedure described in Chapter 3 was utilized to generate samples suitable for SEM viewing within 1 hour of solidification. These photographs show that the initial microstructures of both alloys were extremely fine, and that they coarsened significantly after only 9 days of RT aging. The basic structure of SAC405 (95.5Sn-4.0Ag-0.5Cu) is Sn-based dendrites. The dendrites grow during the solidification process, and the second phase particles precipitate out between the arms of the dendrites. The second phases are easily identified by EDS/EDX to be Ag_3Sn and Cu_6Sn_5. Since the Cu content in the SAC solder is very small, the majority of the second phase particles are needle like Ag_3Sn intermetallics.

During room temperature aging, the Sn-based dendrites grow larger, and the Ag_3Sn and Cu_6Sn_5 second phase intermetallics congregate and grow longer between the arms of the dendrites. As shown in Figures 4.19(a) and 4.19(c), the second phase particles were coarser for reflowed SAC405 specimens relative to the water quenched ones. This trend continued with aging. The dendrites were also bigger for the reflowed samples. The reflow process allows the solder to re-melt and recrystallize into a coarser structure. These effects caused the UTS of the reflowed SAC405 to be lower than water quenched SAC405. Also note that the coarsening of the microstructure occurs much faster for the water-quenched SAC specimens relative to the reflowed ones.

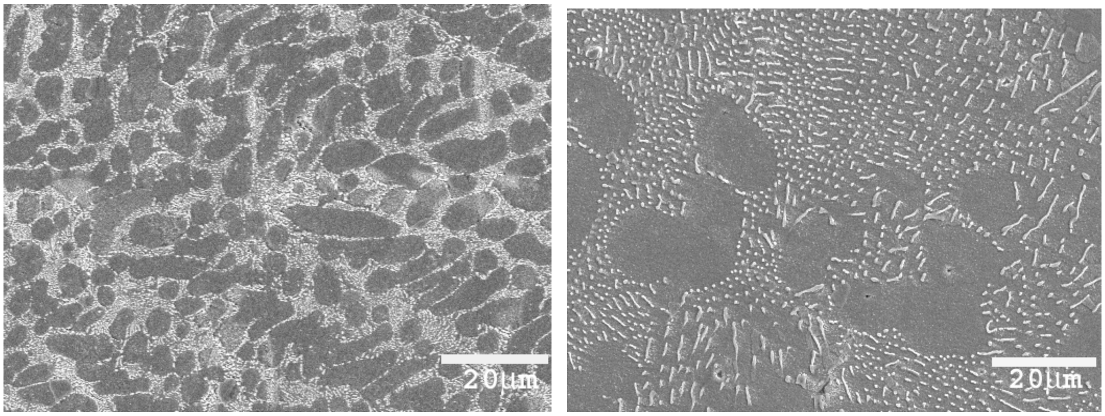

(a) Quenched, No Aging (b) Quenched, 9 Days at RT

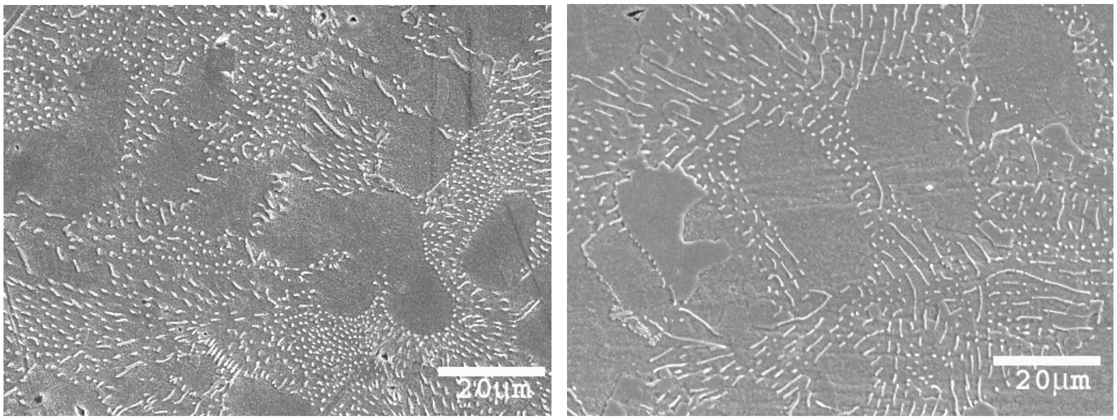

(c) Reflowed, No Aging (d) Reflowed, 9 Days at RT

Figure 4.19 Microstructure Evolution During RT Aging SAC405 (25 ^{o}C)

The equivalent set of Sn-Pb photographs is shown in Figure 4.20. The typical Sn-Pb structure shows the well known Sn-rich and Pb-rich phase structures. This microstructure coarsens with RT aging. The softening occurring in the Sn-Pb solder samples is attributed to the precipitation of beta-tin out of the supersaturated lead-rich phases during room temperature aging.

This transition causes coarsening of both the Sn-rich and Pb-rich phases. The superior tensile properties for the reflowed Sn-Pb samples (relative to the water quenched samples) can also be explained by examining the microstructure. As shown in Figure 4.20(a) and 4.20(c), the phase structure of the water quenched specimens after solidification was coarser than that for the reflowed samples after solidification (opposite to the SAC results). This trend continued with RT aging. The quenched samples likely experienced rapid microstructure transitions during the brief time periods that occurred between placing molten solder into the tubes and immersing the tubes in the water bath. By the time the specimen reached the water, the temperature may well have already dropped below the melting temperature of the solder. The use of a reflow oven is advantageous because it is a more controllable process. For example, the peak temperature in the profile shown in Figure 3.4(b) is much higher than the solder melting point of 183 °C. Thus, there is more cooling required and more time for the alloy to reach a stable status upon cooling. The microstructure evolution corresponds with the mechanical properties well; a coarser microstructure leads to worse mechanical properties for both the lead and lead-free solder alloys.

The microstructure coarsening also corresponded with the tensile properties in the previous section. As mentioned in Chapter 2, increasing grain size and phase

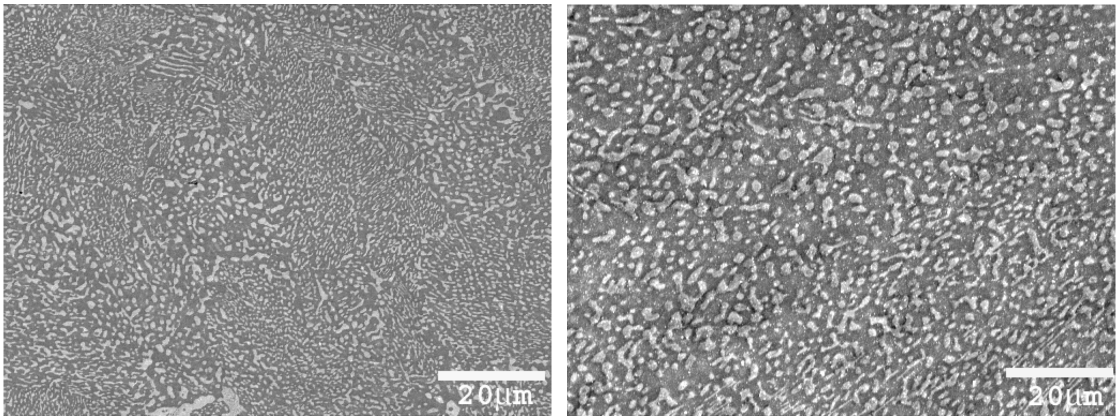

(a) Quenched, No Aging

(b) Quenched, 9 Days at RT

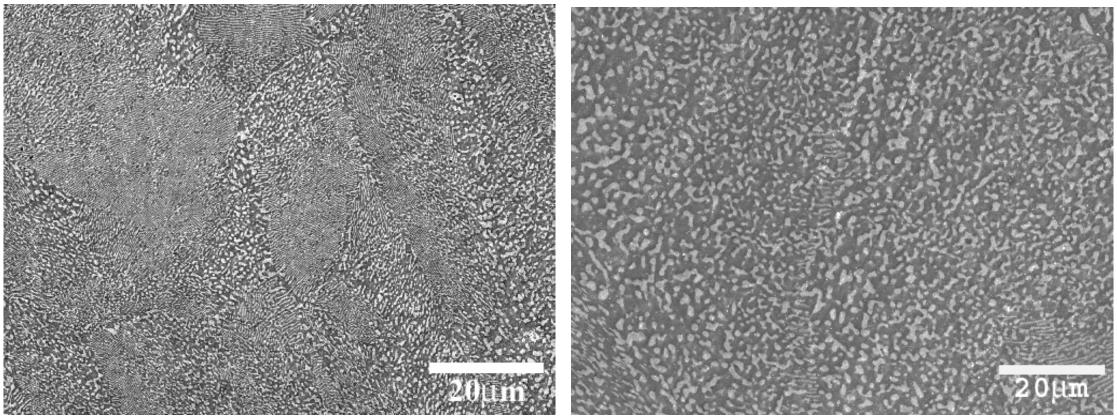

(c) Reflowed, No Aging

(d) Reflowed, 9 Days at RT

Figure 4.20 Microstructure Evolution During RT Aging 63Sn-37Pb (25 ^{o}C).

structure will cause a loss of tensile strength (Eq. 2.1). Grain size coarsening also causes a reduction in the apparent elastic modulus due to the creep contribution to the apparent elastic modulus. However, the reduction in the elastic modulus is relatively smaller than the UTS and YS because the major contribution of the apparent elastic modulus is elastic deformation which is relatively independent of microstructural changes. The UTS and YS are mainly dependent on strain hardening due to the blocking of dislocation movement by the grain boundaries.

4.4 Effects of Room Temperature Aging on Solder Creep Response

As the literature review in Chapter 2 indicated, there is currently no documented data on the effects of room temperature (RT) aging on creep deformation, so an extensive study of the effects of room temperature aging on the creep response of solder was conducted. In this study, the data obtained for SAC and Sn-Pb samples cooled by both water quenching and reflowed conditions is reported. As in the uniaxial stress-strain tests, samples were tested with several levels of RT aging including no aging, 3 days, 6 days, 9 days, 21 days, 42 days, and 63 days. Due to the long test times involved, only 1-3 specimens were tested for any given set of test conditions (alloy, aging time, temperature). The strain versus time responses were recorded, as were the "steady-state" creep strain rates (creep compliance) in the secondary creep region were. Here, the "steady-state" or secondary creep rate was defined to be the minimum and constant value of the observed $\dot{\varepsilon}$ versus t response through the creep curve. Figure 4.21 illustrates a typical creep curve for solders. Figure 4.21 shows the corresponding creep strain rate for the creep curve. The steady-state creep rate is the value in the relatively stable region (Figure 4.22).

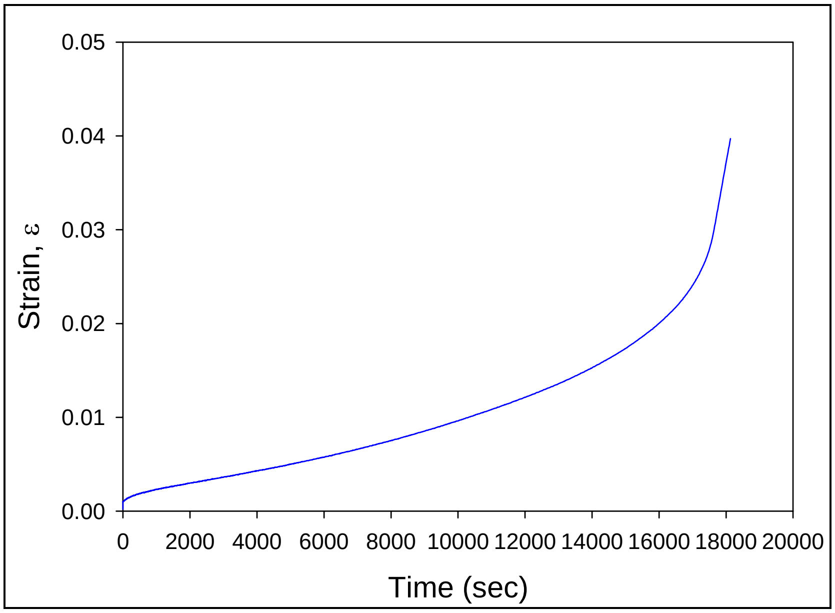

Figure 4.21 Typical Creep Strain vs. Time.

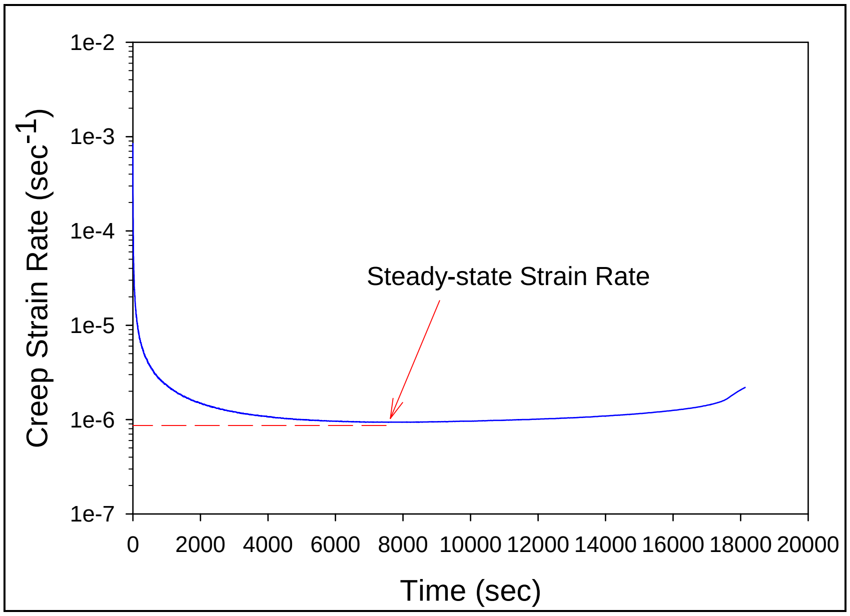

Figure 4.22 Typical Creep Strain Rate vs. Time.

In the SAC405 and SAC305 creep experiments, constant stress levels of σ = 25, 30, and 35 MPa were chosen for the water quenched condition, and σ = 15, 20, and 25 MPa for the reflowed condition. These values cover the range of 40-50% of the non-aged UTS of the water quenched samples, and 60-85% of the non-aged YS of the water quenched samples. The effects of RT aging on the creep responses of the SAC405 samples are illustrated in Figures 4.23-4.24 for the three stress levels. These plots show that the influence of aging duration on creep is even more pronounced than the aging effects observed for the tensile stress-strain behavior. Both the strain rate in the secondary creep region, and the time to tertiary creep and rupture are strongly affected. Figures 4.25-4-26 illustrate the increases in the secondary creep strain rate with aging time for SAC405 for both the water quenched and reflowed conditions. It was necessary to use semi-log plots because of the large magnitude changes that occurred. For water quenched specimens the steady-state strain rate increased by factors 16X, 7X and 2X for the stress levels of 35 MPa, 30 MPa, and 25 MPa respectively. The creep strain rate for the reflowed condition increased by 20X, 4X, and 1X for stress levels of 25 MPa, 20 MPa, and 15 MPa respectively. The corresponding creep curves for the SAC305 alloy are shown in Figures 4.27-4.28, and Figures 4.29-4.30 show the steady-state strain rate changes after room temperature aging for both the water quenched and reflowed conditions. For SAC 305, the creep strain rate increased by factors of 73X, 7X and 1X for the water quenched, and 30X, 5X, and 1X for the reflowed conditions. As previous data showed that the tensile strength values of SAC405 and SAC305 are close, there are no significant difference in elastic modulus, UTS and YS. Although the aging effects are similar for the two lead-free alloys, the magnitude of creep deformation is different.

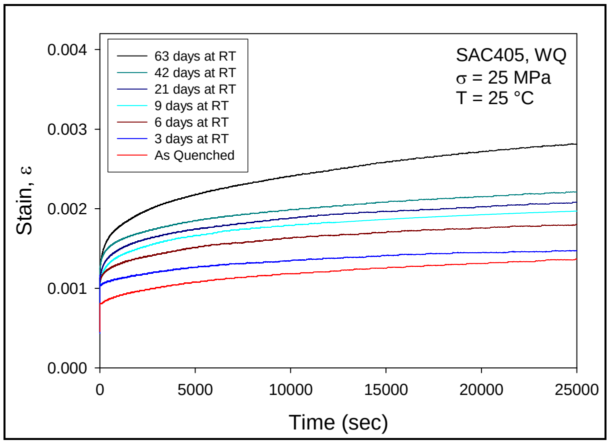

(a) 25 MPa

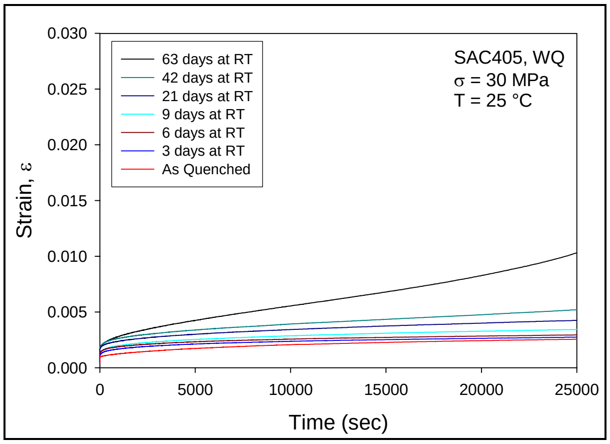

(b) 30 MPa

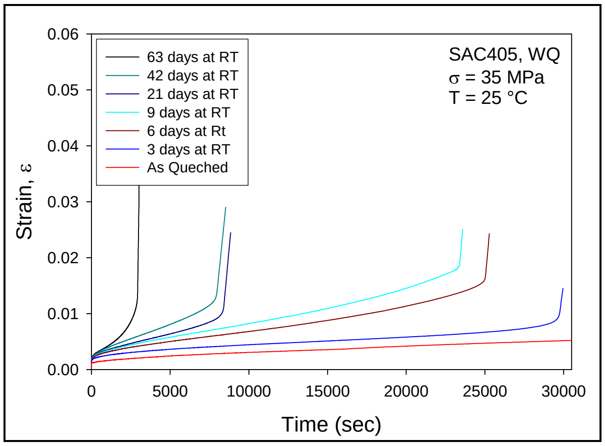

(c) 35 MPa

Figure 4.23 SAC405 Creep Curves for Various RT Aging Times (Water Quenched).

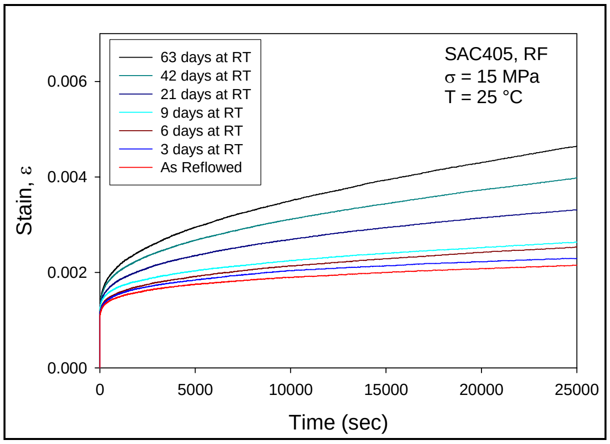

(a) 15 MPa

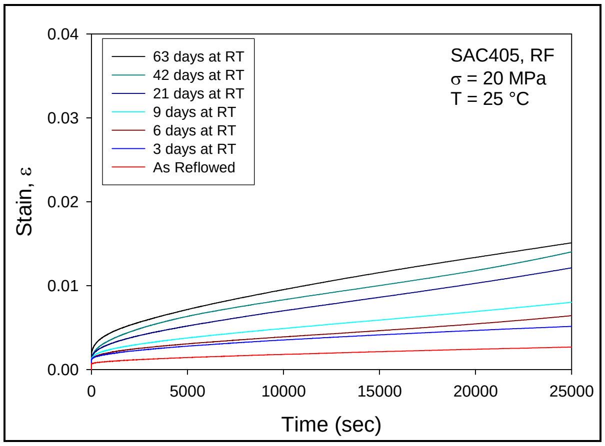

(b) 20 MPa

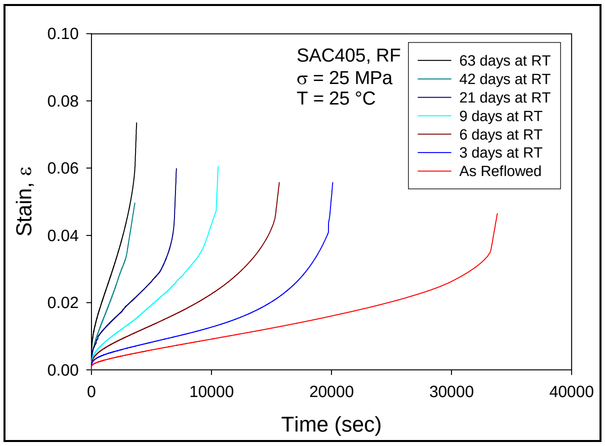

(c) 25 MPa

Figure 4.24 SAC405 Creep Curves for Various RT Aging Times (Reflowed).

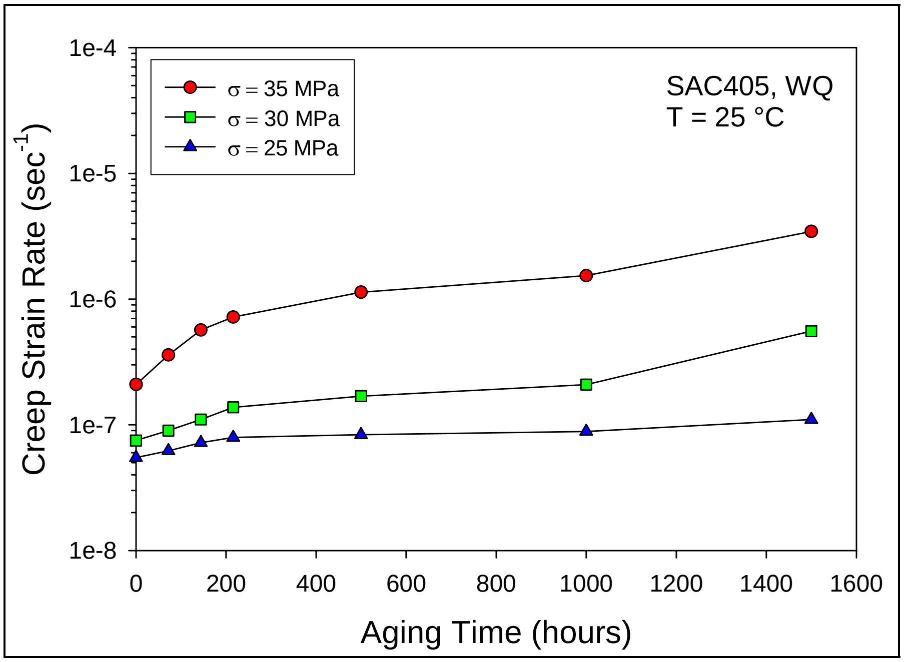

Figure 4.25 SAC405 Creep Strain Rate vs. RT Aging Time (Water Quenched).

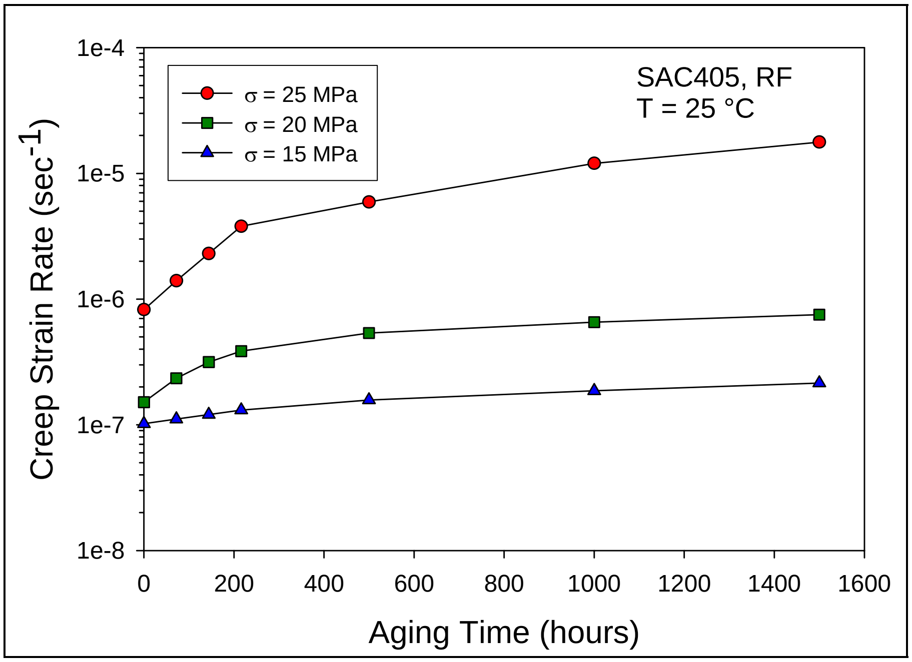

Figure 4.26 SAC405 Creep Strain Rate vs. RT Aging Time (Reflowed).

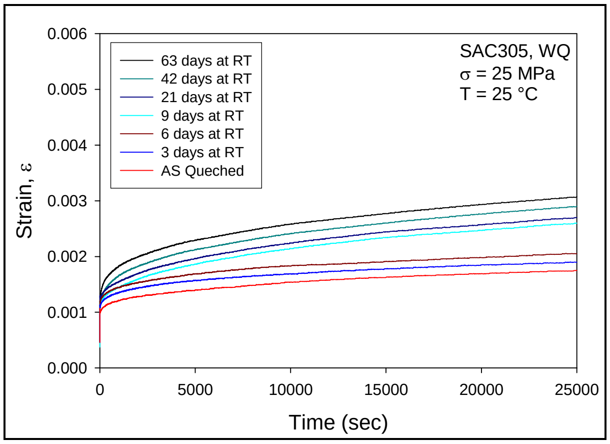

(a) 25 MPa

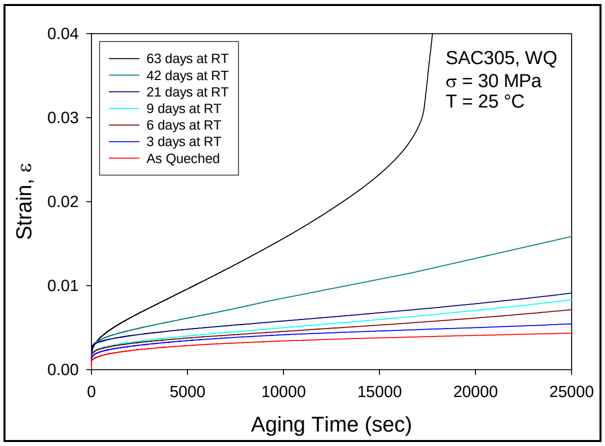

(b) 30 MPa

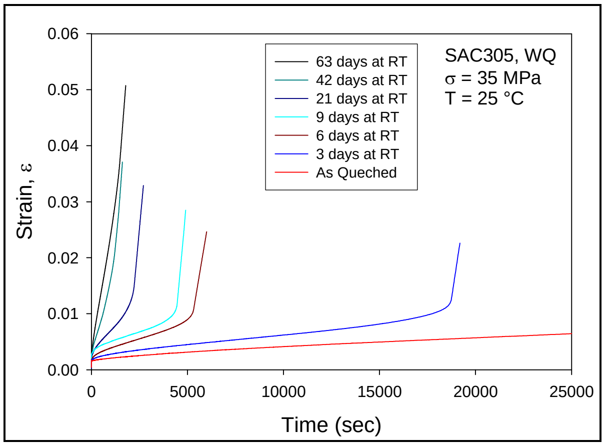

(c) 35 MPa

Figure 4.27 SAC305 Creep Curves for Various RT Aging Times (Water Quenched).

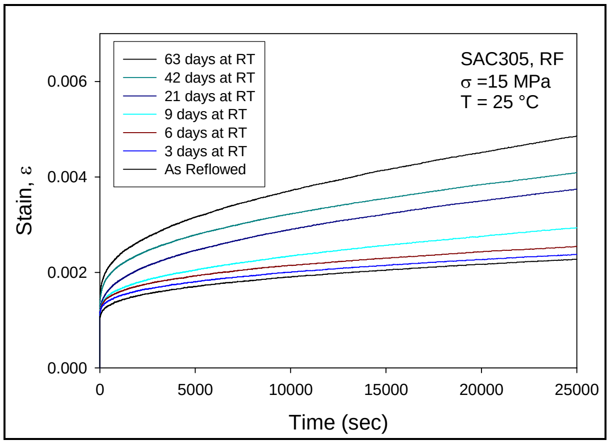

(a) 15 MPa

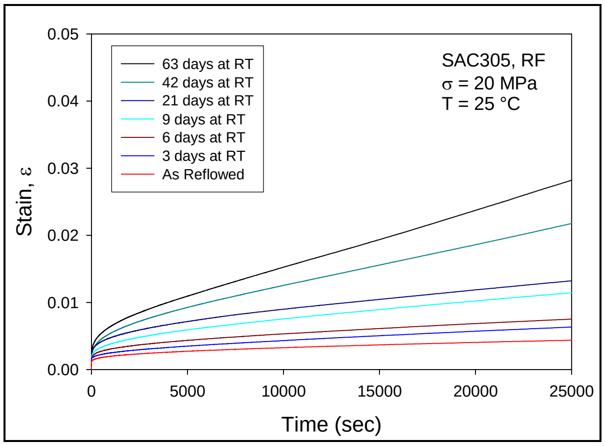

(b) 20 MPa

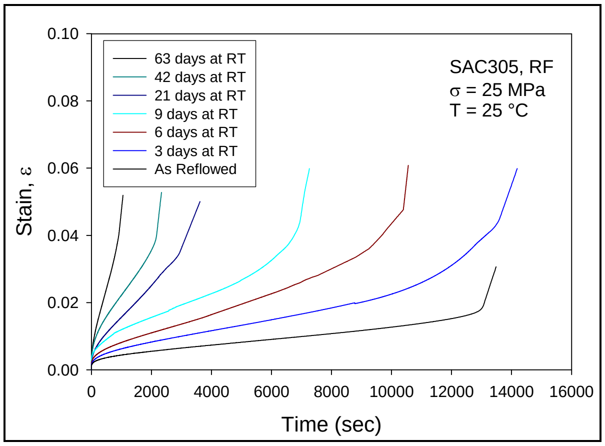

(c) 25 MPa

Figure 4.28 SAC305 Creep Curves for Various RT Aging Times (Reflowed).

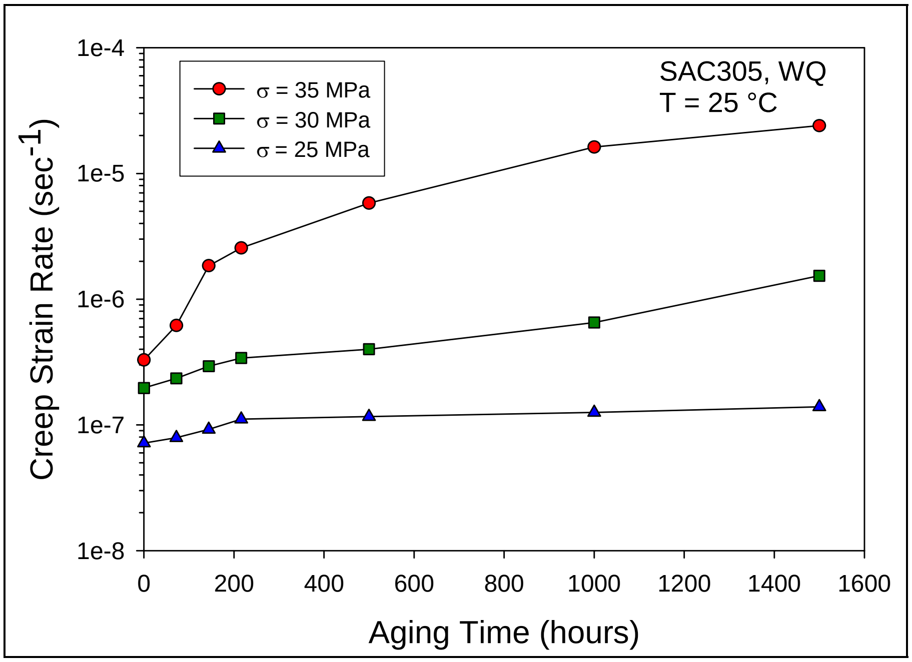

Figure 4.29 SAC305 Creep Strain Rate vs. RT Aging Time (Water Quenched).

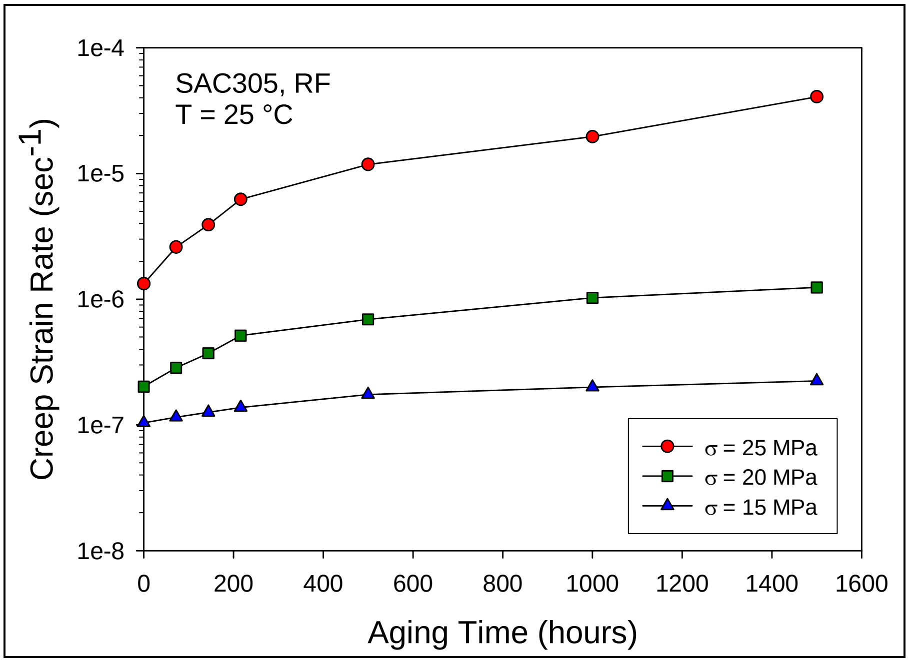

Figure 4.30 SAC305 Creep Strain Rate vs. RT Aging Time (Reflowed).

Figures 4.31-4.32 compare the steady-state strain rate for SAC405 and SAC305 at all stress levels for both water quenched and reflowed conditions. They clearly demonstrate that the creep deformation is more severe for SAC305 under the same stress level specimen conditions and that a higher stress level induces more significant differences. Figure 4.33 and Figure 4.34 compare the specimen condition effects on creep for SAC405 and SAC305. At the same stress level, the water quenched specimens have higher creep resistance than the reflowed specimens, which corresponds with the mechanical properties shown in previous section.

All the above results show that there were significant creep resistance losses during the two month period of room temperature aging. The results are consistent for both SAC405 and SAC305. It is likely that such aging effects are responsible for the large variations in creep strain rate magnitudes for SAC alloys reported by various investigators in the current research database pool.

For the Sn-Pb creep experiments, constant stress levels of σ = 5, 7, and 10 MPa were chosen for water quenched, and 15, 20, 25 MPa for reflowed condition. The effects of RT aging on the creep response of the Sn-Pb samples are illustrated in Figures 4.35-4.36 for the three stress levels of each condition. For the water quenched samples, even though much lower stress levels were utilized (relative to the SAC creep experiments), far higher creep strains were recorded (e.g. ε = 50%). Simply stated, Sn-Pb solder is much more prone to creep than the SAC alloys under water quenched condition which corresponds to the tensile properties stated in previous Section 4.2. Creep resistance for reflowed condition samples were much higher for the water quenched ones, which corresponds with the superior tensile properties and microstructure in previous sections.

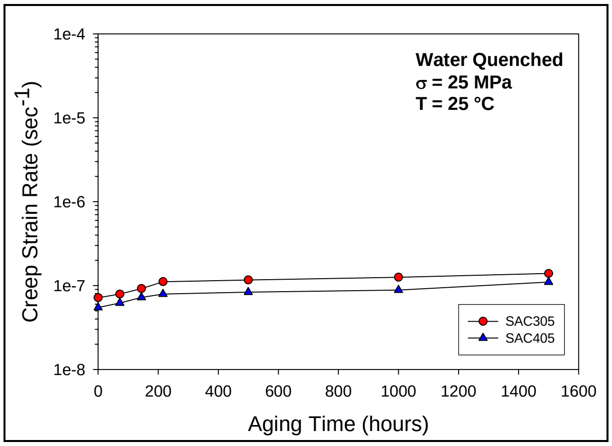

(a) 25 MPa

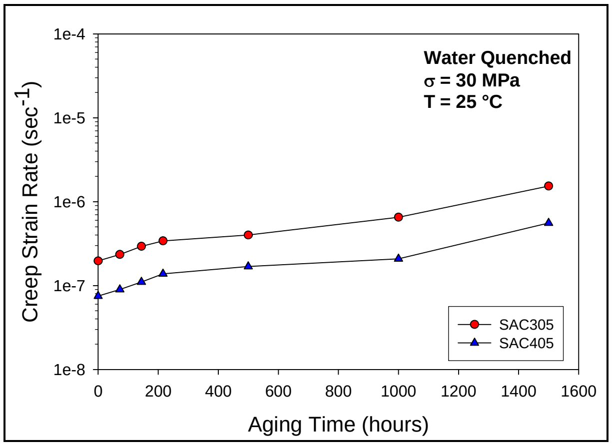

(b) 30 MPa

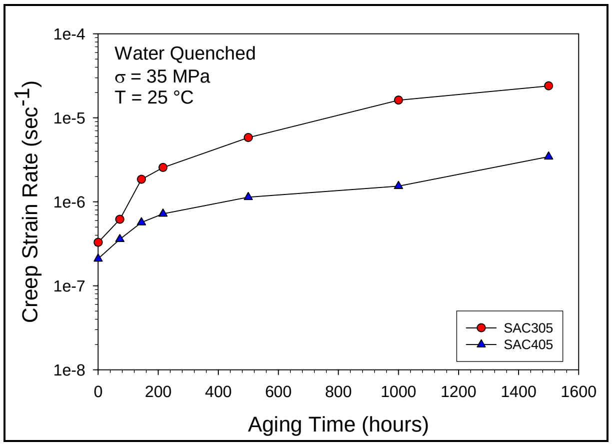

(c) 35 MPa

Figure 4.31 Comparison of SAC405 and SAC305 Creep Rate (Water Quenched).

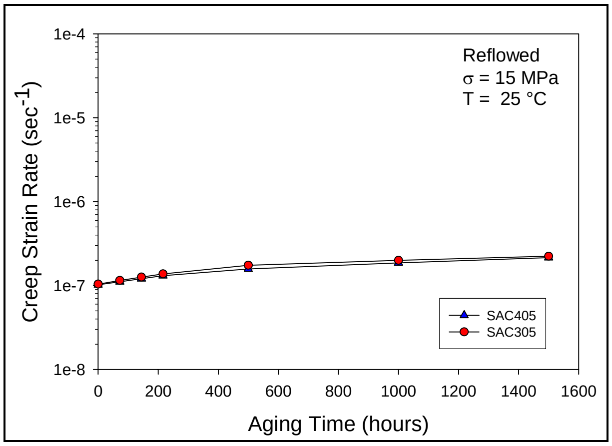

(a) 15 MPa

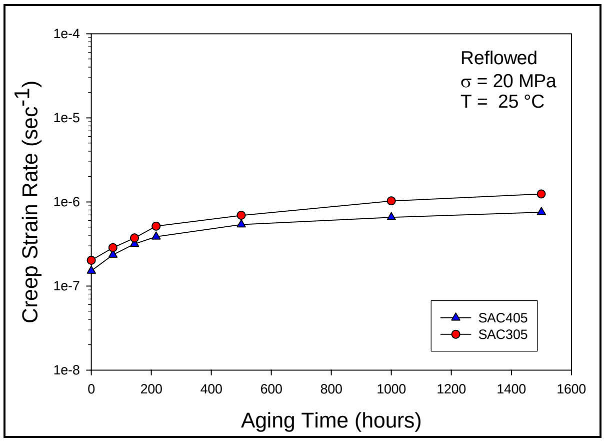

(b) 20 MPa

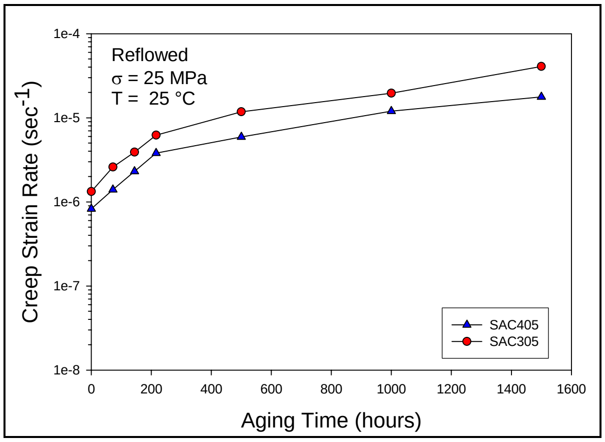

(c) 25 MPa

Figure 4.32 Comparison of SAC405 and SAC305 Creep Rate (Reflowed).

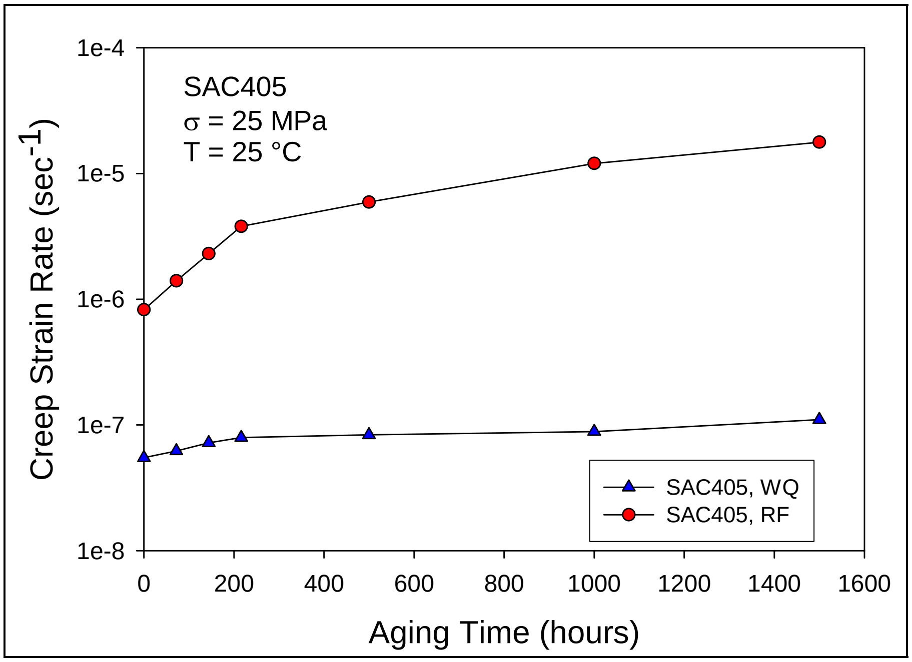

Figure 4.33 Comparison of Water Quenched and Reflowed for SAC405.

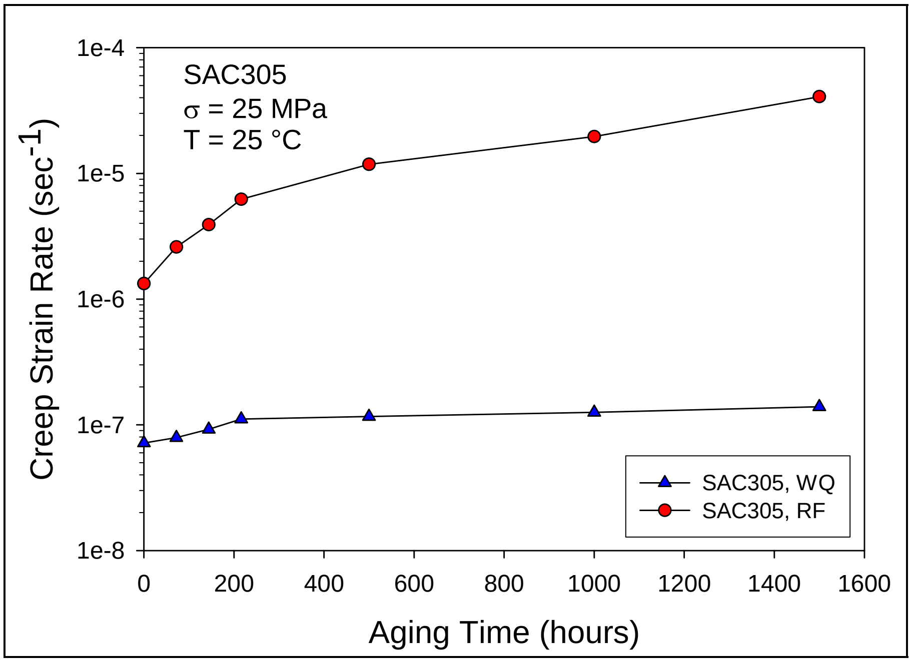

Figure 4.34 Comparison of Water Quenched and Reflowed for SAC305.

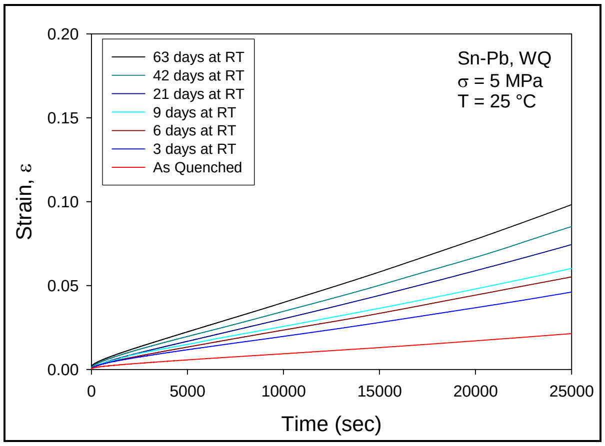

(a) 5 MPa

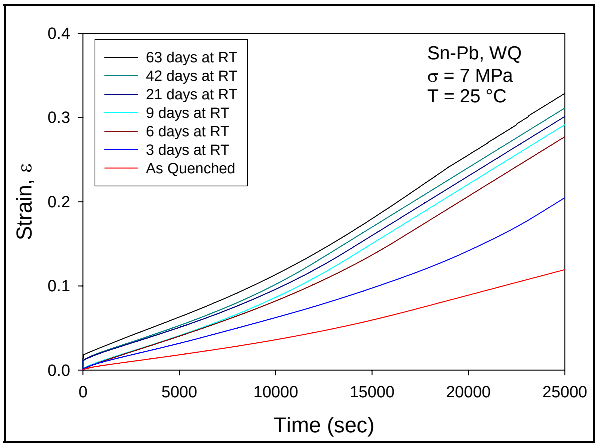

(b) 7 MPa

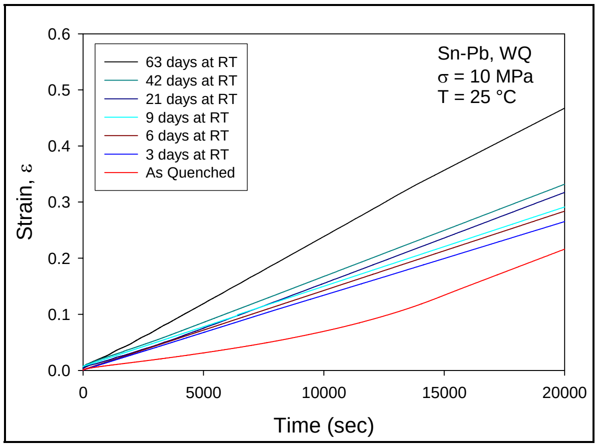

(c) 10 MPa

Figure 4.35 Sn-Pb Creep Curves for Various RT Aging Times (Water Quenched).

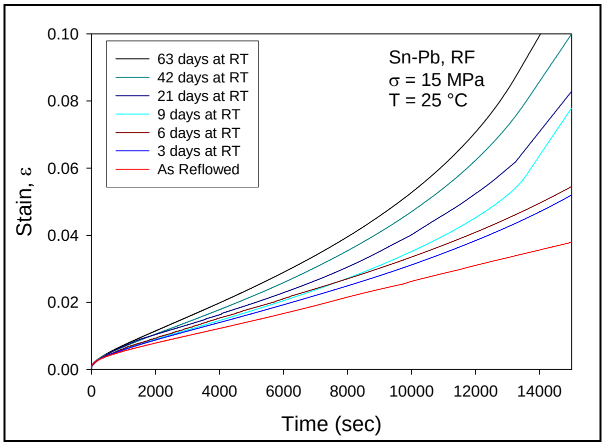

(a) 15 MPa

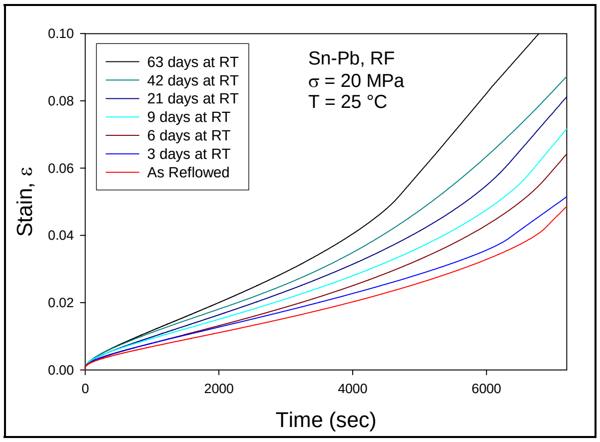

(b) 20 MPa.

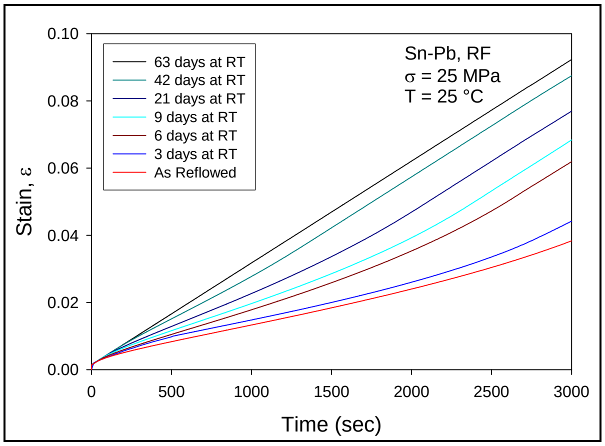

(c) 25 MPa.

Figure 4.36 Sn-Pb Creep Curves for Various RT Aging Times (Reflowed).

The influence of aging on the secondary creep strain rate for Sn-Pb is shown in Figures 4.37-4.38. The effect of room temperature aging on the creep strain rate is relatively less than for the SAC alloys. The creep strain rates for Sn-Pb appear to almost stabilize with longer aging times, in contrast to those for the SAC alloys, which continued to rise rapidly even after 63 days of RT aging. The realized strain rates are much higher than those found for the SAC alloy for both water quenched and reflowed conditions. As shown in Figure 4.39, at the same stress level, the creep deformation of Sn-Pb is more severe than that of either SAC305 or SAC405 for all room temperature aging times.

Table 4.3 summarizes the linear fitting of the steady-state creep rate at long aging time (t > 500 hours) for all solders under both the water quenched and reflowed conditions. At the same stress level (reflowed), it is apparent that the creep rate of SAC alloys increases more dramatically than that of Sn-Pb. For example, at 20 MPa, the creep rate of SAC405 and SAC305 are changing over 2X faster than that of Sn-Pb.

As the data show, for both Sn-Pb and lead-free solder alloys, the RT aging continues to affect the creep deformation rate. SAC alloys have a higher creep resistance than Sn-Pb alloys for both water quenched and reflowed conditions due to the superior creep resistance contributed by the precipitation of Ag_3Sn and Cu_6Sn_5 intermetallic compounds (as shown previously in Figure 4.19). SAC405 has higher creep resistance than SAC305 at the same stress level for both water quenched and reflowed conditions, even with a similar tensile strength. Room temperature aging continuously increases the creep strain rate for SAC alloys even after two months of aging. In contrast, the RT aging effects for Sn-Pb tend to be minimal after longer aging times.

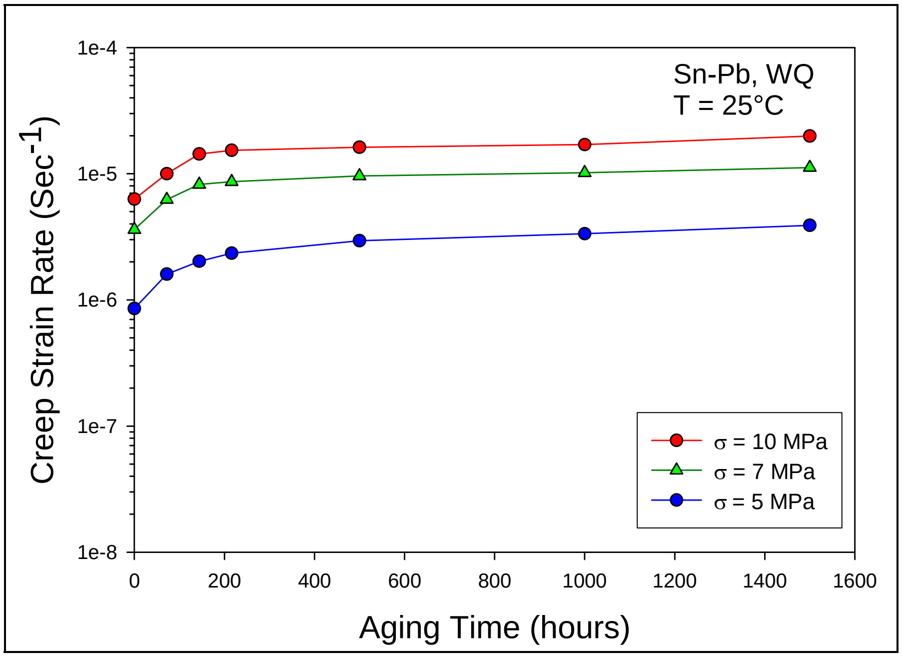

Figure 4.37 SAC305 Creep Strain Rate vs. RT Aging Time (Water Quenched).

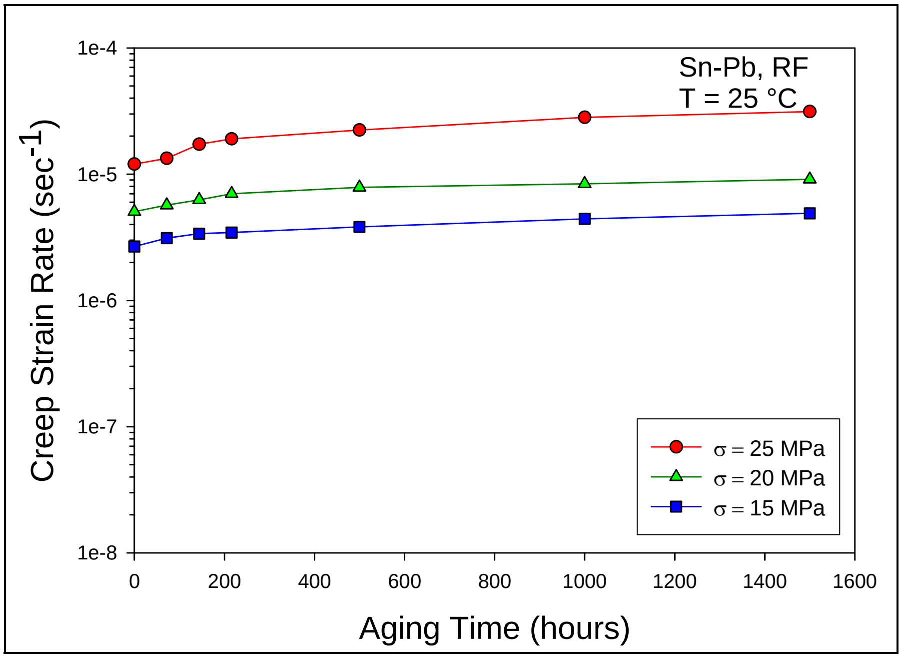

Figure 4.38 SAC305 Creep Strain Rate vs. RT Aging Time (Reflowed).

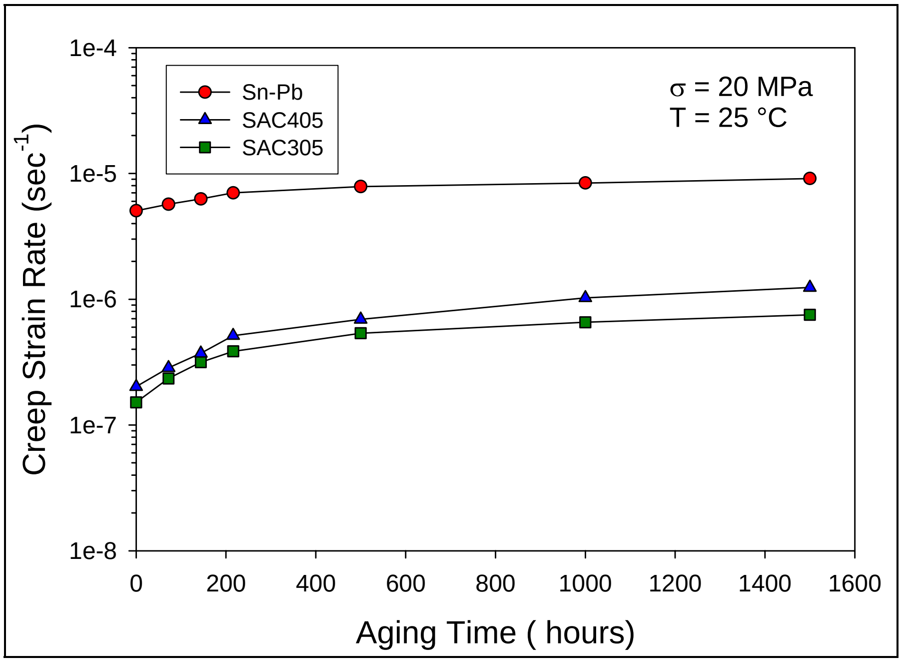

Figure 4.39 Comparison of Sn-Pb and SAC Creep Rate At RT Aging.

Table 4.3 Steady-State Creep Rate vs. Aging Time (t > 500 hours)

Solder	Stress Level	Steady-state Creep Rate
SAC405 Reflowed	15 MPa	$(5.95 \times 10^{-10})t + (1.30 \times 10^{-7})$
	20 MPa	$(1.91 \times 10^{-9})t + (4.65 \times 10^{-7})$
	25 MPa	$(1.56 \times 10^{-8})t + (6.02 \times 10^{-7})$
SAC305 Reflowed	15 MPa	$(4.85 \times 10^{-10})t + (1.59 \times 10^{-7})$
	20 MPa	$(4.25 \times 10^{-9})t + (6.01 \times 10^{-7})$
	25 MPa	$(4.22 \times 10^{-8})t + (2.27\times 10^{-5})$
Sn-Pb Reflowed	15 MPa	$(9.26 \times 10^{-11})t + (3.56 \times 10^{-6})$
	20 MPa	$(4.90 \times 10^{-10})t + (6.94 \times 10^{-6})$
	25 MPa	$(6.32 \times 10^{-9})t + (2.18 \times 10^{-5})$

4.5 Summary and Conclusions

The microstructure, mechanical response, and failure behavior of lead-free solder joints in electronic assemblies are constantly changing when exposed to isothermal aging and environments. The observed material behavior variation during thermal aging/cycling is universally detrimental to reliability and includes reductions in stiffness, yield stress, ultimate strength, and strain to failure, as well as highly accelerated creep. The evolution in the creep response with material aging illustrates large increases in the steady state (secondary) creep strain rate (creep compliance) and a tendency to enter the tertiary creep range (imminent failure) at ever reducing strain levels. The results in this study demonstrate that there are significant aging effects present in lead-free solder joints that remain at room temperature (25 ºC). In addition, the magnitudes of the material behavior evolution occurring in lead-free SAC solder joints are much larger (e.g. 25X) than the corresponding changes occurring in traditional Sn-Pb assemblies. Finally, current finite element models for solder joint reliability are based on traditional solder constitutive and failure models that do not evolve with material aging. Thus, there will be significant errors in calculations with the new lead-free SAC alloys that illustrate dramatic aging phenomena.

In this work, the effects of aging on mechanical behavior have been examined by performing stress-strain and creep tests on SAC405 and SAC305 lead-free samples that were aged for various durations (0-63 days) at room temperature (25 ^{o}C). Analogous RT aging experiments were performed with 63Sn-37Pb eutectic solder samples for comparison purposes. When characterizing solders, it is critical that the uniaxial test specimens used for stress-strain testing reflect the true solder joint reflow profile and post assembly microstructure. A novel and robust fabrication technique has been developed to formulate solder test samples with controlled cooling profile and microstructure. This new technique reproducibly prepares techniques forms 80 mm x 3 mm x 0.5 mm solder uniaxial tension test specimens in rectangular cross-section glass tubes using a vacuum suction process.

Variations in mechanical properties were observed and modeled as a function of aging time. For the SAC alloys, the initial linear behavior varies only slightly with aging, while the post yield behavior changes dramatically. Reductions of up to 40% were observed for the UTS with 63 days of RT aging. The failure stresses (YS and UTS) of the reflowed SAC samples were much smaller than those of the analogous water quenched samples at all aging times. This reaffirms the strong dependence of failure properties of solder joints on the cooling profile used in their formation. There were only small differences (3-5%) between the uniaxial stress-strain responses and mechanical properties of the SAC405 and SAC305 alloys.

The Sn-Pb uniaxial stress-strain data illustrated several different trends relative to the SAC alloys. In particular, the reflowed Sn-Pb samples uniformly showed better (higher) mechanical properties than the water quenched samples, and larger changes were observed during aging for the reflowed samples relative to the quenched samples. This was in direct contradiction to the results found for the high tin content lead-free SAC alloys. SEM observations of the Sn-Pb and SAC samples verified that these differences could be directly linked to the initial microstructure before aging. In general, finer microstructure resulted in superior mechanical properties and reduced creep rates for all alloys. In addition, the mechanical properties of all alloys changed most significantly during the first 10 days of RT aging.

For all alloys, RT aging affects both the strain rate in the secondary creep region, and the elapsed time before tertiary creep and rupture. The steady-state creep strain rate significantly increased during the 63 days of RT aging for water quenched and reflowed for SAC alloys, although the reflowing process slightly reduced the room temperature aging effects. The aging effects were similar for the two lead-free alloys. However, the data clearly showed that SAC405 creeps less than SAC305 for the same levels of stress and aging. For the Sn-Pb creep experiments, much lower stress levels were utilized relative to the SAC creep experiments. However, the measured creep strains were much higher (e.g. $\varepsilon = 50\%$). Sn-Pb solders were much more prone to creep than the SAC alloys at same stress level. The creep strain rates for Sn-Pb appeared to nearly stabilize with longer aging times, while those for the SAC alloys were continuing to rise rapidly even after 63 days of RT aging.

CHAPTER 5

EFFECTS OF ELEVATED TEMPERATURE AGING ON THE MECHANICAL BEHAVIOR OF LEAD-FREE SOLDERS

5.1 Introduction

As mentioned in Chapter 2, there have been numerous studies of the mechanical properties of solders at elevated temperature. However, there have been few studies on aging effects. In this chapter, the effects of elevated temperature aging on the mechanical properties and creep behavior of reflowed lead-free solders is explored. Aging was performed at 125 °C (homologous temperature of $0.81T_m$). The measured data were compared to the room temperature aging results reported in Chapter 4.

5.2 Effects of Thermal Aging on Tensile Properties

Specimens were formed using the methods described in Chapter 3 and then aged at 125 °C for up to 6 months. Only reflowed samples were considered (no water quenched). The specimens were stored in the aging oven immediately after the reflow process to eliminate the possible room temperature aging effects described in Chapter 4. For each aging time, 10 specimens were prepared to ensure the accuracy of the testing results. A single “average” stress-strain curve was found for each sample set (aging duration) with 10 individual curves using the empirical model in Eq. 3.2 and the procedure described in Chapter 3.

Figure 5.1 illustrates the stress-strain curves for SAC405 at various aging times. The tensile strength drops dramatically in the first 100 hours, but tends to slow down afterwards. Figures 5.2-5.3 illustrate in the changes of elastic modulus, UTS and YS with aging time. All these key properties continuously decrease with increasing aging time. The initial aging data can be fitted with materials models similar to that described in Eq. 4.1, becoming stable after a sufficient long aging time. However, the data in Figure 5.2(b) and 5.3(b) show that the elastic modulus, UTS and YS of lead-free solder continue to decrease steadily in a near linear relationship, although at a very slow pace. The thermal aging data can thus be modeled with the following relationship:

$$\text{Material Property} = C_0 + \frac{C_1}{1 + e^{-\left(\frac{t - C_2}{C_3}\right)}} \qquad t \leq 200 \text{ hours} \qquad (5.1)$$

$$\text{Material Property} = -\alpha t + \beta \qquad t \geq 200 \text{ hours} \qquad (5.2)$$

where C_0, C_1, C_2, C_3, α, and β are materials constants. and t is the aging time in hours. The 200 hours aging time represents an experimental data. For the initial period, the tensile properties follow Eq. 5.1, and for aging time longer than 200 hours the tensile properties will follow Eq. 5.2. Table 5.1 summarizes the near linear relationship for aging times longer than 200 hours.

Based on the failure data recorded for this study, the fitting relationships in Table 5.1 show that aging at 125 °C for over 6-8 years would cause the SAC solder to lose its strength to support electronic packaging module almost completely. This would be a great concern for electronic devices designed to operate in harsh environments for example at a constant high temperature of 125 °C, for such long periods of time.

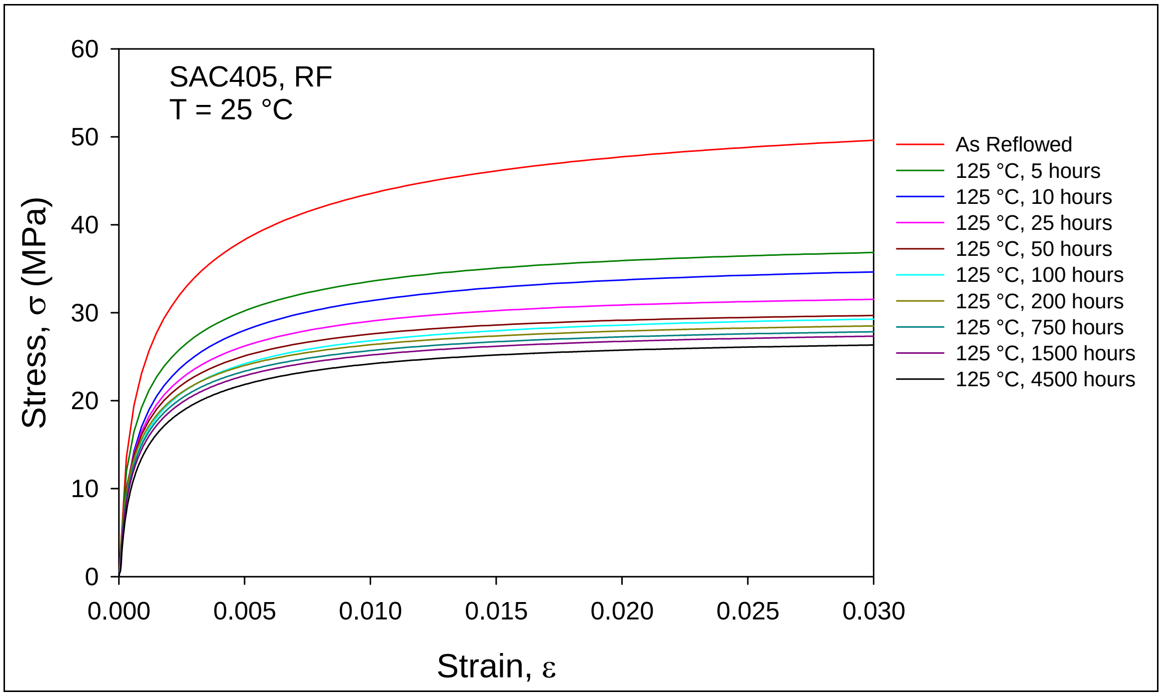

Figure 5.1 SAC405 Stress-Strain Curves Aged at 125 °C for Various Times.

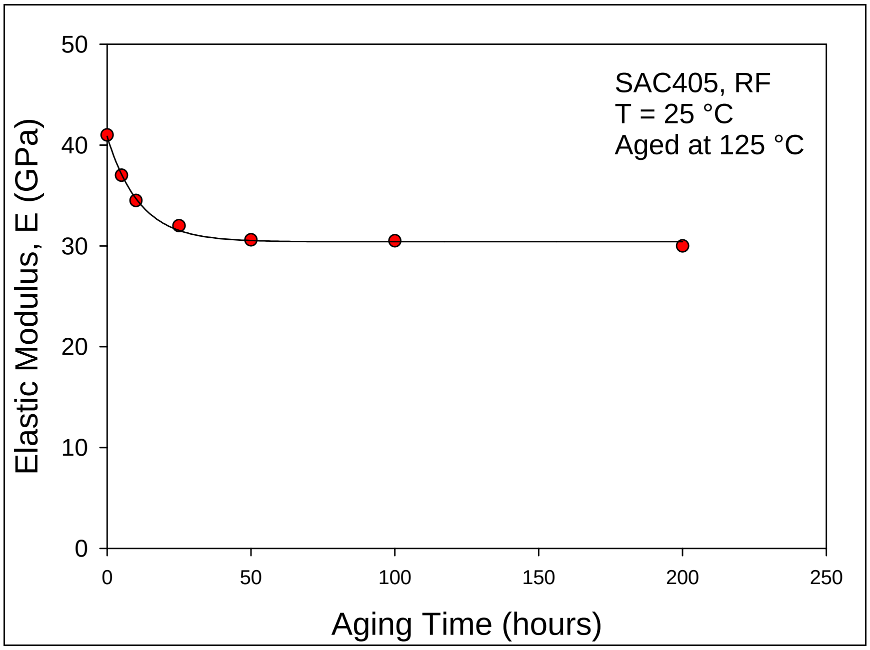

(a) The Initial Period of Aging.

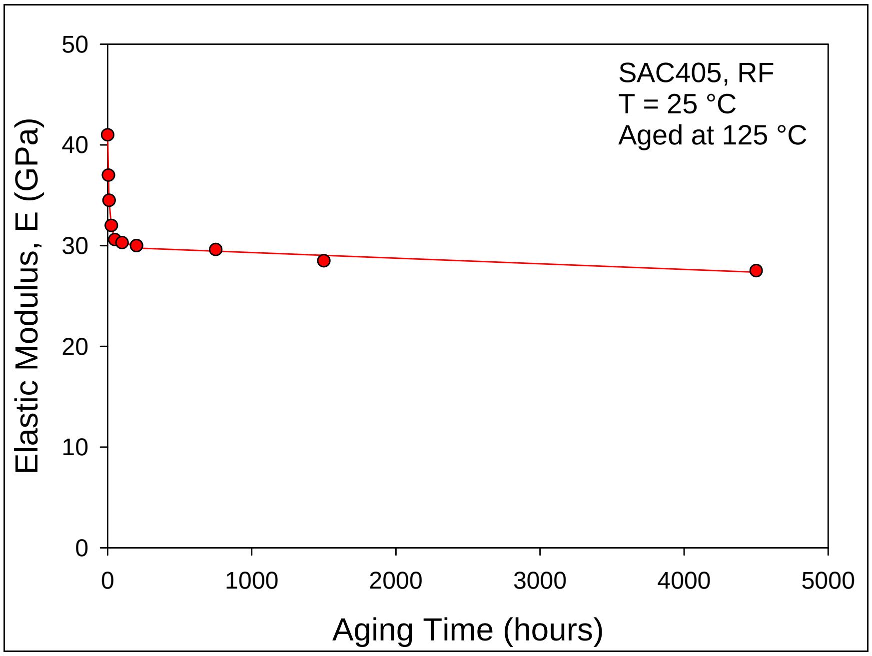

(b) Aging up to 6 Months.

Figure 5.2 SAC405 Elastic Modulus Changes with Various Aging Times.

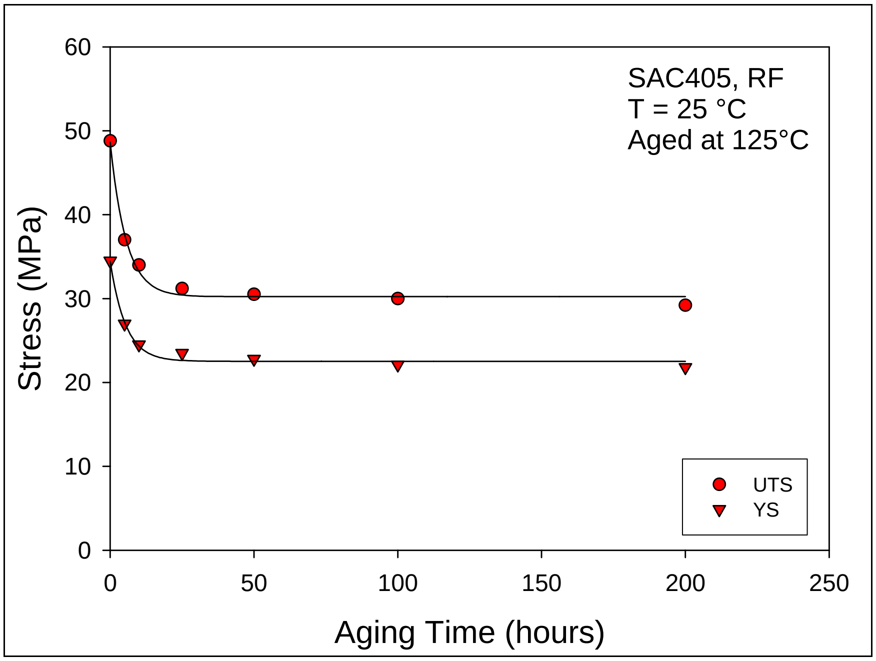

(a) The Initial Period of Aging.

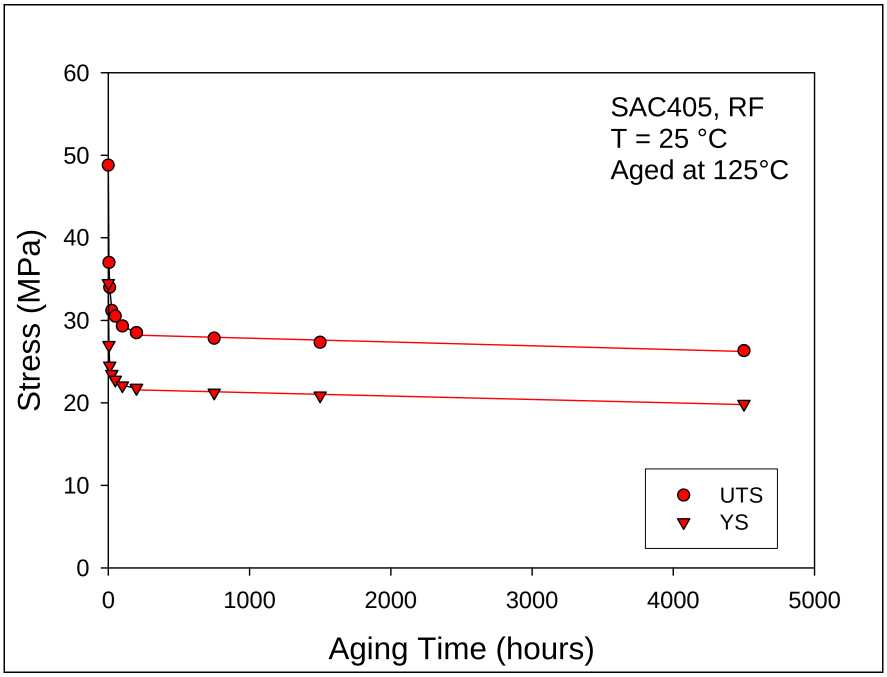

(b) Aging up to 6 Months.

Figure 5.3 SAC405 UTS and YS Changes with Various Aging Times

Table 5.1 Thermal Aging Effects on Tensile Properties (t > 200hours)

Tensile Properties	Aging Time Dependence	R^2
E (GPa)	-0.00055t + 29.87	0.8994
UTS (MPa)	-0.00045t + 28.33	0.9260
YS (MPa)	-0.00040t + 21.66	0.9553

The tensile properties of SAC305 reflowed specimens aged at 125 °C were also collected. Figure 5.4 illustrates the stress-strain curves for SAC305 aged up to 6 months. As with SAC405, the tensile properties of SAC305 continue to decease with increasing aging durations. Figure 5.5 compares the tensile properties of SAC305 and SAC405. The values of the elastic modulus, UTS and YS for both alloys are very similar to each other across the entire aging durations.

Corresponding data were also collected for Sn-Pb eutectic solder under the reflowed condition, as shown in Figures 5.6-5.8. As with the SAC alloys, the tensile properties decreased dramatically during the initial aging period. However, the tensile properties became relatively stable after 200 hours of aging, unlike for the SAC alloys, which continued to steadily decrease with time following a near linear relationship. The thermal aging time effects for Sn-Pb follow Eq. 4.1, which eventually stabilizes for sufficiently long aging times. The tensile reliability of Sn-Pb aged for large durations is therefore more reliable than that of either of the lead-free solder alloys.

Different aging temperatures will also significantly affect the tensile properties. In this study, most testing was carried out with aging at 125 °C. Aging at 150 °C for 100 hours was also performed to compare the aging effects at different temperatures. Figures 5.9-5.10 illustrate the stress-strain changes for SAC405 and Sn-Pb at different aging temperatures for 100 hours. The results clearly shows that higher temperature will cause more reduction in the tensile strength for both the SAC alloy and the Sn-Pb eutectic solder. The underlying reasons are that the higher aging temperature will accelerate the phase coarsening processes. The microstructure evolution after aging at elevated temperature will be reported in later sections.

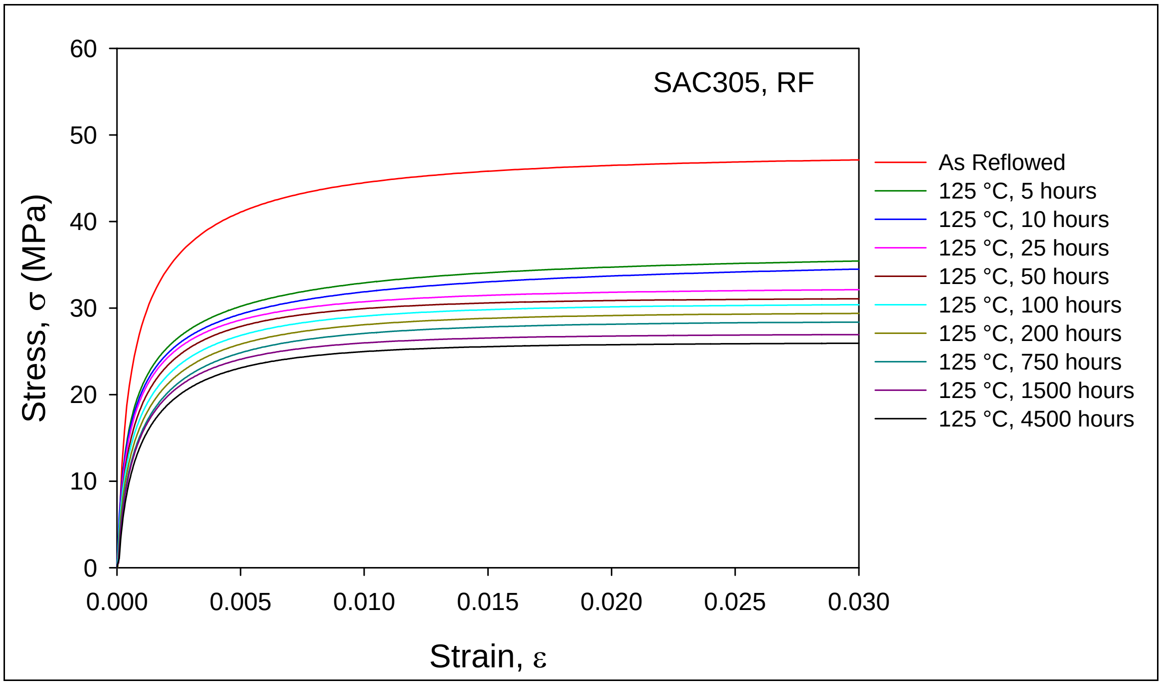

Figure 5.4 SAC305 Stress-Strain Curves Aged at 125 °C for Various Times.

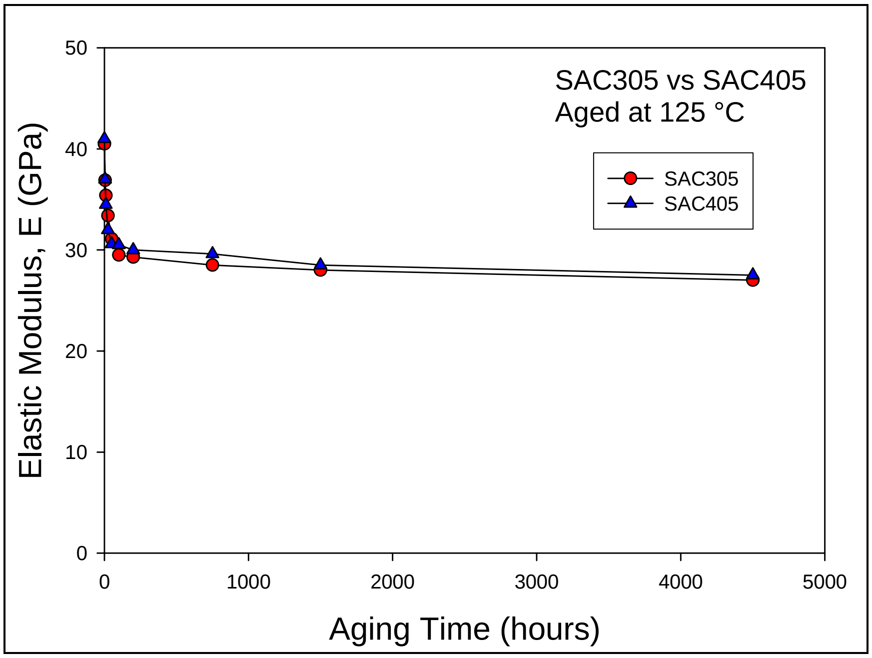

(a) Elastic Modulus

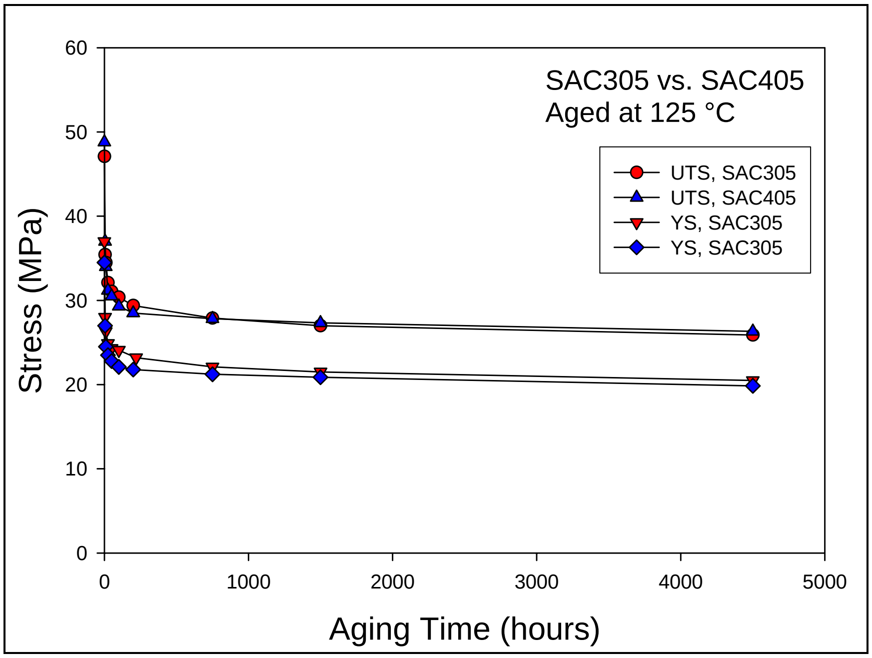

(b) UTS and YS

Figure 5.5 Tensile Properties of SAC 405 vs. SAC305 Aged at 125 ºC.

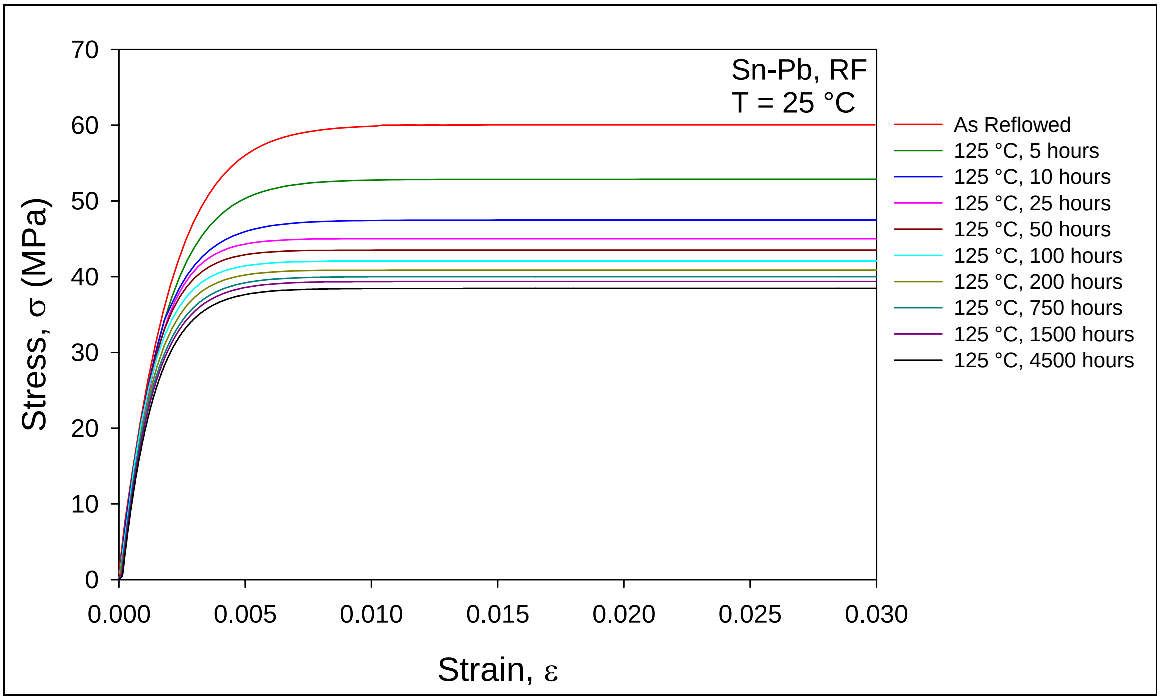

Figure 5.6 Sn-Pb Stress-Strain Curves Aged at 125 °C for Various Times.

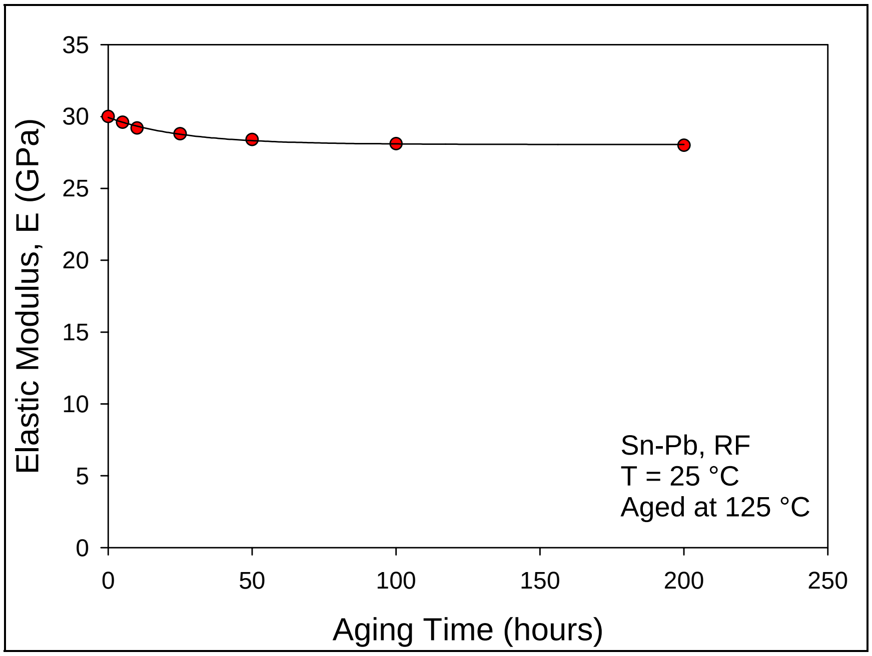

(a) The Initial Period of Aging.

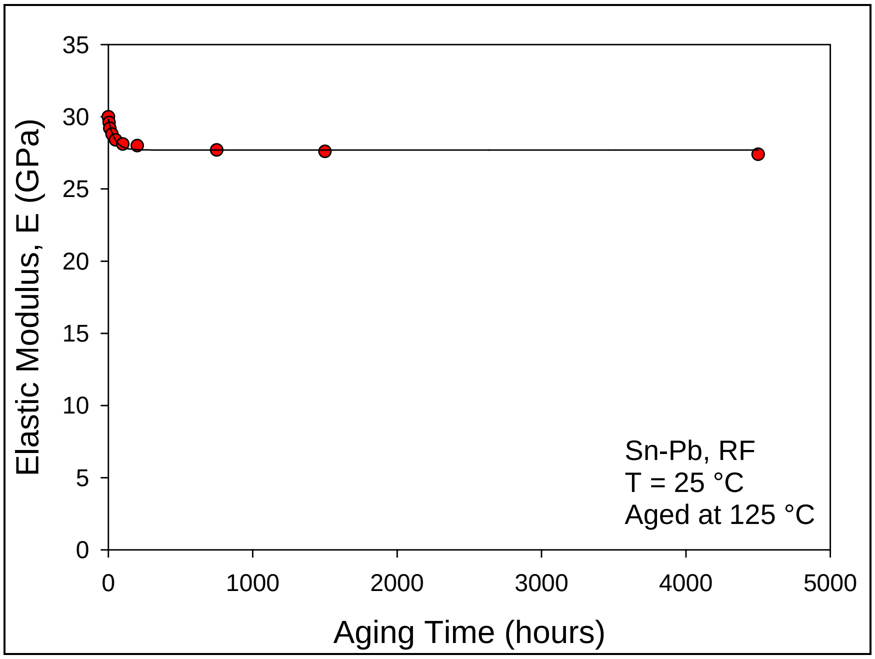

(b) Aging up to 6 Months.

Figure 5.7 Sn-Pb Elastic Modulus Changes with Various Aging Times.

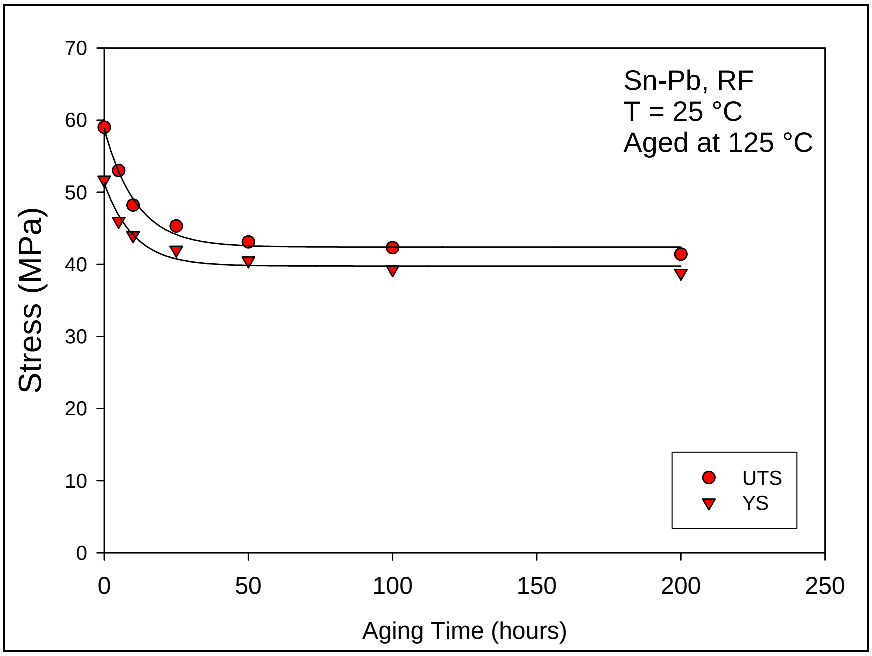

(a) The Initial Period of Aging.

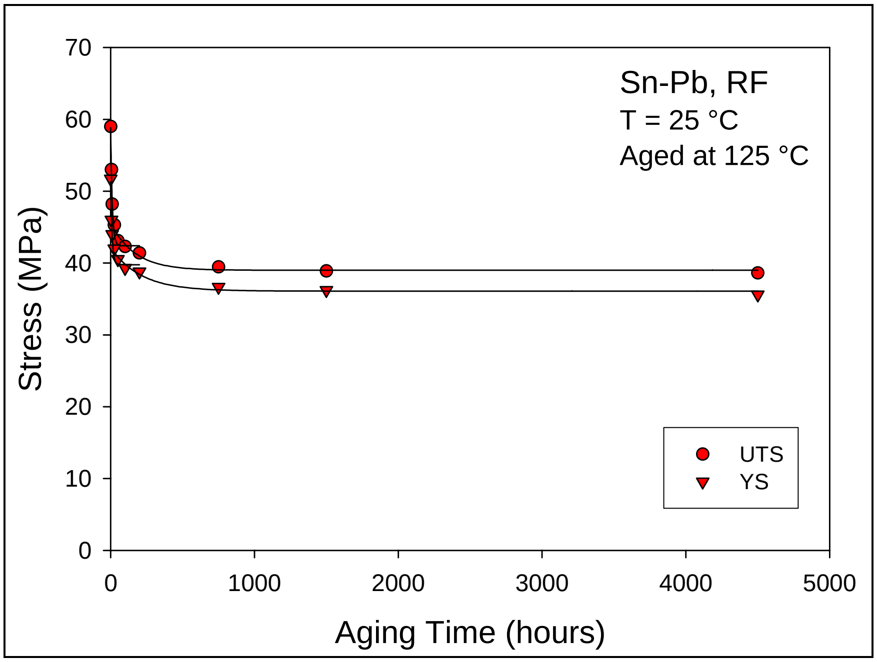

(b) Aging up to 6 Months.

Figure 5.8 Sn-Pb UTS and YS Changes with Various Aging Times.

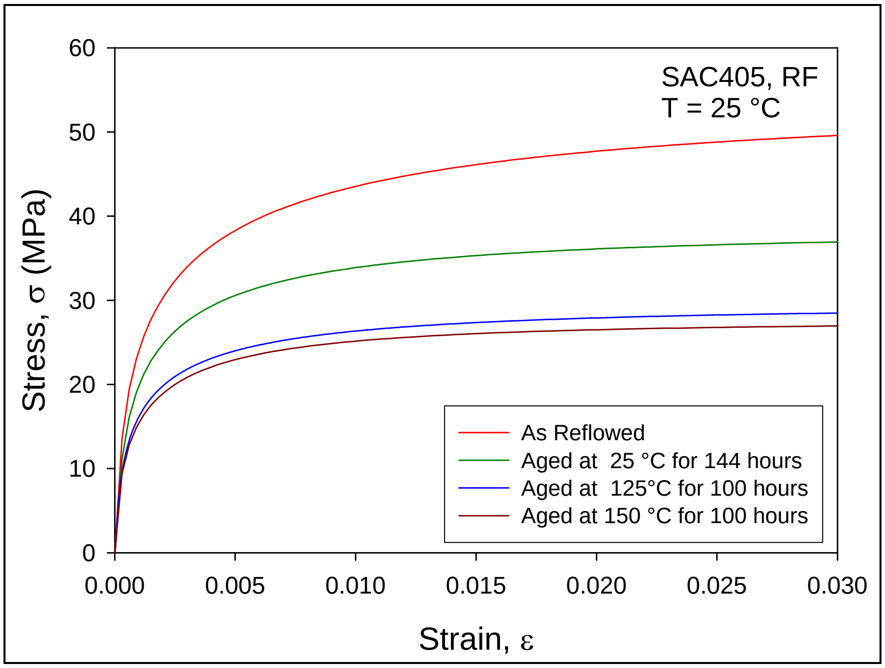

Figure 5.9 SAC405 Stress-Strain Changes at Various Aging Temperatures.

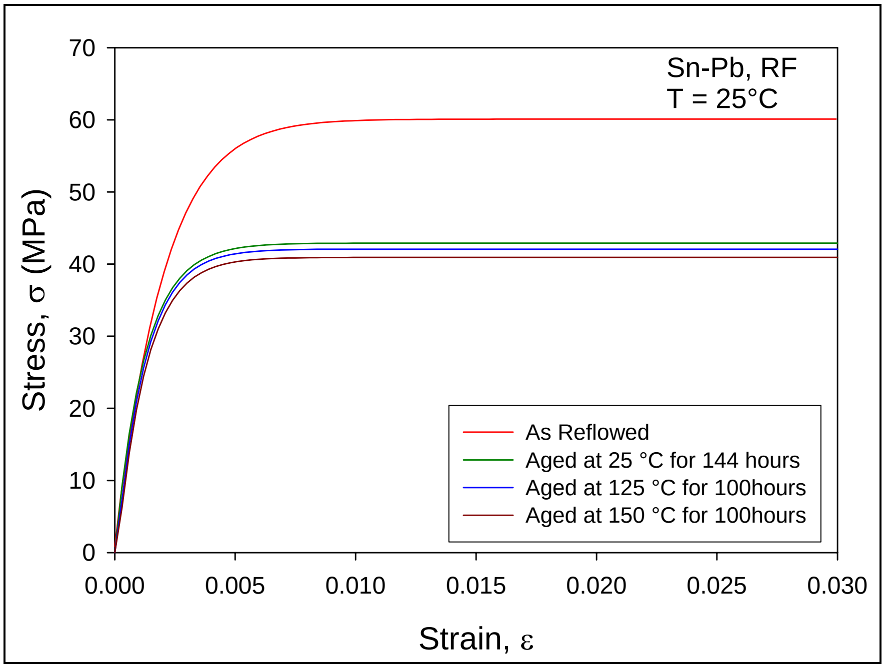

Figure 5.10 Sn-Pb Stress-Strain Changes at Various Aging Temperatures.

5.3 Thermal Aging Effects on Creep Deformation

Creep testing was performed at a constant stress level of 20 MPa, and the testing were carried out at room temperature for SAC and Sn-Pb specimens aged with various aging durations at 125 °C. The testing method and data acquisition procedure were as discussed in Chapter 3 and Chapter 4. The steady-state strain rates were collected and compared.

As illustrated in Figure 5.11, the creep deformation of SAC405 was more severe after longer aging durations and the creep rupture was also faster. The steady-state creep strain rates for SAC405 are compared in Figure 5.12. During the initial aging durations, the creep strain rates increased dramatically with increasing aging time. The stain rate increase tended to slow down after 100 hours of aging, although it continued to steadily increase with aging time. The relationship between strain rate and aging time followed a similar relationship to that shown in Eq. 5.1 and 5.2. When the aging time was less than 200 hours, the strain rate changes followed Eq. 5.1, while it followed Eq. 5.2 when aging time was greater than 200 hours. The experimental data reveal that as the aging times continue to increase, the stress applied will eventually exceed the yield stress of the material, resulting in a very fast failure that is similar to that of tensile failure.

Creep testing was also carried out for SAC305 after aging at 125 °C (Figure 5.13). The aging effects on SAC305 were similar to those for SAC405. Figure 5.14 compares the creep rates changes for SAC305 and SAC405. Although, the study reported in Chapter 4 showed that the creep resistance of SAC405 appear to be better than SAC305 at room temperature, after aging at elevated temperature the differences in the creep rates of the two alloys are diminished.

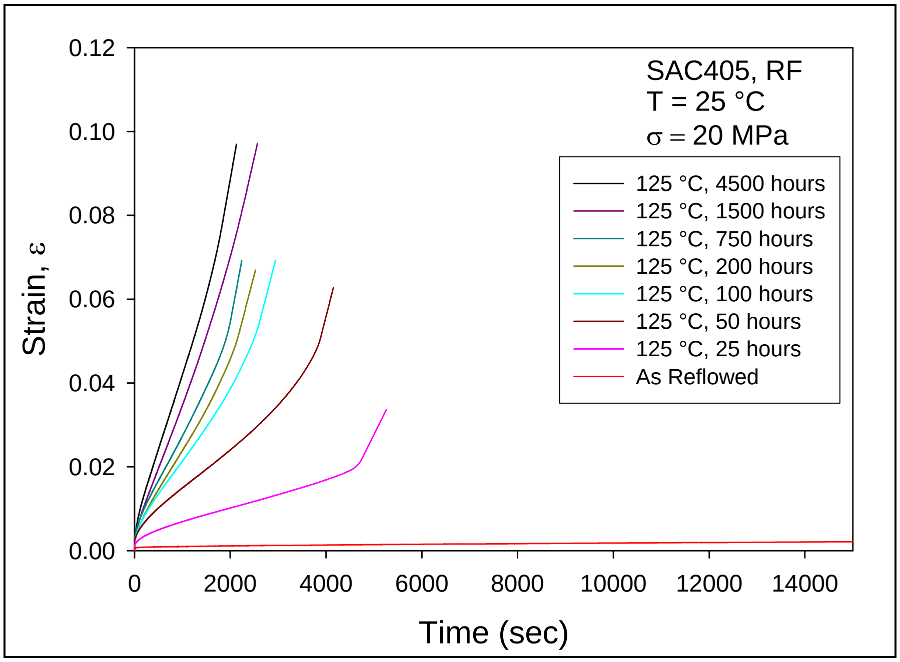

Figure 5.11 SAC405 Creep Curves for Various Aging Times at 125 °C.

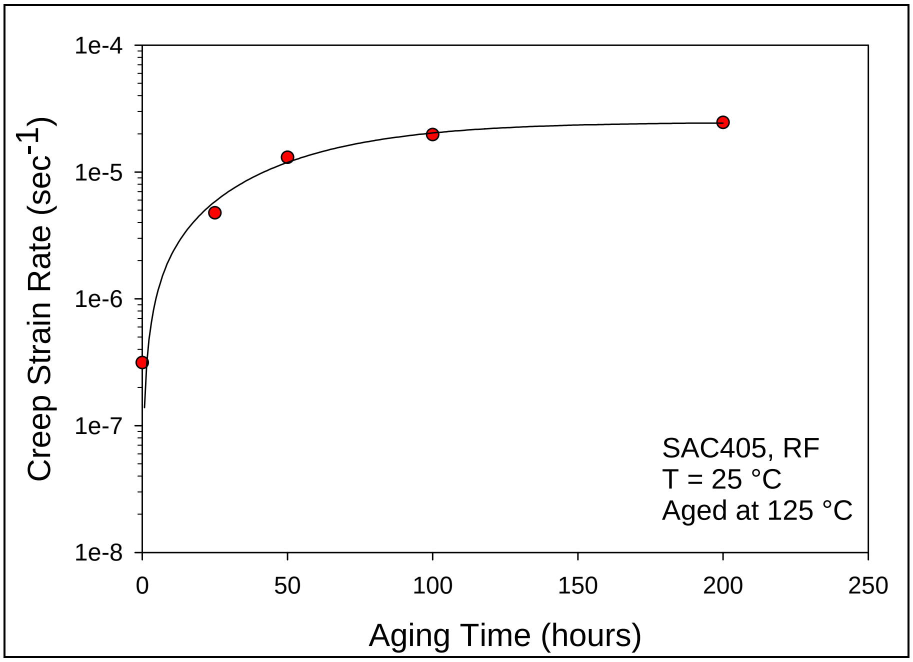

(a) The Initial Period of Aging.

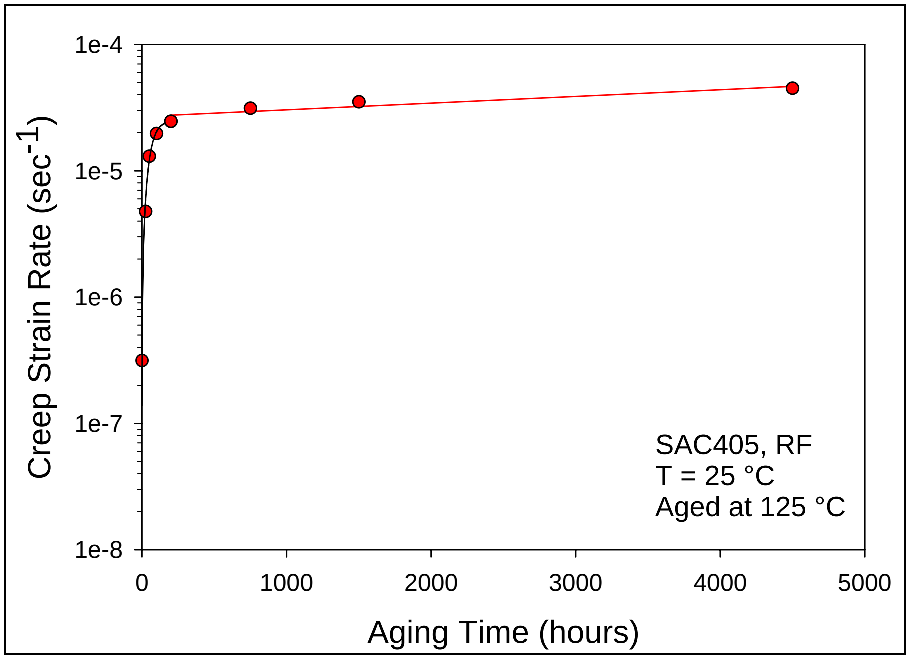

(b) Aging up to 6 Months.

Figure 5.12 SAC405 Creep Strain Rate vs. Aging Time at 125 °C.

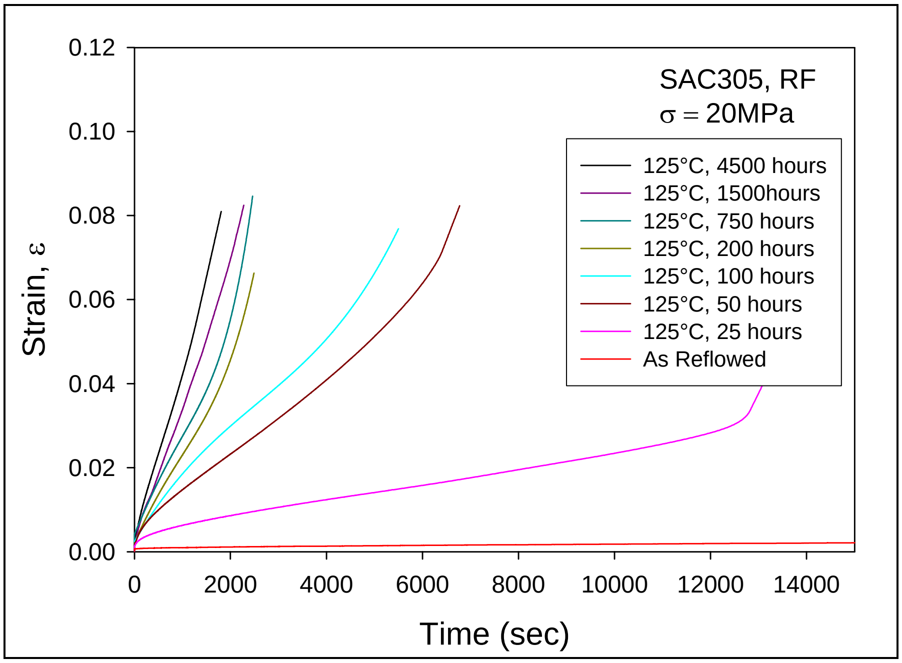

Figure 5.13 SAC305 Creep Curves for Various Aging Times at 125 °C.

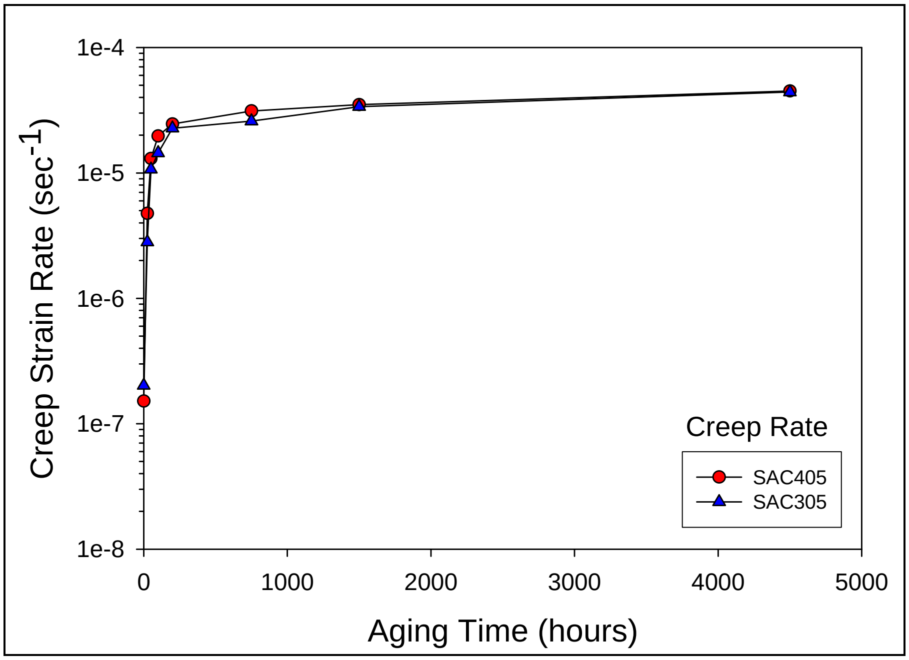

Figure 5.14 Creep Strain Rate of SAC305 vs. SAC405.

To understand the underlying reason for the differences in the creep responses of SAC405 and SAC305, it is necessary to consider the microstructure changes involved. At room temperature the secondary phases, which are intermetallic compounds, are fine and uniformly distributed. They are very effective dislocation blockers and thus significantly increasing the creep resistance of lead-free solders. SAC405 possesses a higher proportion of intermetallic compounds than SAC305 at room temperature, which is why SAC405 has higher creep resistance than SAC305. Aging at elevated temperatures will significantly coarsen the microstructure, causing the intermetallic compounds to grow in large pieces. The large secondary phases created no longer act as effective dislocation blockers, so the contribution to the creep resistance strengthening by secondary phases will diminish with time spent at an elevated temperature.

Corresponding creep data were recorded for reflowed Sn-Pb specimens. Figure 5.15 illustrates the creep deformation changes with various thermal aging durations. Figure 5.16 shows the creep strain rate changes with aging at 125 ºC. As with the SAC alloys, the initial creep deformation increases are significant. However, after aging for 50 hours, the creep rate tends to slow down, and creep rate changes become relatively uniform. The creep rate changes with aging time follow Eq. 4.1.

As shown in Chapter 4, room temperature aging will significantly increase the creep deformation. The room temperature aging and elevated temperature aging effects can be compared at the same applied stress level.

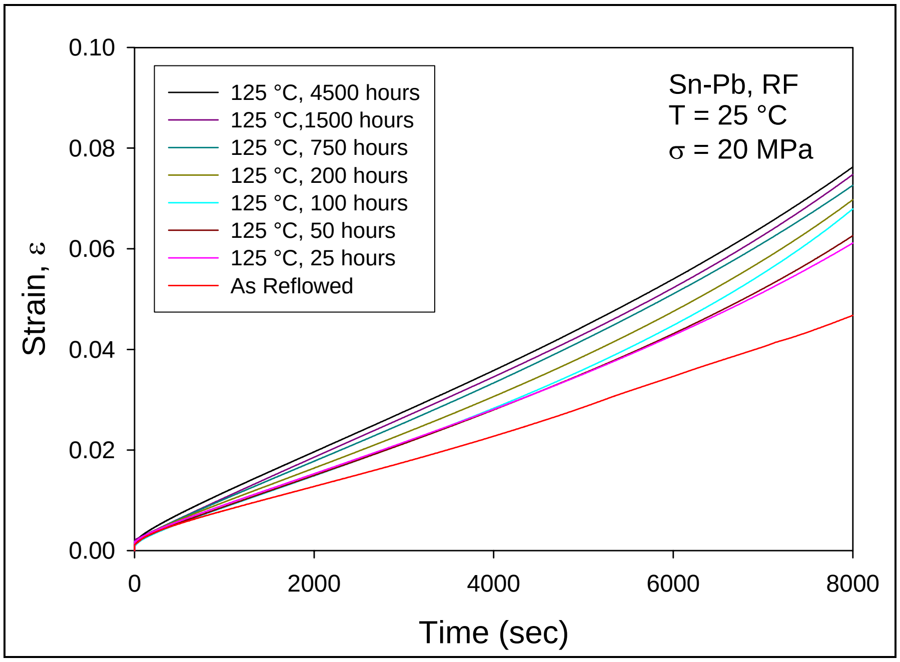

Figure 5.15 Sn-Pb Creep Curves for Various Aging Times at 125 °C.

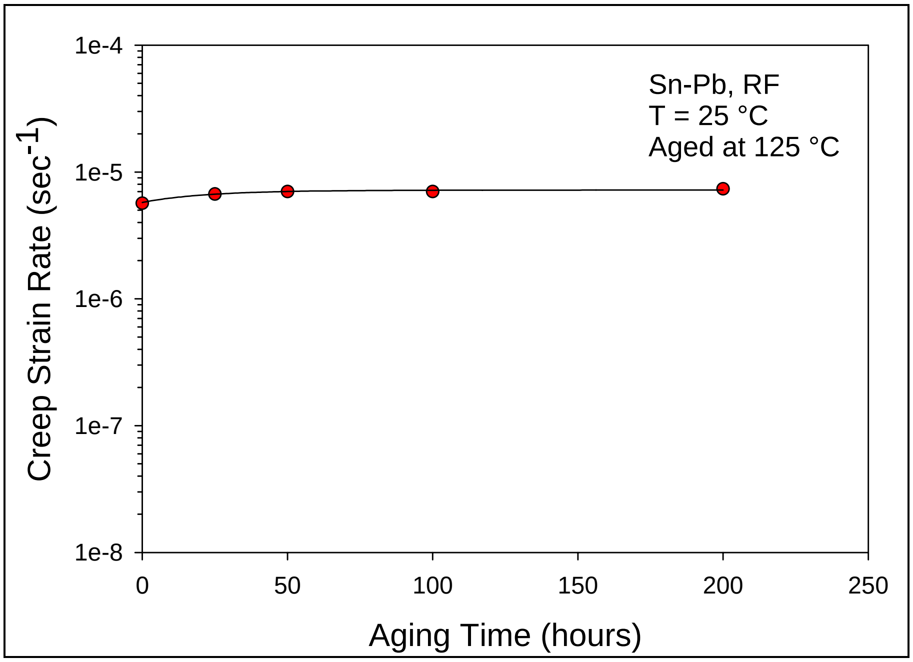

(a) The Initial Period of Aging.

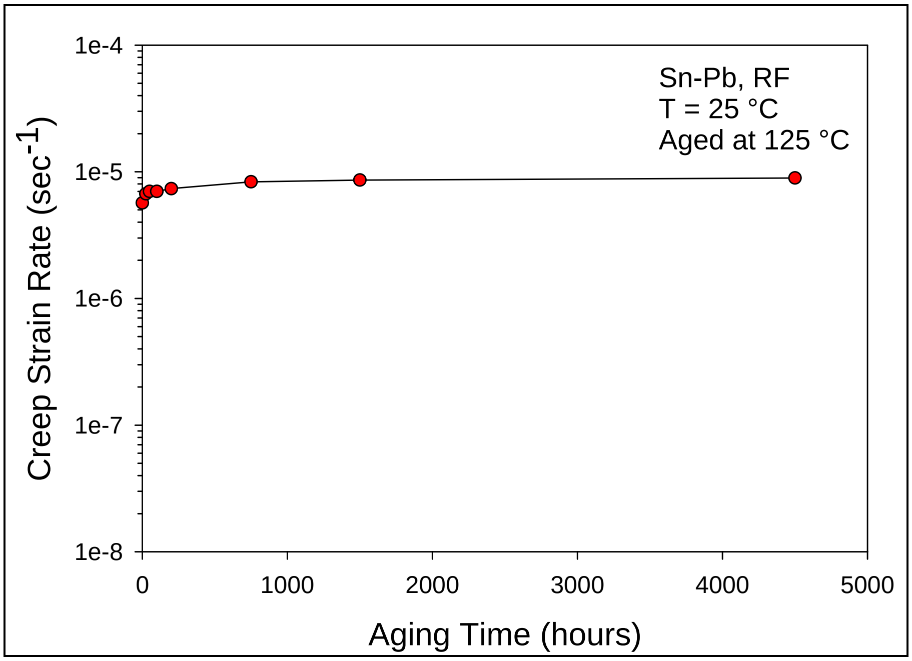

(b) Aging up to 6 Months.

Figure 5.16 Sn-Pb Creep Strain Rate vs. Aging Time at 125 °C.

Figures 5.17-5.19 compare the aging effects at room temperature and at 125 °C for up to 1500 hours for SAC405, SAC305 and Sn-Pb. It is apparent that elevated temperature aging results in a higher creep deformation rate for all the solders alloys. However, the differences are more pronounced for SAC alloys.

Figure 5.20 shows a comparison of the creep strain rate between Sn-Pb and SAC405 after aging at 125 °C for various aging durations. At the same stress level, SAC405 has higher creep resistance for shorter aging times. When aging durations are longer, there is a cross-over point at about 50 hours, after which Sn-Pb shows better creep resistance than that of SAC405. The creep rate results show that SAC405 is more sensitive to aging temperature and aging time than Sn-Pb. Overall, Sn-Pb is relatively more stable than SAC.

The creep rate difference between the Sn-Pb and SAC alloys after aging can also be explained by the coarsening of the microstructure. At shorter aging times, the microstructure is still relatively fine. Secondary phases play a major role in blocking the dislocation movement and increase the creep resistance for SAC alloys, resulting in a higher creep resistance for the SAC alloys than Sn-Pb at shorter aging times (50 hours). However, after aging for longer periods, the contribution of the secondary phases to the creep resistance has diminished. For Sn-Pb, the microstructure is a simple two phase eutectic structure. Even after aging at elevated temperatures, the coarsening of the eutectic phases does not affect the creep as significantly as the intermetallic compounds in SAC alloys do.

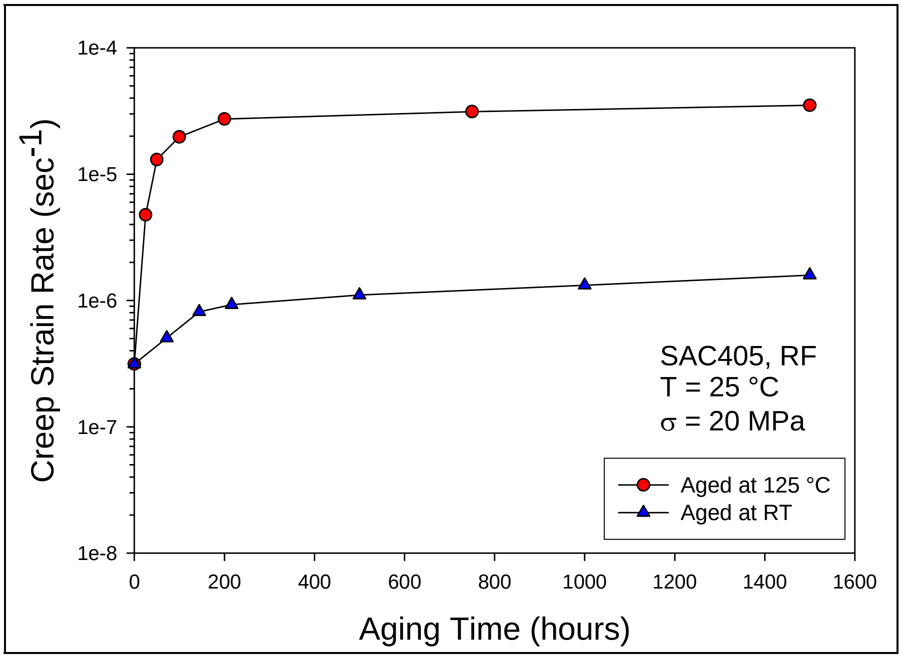

Figure 5.17 SAC405 Creep Rate Comparison of RT Aging and Elevated Temperature Aging at 125 °C.

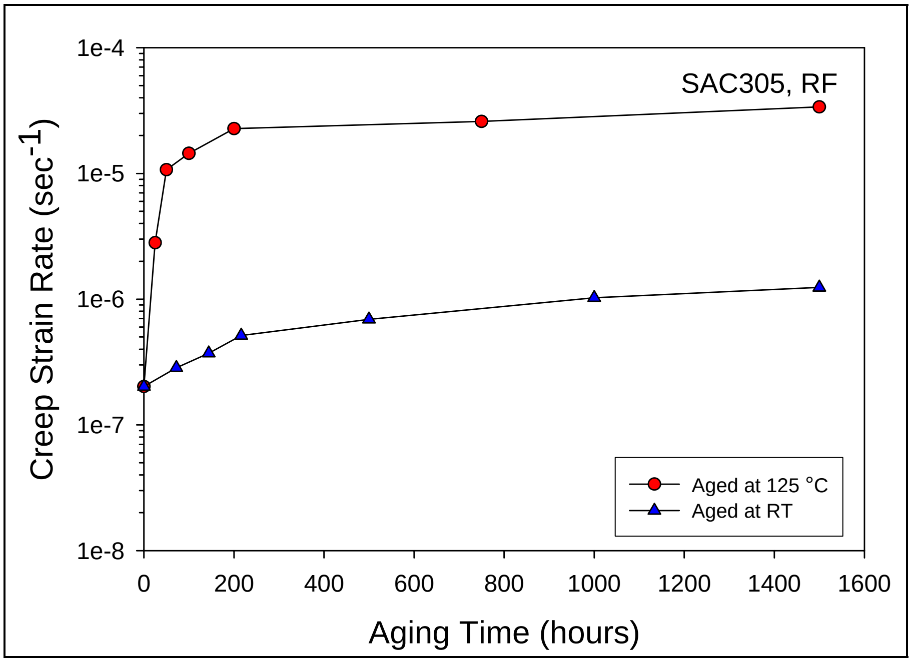

Figure 5.18 SAC305 Creep Rate Comparison of RT Aging and Elevated Temperature Aging at 125 °C.

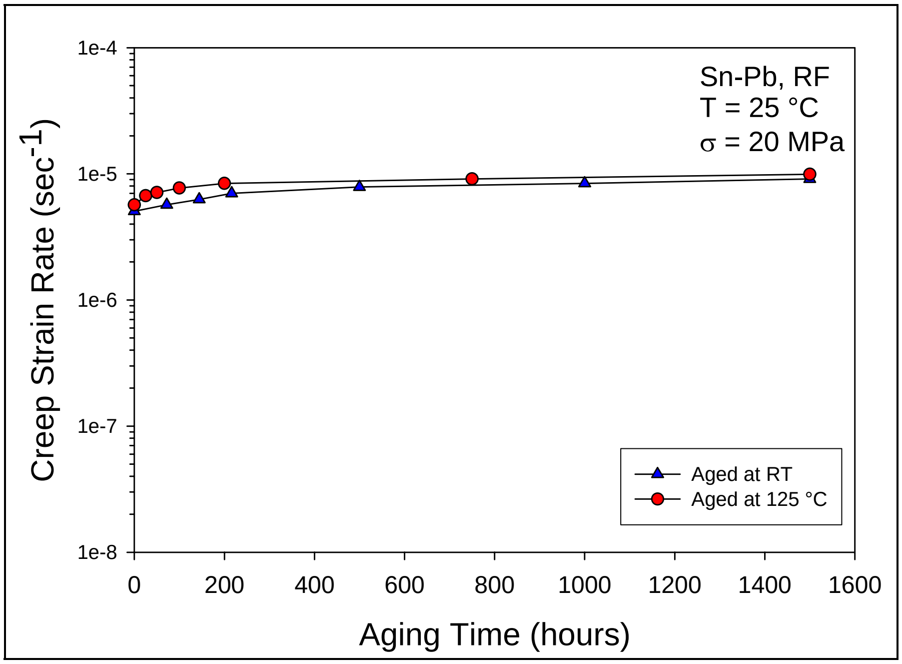

Figure 5.19 Sn-Pb Creep Rate Comparison of RT Aging and Elevated Temperature Aging at 125 °C.

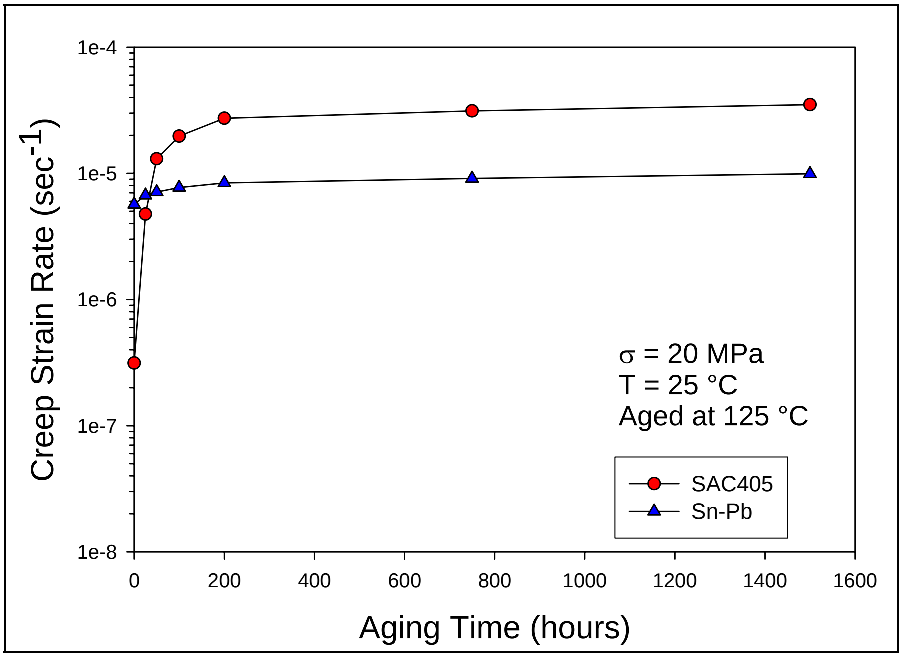

Figure 5.20 Comparison of Sn-Pb and SAC Creep Rates for Aging at 125 °C.

5.4 Microstructure Evolution with Aging Time and Aging Temperature

Aging at elevated temperatures dramatically changes the microstructure of both Sn-Pb and SAC alloys. As mentioned in Chapter 2, the microstructure coarsening during aging is the underlying reason for the changes in the mechanical properties of the solder alloys.

Figure 5.21 and Figure 5.22 show the SEM images of reflowed Sn-Pb eutectic solder and reflowed SAC405 at 125 °C and 150 °C at various aging times. Comparing the images after thermal aging to those of the as reflowed conditions in Figures 4.19-4.20, the coarsening of the microstructure for both alloys is clearly more significant at the elevated temperatures. A typical Sn-Pb microstructure includes the Sn rich β phase and Pb rich α phase. After aging, both of these phases grew even larger at higher temperatures for Sn-Pb than for the room temperature aging, which corresponds with the mechanical properties observed. The mechanical properties decrease much more significantly for the thermally aged specimens. The typical microstructure of SAC alloys consists of a Sn matrix and Ag_3Sn and Cu_6Sn_5 second phases. After aging, the dendrites grow larger and at the same time the second phases develop into much larger needle like particles at higher aging temperatures and longer aging durations. This coarsening of the second phase particles is caused by diffusion. The diffusion rate of Ag and Cu at elevated temperatures will be much higher than at room temperature. As mentioned in Chapter 2, the creep deformation mechanism for solders are mainly dislocation creep and grain sliding, which means the major reason for creep is dislocation movement related. Coarsened second phases will not be able to effectively block this dislocation movement and the resulting loss of strength. At the same time the large secondary phases

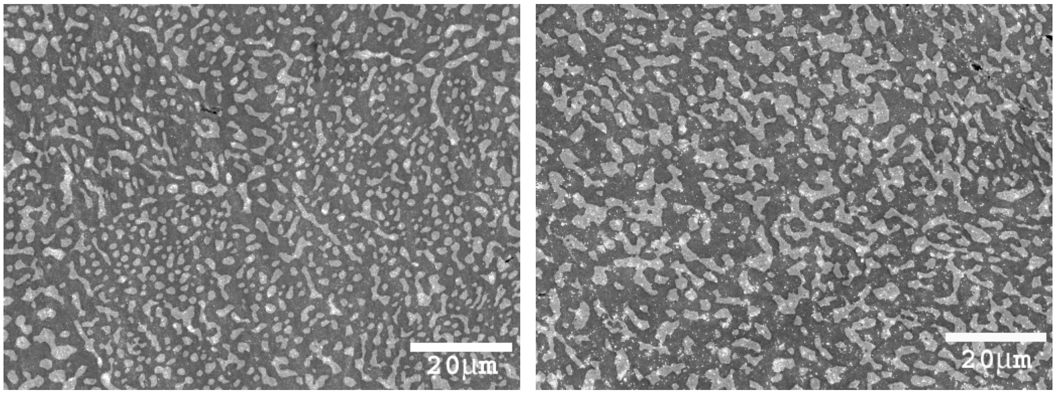

(a) 25 hours at 125 °C

(b) 100 hours at 125 °C

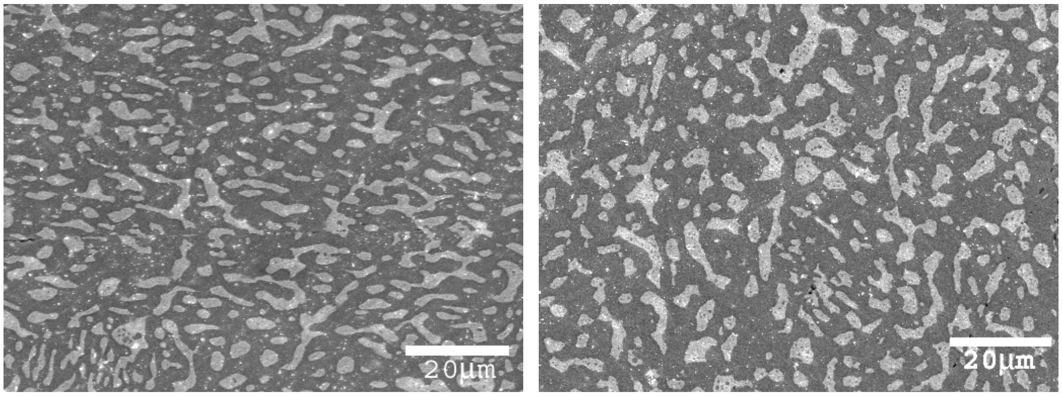

(c) 25 hours at 150 °C

(d) 100 hours at 150 °C

Figure 5.21 Sn-Pb Aging for Various Aging Times and Aging Temperature.

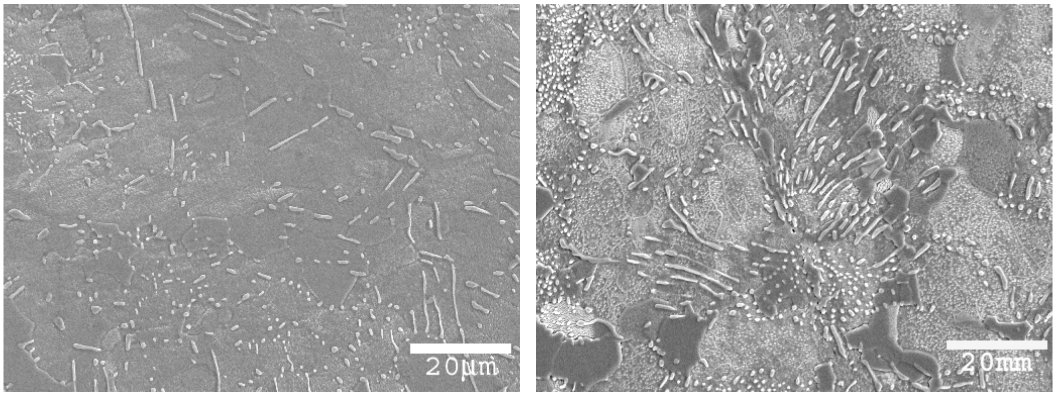

(a) 50 hours at 125 °C (b) 100 hours at 125 °C

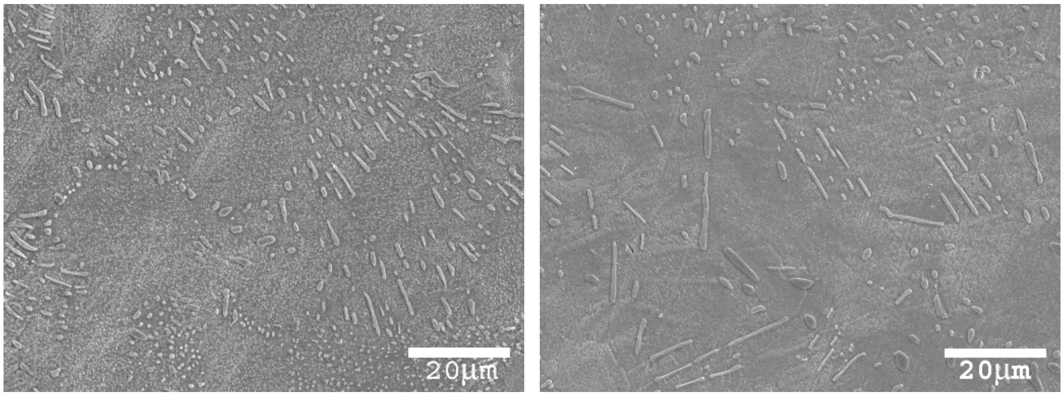

(c) 50 hours at 150 °C (d) 100 hours at 150 °C

Figure 5.22 SAC405 Aging for Various Aging Times and Aging Temperature.

themselves become weak points in the materials.

Fine intermetallic compounds particles can also significantly reduce sliding of the grain boundaries. The coarsened particles will also lose the ability to block grain boundary sliding. In all, the coarsening of the secondary phases particles leads to a dramatic loss of creep resistance in SAC alloys.

Figure 5.23 shows the SEM images of the fracture surface of SAC405. The images show more “dimple rupture” after aging and at higher aging temperature, which indicates a typical ductile fracture and corresponds to lower strength at higher aging temperatures.

5.5 Summary and Conclusions

Elevated temperature aging effects were investigated for aging durations of up to 6 months. Thermal aging significantly decreases the mechanical properties of both eutectic SAC and Sn-Pb solder alloys. Compared to the room temperature aging described in Chapter 4, the aging at elevated temperature has a much more significant effect on both the mechanical properties and microstructure evolution. The aging effects are more significant at higher temperature and for longer aging durations.

Comparing the SAC solder with Sn-Pb, Sn-Pb eutectic solder proved to be more stable regarding elevated temperature aging. The mechanical properties became relatively stable after about 200 hours of aging. However, for the SAC alloy, the tensile properties and creep deformation continued to change with longer aging durations. It is worth noting that the creep deformation of the SAC alloys is only better than Sn-Pb at room temperature and for shorter aging times at elevated temperature. There is a cross-

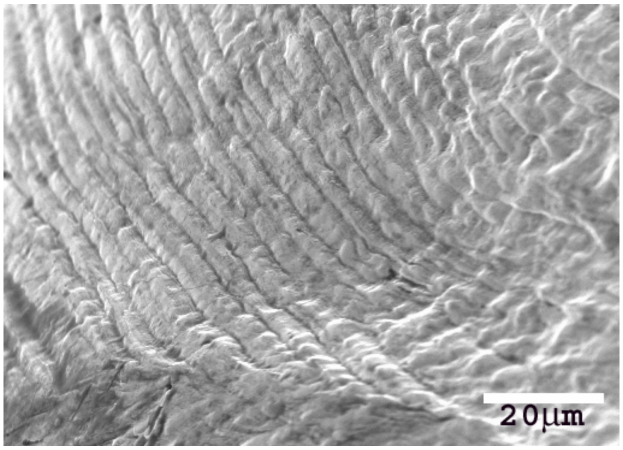

(a) As Reflowed

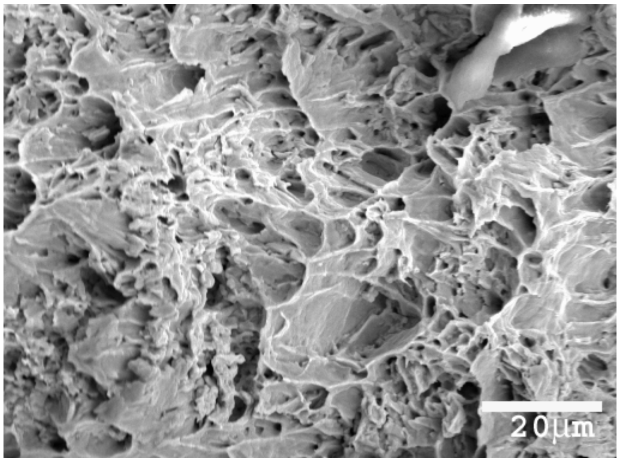

(b) 100 hours 125 °C

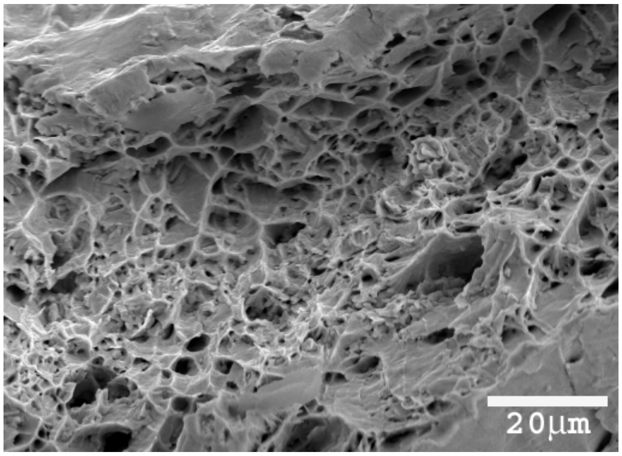

(b) 100 hours at 150 °C

Figure 5.23 The Fractography of SAC405.

over point at about 50 hours of aging at 125 °C, and the creep resistance of SAC alloy was lower than that of Sn-Pb for longer aging durations.

The continuous degradation of the mechanical properties is caused by the dramatic coarsening of the secondary intermetallic particles. When the particles are small and fine precipitations, they can effectively block the movement of dislocations and reduce grain boundaries sliding, thus strengthening the materials. When the second phases particle grows coarser, their ability to block the dislocation movements and grain boundary sliding, which are known to be the major reasons of creep failure, are significantly reduced.

CHAPTER 6

EFFECTS OF TEMPERATURE AND STRAIN RATE ON THE TENSILE PROPERTIES OF LEAD-FREE SOLDERS

6.1 Introduction

In actual electronic packages, due to the CTE mismatch and complexity of the operating conditions, solder joints will be under constant stress at various temperature and strain rates. Due to the high homologous temperature of solder alloys ($T_h > 0.5T_m$), the mechanical properties of solder alloys are strongly temperature and strain rate dependent and their properties will be significantly different under various conditions. The investigation of this dependence on temperature and strain rates is therefore important in order to fully understand the materials behavior of solder alloys, and accurately predict the reliability of solder joints.

As mention previously in Chapter 2, there have been various studies on the temperature and strain rate dependence. However, none of the currently available documented data has considered the possible room temperature contribution in their data. As the presented data in Chapter 4 shows, room temperature aging effects will dramatically affect the mechanical properties of solder alloys. Any difference in the testing conditions of specimens could seriously affect the accuracy of the data. The data in Chapter 4 shows that the tensile properties of both lead-free solders and Sn-Pb solders tend to become relatively stable after 10 days of aging at room temperature. In this study, in order to reduce any room temperature aging contribution in the investigation of the dependence of temperature and strain rates, all specimen tested were preconditioned after 10 days of aging at room temperature. All tests were conducted under the same conditions.

6.2 Effects of Temperature and Strain Rate on Tensile Properties

As mentioned in Chapter 2, the tensile strength follows a near linear relationship with changes in temperature (Eq. 2.4), and a power relationship with strain rates (Eq. 2-3).

In this study, reflowed specimens were aged at room temperature for 10 days before testing. 10 specimens were prepared for each testing condition, and stress-strain data were processed as described in Chapter 3. Three strain rates were chosen, 10^{-3} sec^{-1}, 10^{-4} sec^{-1}, 10^{-5} sec^{-1}, and testing temperature ranges from -40 to 150 °C.

Figures 6.1-6.3 show the stress-strain curves for SAC405 tested at three strain rates and various temperatures. Figures 6.4-6.6 illustrated the elastic modulus (Figure 6.4), UTS (Figure 6.5) and YS (Figure 6.6) values change with temperature at the three strain rates. The tensile properties are nearly linear with the changing temperature. The tensile properties of the SAC alloy decrease linearly with increasing temperature. The linear relationships of the tensile properties at three strain rates are summarized in Table 6.1. At a given strain rate, the tensile properties at various temperatures can be predicted with these linear models. Figures 6.7-6.9 illustrate how the tensile properties changes with the changing strain rates at different temperatures. The tensile properties follow a power law relationship. The models are summarized in Table 6.2, for various

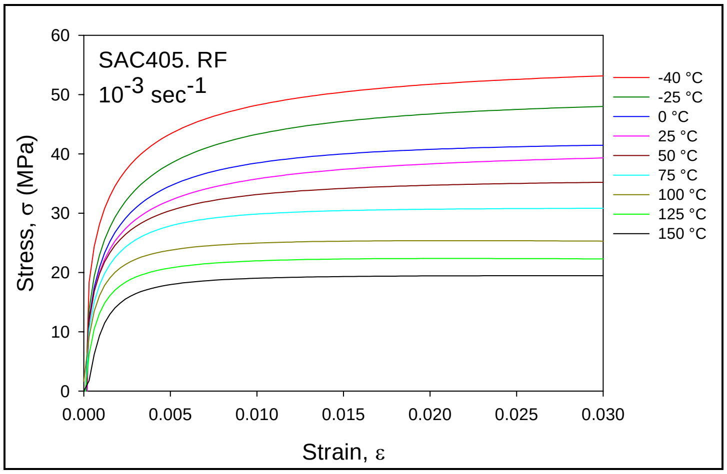

Figure 6.1 SAC405 Stress-Strain Curves at Various Temperatures and at 10^{-3} sec^{-1}.

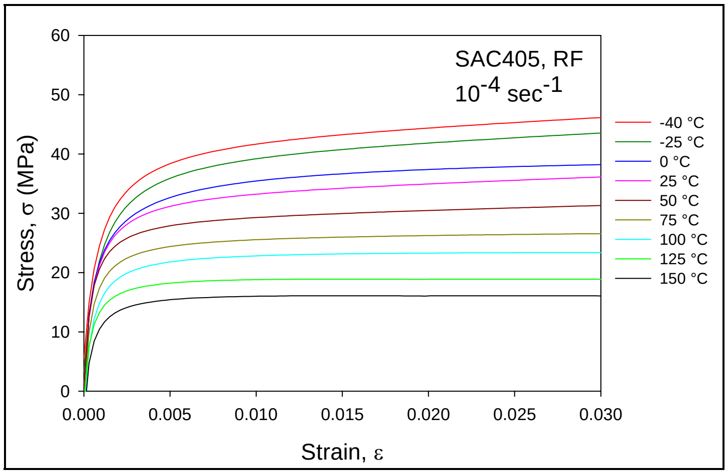

Figure 6.2 SAC405 Stress-Strain Curves at Various Temperatures and at 10^{-4} sec^{-1}.

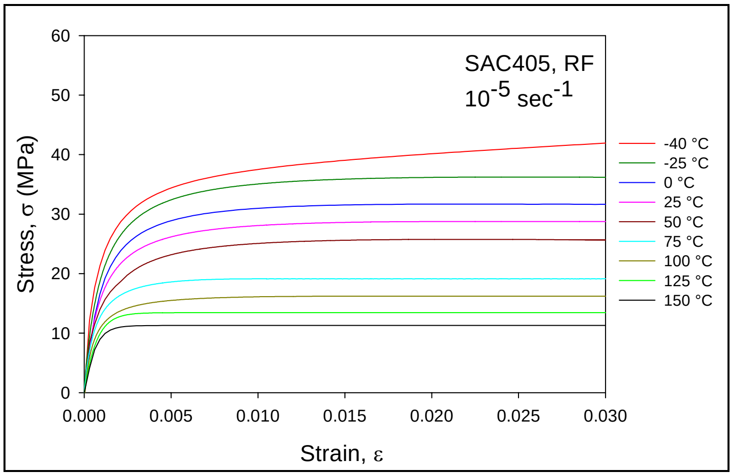

Figure 6.3 SAC405 Stress-Strain Curves at Various Temperatures and at 10^{-5} sec^{-1}.

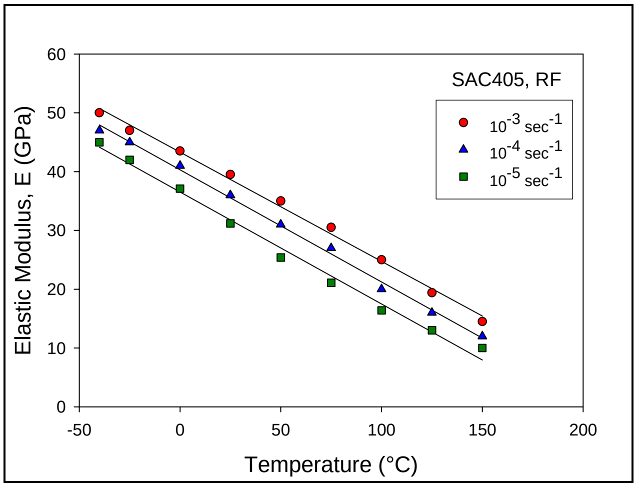

Figure 6.4 SAC405 Elastic Modulus vs. Temperature at Different Strain Rates.

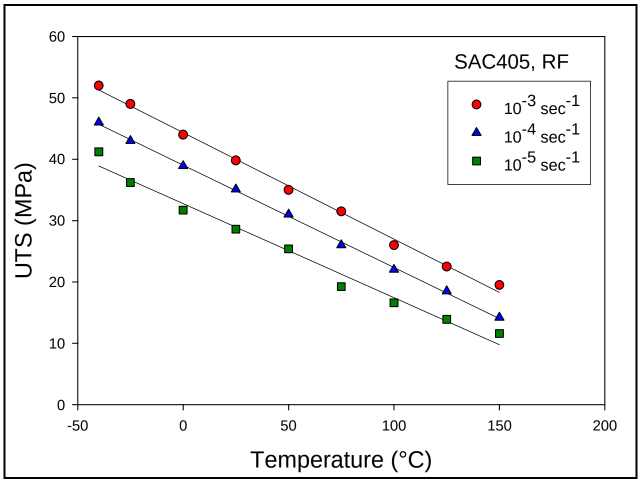

Figure 6.5 SAC405 UTS vs. Temperature at Different Strain Rates.

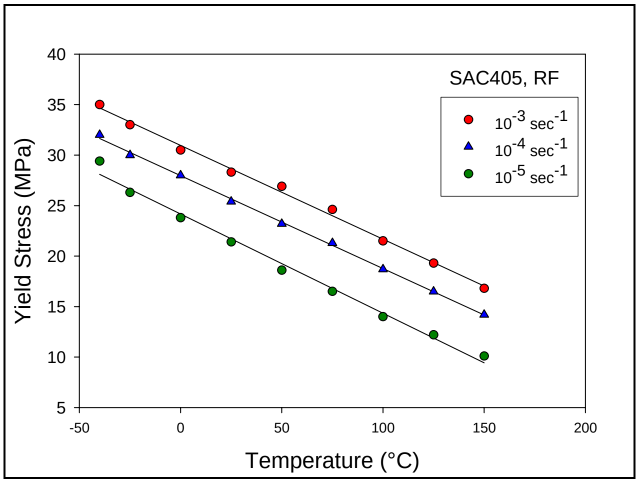

Figure 6.6 SAC405 Yield Stress vs. Temperature at Different Strain Rates.

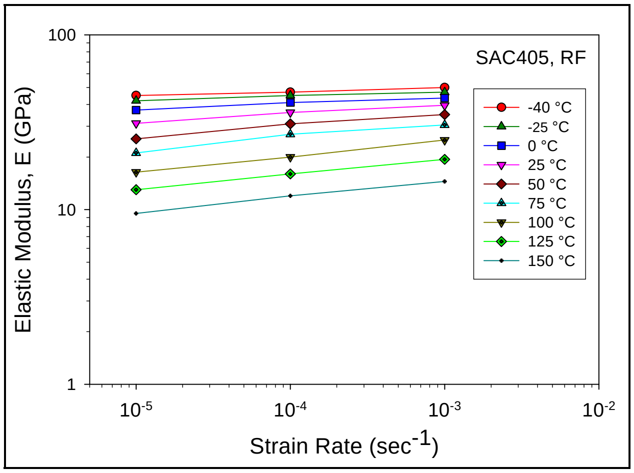

Figure 6.7 SAC405 Elastic Modulus vs. Strain Rate at Various Temperatures.

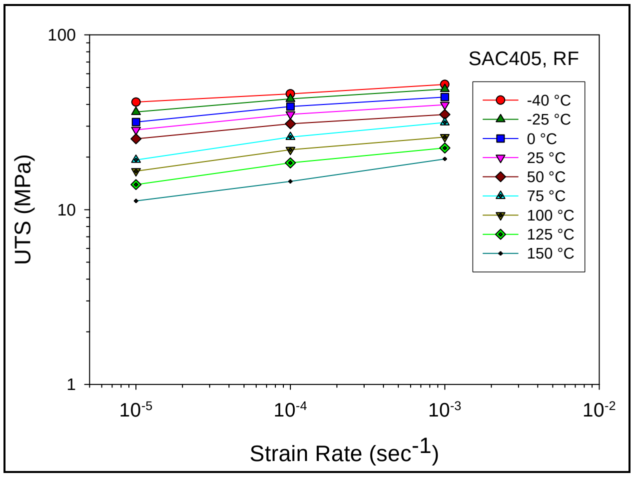

Figure 6.8 SAC405 UTS vs. Strain Rate at Various Temperatures.

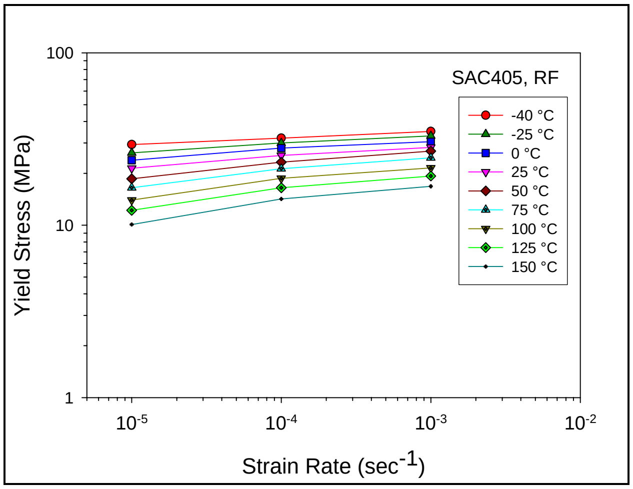

Figure 6.9 SAC405 Yield Stress vs. Strain Rate at Various Temperature.

Table 6.1 SAC405 Tensile Properties vs. Temperature at Different Strain Rates.

Strain Rate	Temperature Range	Temperature Dependence	R^2
10^{-3} sec^{-1}	E	$E = -0.1857T + 43.313$	0.9953
	UTS	$\sigma_{UTS} = -0.1736T + 44.353$	0.9966
	YS	$\sigma_{0.2} = -0.0928T + 30.953$	0.9958
10^{-4} sec^{-1}	E	$E = -0.1907T + 40.301$	0.9966
	UTS	$\sigma_{UTS} = -0.1659T + 39.037$	0.9992
	YS	$\sigma_{0.2} = -0.092T + 27.955$	0.9988
10^{-5} sec^{-1}	E	$E = -0.1919T + 36.553$	0.9930
	UTS	$\sigma_{UTS} = -0.1545T + 32.79$	0.9841
	YS	$\sigma_{0.2} = -0.0983T + 24.167$	0.9907

Table 6.2 SAC405 Tensile Properties vs. Strain Rates at Various Temperatures.

Temperature (°C)	Elastic Modulus		UTS		YS	
	E	R^2	σ_{UTS}	R^2	$\sigma_{0.2}$	R^2
-40 °C	$58.383(\dot{\varepsilon})^{0.0229}$	0.9899	$73.581(\dot{\varepsilon})^{0.0506}$	0.9991	$45.425(\dot{\varepsilon})^{0.0379}$	0.9997
-25 °C	$55.875(\dot{\varepsilon})^{0.0244}$	0.9831	$77.702(\dot{\varepsilon})^{0.0657}$	0.9938	$46.664(\dot{\varepsilon})^{0.0493}$	0.9915
0 °C	$55.605(\dot{\varepsilon})^{0.0346}$	0.9786	$72.936(\dot{\varepsilon})^{0.0712}$	0.9798	$44.819(\dot{\varepsilon})^{0.0539}$	0.9689
25 °C	$56.742(\dot{\varepsilon})^{0.0512}$	0.9851	$66.204(\dot{\varepsilon})^{0.0718}$	0.9812	$43.493(\dot{\varepsilon})^{0.0607}$	0.9832
50 °C	$57.353(\dot{\varepsilon})^{0.0696}$	0.9807	$57.353(\dot{\varepsilon})^{0.0696}$	0.9807	$47.358(\dot{\varepsilon})^{0.0801}$	0.9871
75 °C	$54.119(\dot{\varepsilon})^{0.0800}$	0.9632	$67.201(\dot{\varepsilon})^{0.1071}$	0.9839	$45.621(\dot{\varepsilon})^{0.0867}$	0.9748
100 °C	$46.859(\dot{\varepsilon})^{0.0915}$	0.9989	$51.948(\dot{\varepsilon})^{0.0974}$	0.9787	$41.952(\dot{\varepsilon})^{0.0932}$	0.9609
125 °C	$35.455(\dot{\varepsilon})^{0.0869}$	0.9995	$46.983(\dot{\varepsilon})^{0.1044}$	0.9886	$39.343(\dot{\varepsilon})^{0.0998}$	0.9677
150 °C	$27.545(\dot{\varepsilon})^{0.0918}$	0.9963	$44.515(\dot{\varepsilon})^{0.1204}$	0.9984	$37.092(\dot{\varepsilon})^{0.1105}$	0.9631

temperatures, the tensile properties of the solder alloy can be predicted using the power law models presented in this study at various strain rates. The power constants continue to increase with increasing temperature, which implies that the properties are more sensitive to strain rates at higher temperatures.

Corresponding tensile data for Sn-Pb were also collected at various strain rates and temperatures. Figures 6.10-6.12 show the stress-strain curves of Sn-Pb solder at the various strain rates and temperature. As with the SAC alloy, the stress-strain curves for Sn-Pb clearly show that the tensile strength decreased with increasing testing temperature and increased with increasing strain rates. Figures 6.13-6.15 summarize changes in the elastic modulus (Figure 6.13), UTS (Figure 6.14), and YS (Figure 6.15) with changing temperature at three different strain rates. Near linear relationships were also found between key tensile properties (E, UTS, and YS) and temperature. Similar to that of SAC alloy, the tensile properties decreased dramatically with increasing temperature. The linear models at all three strain rates are summarized in Table 6.3. Figures 6.16-6.18 illustrate how the tensile properties (E, UTS, YS) change with changing strain rates. Tensile strength follows a power law relationship with the strain rates. The power law models for Sn-Pb solder at different temperatures are summarized in Table 6.4. The power constants continue to increase with increasing temperature. Compared to the power constants in SAC, the Sn-Pb solder has noticeably higher constants at higher temperatures, which implies that the Sn-Pb is more strain rate sensitive at higher temperatures. The previous data shows that both lead-free solder and Sn-Pb solder alloys follow a similar relationship between the tensile properties, temperature and strain rates. Figures 6.19-6.20 show the comparison of between Sn-Pb and SAC405, the elastic

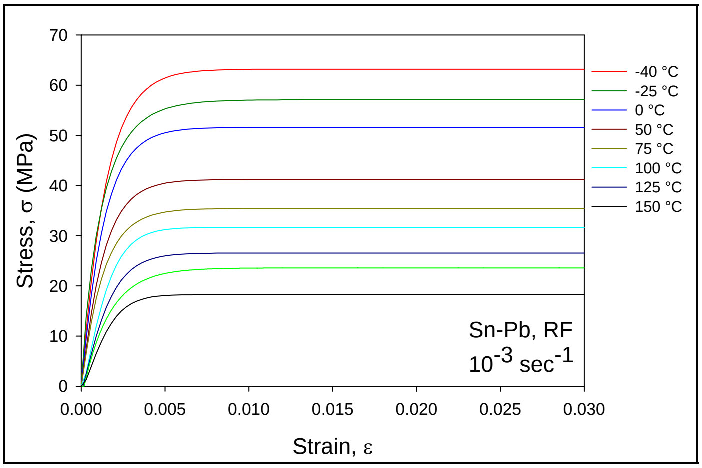

Figure 6.10 Sn-Pb Stress-Strain Curves at Various Temperatures and at 10^{-3} sec^{-1}.

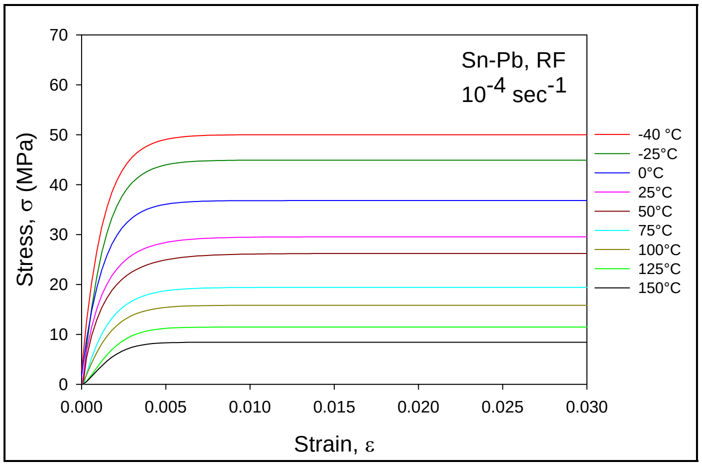

Figure 6.11 Sn-Pb Stress-Strain Curves at Various Temperatures and at 10^{-4} sec^{-1}.

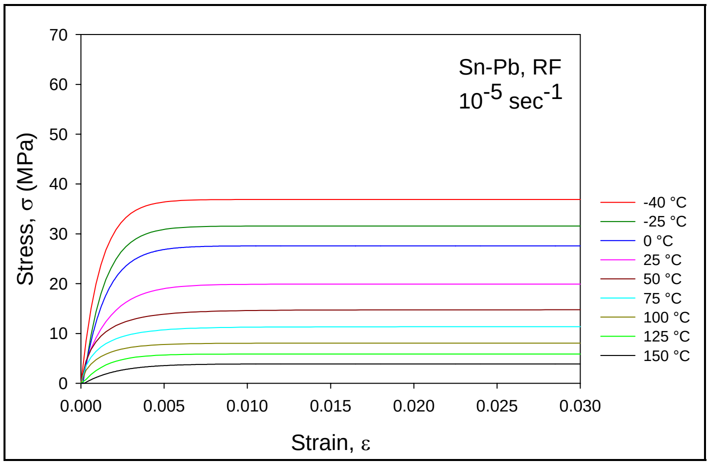

Figure 6.12 Sn-Pb Stress-Strain Curves at Various Temperatures and at 10^{-5} sec^{-1}.

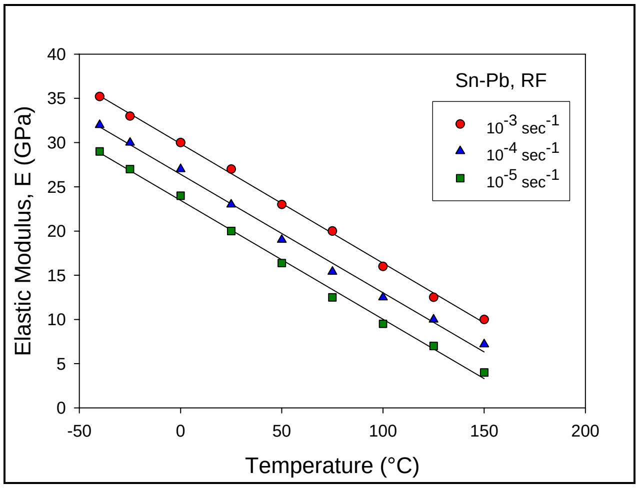

Figure 6.13 Sn-Pb Elastic Modulus vs. Temperature at Different Strain Rates.

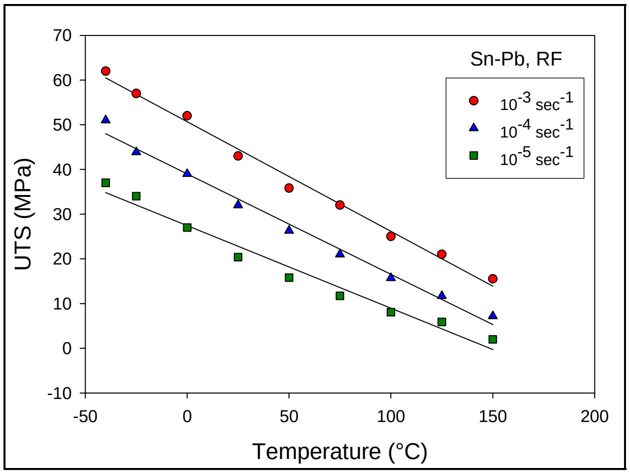

Figure 6.14 Sn-Pb UTS vs. Temperature at Different Strain Rates.

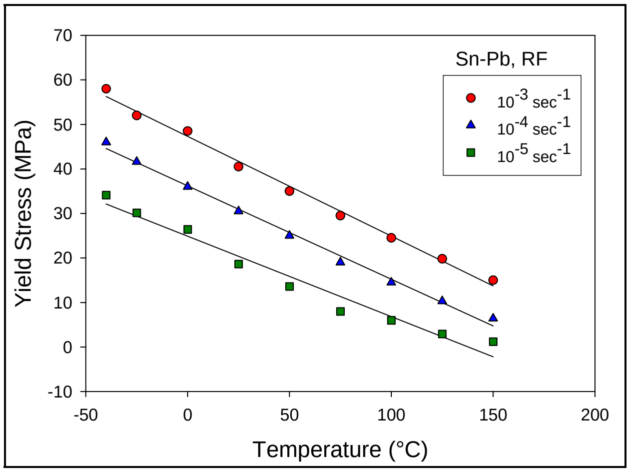

Figure 6.15 Sn-Pb Yield Stress vs. Temperature at Different Strain Rates.

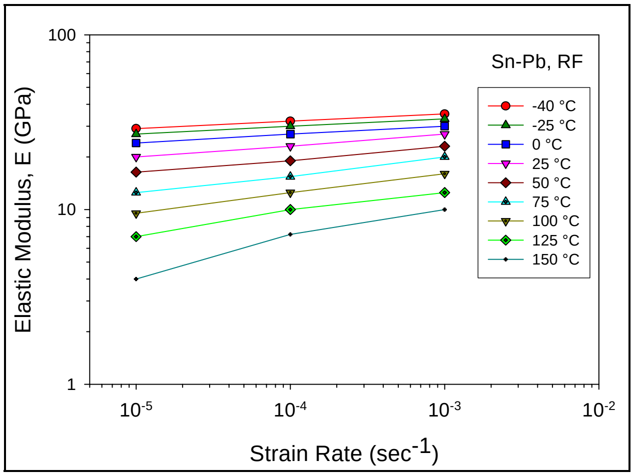

Figure 6.16 Sn-Pb Elastic Modulus vs. Strain Rate at Various Temperatures.

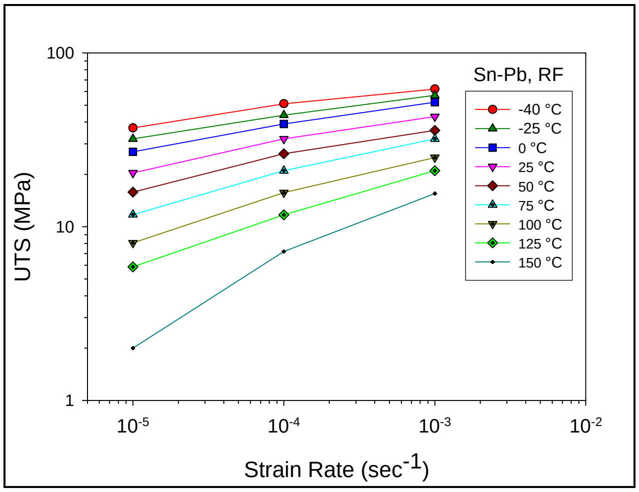

Figure 6.17 Sn-Pb UTS vs. Strain Rate at Various Temperatures.

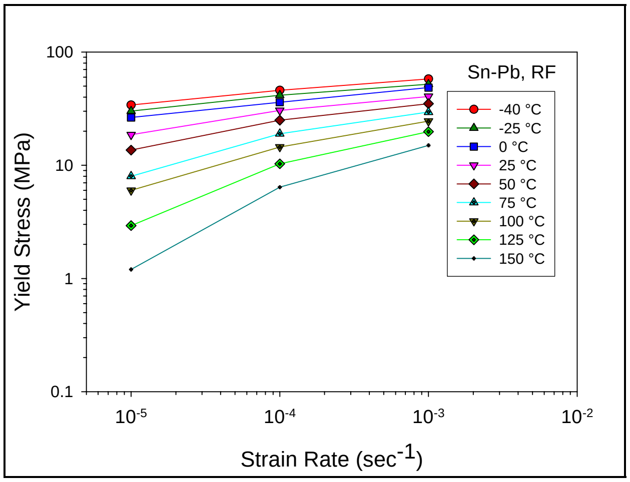

Figure 6.18 Sn-Pb Yield Stress vs. Strain Rate at Various Temperatures.

Table 6.3 Sn-Pb Tensile Properties vs. Temperature at Different Strain Rates.

Strain Rate	Temperature Range	Temperature Dependence	R^2
10^{-3} sec^{-1}	E	$E = -0.1352T + 29.875$	0.9986
	UTS	$\sigma_{UTS} = -0.2455T + 50.691$	0.9916
	YS	$\sigma_{0.2} = -0.2239T + 47.311$	0.9939
10^{-4} sec^{-1}	E	$E = -0.134T + 26.418$	0.9952
	UTS	$\sigma_{UTS} = -0.2325T + 39.817$	0.9877
	YS	$\sigma_{0.2} = -0.2097T + 36.196$	0.9946
10^{-5} sec^{-1}	E	$E = -0.1345T+ 23.474$	0.9967
	UTS	$\sigma_{UTS} = -0.185T+27.437$	0.9744
	YS	$\sigma_{0.2} = -0.1806T + 24.891$	0.9677

Table 6.4 Sn-Pb Tensile Properties vs. Strain Rates at Various Temperatures.

Temperature (°C)	Elastic Modulus		UTS		YS	
	E	R^2	σ_{UTS}	R^2	$\sigma_{0.2}$	R^2
-40 °C	$47.096(\dot{\varepsilon})^{0.0421}$	0.9999	$137.33(\dot{\varepsilon})^{0.1121}$	0.9806	$130.11(\dot{\varepsilon})^{0.1153}$	0.9946
-25 °C	$44.665(\dot{\varepsilon})^{0.0436}$	0.9902	$136.71(\dot{\varepsilon})^{0.1254}$	0.9972	$120.06(\dot{\varepsilon})^{0.1187}$	0.9890
0 °C	$42.013(\dot{\varepsilon})^{0.0485}$	0.9990	$140.85(\dot{\varepsilon})^{0.1432}$	0.9951	$121.01(\dot{\varepsilon})^{0.1321}$	0.9999
25 °C	$42.206(\dot{\varepsilon})^{0.0652}$	0.9984	$135.03(\dot{\varepsilon})^{0.1619}$	0.9858	$134.78(\dot{\varepsilon})^{0.1690}$	0.9761
50 °C	$38.044(\dot{\varepsilon})^{0.0739}$	0.9950	$126.27(\dot{\varepsilon})^{0.1776}$	0.9802	$151.21(\dot{\varepsilon})^{0.2053}$	0.9731
75 °C	$40.109(\dot{\varepsilon})^{0.1020}$	0.9958	$148.11(\dot{\varepsilon})^{0.2179}$	0.9915	$224.23(\dot{\varepsilon})^{0.2834}$	0.9658
100 °C	$35.133(\dot{\varepsilon})^{0.1132}$	0.9991	$141.23(\dot{\varepsilon})^{0.2458}$	0.9895	$214.58(\dot{\varepsilon})^{0.3055}$	0.9789
125 °C	$30.500(\dot{\varepsilon})^{0.1259}$	0.9826	$144.60(\dot{\varepsilon})^{0.2768}$	0.9978	$384.44(\dot{\varepsilon})^{0.4148}$	0.9678
150 °C	$41.274(\dot{\varepsilon})^{0.1990}$	0.9740	$364.34(\dot{\varepsilon})^{0.4447}$	0.9794	$760.28(\dot{\varepsilon})^{0.5485}$	0.9659

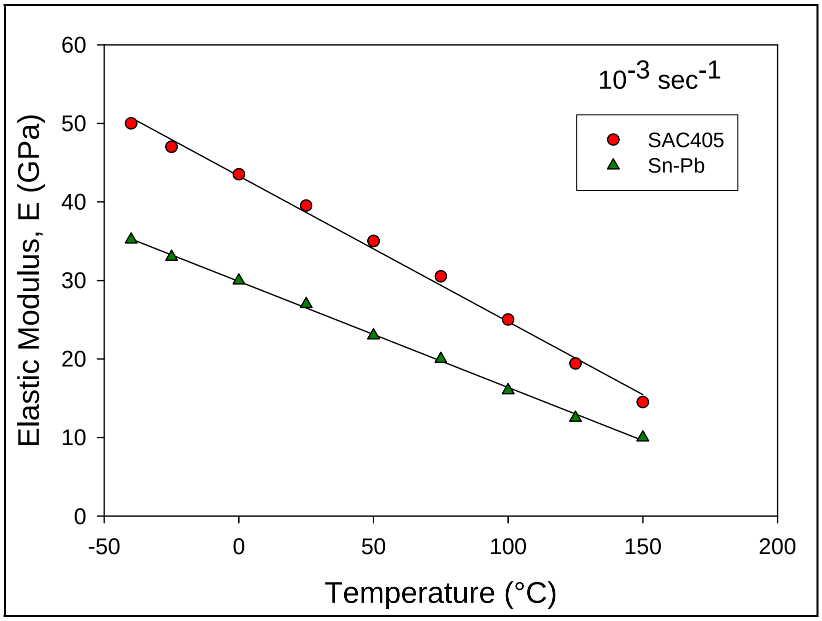

Figure 6.19 Elastic Modulus vs. Temperature for Sn-Pb and SAC405.

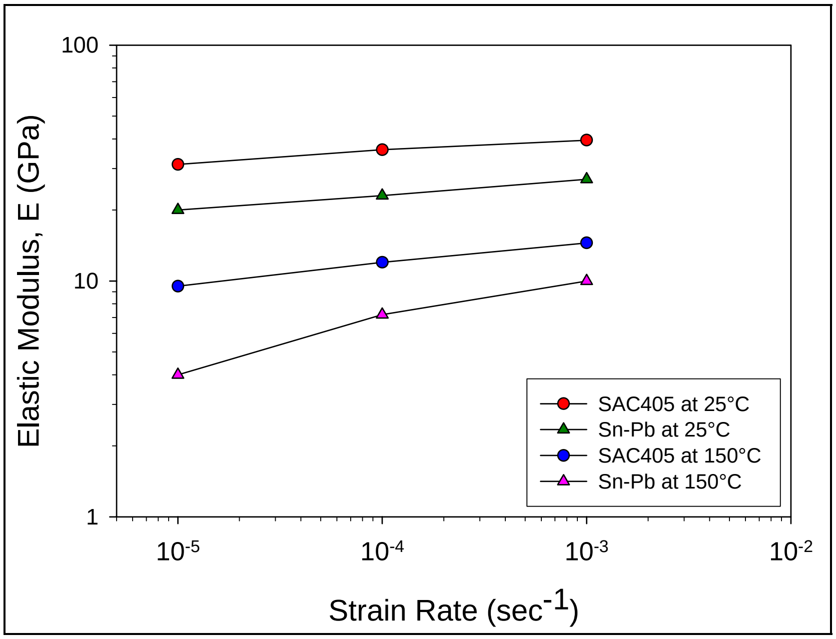

Figure 6.20 Elastic Modulus vs. Strain Rate for Sn-Pb and SAC405.

modulus of SAC405 is higher than Sn-Pb. Figure 6.19 shows that the elastic modulus of SAC405 is more sensitive to temperature than that of Sn-Pb. The strain rate dependency is similar for both alloys at lower temperature. Sn-Pb is more sensitive to strain rates at higher temperatures, which may be due to the low melting temperature of Sn-Pb.

As mentioned in Chapter 2, higher temperature is thought to induce transitions in macroscopic fractures, which leads to a reduction in the tensile strength at higher temperature [21]. The elastic modulus is believed to be related to the interatomic bonds [21], and is negatively proportional to a power of the distance between adjacent atoms [23]. Higher temperatures will cause an increase in the distance between adjacent atoms, which will therefore lead to the reduction in the elastic modulus.

The strain rate dependence is believed to be related to the strain hardening process during testing. At higher strain rates, strain hardening produces a dramatic increase in the number of dislocations and dislocation interactions in the materials. High dislocation densities will quickly increase the strength of the material.

6.3 Constitutive Modeling of the Effects of Strain Rate and Temperature on Tensile Properties of Lead-free Solders

In the previous section, a near linear relationship was found between tensile properties and testing temperature and a near power law relationship was found between tensile properties and strain rates. The underlying mechanism was also discussed in the previous section. In real solder joints, the temperature and strain rates may be random, so a constitutive model that takes into account both temperature and strain rate is needed to effectively predict the material behavior of solder alloys.

Most current reports have focused on a single variation such as linear relationship with respect to temperature, or the of power relationship with strain rate [119-122]. Shi, Pang and co-workers have proposed the following constitutive models for eutectic Sn-Pb solder that include variables for both temperature and strain rate [39, 118]:

$$E(T,\dot{\varepsilon}) = (k_1 T + k_2)\log(\dot{\varepsilon}) + (k_3 T + k_4) + k_0 \tag{6.1}$$

$$\sigma_{UTS,\,YS}(T,\dot{\varepsilon}) = (C_1 + C_2)\left[\dot{\varepsilon}\right]^{(C_3 T + C_4)} \tag{6.2}$$

where, k_0-k_4, and C_1-C_4 are materials constants. The model for the elastic modulus (Eq. 6.1) considers both the near linear temperature effects and strain rate contribution. The UTS and YS model also consider both the effects of temperature and strain rate. Shi *et al.* [39] used experimental data for both the temperature variable and the strain rate variable. In this study, the commercial software suite, “Datafit”, was used to fit multiple variables to the experimental data for both lead-free and Sn-Pb solders according to Shi’s models. The data fit the models perfectly. Figures 6.21-6.23 illustrate the 3-D mesh fitting to the elastic modulus (Figure 6.21), UTS (Figure 6.22), and yield stress (Figure 6.23) for SAC405, corresponding to the multiple variables mesh fitting of tensile properties for Sn-Pb illustrated in Figures 6.24-6.27. The constitutive models and all the materials constants were obtained for both alloys and are summarized in Table 6.5. The R-square values indicate a near perfect fit to our experimental data with the constitutive models to both lead-free and Sn-Pb solders. Figures 6.27-6.29 illustrate the comparison of the constitutive models obtained to the experimental data for the SAC alloys. Corresponding comparisons between the models and the experimental for Sn-Pb are illustrated in Figure 6.30-6.32, which also indicate a near perfect fitting to the models.

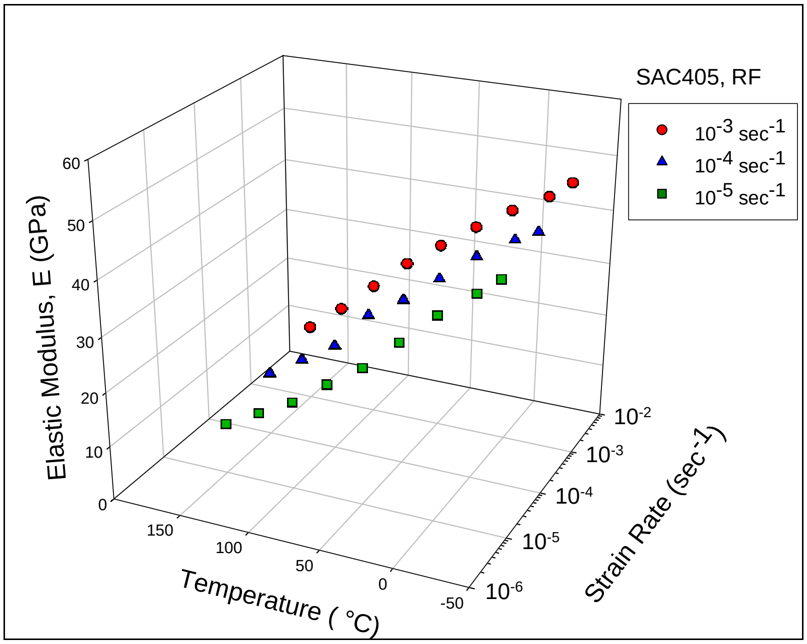

(a) Experimental Data

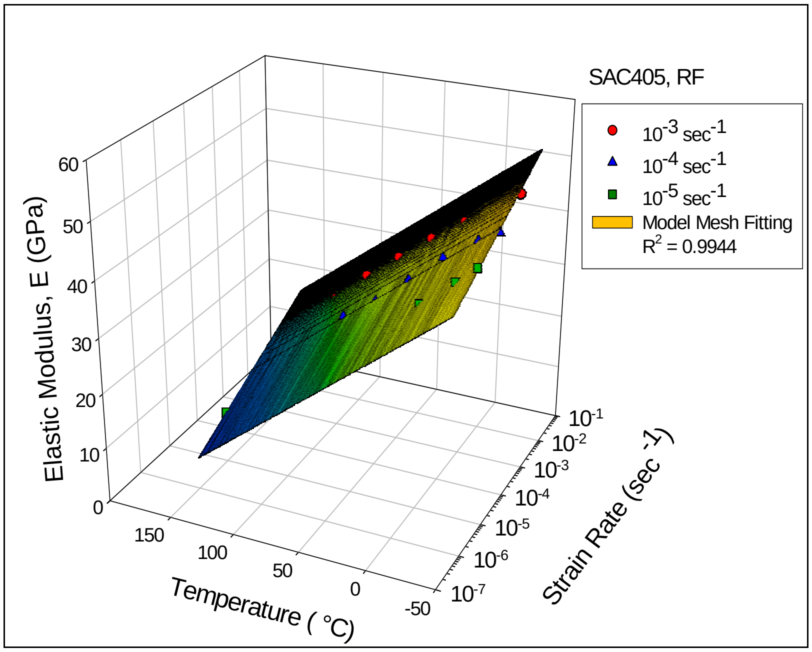

(b) Mesh Fitting with Constitutive Model

Figure 6.21 SAC405 Elastic Modulus vs. Temperature and Strain Rate.

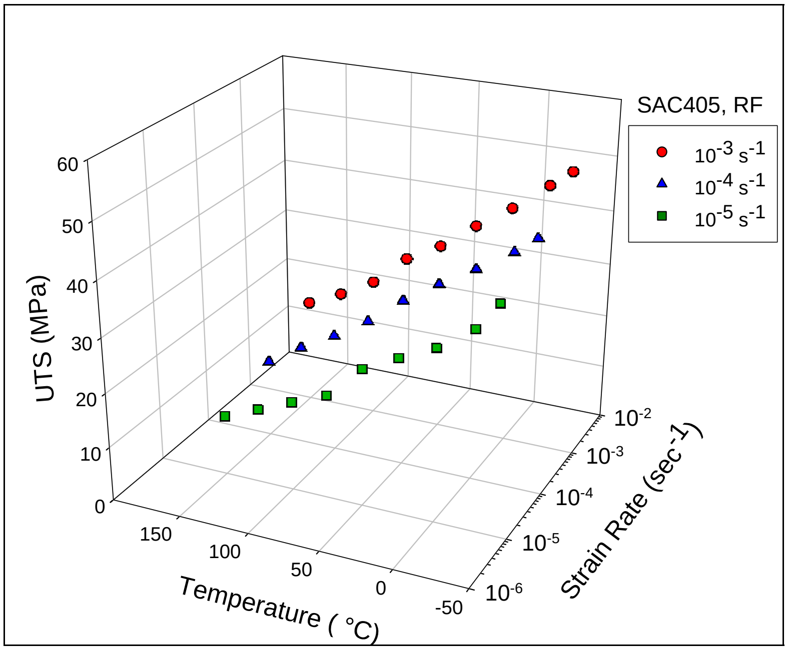

(a) Experimental Data

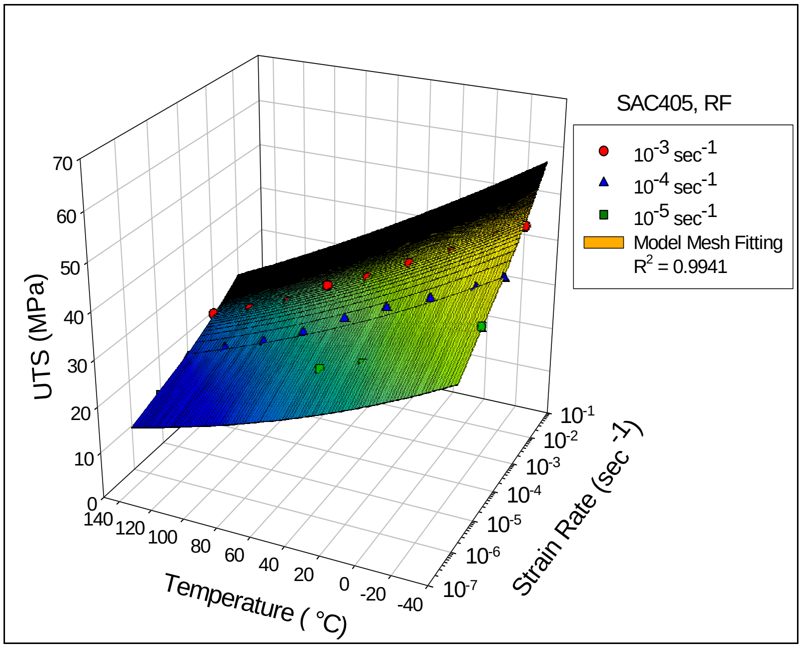

(b) Mesh Fitting with Constitutive Model

Figure 6.22 SAC405 UTS vs. Temperature and Strain Rate.

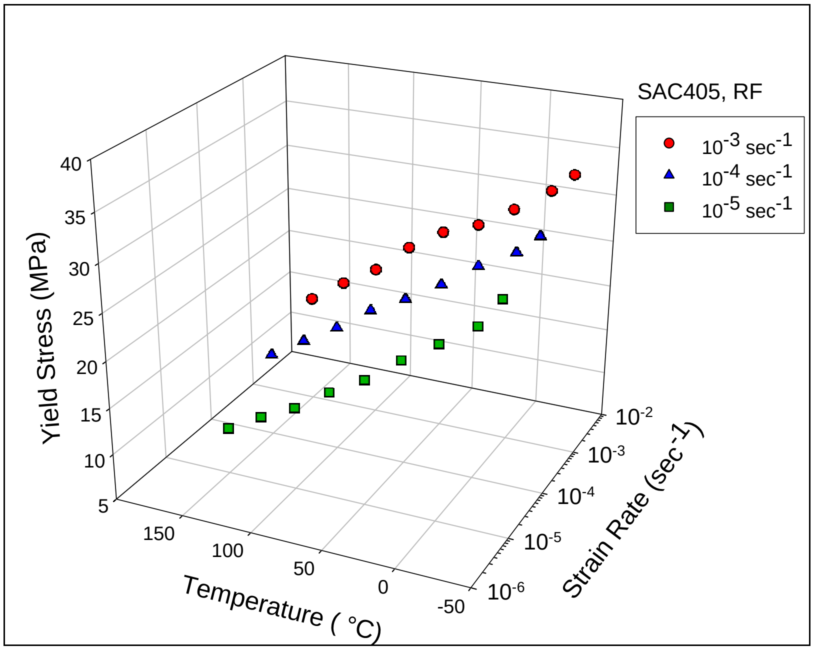

(a) Experimental Data

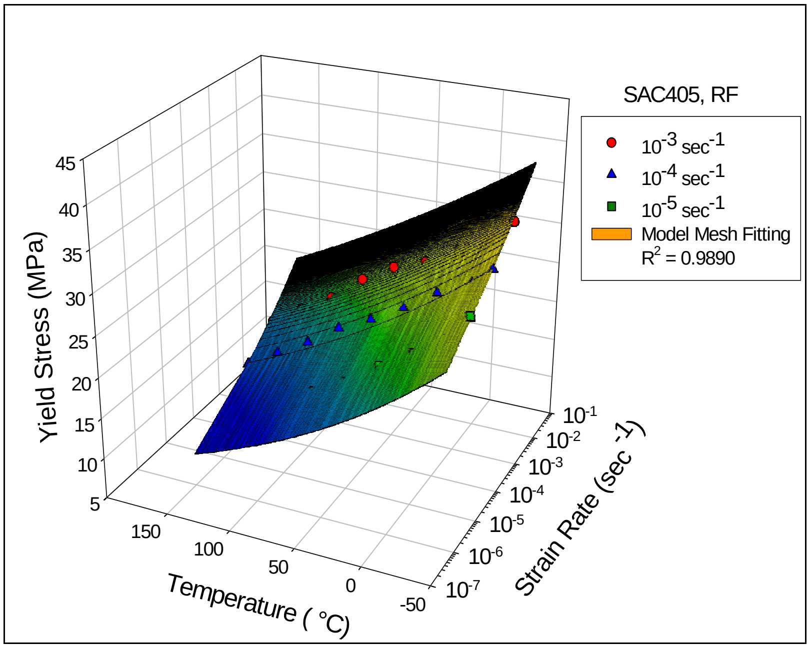

(b) Mesh Fitting with Constitutive Model

Figure 6.23 SAC405 Yield Stress vs. Temperature and Strain Rate.

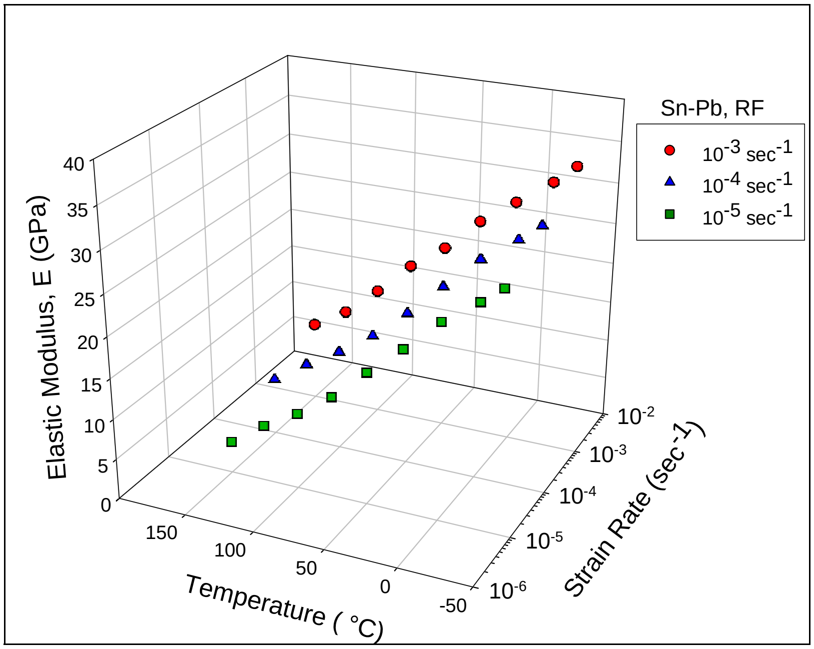

(a) Experimental Data

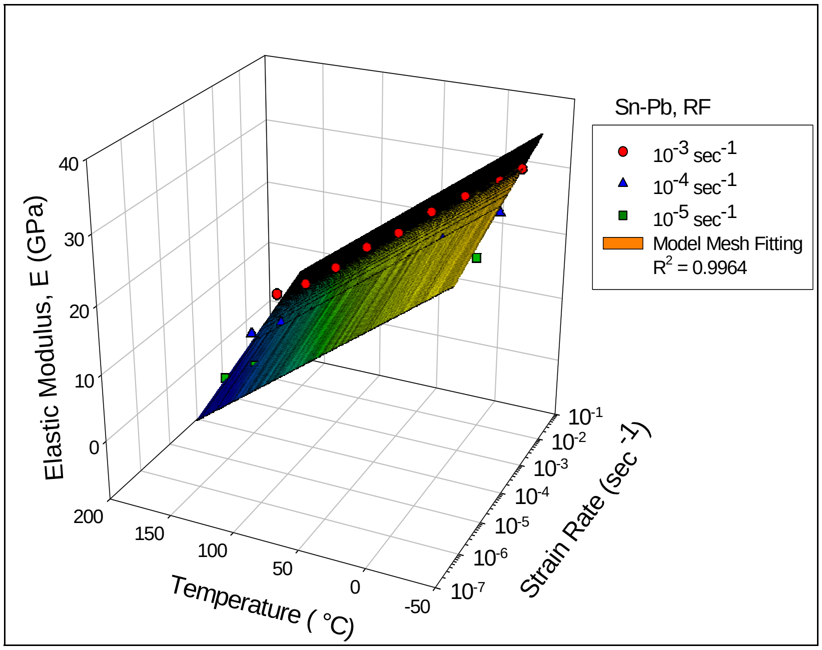

(b) Mesh Fitting with Constitutive Model

Figure 6.24 Sn-Pb Elastic Modulus vs. Temperature and Strain Rate.

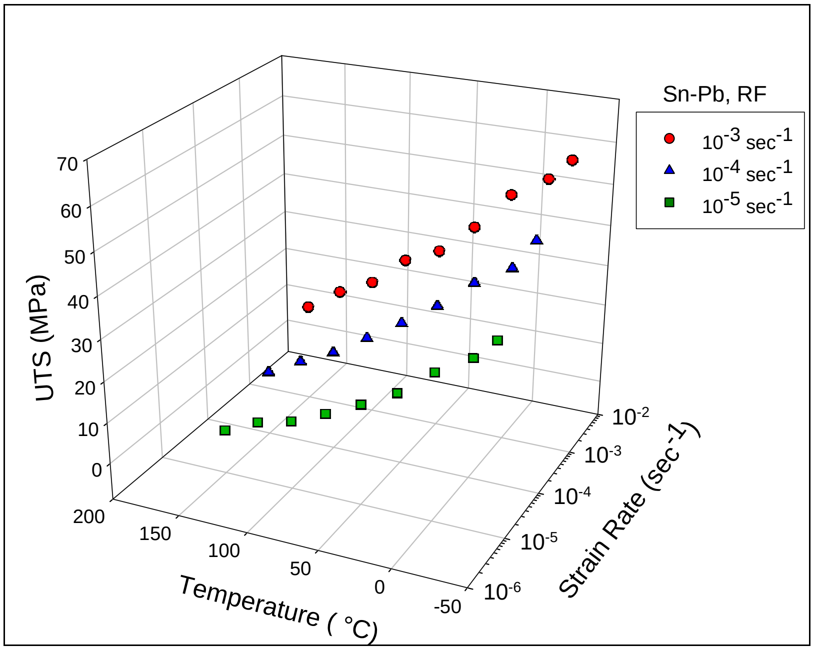

(a) Experimental Data

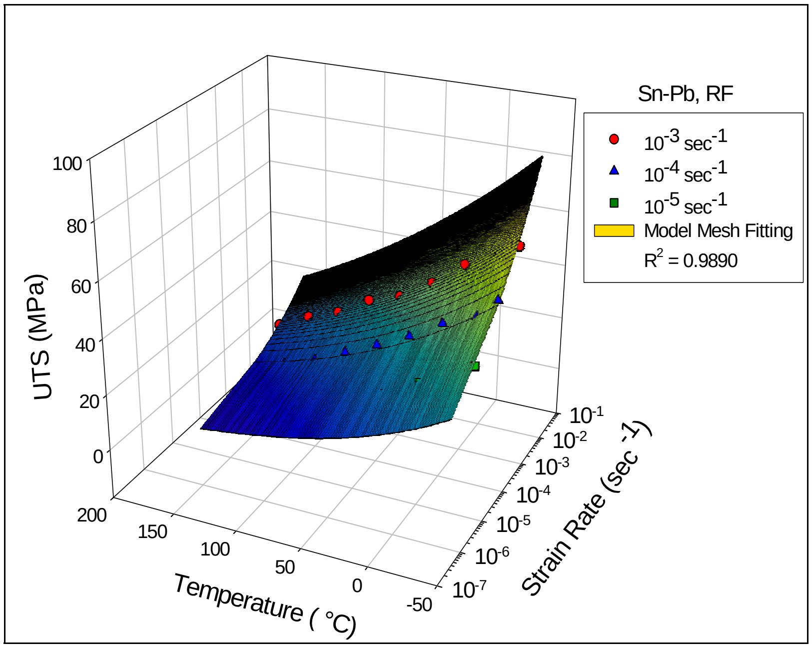

(b) Mesh Fitting with Constitutive Model

Figure 6.25 Sn-Pb UTS vs. Temperature and Strain Rate.

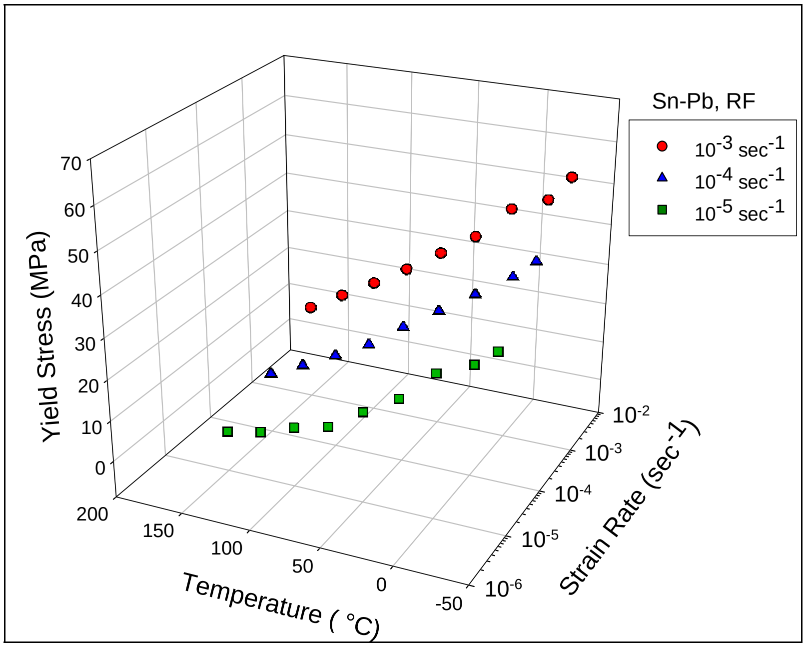

(a) Experimental Data

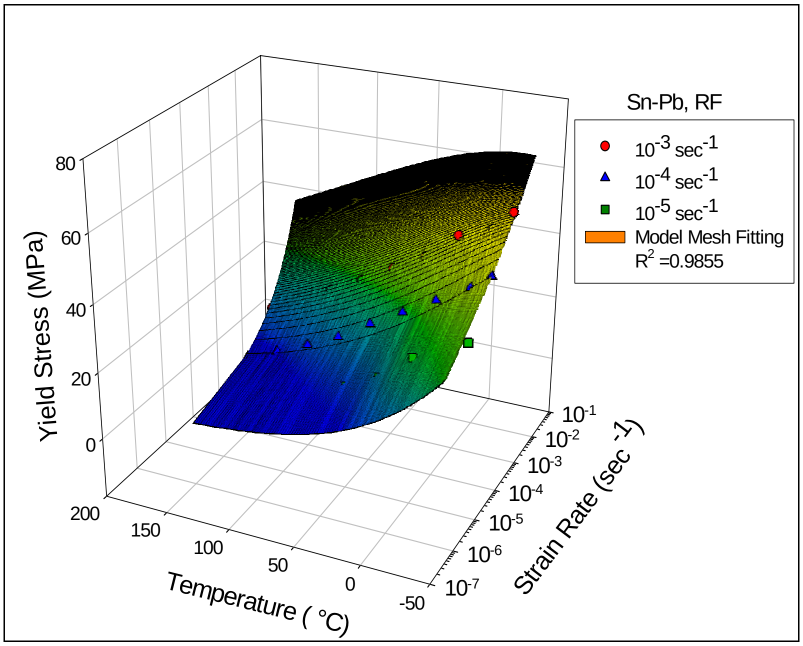

(b) Mesh Fitting with Constitutive Model

Figure 6.26 Sn-Pb Yield Stress vs. Temperature and Strain Rate.

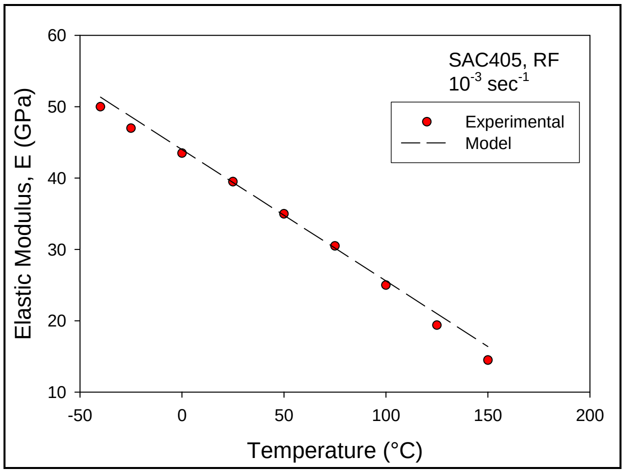

Figure 6.27 SAC405 Elastic Modulus Experimental vs. Constitutive Model.

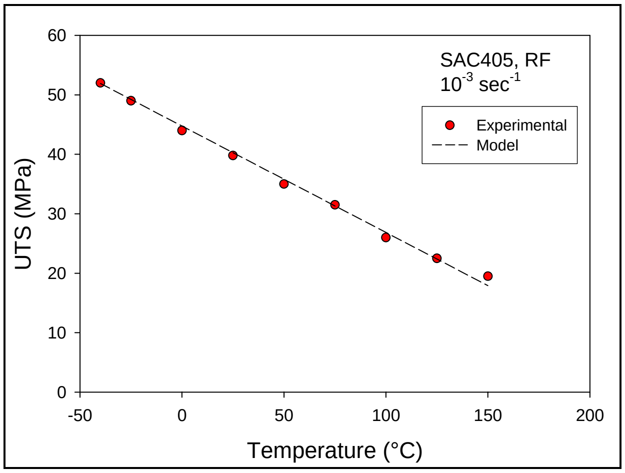

Figure 6.28 SAC405 UTS Experimental vs. Constitutive Model.

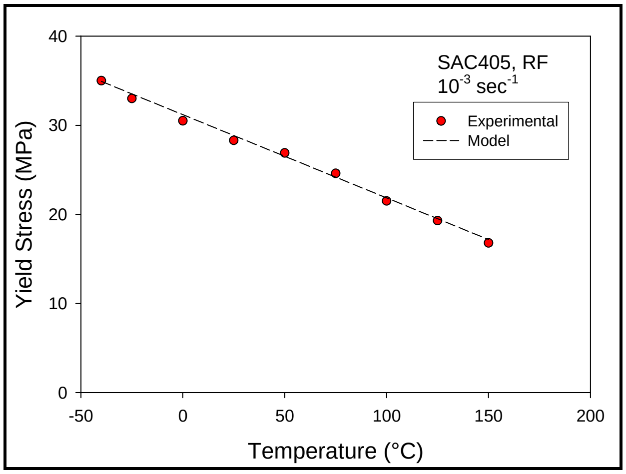

Figure 6.29 SAC405 Yield Stress Experimental vs. Constitutive Model.

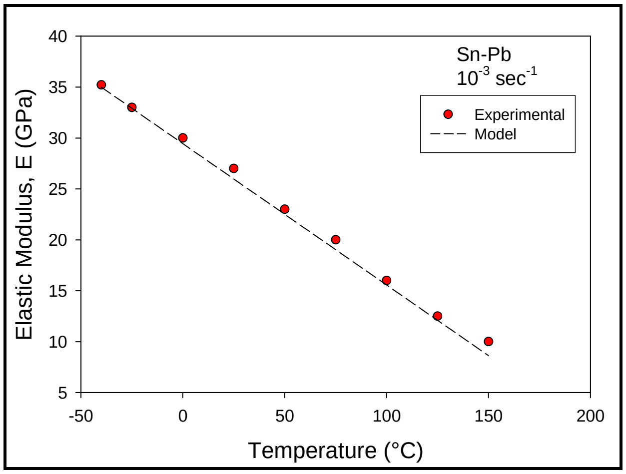

Figure 6.30 Sn-Pb Elastic Modulus Experimental vs. Constitutive Model.

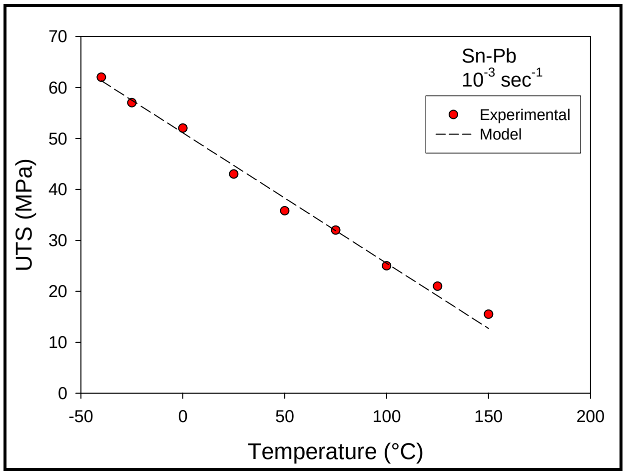

Figure 6.31 Sn-Pb UTS Experimental vs. Constitutive Model.

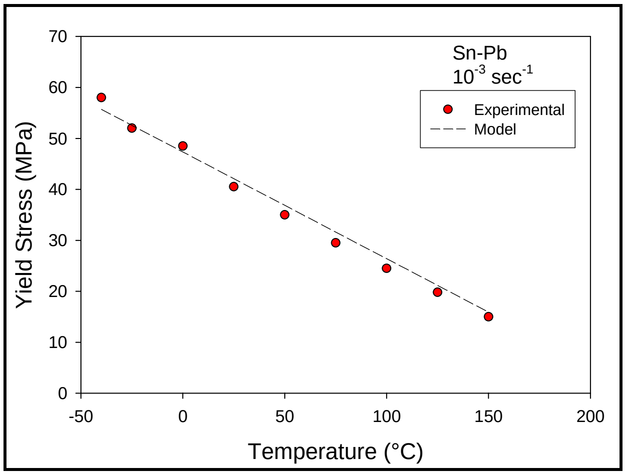

Figure 6.32 Sn-Pb Yield Stress Experimental vs. Constitutive Model.

Table 6.5 Constitutive Models of Tensile Properties at Various Temperature and Strain Rates for SAC405 and Sn-Pb Eutectic Solders.

Solder Type	Constitutive Models	R^2
SAC405	$E\ (T,\ \dot{\varepsilon}) = (1.35E\text{-}03T+3.20)\log(\dot{\varepsilon})+\text{-}0.17701T+55.57$	0.9944
	$\sigma_{UTS}\ (T,\ \dot{\varepsilon}) = (-0.2241T+70.98)\ [\dot{\varepsilon}]^{(2.00E\text{-}04T+0.06766)}$	0.9941
	$\sigma_{YS}\ (T,\ \dot{\varepsilon}) = (-0.7103T+45.59)\ [\dot{\varepsilon}]^{(2.76E\text{-}04T+0.05578)}$	0.9890
Sn-Pb Eutectic	$E\ (T,\ \dot{\varepsilon}) = (-1.33E\text{-}04T+2.20)\log(\dot{\varepsilon})+\text{-}0.14281T+36.12$	0.9964
	$\sigma_{UTS}\ (T,\ \dot{\varepsilon}) = (-0.4197T+132.83)\ [\dot{\varepsilon}]^{(4.92E\text{-}04T+0.1403)}$	0.9890
	$\sigma_{YS}\ (T,\ \dot{\varepsilon}) = (0.7689T+132.03)\ [\dot{\varepsilon}]^{(1.55E\text{-}03T+0.14768)}$	0.9655

The Shi *et al.*'s models were originally developed for Sn-Pb eutectic solder [39]. The data in this study proves that the constitutive models (Eq. 6.1 and 6.2) are also a good fit for SAC alloys. Compare with Shi *et al.*'s model for eutectic Sn-Pb, however, there are large variations. Figure 6.33 shows comparison of the elastic constitutive models for elastic modulus between Shi *et al.*'s model and our model at 10^{-3} sec^{-1}. The data variation may be caused by the differences of specimen preparation (Shi's specimens were machined), specimen geometry (Shi's are cylindrical) and size (Shi's dimensions are 30mm in gage length and 6 mm in diameter). It is also possible, as the data in Chapter 4 indicates, that the room temperature aging effects may also contribute to these inconsistencies. Shi *et al.*'s specimen was aged at 60 °C for 24 hours to reduce the machining residual stress. As explained previously, the machining method is not suitable for bulk specimen preparation for solder alloys due to the dramatic heating effects generated during the machining process. The testing conditions of Shi *et al*'s room temperature aging periods are also unclear.

6.4 Summary and Conclusions

Due to the CTE mismatch and variations in the operating conditions, solder joints will experience constant stresses at different strain rates and temperatures. Solder alloys are extremely sensitive to strain rates and temperature changes due to their high homologous temperatures. In this study, the effects of strain rates and temperature on the tensile properties of lead-free solder and Sn-Pb solders were investigated. The effects of room temperature aging on the tensile properties was considered and eliminated by aging the specimens at room temperature for up to 10 days to reach a relatively stable region.

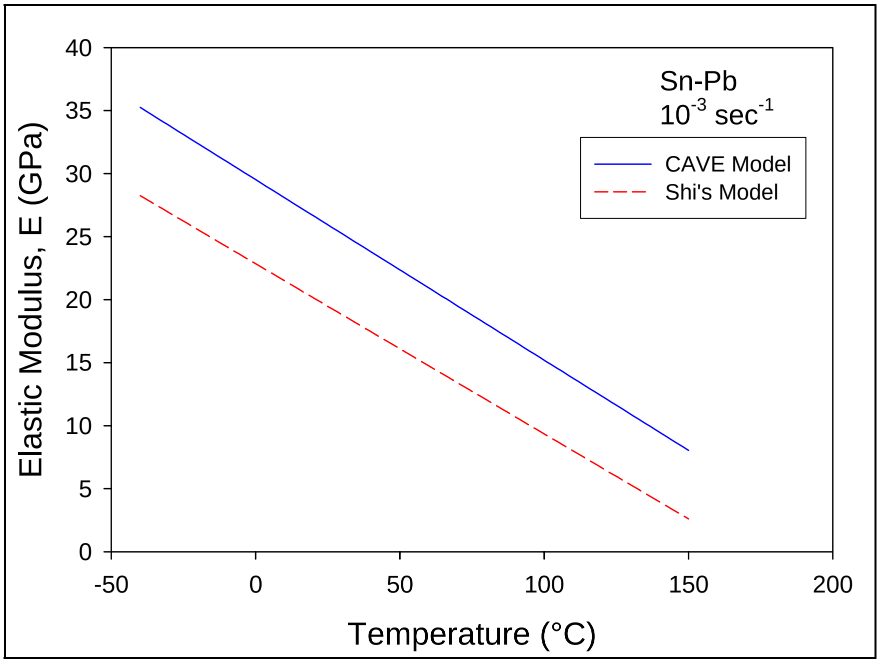

Figure 6.33 Comparison of the Constitutive Models with Shi's Model.

Constitutive models were obtained for both SAC405 and Sn-Pb solder alloys by fitting experimental data with Shi *et al.*'s models. The constitutive models provided a near perfect fit with the experimental data. Using the new constitutive models, the mechanical properties of solder alloys can be predicted for any testing conditions by applying both variables of strain rate and temperature. This data provided the baseline for finite element analysis by which the mechanical properties of the alloys at other conditions could be predicted. The data also shows a large deviation between our models and Shi *et al.*'s data for Sn-Pb eutectic solder. These discrepancies may be caused by the differences in specimen preparation and specimen dimensions. Room temperature aging effects may also have contributed to this discrepancy.

CHAPTER 7

CONSTITUTIVE MODELS OF CREEP FOR LEAD-FREE SOLDERS

7.1 Introduction

Solder joints in electronic packaging components are very complex elements. The study of solder joint reliability is also complex, especially in determining the mechanical reliability. Creep deformation is the dominate deformation in solder joints due to its high homologous temperature. Creep analysis is often adopted as one of the major approaches used to predict the end-of-life for solder joints by finite element analysis. As the literature review in Chapter 2 revealed, creep analysis of solders has been heavily studied. However, there are large discrepancies in the current data. This data scattering is probably due to differences in specimen preparation, geometry and size. As the data in Chapter 4 shows, room temperature aging has a significant effect on creep deformation, although none of the currently documented data has recognized this. In this study, reflowed specimens were aged at room temperature for 10 days before testing to reduce the contribution of decreasing creep resistance at room temperature. All specimens were tested under the same testing conditions. As previously mentioned in Chapters 1 and 2, the most widely accepted constitutive models for solder creep of are the Garofalo Hyperbolic Sine Law model (Eq. 1.6) and Dorn power-law model (Eq.1.7). Steady-state creep strain rates were obtained and data fitted with the available constitutive models in this study.

7.2 The Constitutive Relationship for Lead-free and Sn-Pb Eutectic Solders

Creep testing was carried out at different stress levels and various temperatures. Four stress levels were chosen, 20 MPa, 15 MPa, 10 MPa, and 7 MPa for both reflowed SAC405 and Sn-Pb specimens. Testing was completed at five temperature levels, 25 °C, 75 °C, 100 °C, 125 °C and 150 °C. All tests were conducted using the MT-200 Micro-tester with the thermal chamber attached. Figure 7.1 illustrates a typical set of creep curves at different stress levels for SAC405 solder. The creep deformation increases with increasing stress levels. Higher stresses will accelerate the movement of dislocations, which includes dislocation gliding and climb. Higher stresses will also induce greater grain boundary gliding. Dislocation gliding and grain boundary sliding are the major creep mechanisms for creep deformation. Figure 7.2 shows a set of typical creep curves at various temperatures and the same stress level, indicating that higher temperatures induces more severe creep deformation in solder alloys. Creep deformation is diffusion controlled, so a higher temperature will lead to a higher diffusion rate and a higher creep rate (Eq. 2.2). Figure 7.3 summarizes the steady-state creep strain rates vs. stress levels at various temperatures. The experimental data were fitted by multiple variables data fitting according to both the Garofalo Hyperbolic Sine Law and the Dorn power-law. Figure 7.4 shows the hyperbolic fitting of the experimental data, and Figure 7.5 illustrates the power-law fitting to the same experimental data.

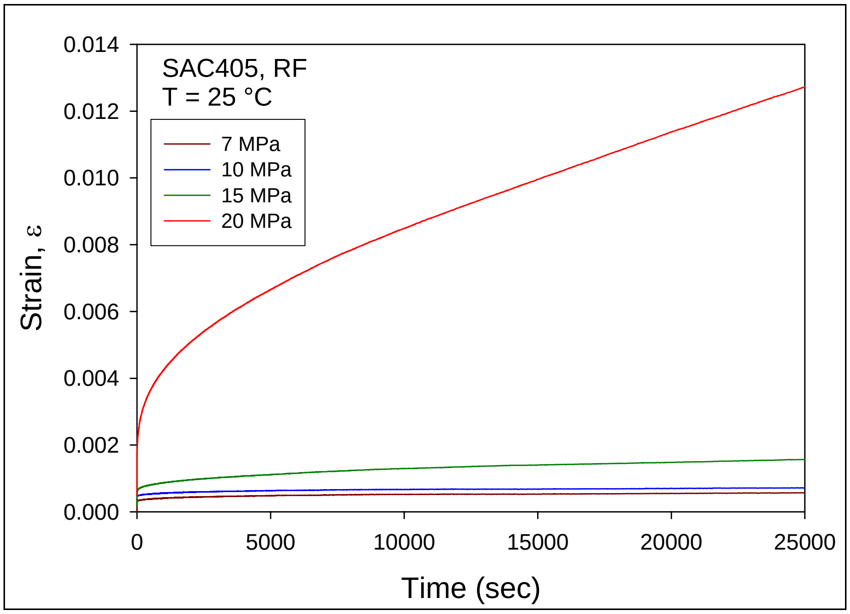

Figure 7.1 SAC405 Creep Curves at Different Stress Levels.

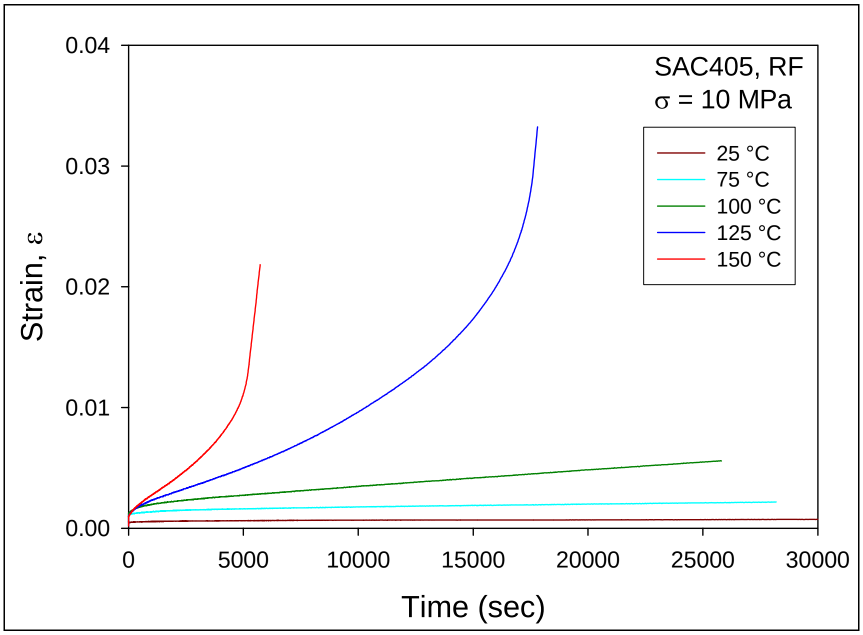

Figure 7.2 SAC 405 Creep Curves at Different Testing Temperatures.

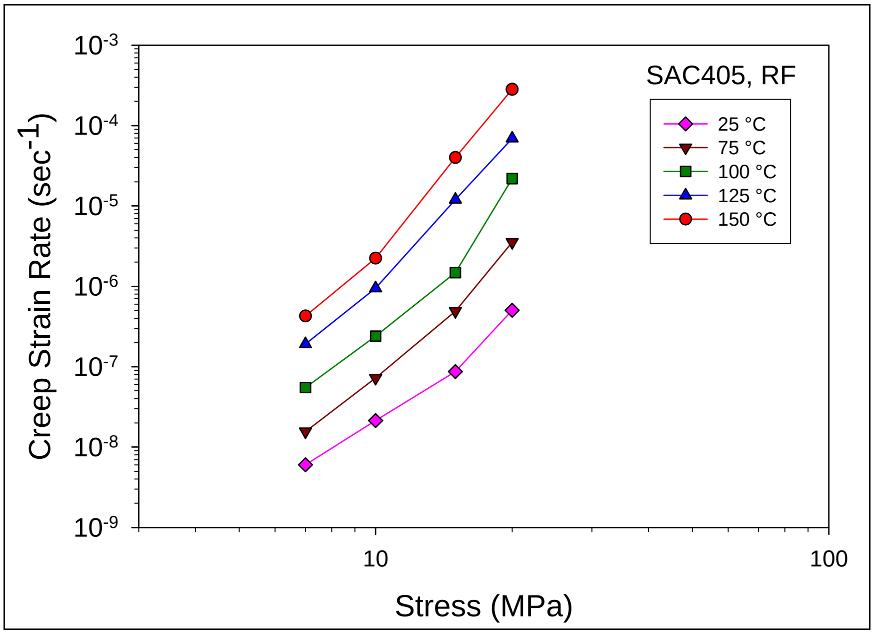

Figure 7.3 SAC405 Steady-State Creep Strain Rate vs. Stress.

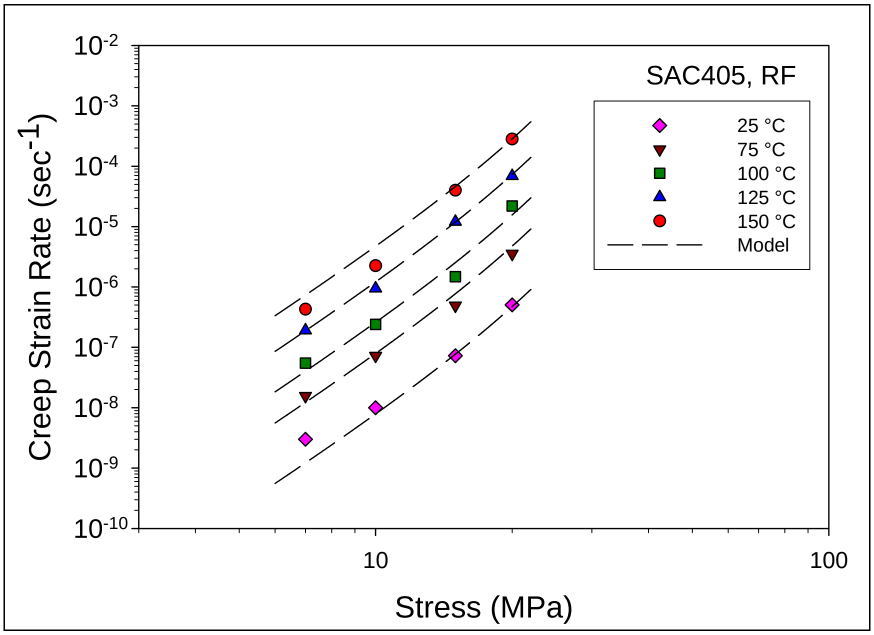

Figure 7.4 Hyperbolic Sine Creep Model of SAC405 Steady-state Creep Strain Rate.

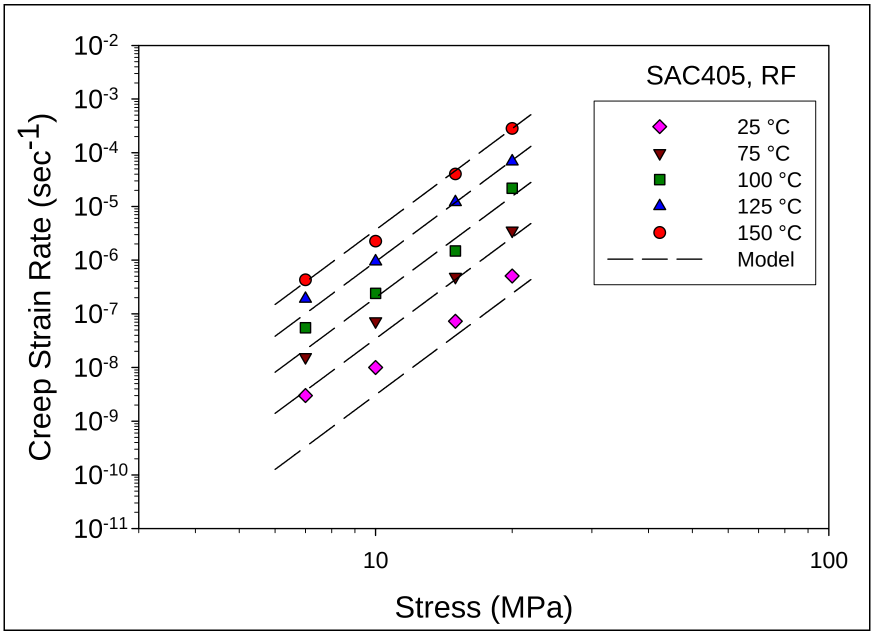

Figure 7.5 The Power- Law Model of Steady State Creep Strain Rate of SAC405.

All the materials constants were obtained by multiple variable data fitting methods. Eq. 7.1 is the hyperbolic sine law fitting of the SAC405 creep model. Eq. 7.2 is the fitting for the power-law model. Figure 7.6 compares the two models at the same testing temperature and stress level for the SAC405 alloy. The results indicate that at higher stress levels above 15 MPa, both models have an almost identical fit to the experimental data. However, at lower stress levels, hyperbolic sine model fits the experimental data better than the power-law model. The obtained constitutive models can be used to predict the end-of-life of the solder joints in numerical techniques such as finite element methods. Overall, Garofalo's hyperbolic model is a better model to fit the current experimental data. Figure 7.7 illustrates the comparison of the new constitutive model for SAC solder alloy with the models proposed by other researches (reviewed in Chapter 2), indicating that the new model appears to lie in the middle of all the current models for SAC alloys. As previously mentioned in Chapter 2, there are large discrepancies in the current data on constitutive modeling of creep. The discrepancies and data scattering may be caused by many factors, such as specimen preparation and cooling rate, specimen geometry and size, and testing conditions and testing methods. However, none of the currently documented data have recognized the possible contribution of room temperature aging effects in their studies of creep deformation analysis. Room temperature aging effects may be one of the major factors that are causing the large discrepancies in the current data.

$$\dot{\varepsilon} = 1.77\mathrm{E}+05\left[\sinh\left(5.48\mathrm{E}-02\sigma\right)\right]^{4.89}\exp\left(-\frac{76.13}{\mathrm{RT}}\right) \tag{7.1}$$

$$\dot{\varepsilon} = 5.09\mathrm{E}-03\sigma^{6.27}\exp\left(-\frac{76.2}{\mathrm{RT}}\right) \tag{7.2}$$

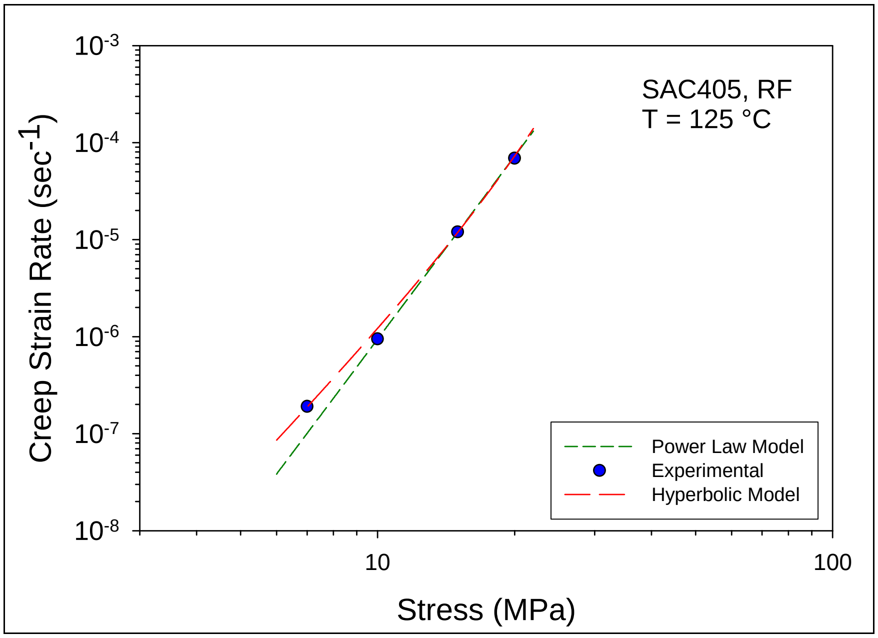

Figure 7.6 Comparison of Hyperbolic Sine Model and Power Law Model (SAC405).

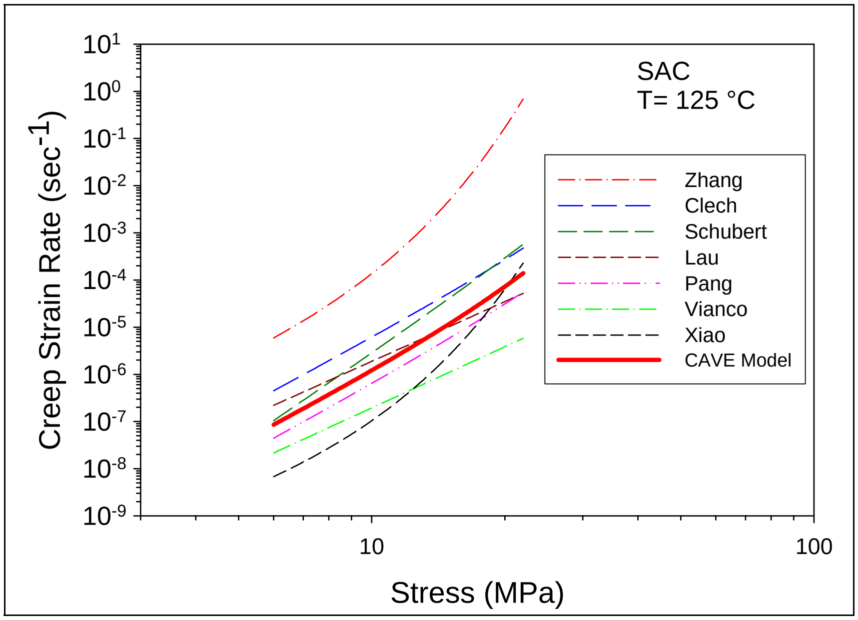

Figure 7.7 Comparison of Constitutive Creep Models of SAC Solder Alloys.

Corresponding data were also collected for reflowed Sn-Pb eutectic solder alloy and are illustrated in Figures 7.8-7.13. The figures reveal a similar trend as that of SAC405, where the higher stress and higher temperature induced more severe creep deformation (Figures 7.8-7.9).

The collected experimental data (Figure 7.10) were also fitted with multiple variables data fitting for both the Garofalo Hyperbolic Sine Law and the Dorn power-law models. The hyperbolic sine model for Sn-Pb is shown in Equation 7.3, and the power-law model is shown in Equation 7.4. Figure 7.13 shows the comparison between the two models for Sn-Pb eutectic solder alloy, and indicates similar results to those for SAC405. The two models show similar perfect fitting at higher stress levels above 15 MPa, and once again, the hyperbolic sine law model exhibits a better fit at lower stress levels. Overall, the Garofalo Hyperbolic Sine Law provides a better fit for the experimental data for Sn-Pb.

$$\dot{\varepsilon} = 0.908[\sinh(0.105\sigma)]^{1.51}\exp\left(-\frac{35.74}{RT}\right) \tag{7.3}$$

$$\dot{\varepsilon} = 2.87E-04\sigma^{2.58}\exp\left(-\frac{33.30}{RT}\right) \tag{7.4}$$

Comparing to the materials constants of Sn-Pb (Eq. 7.3-7.4) with that of SAC405 (Eq. 7.1-7.2), the activation energy of Sn-Pb is significantly smaller than that of the SAC405 alloy, indicating that the creep resistance of SAC405 is higher than that of the Sn-Pb. The stress component of Sn-Pb is also significantly smaller than that of SAC405, which also indicates lower creep resistance for Sn-Pb.

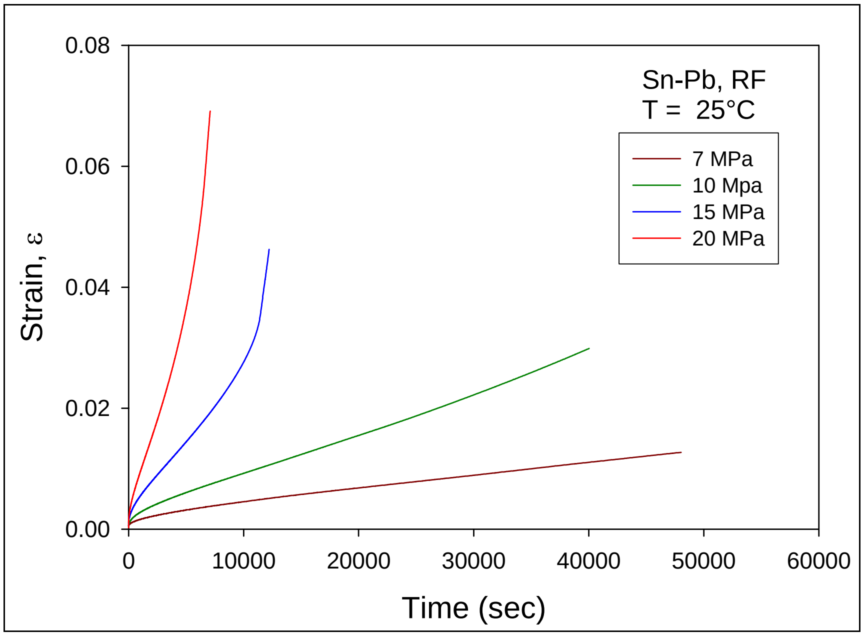

Figure 7.8 Sn-Pb Creep Curves at Different Stress Levels.

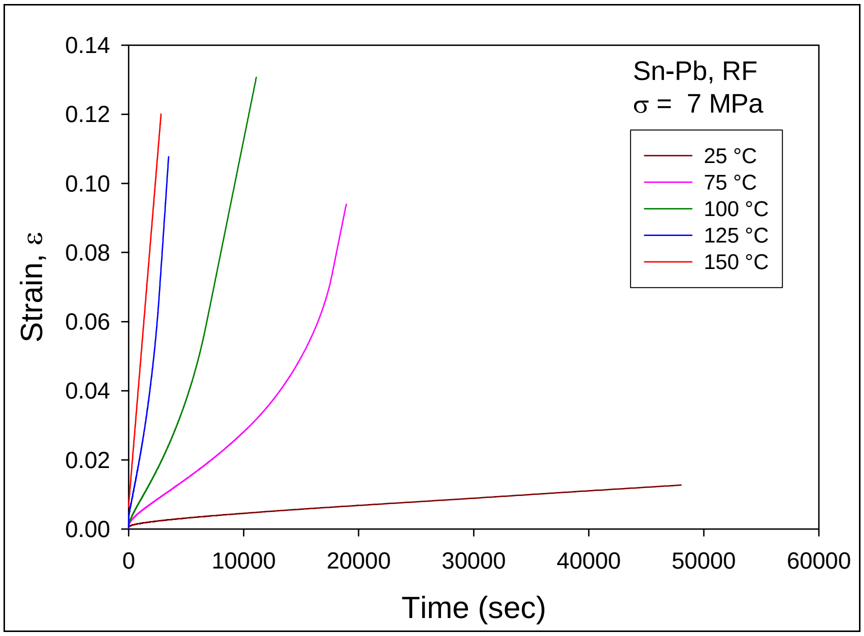

Figure 7.9 Sn-Pb Creep Curves at Different Testing Temperatures.

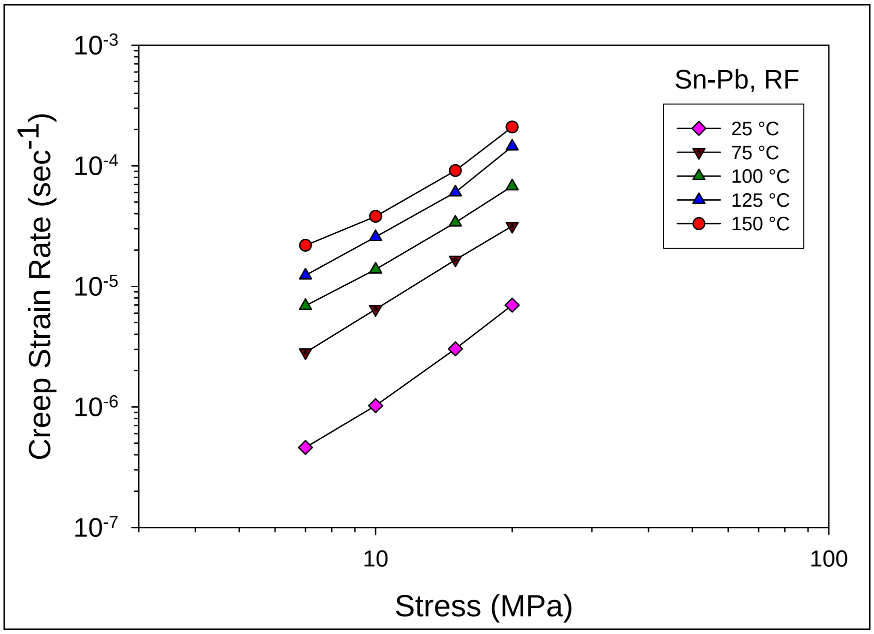

Figure 7.10 Sn-Pb Steady-State Creep Strain Rate vs. Stresses

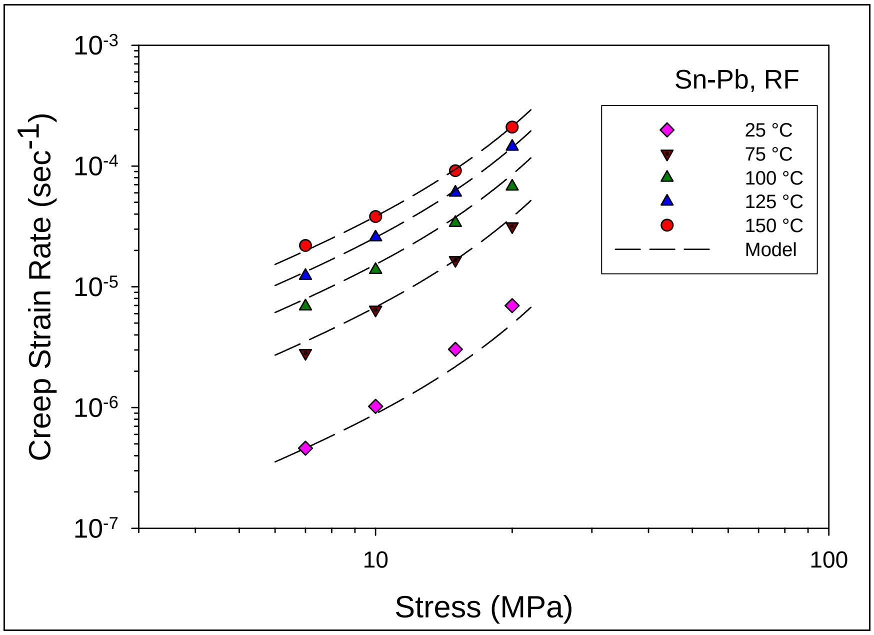

Figure 7.11 Hyperbolic Sine Creep Model of Sn-Pb Steady-State Creep Strain Rate.

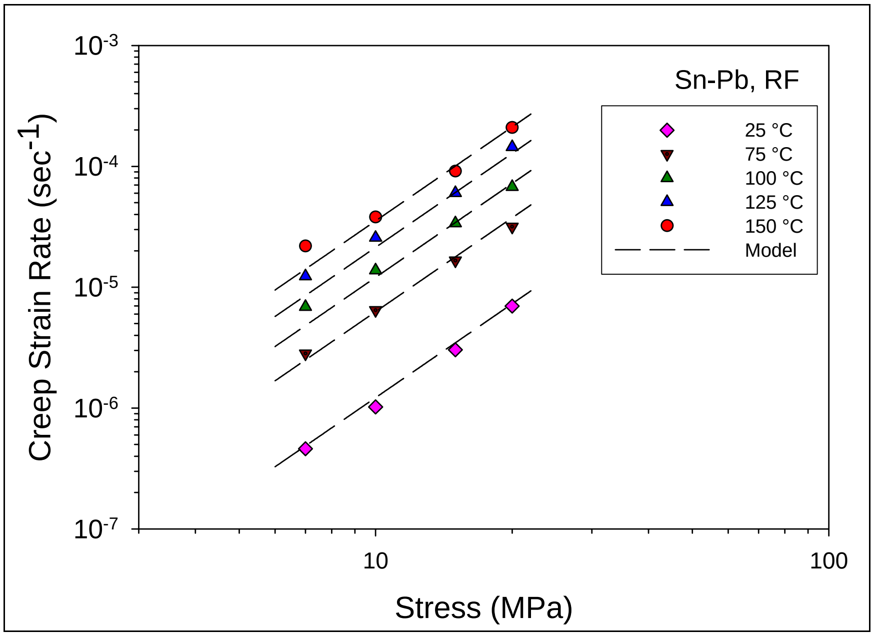

Figure 7.12 The Power- Law Model of Steady State Creep Strain Rate for Sn-Pb.

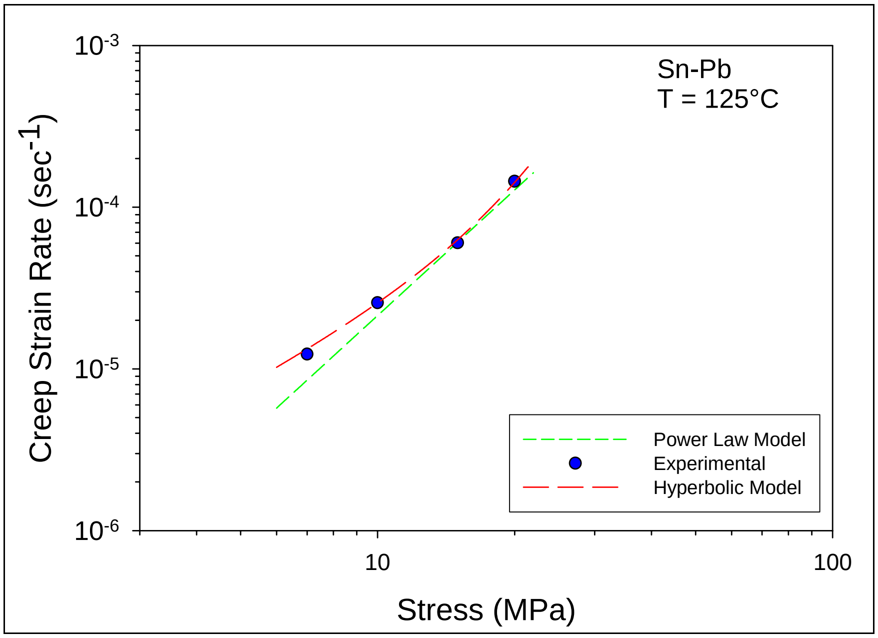

Figure 7.13 Comparison of Constitutive Creep Models (Sn-Pb).

Comparing Sn-Pb and SAC405, SAC405 has a higher creep resistance than Sn-Pb at the same stress level and testing temperature (Figure 7.14). The constitutive models also show that the SAC alloy possesses higher activation energy than Sn-Pb, which indicates that the SAC alloy has a higher creep resistance than Sn-Pb. Activation energy represents the height of the energy barrier the atoms have to overcome to diffuse and move to lower energy levels (Figure 7.15). Dorn, Garofalo and Weertman independently found that the creep activation energy equals the self-diffusion activation energy when $T_h \geq 0.5T_m$ [21, 27, 132, 133]. The homologous temperatures in the operational temperature range of solder alloys are greater than half of the melting points, indicating that the self-diffusion activation energy is the barrier that atoms must overcome to cause creep deformation in solder alloys.

The stress component in creep models represents the contribution of the applied stress effects to creep deformation. The values of these stress components are spread over a very large range. Hanke *et al*. proposed that the steady-state creep rate can be categorized in four regions [135]. As illustrated in Figure 7.16, regions I and II are grain or phase size dependent which possess low stress component ranges from 1 to 3. Region III and IV are independent of grain or phase size, and have higher stress components ranging from 3 to above 10. *Schubert et al.* concluded that the steady-state creep rate for lead-free solders fit into region III and IV, and thus can be predict by Garofalo Hyperbolic Sine Model [68]. Grivas *et al*. studied the Sn-Pb solder creep phenomena [136], and found that the steady-state creep model for Sn-Pb lies in region II and III. The differences of creep phenomena between lead-free and Sn-Pb solders are very apparent.

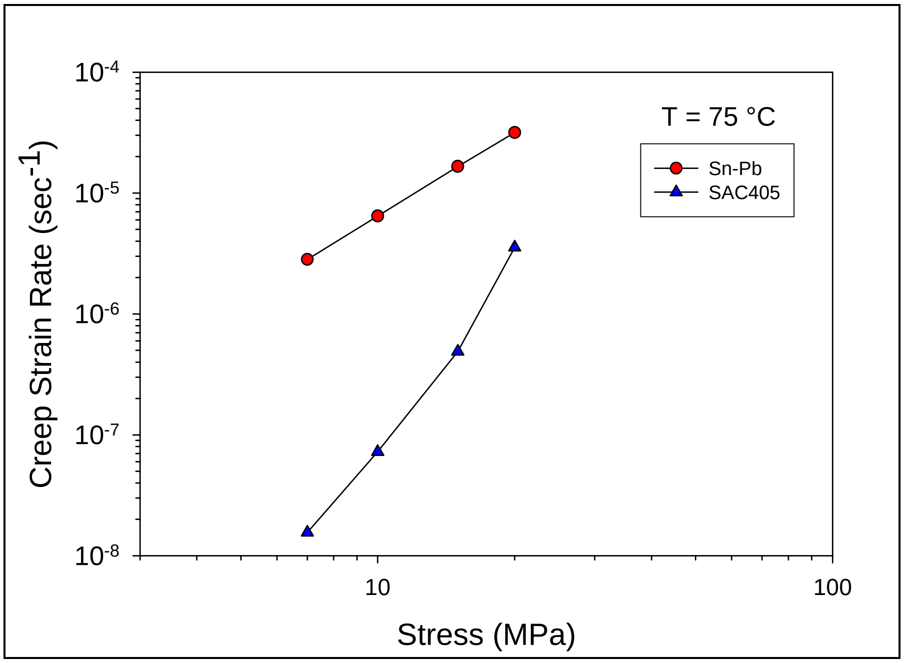

Figure 7.14 Comparison of Creep Rate of Sn-Pb vs. SAC405.

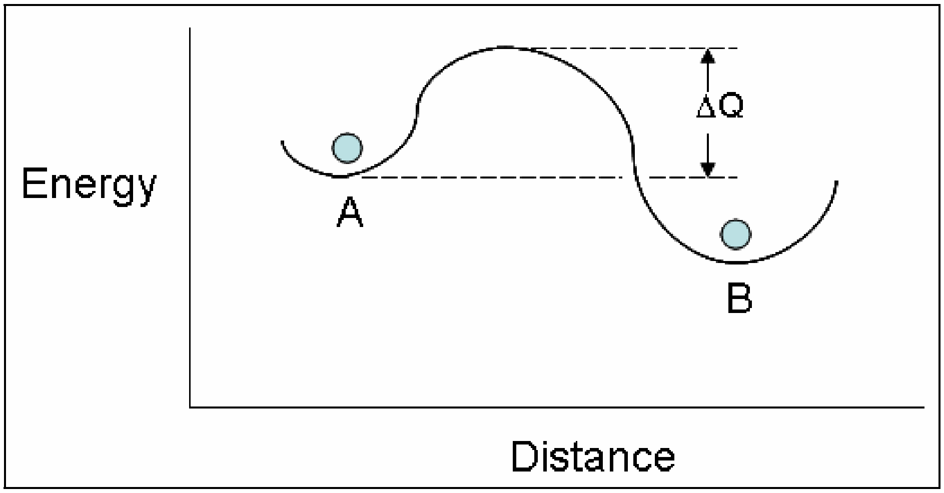

Figure 7.15 Activation Energy Required for Atomic Diffusion.

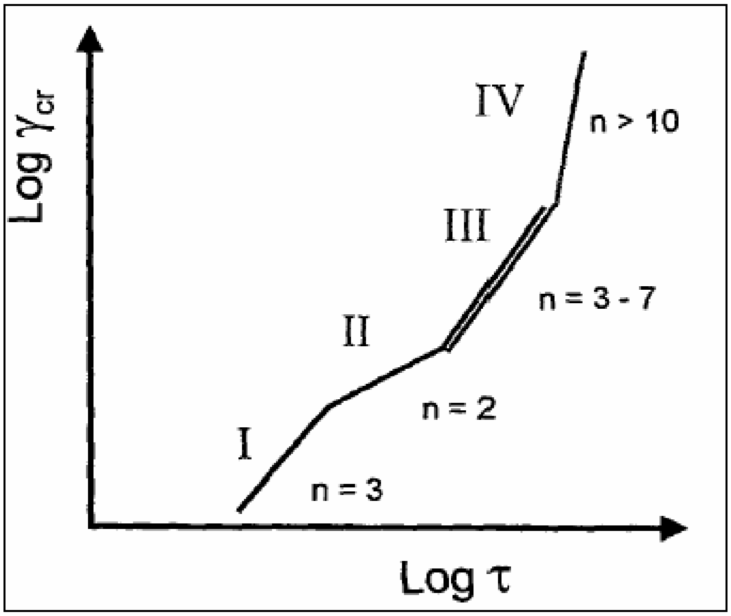

Figure 7.16 Steady-State Shear Creep Rate vs. Applied Shear Stress [68,135].

In this study, the stress component n is 4.9 for SAC405, which falls in region III, and 1.5 for Sn-Pb, which lies in region II.

7.3 The Mechanisms of Creep in Lead-free Solder Alloys

As discussed previously in Chapter 1, many mechanisms have been proposed for creep deformation (Figure 1.11). At higher stress levels the creep deformation is likely to involve dislocation glide and climb, while grain boundary diffusion (Coble Creep) and lattice diffusion (Nabarro-Herring Creep) may be the dominate creep mechanism at lower stress levels. Solder alloys are unique among other metals due to their extremely high homologous temperatures. At higher stresses, it is believed that dislocation creep is the dominate creep mechanism in solders, involving the dislocation climb and moving away from barriers. At lower stresses, the lattice diffusion is believed to be the dominate mechanism for solder alloys, involving the diffusion and migration of interstitial atoms and lattice vacancies along the grain boundaries due to the applied tension stresses. Grain boundary sliding can be accompanied with the above mechanisms at any stress level.

Dutta *et al.* proposed a so-called glide-climb mechanism at lower stress regime and particle-limited climb at high stresses for lead-free solders [134], arguing that creep is induced by dislocation glide and climb at lower stress levels. The second phase particles (Ag_3Sn and Cu_6Sn_5) act to pin down the dislocations, preventing them from contributing to deformation via climb at lower stresses. When stresses are high enough for the dislocation to break the threshold stress, the previously stuck dislocations will move rapidly to cause creep deformation, so the creep rate will increase rapidly after the applied stresses exceed the threshold stress needed for dislocations to break through.

Grivas *et al*. suggested that the creep of Sn-Pb eutectic solder alloys exhibits both superplastic deformation and matrix creep [136]. Superplasticity occurs at high temperatures (> $0.5T_m$), where the material exhibits great ductility before failure. The total strain can reach 1000% [21]. The dominant superplasticity mechanism is grain boundary sliding. For Sn-Pb, especially at elevated temperatures and low stress levels, the creep mechanism will be a combination of superplastic and matrix creep, involving both dislocation creep and lattice diffusion creep.

7.4 Summary and Conclusions

Creep failure has been one of the major failure modes for solder joints in electronic packaging applications due to the high homologous temperature of solders. Constitutive models can be utilized to predict the end-of-life for electronic packaging products using finite elements methods. As previous discussed in Chapter 2, there are large discrepancies in the published data. In this study, the possible contribution of room temperature aging effects has been taken into account and minimized. All creep testing was carried out under controlled pre-testing conditions.

SAC405 was found to have a higher creep resistance than Sn-Pb solder at the same stress level and testing temperature. The constitutive models obtained showed that the activation energy for SAC405 is much higher than that of Sn-Pb, which also indicates that SAC405 possesses higher creep resistance. This higher creep resistance is contributed by the second phase intermetallic compounds, Ag_3Sn and Cu_6Sn_5, which can effectively block dislocation movement. The constitutive models can be used in finite element analysis of actual electronic packages to predict the solder joints failure.

Creep mechanisms at high stresses involve both dislocation gliding and dislocation climb. At low stresses, lattice diffusion and grain boundary diffusion are believed to be the major mechanisms for both SAC405 and Sn-Pb. At lower stresses, the superplastic deformation due to grain boundaries sliding is also believed to be a major creep mechanism for Sn-Pb.

CHAPTER 8

CONCLUSIONS

8.1 Literature Review on the Properties of Lead-free Solders

Tensile properties and creep analysis were extensively reviewed for Sn-Ag-Cu (SAC) series lead-free solder alloys. The review revealed large discrepancies in the documented research database. The elastic modulus values for SAC alloys range from 30-54 GPa, the UTS values are in the range of 30-60 MPa, and yield stresses range from 20-47 MPa. The constitutive creep modeling data are also widely scattered for both SAC alloys and Sn-Pb eutectic solder. These large discrepancies of data may be due to the differences in testing conditions, such as specimen preparation, specimen geometry and dimensions, testing methods, and testing strain rates. However, none of the sources took into account room temperature aging effects, which may lead to significant data variations even under the same testing conditions due to the high homologous temperatures of solder alloys. Room temperature aging effects may have played a major role in the discrepancies in the data.

8.2 Unique Specimen Preparation Procedure

A unique specimen preparation procedure was successfully developed for this study using a vacuum suction process. Using this method, a controlled microstructure can be achieved. Another advantage of this approach is that the specimen can be reflowed with the glass tube mold on with an existing reflow profile which is similar to the real electronic packaging reflow profile. As a result of this, it is hope that more researchers will adopt this method of acquiring outstanding bulk specimen in the future. Allowing data can be compared and reducing deviations in the data.

8.3 Room Temperature Aging Effects

Room temperature aging effects for tensile and creep properties for both lead-free and Sn-Pb eutectic solders were investigated. The results showed that there are significant tensile strength reductions over a two month long room temperature aging period. The tensile strength reduced by up to 40% for the water quenched condition, and up to 30% for the reflowed condition samples. The reflowing process slightly reduces the effects of room temperature aging on tensile strength loss. The tensile properties of SAC305 are slightly poorer than that of SAC405.

Room temperature aging also significantly deteriorated the creep resistance of both lead-free and Sn-Pb solders. Creep deformation increased dramatically with increasing aging time. The results also showed that although the tensile strength of SAC305 is only slightly less than that of SAC405, the creep deformation at the same stress level for SAC305 is much more severe than that of SAC405, although the difference becomes smaller at lower stress level.

Microstructure coarsening during room temperature aging was also observed. The phase structure grew coarser at longer aging durations for both lead-free and Sn-Pb solders. In Sn-Pb solders, both the Sn-rich phase and Pb-rich phase grew into a coarser phase structure. In SAC alloys, the dendrites grew into larger dendrites, and the second phase intermetallic compounds, Ag_3Sn and Cu_6Sn_5, grew into a much coarser structure as the aging time increased.

By emphasizing the uniqueness of high homologous temperatures of solders alloys, this study of the effect of room temperature aging on the mechanical properties of solders provides a baseline for further studies in this area. The experimental procedure given here can be used to investigate the properties of any other tin based lead-free or lead content solder alloys in a reproducible fashion. The recognition of the importance of room temperature effects is likely to significantly reduce the scattering of the research data due the variations in the testing conditions for specimens.

8.4 Aging at Elevated Temperatures

Elevated temperature aging effects were also studied by eliminating the possible contributions due to room temperature aging on the mechanical properties of solders. Aging at elevated temperatures exhibited much more significant effects than for the room temperature aging. Thermal aging causes significant losses in tensile strength and increases in of creep deformation. Thermal aging results also show that after an initial tensile strength drop, the Sn-Pb eutectic solder reached a relatively stable stage after 200 hours of aging. However, for the SAC alloy, both the tensile and creep properties continued to degrade with increasing aging time.

It is worth noting that the creep deformation of SAC alloy is only better than Sn-Pb at room temperature and shorter aging times at elevated temperature. There is a cross-over point at about 50 hours of aging at 125 °C. The creep resistance of the SAC alloy was lower than that of Sn-Pb for longer aging durations.

8.5 Temperature and Strain Rate Effects

The mechanical properties of solder alloys are both temperature and strain rate dependent due to their high homologous temperatures. In this study, both the effects of strain rate and temperature were investigated for lead-free and Sn-Pb solders by preconditioning the specimen at room temperature for 10 days to eliminate possible contributions due to room temperature aging. Linear relationships were then found between the temperature and tensile properties. The tensile strength deteriorated dramatically with higher testing temperatures. Power law relationships were found between strain rate and the tensile properties. The tensile strength increased with increasing testing strain rates in power relationship. Comprehensive constitutive models were also obtained for both strain rate and temperature. The constitutive functions can be used to predict key mechanical properties under other testing conditions.

8.6 Investigation of Constitutive Modeling of Solder Creep

Previous studies of the constitutive modeling of creep have been extensive studies due to the important of the creep failure mode in solder joints. However, none of the research data has considered, or even mentioned, the effects of room temperature aging. This study investigated constitutive modeling of creep of solders by taking into account the possible contribution room temperature aging.

Lead-free solder (SAC405) was found to have a higher creep resistance than Sn-Pb solder at the same stress level and testing temperature. The higher creep resistance was contributed by the second phase intermetallic compounds, Ag_3Sn and Cu_6Sn_5. The precipitation of these intermetallic compounds can significantly block the movement of dislocations and increase the creep resistance of the material.

Constitutive models of creep for both lead-free and Sn-Pb eutectic solders were constructed based on the experimental data. The activation energy for SAC405 is much higher than that of Sn-Pb, which also indicates that SAC405 possesses higher creep resistance. The constitutive models can be used in finite element analysis of actual electronic packages to predict solder joint failure. The creep mechanisms of both lead-free and Sn-Pb eutectic solders were also extensively discussed in this dissertation. Dislocation gliding and climb is believed to be the major failure mode at high stresses, while lattice diffusion and grain boundary diffusion is believed to be the major failure mode at low stress levels. Grain boundary sliding is believed to contribute to creep deformation at both high stresses and low stresses. For eutectic Sn-Pb, superplastic deformation is a major the creep mechanism at low stresses and high temperatures.

REFERENCES

1. Allenby, B. R., Ciccarelli, J. P., "An Assessment of the Use of Lead in Electronic Assembly," *Proceeding of Surface Mount International Conference*, pp. 1-28, 1992.
2. Turbini, L. J., "Examining the Environmental Impact of Lead-free Soldering Alternatives," *IEEE Transaction on Electronics Packaging Manufacturing*, Vol. 24 (1), pp. 4-9, 2001.
3. Hwang, J. S., *Implementing Lead-free Electronics*, McGraw-Hill, pp. 1-9, 2004.
4. http://www.jeita.or.jp/english/press/2002/1217/attached.htm.
5. Grusd, A., "Integrity of Solder Joints from Lead-free Solder Paste," *Proceedings of the Technical Program NEPCON West*, pp. 212-221, 1999.
6. IPC Roadmap: *A Guide for Assembly of Lead-free Electronics*, IPC, Northbrook, IL, 2000.
7. Abtew, M., Selvaduray, G., "Lead-Free Solders in Microelectronics," *Materials Science and Engineering*, Vol. 27, 2000, pp. 95-141.
8. Zeng, K., Tu, K. N., "Six Cases of Reliability Study of Pb-free Solder Joints in Electronic Packaging Technology," *Materials Science and Engineering*, Vol. 38, 2002, pp. 55-105.
9. Karlya, Y., Gagg, C., Plumbridge, W. J., "The Tin Pest in Lead-free Solders," *Soldering and surface Mount Technology*, Vol. 13, pp. 39-40, 2000.
10. Lee, N. C., "Getting Ready for Lead-free Solders," *Soldering & Surface Mount Technology*, Vol. 26, pp.65-74, 1997.
11. Soldertec, *European Lead-free Roadmap*, Ver.1, pp. 1-26, 2002.
12. Deubzer, O., Hamano, H., Suga, T., "Lead-free – Toxicity, Energy and Resource Consumption," *Proceedings of the 2001 IEEE International Symposium on Electronics and the Environment*, pp. 290-295, 2001.
13. Nimmo, K., "Alloy Selection," Chapter 3 of *Lead-free Soldering in Electronics: Science, Technology and Environmental Impact*, edited by K. Suganuma, New York, Marcel Dekker, pp. 61-62, 2004.
14. http://www.tulane.edu/~sanelson/geol212/ternaryphdiag.htm.
15. http://www.metallurgy.nist.gov/phase/solder/solder.html.
16. Ye, L., Lai, Z. H., Liu, J., Thölén, A., "Microstructure Investigation of Sn-0.5Cu-3.5Ag and Sn-3.5Ag-0.5Cu-0.5B Lead-free Solders," *Soldering & Surface Mount*

Technology, Vol. 13, pp. 16-20, 2001.

17. Iting, T., Li, J. T., Yen, S. F., Chuang, T. H., Lo, R., Ku, T., Wu, E., "Identification of Mechanical Properties of Intermetallic Compounds on Lead Free Solder," *Proceedings of the 55th Electronic Components and Technology Conference*, pp. 687-691, 2005.
18. Fields, R. J., Low, S. R., "Physical and Mechanical Properties of Intermetallic Compounds Commonly Found in Solder Joints," available online at: http://www.metallurgy.nist.gov/mechanical_properties/solder_paper.html.
19. Ganesan, S., Pecht, M., *Lead-free Electronics*, Wiley-Interscience Publication, pp. 51-52, 2006.
20. Hwang, J., *Environment-Friendly Electronics: Lead Free Technology*, Electrochemical Publications, pp. 134-137, 2001.
21. Hertzberg, R. W., *Deformation and Fracture Mechanics of Engineering Materials*, John Wiley & Sons Inc, 4th edition, 1996.
22. Thornton, P. A., Colangelo V. J., *Fundamentals of Engineering Materials*, Prentice-Hall, Inc., pp. 227-229, 1985.
23. Gilman, J. J., *Micromechanics of Flow in Solids*, McGraw-Hill, New York, 1969.
24. Ralls, K. M., Courtney, T. H., Wulff, J., I*ntroduction to Materials Science and Engineering*, Wiley, 1976.
25. Lau, J. H., Pao, Y. H., *Solder Joints Reliability of BGA, CSP, Flip-Chip, and Fine Pitch SMT Assemblies*, McGraw-Hill, 1997.
26. Cadek, J., *Creep in Metallic Materials*, Elsevier Science Publisher, 1988.
27. Garofalo, F., *Fundamentals of Creep and Creep-Rupture in Metals*, The Macmillan Company, 1966.
28. Evans, R. W., Wilshire, B., *Creep of Metals and Alloys*, The Institute of Metals, 1985.
29. Ashby, M. F., "A First Report on Deformation-mechanism Maps," *Acta Metallurgica*, Vol. 20, pp. 887-897, 1972.
30. Weertman, J., "Steady-State Creep through Dislocation Climb," *Journal of Applied Physics*, Vol. 28, 1957, pp. 362-366.
31. Coble, R. L., "A Model for Boundary Diffusion Controlled Creep in Polycrystalline Materials," *Journal of Applied Physics*, Vol. 34, pp. 1679-1682, 1963.
32. Nabarro, F. R. N., "Report of a Conference on the Strength of Solids," *Physical Society*, London, pp. 75-81, 1948.
33. Herring, C., "Diffusional Viscosity of a Polycrystalline Solid," *Journal of Applied Physics*, Vol.21, pp. 437-445, 1950.
34. Shi, X. Q., Wang, Z. P., Yang, Q. J., Pang, H. L. J., "Creep Behavior and Deformation Mechanism Map of Sn-Pb Eutectic Solder Alloy,"

Journal of Engineering Materials and Technology, Vol. 125, pp. 81-88, 2003.

35. Mukherjee, A. K., Bird, J. E., and Dorn, J. E., "Experimental Correlation for High-Temperature Creep," *Transactions of American Society for Metals*, Vol. 62, pp. 155-179, 1969.
36. Puttlitz, K. J., Stalter, K. A., *Handbook of Lead-free Solder Technology for Microelectronic Assemblies*, Marcel Dekker Publication, 2004.
37. Nose, H., Sakane, M., Tsukada, Y., Nishimura, H., "Temperature and Strain Rate Effects on Tensile Strength and Inelastic Constitutive Relationship of Sn-Pb Solders," *Journal of Electronic Packaging*, Vol. 125 (1), pp. 59-66, 2003.
38. McCormack, M., Chen, H. S., Jin, S., "New Lead-Free Sn-Ag-Zn-Cu Solder Alloys with Improved Mechanical Properties," *Applied Physics Letters*, Vol. 65 (10), pp. 1233-1235, 1994.
39. Shi, X. Q., Zhou, W., Pang, H. L. J., Wang, Z. P., "Effect of Temperature and Strain Rate on Mechanical Properties of 63Sn/37Pb Solder Alloy," *Journal of Electronic Packaging*, Vol. 121 (3), pp. 179-185, 1999.
40. Pang, J. H. L., Xiong, B. S., Neo, C. C., Zhang, X. R., and Low, T. H., "Bulk Solder and Solder Properties for Lead Free 95.5Sn-3.8Ag-0.7Cu Solder Alloy," *Proceeding of the 53rd Electronic Components and Technology Conference*, pp. 673-679, 2003.
41. Pang, J. H. L., Xiong, B. S., Low, T. H., "Low Cycle Fatigue Models for Lead-Free Solders," *Thin Solid Films*, Vol. 462-463, pp. 408-412, 2004.
42. Yeung, B., Jang, J. W., "Correlation Between Mechanical Tensile Properties and Microstructure of Eutectic Sn-3.5Ag Solder," *Journal of Materials Science Letters*, Vol. 21, pp. 723-726, 2002.
43. Kim, K. S., Huh, S. H., Suganuma, K., "Effects of Cooling Speed on Microstructure and Tensile Properties of Sn-Ag-Cu Alloys," *Materials Science and Engineering*, Vol. A333, pp. 106–114, 2002.
44. Madeni, J. C., Liu, S., Siewert, T., "Casting of Lead-free Solder Bulk Specimens with Various Solidification Rates," *Proceedings of the ASM International Conference*, 2002.
45. Lin, J. K., De Silva, A., Frear, D., Guo, Y., Hayes, S., Jang, J. W., Li, L., Mitchell, D., Yeung, B., Zhang, C., "Characterization of Lead-Free Solders and Under Bump Metallurgies for Flip-Chip Packages," *IEEE Transactions on Electronics Packaging Manufacturing*, Vol. 25 (4), pp. 300-307, 2002.
46. Chuang, C. M., Liu, T. S., Chen, L. H., "Effect of Aluminum Addition on Tensile Properties of Naturally Aged Sn-9Zn Eutectic Solder," *Journal of Materials Science*, Vol. 37 (1), pp. 191-195, 2002.
47. Vianco P. T., Rejent J. A., Grant, R., "Development of Sn-Based, Low- Melting Temperature Pb-free Solder Alloys," *Transaction of Japan Institute of Metallurgy*, Vol. 45, pp. 765-775, 2004.

48. Xiao, Q., Nguyen, L., Armstrong, W. D., "Aging and Creep Behavior of Sn3.9Ag0.6Cu Solder Alloy," *Proceedings of the 54th Electronic Components and Technology Conference*, pp. 1325-1332, 2004.

49. Xiao, Q., Bailey, H. J, Armstrong, W. D., "Aging Effects on Microstructure and Tensile Property of Sn3.9Ag0.6Cu Solder Alloy," *Journal of Electronic Packaging*, Vol. 126 (2), pp. 208-212, 2004.

50. Shohji, I., Yoshida, T., Takahashi, T., Hioki, S., "Tensile Properties of Sn-Ag Based Lead-Free Solders and Strain Rate Sensitivity," *Materials Science and Engineering*, Vol. A366, pp. 50-55, 2004.

51. Tsukada, Y., Nishimura, H., Yamamoto, H., and Sakane, M., "A Strain Rate Ratio Approach for Assessing Creep-Fatigue Life of 63Sn-37Pb Solder Under Shear Loading, *Journal of Electronic Packaging*, Vol. 127 (4), pp. 407-414, 2005.

52. Yang, H., Phillip, D., Paul, M., Murty, K. L., "Creep Deformation of 96.5Sn-3.5Ag Solder Joints in a Flip Chip Package," *Proceeding of 46th Electronic Components and Technology Conference*, pp. 1136-1142, 1996.

53. Liu, C. Y. Chen, C., Mal, A. K., Tu, K. N., "Direct Correlation between Mechanical Failure and Metallurgical Reaction in Flip Chip Solder Joints," *Journal of Applied Physics*, Vol. 85 (7), pp. 3882-3886, 1999.

54. Rhee, H., Subramanian, K. N., Lee, A., Lee, J. G., "Mechanical Characterization of Sn-3.5Ag Solder Joints at Various Temperatures," *Soldering and Surface Mount Technology*, Vol. 15 (3), pp. 21-26, 2003.

55. Pang, J. H. L., Low, T. H., Xiong, B. S., Xu, L., Neo, C. C., "Thermal Cycling Aging Effects on Sn–Ag–Cu solder Joint Microstructure, IMC and Strength," *Thin Solid Films*, Vol. 462-463, pp. 370-375, 2004.

56. Darveaux, R., "Shear Deformation of Lead Free Solder Joints," *Proceedings of the 55th Electronic Components and Technology Conference*, pp. 882-893, 2005.

57. Obaid, A. A., Sloan, J. G., Lamontia, M. A., Paesano, A., Khan, S., Gillespie, J. W., "Test Method Development to Quantify the In Situ Elastic and Plastic Behavior of 62%Sn-36%Pb-2%Ag Solder Ball Arrays in Commercial Area Array Packages at −40 °C, 23 °C, and 125 °C," *Journal of Electronic Packaging*, Vol. 127 (4), pp. 483-495, 2005.

58. Zhang, Q., Dasgupta, A., Nelson, D., Pallavicini, H., "Systematic Study on Thermo-Mechanical Durability of Pb-Free Assemblies: Experiments and FE Analysis," *Journal of Electronic Packaging*, Vol. 127 (4), pp. 415-429, 2005.

59. Chromik, R. R., Vinci, R. P., Allen, S. L., Notis, M. R., "Measuring the Mechanical Properties of Pb-Free Solder and Sn-Based Intermetallics by Nanoindentation," *JOM*, Vol. 55 (6), pp. 66-69, 2003.

60. Vianco P. T., Rejent J. A., Martin J. J., "The Compression Stress-Strain Behavior of Sn-Ag-Cu Solder," *JOM*, Vol. 55 (6), pp. 50-55, 2003.

61. Vianco P. T., Rejent J. A., "Compression Deformation Response of 95.5Sn-3.9Ag-0.6Cu Solder," *UCLA Workshop on Pb-free Electronics*, 2002. Available at: http://www.seas.ucla.edu/eThinFilm/PbfreeWorkshop/pdf/vianco.pdf.

62. Vianco P. T., "Fatigue and Creep of Lead-free Solder Alloys: Fundamental Properties," Chapter 3 *Lead-free Solder Interconnect Reliability*, Edited by D. Shangguan, ASM International, pp. 67-106, 2006.

63. Vianco, P. T., Rejent, J.A., Kilgo, A.C., "Time-independent Mechanical and Physical Properties of the Ternary 95.5Sn-3.9Ag-0.6Cu Solder, *Journal of Electronic Materials*, Vol. 32 (3), pp. 142-151, 2003.

64. Xu, L., Pang, J. H. L., "Nanoindentation on SnAgCu Lead-free Solder and Analysis," *Proceeding of the 55th Electronics Packaging Technology Conference*, pp. 357-362, 2005.

65. Fouassier, O., Heintz, J.-M., Chazelas, J., Geffroy, P.-M., Silvaina, J.-F., "Microstructural Evolution and Mechanical Properties of SnAgCu Alloys," *Journal of Applied Physics*, Vol. 100, pp. 1-8, 2006.

66. Pang, J. H. L., Xiong, B. S., "Mechanical Properties for 95.5Sn-3.8Cu-0.7Cu Lead-free Solder Alloy," *IEEE Transaction on Component and Packaging Technology*, Vol. 28 (4), pp. 830-840, 2005.

67. Wiese, S., Schubert, A., Walter, H., Dudek, R., Feustel, F., Meusel, E., Michel, B., "Constitutive Behavior of Lead-free Solders vs. Lead-containing Solders - Experiments on Bulk Specimens and Flip-Chip Joints," *Proceeding of the 51st Electronic Components and Technology Conference*, pp. 890-902, 2001.

68. Schubert, A., Walter, H., Dudek, R., Michel, B., Lefranc, G., Otto, J., Mitic, G., "Thermo-Mechanical Properties and Creep Deformation of Lead-Containing and Lead-Free Solders," *International Symposium on Advanced Packaging Materials*, pp. 129-134, 2001.

69. Li, D., Liu, C., Conway, P., "Micromechanical Characterization of Sn-Ag-Cu Solder FCOB Interconnects at Ambient and Elevated Temperatures," *Proceeding of the 54th Electronic Components and Technology Conference*, pp. 128-133, 2004.

70. Harrison, M. R., Vincent J. H., Steen, H. A. H., "Lead-free Reflow Soldering for Electronic Assembly," *Soldering & Surface Mount Technology*, Vol. 13 (3), pp. 21-38, 2001.

71. Rhee, H., Lucas, J. P., Subramanian, K. N., "Micromechanical Characterization of Thermo-mechanically Fatigued Lead-free Solder Joints," *Journal of Materials Science: Materials in Electronics*, Vol. 13, pp. 477-484, 2002.

72. Allen, S. L., Notis, M. R., Chromik, R. R., Vinci, R. P., "Microstructural Evolution in Lead-free Solder Alloys. Part I: Cast Sn-Ag-Cu Eutectic," *Journal of Materials Research*, Vol. 19, pp. 1417-1424, 2004.

73. Allen, S. L., Notis, M. R., Chromik, R. R., Vinci, R. P., Lewis, D. J., Schaefer, R., "Microstructural Evolution in Lead-free Solder Alloys. Part II: Directionally Solidified Eutectic Sn-Ag-Cu, Sn-Cu and Sn-Ag alloys," *Journal of Materials*

Research, Vol. 19, pp. 1425-1431, 2004.

74. Xiao, L., Liu, J., Lai, A., Ye, L., Tholen, A., "Characterization of Mechanical Properties of Bulk Lead-free Solders," *International Symposium on Advanced Packaging Materials*, pp. 145-151, 2000.

75. Kanchanomai, C., Miyashita, Y., Mutoh, Y., "Low Cycle Fatigue Behavior of Sn-Ag, Sn-Ag-Cu and Sn-Ag-Cu-Bi Lead-free Solders," *Journal of Electronic Materials*, Vol. 31, pp. 456-465, 2002.

76. Zhu, F., Wang, Z., Guan, R., Zhang, H., "Mechanical Properties of Lead-Free Solder Alloys," *2005 International Conference on Asian Green Electronics*, pp. 107-112, 2005.

77. Madeni, J., Liu, S., Siewert, T., "Casting of Lead-free Solder Bulk Specimens with Various Solidification Rates," *NIST Pb-free data*. Available at: http://www.boulder.nist.gov/.

78. Biglari, M. H., Oddy, M., Oud, M. A., Davis, P., "Pb-Free Solders Based on SnAgCu, SnAgBi, SnCu and SnCu for Wave Soldering of Electronic Assemblies," *Proceeding of Electronics Goes Green 2000+ Conference*, pp. 73-82, 2000.

79. Seelig K., Suraski, D., "The Status of Lead-free Solder Alloys," *Proceeding of the 50th Electronic Components and Technology Conference*, pp. 1405-1409, 2000.

80. *AIM Lead-free Guide*, 2003.

81. Enke, N. F., Kilinski, T. J., Schroeder, S. A., Lesniak, J. R., "Mechanical Behaviors of 60/40 Tin-lead Solder Lap Joints," *IEEE Transactions on Components, Hybrids, and Manufacturing Technology*, Vol. 12 (4), pp. 459-468, 1989.

82. McCabe, R. J., Fine, M. E., "Athermal and Thermally Activated Plastic Flow in Low Melting Temperature Solders at Small Stresses," *Scripta Materialia*, Vol. 39(2), pp. 189-195, 1998.

83. Lau, J. H., Pao, Y.-H., "*Solder Joint Reliability of BGA, CSP, Flip Chip, and Fine Pitch SMT Assemblies*," McGraw-Hill, New York, 1997.

84. Technical Reports for the Lead Free Solder Project: Properties Reports: "Room Temperature Tensile Properties of Lead-Free Solder Alloys." *Lead Free Solder Project CD-ROM*, National Center for Manufacturing Sciences (NCMS), 1998. Available at: *http://www.boulder.nist.gov/*.

85. Lau, J. H., Chang, C., Lee, S. W. R., Chen, T. Y., Cheng, D., Tseng, T. J. and Lin, D., "Thermal-Fatigue Life of Solder Bumped Flip Chip on Micro Via-In-Pad (VIP) Low Cost Substrates," *Proceeding of NEPCON-West 2000*, pp. 554-562, 2000.

86. Wong, T., Matsunaga, A. H., "Ceramic Ball Grid Array Solder Joint Thermal Fatigue Life Enhancement," *Proceeding of NEPCON West Conference*, 1995. Available at: *http://www.boulder.nist.gov/*.

87. Sigelko, J. D., Subramanian, K. N., "Overview of Lead-free Solders," *Advanced Materials and Processing*, pp. 47-48, 2000.

88. Welco Castings, *Solder Data Sheet*, 2 Hillyard Street, Hamilton, Ontario, Canada. Available at: http://www.boulder.nist.gov/.

89. Hernandez, C. L., Vianco, P. T., Rejent, J. A., "Effect of Interface Microstructure on the Mechanical Properties of Pb-Free Hybrid Microcircuit Solder Joints," *IPC/SMTA Electronics Assembly Expo,* pp. S19-2-1, 1998. Available at: http://www.boulder.nist.gov/.

90. Darveaux, R., Banerji, K., Mawer, A., Dody, G., "Reliability of Plastic Ball Grid Array Assembly," in *Ball Grid Array Technology* (ed. J. L. Lau), McGraw-Hill, New York, pp. 379-442, 1995.

91. Lau, J. H., Chang, C., "TMA, DMA, DSC, and TGA of Lead Free Solders," *Proceeding of the 48th Electronic Component and Technology Conference*, pp. 1339-1344, 1998.

92. Kim, K. S., Huh, S. H., Suganuma, K., "Effects of Cooling Speed on Microstructure and Tensile Properties of Sn–Ag–Cu Alloys," *Materials Science and Engineering A,* pp. 106-114, 2002.

93. Amagai, M., Watanabe, M., Omiya, M., Kishimoto, K., Shibuya, T., "Mechanical characterization of Sn–Ag–based lead-free solders," *Microelectronics Reliability*, Vol. 42, pp. 951-966, 2002.

94. Kariya, Y., Plumbridge, J., "Mechanical properties of Sn-3.0mass% Ag 0.5mass%Cu alloy," *7th Symp. Microjoining and Assembly in Electronics*, pp. 383-388, 2001.

95. Shohji, I., Yoshida, T., Takahashi, T., Hioki, S., "Tensile Properties of Sn-Ag Based Lead-free Solders and Strain Rate Sensitivity," *Materials Science and Engineering A*, Vol. A366, pp. 50-55, 2004.

96. Medvedev, A. S., "Aging of Tin-Lead Solders and Joints Soldered by Them," *Metallovedenie i Obrabotka Metallov,* No. 7, pp. 16-23, 1956.

97. Lampe, B. T. "Room Temperature Aging Properties of Some Solder Alloys," *Welding Journal*, Vol. 55 (10), pp. 330s-340s, 1976.

98. Miyazawa, Y., Ariga, T., "Microstructural Change and Hardness of Lead Free Solder Alloys," *Proceedings of the First International Symposium on Environmentally Conscious Design and Inverse Manufacturing*, pp. 616-619, 1999.

99. Miyazawa, Y., Ariga T., "Influences of Aging Treatment on Microstructure and Hardness of Sn-(Ag, Bi, Zn) Eutectic Solder Alloys," *Materials Transactions of the Japan Institute of Metals*, Vol. 42 (5), pp. 776-782, 2001.

100. Chilton, A. C., Whitmore, M. A., Hampshire, W. B., "Fatigue Failure in a Model SMD Joint," *Soldering and Surface Mount Technology*, Vol. 3, pp. 21-24, 1989.

101. Gagliano, R. A., Fine, M. E., Vaynman, S., Stolkarts, V., "Shear Testing of Solder Joints: The Effect of Various Parameters on the Maximum Shear Stress of Eutectic Tin-Lead Solder," *Advanced Materials for the 21st Century: Proceedings of the 1999 Julia R. Weertman Symposium*, pp. 107-116, 1999.

102. Coyle, R. J., Solan, P. P., Serafino, A. J., Gahr, S. A., "The Influence of Room Temperature Aging on Ball Shear Strength and Microstructure of Area Array Solder Balls," *Proceedings of the 50th Electronic Components and Technology Conference*, pp. 160-169, 2000.

103. Tsui, Y. K., Lee, S. W., Huang, X., "Experimental Investigation on the Degradation of BGA Solder Ball Shear Strength Due to Room Temperature Aging," *Proceedings of the 4th International Symposium on Electronic Materials and Packaging*, pp. 478-481, 2002.

104. Lee, S. W. R., Tsui, Y. K., Huang, X., Yan, C. C., "Effects of Room Temperature Storage Time on the Shear Strength of PBGA Solder Balls," *Proceedings of the 2002 ASME International Mechanical Engineering Congress and Exposition*, pp. 1-4, 2002.

105. Hasegawa, K., Noudou, T., Takahashi, A., Nakaso, A., "Thermal Aging Reliability of Solder Ball Joint for Semiconductor Package Substrate," *Proceedings of the 2001 SMTA International*, pp. 1-8, 2001.

106. Li, M., Lee, K. Y., Olsen, D. R., Chen, W. T., Tan, B. T. C., Mhaisalkar, S., "Microstructure, Joint Strength and Failure Mechanisms of SnPb and Pb-Free Solders in BGA Packages," *IEEE Transactions on Electronics Packaging*, Vol. 25(3), pp. 185-192, 2002.

107. Chou, G. J. S., "Microstructure Evolution of SnPb and SnAgCu BGA Solder Joints During Thermal Aging," *Proceedings of the 8th Symposium on Advanced Packaging Materials*, pp. 39-46, 2002.

108. Law, C. M. T., Wu, C. M. L., "Microstructure Evolution and Shear Strength of Sn-3.5Ag-RE Lead Free BGA Solder Balls," *Proceedings of HDP'04*, pp. 60-65, 2004.

109. Wang, Q., Johnson, R. W, Ma, H., Gale, W. F., "Properties of Lead-Free Solder Alloys as a Function of Composition Variation," *10th Electronic Circuit and World Convention Conference (ECWC 10)*, 2005.

110. Ding, Y., Wang, C., Li, M., Bang, H. S., "Aging Effects on Fracture Behavior of 63Sn37Pb Eutectic Solder During Tensile Tests under the SEM," *Materials Science and Engineering*, Vol. A384, pp. 314-323, 2004.

111. Darveaux, R., "Shear deformation of lead free solder joints," *Proceedings of the 55th Electronic Components and Technology Conference*, pp. 882-893, 2005.

112. Lin, J.-K., Jang, J.-W., Hayes, S., Frear, D, "Lead-Free Flip Chip Interconnect Reliability for DCA and FC-PBGA Packages," *Proceeding of the 54th Electronics Packaging Technology Conference*, pp. 642-649, 2004.

113. Wiese, S., Meusel, E., Wolter, K.-J., "Microstructural Dependence of Constitutive Properties of Eutectic SnAg and SnAgCu Solders," *Proceeding of the 53rd Electronics Packaging Technology Conference*, pp. 197-206, 2003.

114. Banerji, K., Darveaux, R., "Effect of Aging on the Strength and Ductility of Controlled Collapse Solder Joints," *Proceeding of TMS-AIME Symposium*, pp. 431-442, 1992.

115. Sasaki, K., Kobayashi, T., "Correlation between Creep and Uniaxial Ratchetting of Sn/37Pb and Sn/3Ag/0.5cu Solder Alloys," *Proceeding of the ASME InterPACK'05*, 2005.

116. Jones, W. K., Liu, Y., Zampino, M. A., Gonzalez, G., Shah, M., *Design and Reliability of Solders and Solder Interconnections*, TMS, 1997.

117. Jones, W. K., Liu, Y., Zampino, M. A., Gonzalez, G., "The At-Temperature Mechanical Properties of Lead-Tin Based Alloys," *Advanced Microelectronics*, pp. 30-34, 1997.

118. Pang, H. L. J., Wang, Y. P., Shi, X. Q., Wang, Z. P., "Sensitivity of Temperature and Strain Rate Dependent Properties on Solder Joints Fatigue Life," *IEEE/CPMT Electronics Packaging Technology Conference*, pp. 184-189, 1998.

119. Nose, H., Sakane, M., Tsukada, T., Nishimura, H., "Temperature and Strain Rate Effects on Tensile Strength and Inelastic Constitutive Relationship of Sn-Pb Solders," *Journal of Electronic Packaging*, Vol. 124, pp. 59-66, 2003.

120. Plumbridge, W. J., Gagg. C. R., "Effects of Strain Rate and Temperature on the Stress-strain Response of Solder Alloys," *Journal of Materials Science: Materials in Electronics*, Vol. 10, pp. 461-468, 1999.

121. Lang, R., Tanaka, H., Munegata, O., Taguchi, T., Narita, T., "The Effect of Strain Rate and Temperature on the Tensile Properties of Sn-3.5Ag Solder," *Materials Characterization*, Vol. 54, pp. 223-229, 2005.

122. Dai, L. H., Lee, S. R., "Characterization of Strain Rate-Dependent Behavior of 63Sn-37Pb Solder Alloy," *Proceeding of the ASME InterPACK'05*, pp. 307-313, 2001.

123. Darveaux, R., Banerji, K., "Constitutive Relations for Tin-Based Solder Joints," *IEEE Transaction on Components, Hybrids, and Manufacturing Technology*, Vol.15 (6), pp. 1013-1024, 1992.

124. Xiao, Q., Armstrong, W. D., "Tensile Creep and Microstructural Characterization of Bulk Sn3.9Sg0.6Cu Lead-free Solder," *Journal of Electronic Material*s, Vol. 34 (2), pp. 196-210, 2005.

125. Lau, J., Dauksher, W., Vianco, P., "Acceleration Models, Constitutive Equations, Reliability of Lead-free Solders and Joints," *Proceeding of the 53rd Electronic Components and Technology Conference*, pp. 229-236, 2003.

126. Pang, J. H. L., Xiong, B. S., Low, T. H., "Creep and Fatigue Characterization of Lead-free 95.5Sn-3.8Ag-0.7Cu Solder," *Proceeding of 54th Electronic Components and Technology Conference*, pp. 1333-1337, 2004.

127. Zhang, Q., Dasgupta, A., Haswell, P., "Viscoplastic Constitutive Properties and Energy-Partitioning Model of Lead-free Sn3.9Ag0.6Cu Solder Alloy," *Proceeding of the 53rd Electronic Components and Technology Conference*, pp. 1862-1868, 2003.

128. Schubert, A., Dudek, R., Auerswald, E., Gollbardt, A., Michel, B., Reichl, H., "Fatigue Life Models for SnAgCu and SnPb Solder Joints Evaluated by Experiments and Simulation," *Proceeding of the 53rd Electronic Components and Technology Conference*, pp. 603-610, 2003.

129. Clech, J. P., "Review and Analysis of Lead-free Materials Properties," NIST, Available at: *http://www.metallurgy.nist.gov/solder/clech/Sn-Ag-Cu_Main.htm*

130. Hall, E. O., "The Deformation and Aging of Mild Steel: III Discussion of Results," *Proceedings of the Physical Society*, Vol. 64, pp. 747-753, 1951.

131. Petch, N. J., "The Cleavage Strength of Polycrystals," *Journal of the Iron and Steel Institute*, Vol. 174, pp. 25-28, 1953.

132. Dorn, J. E., *Creep and Recovery*, ASM Publication, Metal Park, OH, pp. 255-259, 1957.

133. Weertman, J., "Dislocation Climb Theory of Steady-State Creep, noting Necessity of Self Diffusion Mechanism in any High Temperature Creep Theory," *ASM Transactions Quarterly,* Vol. 61, pp. 681-694. 1968.

134. Dutta, I., Park, C., Choi, S., "Impression Creep Characterization of Rapidly cooled Sn-3.5Ag Solders," *Materials Science and Engineering A*, Vol. 379, pp. 401-410, 2004.

135. Hanke, P. L., Sprecher, A. F., Conrad, H., "Microstructure Coarsening During Thermo-Mechanical Fatigue of Pb-Sn Solder Joints," *Journal of Electronic Materials*, Vol. 26, pp. 774-782, 1997.

136. Grivas, D., Murty, K. L., Morris, J. W. Jr., "Deformation of Pb--Sn eutectic alloys at relatively high strain rates," *Acta Metallurgica*, Vol. 27, pp. 731-737, 1979.

137. Anand, L., "Constitutive Equations for Hot-working of Metals," *International Journal of Plasticity*, Vol. 1, pp. 213-231, 1985.

138. Pei, M., Qu, J., "Constitutive Modeling of Lead-free Solders," *International Symposium on Advanced Packaging Materials: Processes, Properties and Interfaces*, pp. 45-49, 2005.

139. Pang, J. H. L., Low, P. T. H., Xiong, B. S., "Lead-free 95.5Sn-3.8Ag-0.7Cu Solder Joint Reliability Analysis for Micro-BGA assembly," *Proceeding of ITHERM '04*. Vol. 2, pp. 131-136, 2004.

140. Rodgers, B., Flood, B., Punch, J., Waldron, F., "Experimental Determination and Finite Element Model Validation of the Anand Viscoplasticity Model Constants for SnAgCu," *Proceedings of the 6th International Conference on Thermal, Mechanical and Multi-Physics Simulation and Experiments in Micro-Electronics and Micro-Systems*, pp. 490-496, 2005.